Structures Research
Report 2012/92174

University of Florida
Civil and Coastal Engineering

UF

University of Florida
Civil and Coastal Engineering

Final Report **July 2012**

Pendulum impact testing of an impact-breakaway, wind-resistant base connection for multi-post ground signs

Principal investigator:
Gary R. Consolazio, Ph.D.

Research assistants:
Long H. Bui
Robert A. Walters

Department of Civil and Coastal Engineering
University of Florida
P.O. Box 116580
Gainesville, Florida 32611

Sponsor:
Florida Department of Transportation (FDOT)
William Potter, P.E. – Project manager

Contract:
UF Project No. 92174
FDOT Contract No. BDK75 977-40

DISCLAIMER

The opinions, findings, and conclusions expressed in this publication are those of the authors and not necessarily those of the State of Florida Department of Transportation.

SI (MODERN METRIC) CONVERSION FACTORS

*APPROXIMATE CONVERSIONS **TO** SI UNITS*

SYMBOL	WHEN YOU KNOW	MULTIPLY BY	TO FIND	SYMBOL
LENGTH				
in	inches	25.4	millimeters	mm
ft	feet	0.305	meters	m
yd	yards	0.914	meters	m
mi	miles	1.61	kilometers	km
AREA				
in^2	square inches	645.2	square millimeters	mm^2
ft^2	square feet	0.093	square meters	m^2
yd^2	square yard	0.836	square meters	m^2
ac	acres	0.405	hectares	ha
mi^2	square miles	2.59	square kilometers	km^2
VOLUME				
fl oz	fluid ounces	29.57	milliliters	mL
gal	gallons	3.785	liters	L
ft^3	cubic feet	0.028	cubic meters	m^3
yd^3	cubic yards	0.765	cubic meters	m^3
NOTE: volumes greater than 1000 L shall be shown in m^3				
MASS				
oz	ounces	28.35	grams	g
lb	pounds	0.454	kilograms	kg
T	short tons (2000 lb)	0.907	Megagrams	Mg (or "t")
TEMPERATURE (exact degrees)				
^oF	Fahrenheit	5(F-32)/9 or (F-32)/1.8	Celsius	^oC
ILLUMINATION				
fc	foot-candles	10.76	lux	lx
fl	foot-Lamberts	3.426	$candela/m^2$	cd/m^2
FORCE and PRESSURE or STRESS				
kip	1000 pound force	4.45	Kilonewtons	kN
lbf	pound force	4.45	newtons	N
lbf/in^2	pound force per square inch	6.89	kilopascals	kPa

1. Report No.	2. Government Accession No.	3. Recipient's Catalog No.

4. Title and Subtitle	5. Report Date
Pendulum Impact Testing of an Impact-Breakaway, Wind-Resistant Base Connection for Multi-Post Ground Signs	July 2012
	6. Performing Organization Code
	8. Performing Organization Report No.
7. Author(s) Gary R. Consolazio, Long H. Bui, Robert A. Walters	2012/92174
9. Performing Organization Name and Address University of Florida Department of Civil and Coastal Engineering 365 Weil Hall, P.O. Box 116580 Gainesville, FL 32611-6580	10. Work Unit No. (TRAIS)
	11. Contract or Grant No. BDK75 977-40
12. Sponsoring Agency Name and Address Florida Department of Transportation Research Management Center 605 Suwannee Street, MS 30 Tallahassee, FL 32399-0450	13. Type of Report and Period Covered Final Report February 2011 – May 2012
	14. Sponsoring Agency Code

15. Supplementary Notes

16. Abstract

Roadside signs play an important role in traffic control systems and must be placed adjacent to roadways. If they are not designed, fabricated, and installed properly, ground signs may pose potential hazards to vehicle passengers in the event of a vehicular collision with a sign structure. Ground signs must be strong enough to resist hurricane wind loading and self-weight, and yet sufficiently frangible to avoid extreme vehicular deceleration on impact. Such deceleration can cause abrupt occupant deceleration or excessive vehicle compartment deformation, either of which can cause serious or fatal occupant injuries. Consequently, sign structures located adjacent to roadways are generally designed to break away or yield under vehicle impact loading. Presently, a breakaway slip-base connection system is used in Florida. The breakaway mechanism of this system, however, depends on specific pretension levels in the bolts of the connection. Therefore, the performance of this system is undesirably sensitive to the level of bolt-torque that is imposed during installation and maintenance.

In this study, a new breakaway sign post base connection, the 'shear-controlled moment collar', was developed and subjected to static and dynamic testing. The new connection system is capable of resisting code-specified equivalent static hurricane wind loads, but also breaks away under low energy impact (vehicular) loads. Development of the connection involved several phases: conceptual development using nonlinear dynamic finite element analysis; structural design; validation of wind load capacity using static experimental testing; and validation of breakaway performance using pendulum impact testing. Experimental determination of friction coefficients for Teflon sheets, used in conjunction with structural steel, was also carried out. In addition, a permanent high-energy impact pendulum test facility was designed and constructed as part of this research and used to conduct dynamic impact tests on the newly developed breakaway connection.

17. Key Words	18. Distribution Statement
Sign, support structure, impact, collision, breakaway, finite element analysis, dynamic analysis, experimental static testing, structural support design specifications, friction.	No restrictions.

19. Security Classif. (of this report)	20. Security Classif. (of this page)	21. No. of Pages	22. Price
Unclassified	Unclassified	269	

Form DOT F 1700.7 (8-72). Reproduction of completed page authorized

ACKNOWLEDGEMENTS

The authors thank the Florida Department of Transportation (FDOT) for providing the funding that made this research possible. Additionally, the authors acknowledge the significant contributions made by FDOT personnel, especially FDOT Structures Research Center personnel. First and foremost, the forward-looking research vision of the late Marcus H. Ansley resulted in the development of the FDOT high-energy impact pendulum that was constructed as part of this project. Marc envisioned a pendulum impact facility capable not only of serving the needs of this project, but also of a broad range of future projects focusing on increasing the safety of Florida's highways through improved understanding of impact loading conditions. Marc's vision, guidance, and enthusiasm were keys to bringing about the successful construction of the FDOT impact pendulum. In addition, the following individuals also contributed greatly to the success of this project by providing technical insights and suggestions; reviewing proposed designs; fabricating pendulum components and test-articles; providing data acquisition; and conducting pendulum impact tests: Sam Fallaha, William Potter, David Wagner, Andre Pavlov, Stephen Eudy, Chris Weigly, Paul Tighe, Tony Hobbs, David Allen, Frank Cobb, and several others. The contributions of these individuals made this project a truly collaborative effort between the FDOT Structures Research Center and the University of Florida (UF) and directly led to the success of the project.

The authors would also like to thank Martin Hargrave of the Federal Highway Administration (FHWA) Turner-Fairbank Highway Research Center (TFHRC) and Dhafer Marzougui of the National Crash Analysis Center (NCAC) at The George Washington University (GWU) for hosting, in 2006, a visit by Marc Ansley (FDOT) and Gary Consolazio (UF) to the FHWA Federal Outdoor Impact Laboratory (FOIL). During that visit, Mr. Hargrave and Dr. Marzougui offered numerous technical insights and suggestions that influenced the design and construction of the FDOT impact pendulum in a positive manner.

EXECUTIVE SUMMARY

Roadside signs play an important role in traffic control systems and must be placed adjacent to roadways. If they are not designed, fabricated, and installed properly, ground signs may pose potential hazards to vehicle passengers in the event of a vehicular collision with a sign structure. Ground signs must be strong enough to resist hurricane wind loading and self-weight, and yet sufficiently frangible to avoid extreme vehicular deceleration on impact. Such deceleration can cause abrupt occupant deceleration or excessive vehicle compartment deformation, either of which can cause serious or fatal occupant injuries. Consequently, sign structures located adjacent to roadways are generally designed to break away or yield under vehicle impact loading. Presently, a breakaway slip-base connection system is used in Florida. The breakaway mechanism of this system, however, depends on specific pretension levels in the bolts of the connection. Therefore, the performance of this system is undesirably sensitive to the level of bolt-torque that is imposed during installation and maintenance.

In this study, a new breakaway sign post base connection, the 'shear-controlled moment collar', was developed and subjected to static and dynamic testing. The new connection system is capable of resisting code-specified equivalent static hurricane wind loads, but also breaks away under low energy impact (vehicular) loads. Development of the connection involved several phases: conceptual development using nonlinear dynamic finite element analysis; structural design; validation of wind load capacity using static experimental testing; and validation of breakaway performance using pendulum impact testing. Experimental determination of friction coefficients for Teflon sheets, used in conjunction with structural steel, was also carried out. In addition, a permanent high-energy impact pendulum test facility was designed and constructed as part of this research and used to conduct dynamic impact tests on the newly developed breakaway connection.

TABLE OF CONTENTS

LIST OF FIGURES

Figure Page

LIST OF TABLES

Table Page

CHAPTER 1
INTRODUCTION

1.1 Introduction

While measures to prevent vehicles from running off roadways are necessary, measures to build a more forgiving roadside environment, where collision severity can be reduced, are also very important. From the perspective of roadside safety, it is desired that an errant vehicle can encroach onto the roadside without striking fixed, rigid objects. Ideally, positioning fixed objects at less vulnerable locations is typically a good strategy for minimizing collision consequences. However, as a component of traffic control systems, multi-post ground signs must be located adjacent to roadways. As a result, such ground signs will pose potential hazards to passengers if they are not designed, fabricated, and installed so that they break away during a vehicular collision.

Survivability requirements for ground signs require that they must be strong enough to resist hurricane wind loading as well as gravity loading (self-weight). One means of meeting this requirement is to use sign supports (posts) that are rigidly connected to a ground-level foundation system. However, satisfying wind and gravity loading requirements in this manner unfortunately makes sign structures more dangerous to vehicle occupants, should a vehicle-sign collision occur. A vehicle striking a fixed object usually leads to abrupt deceleration or excessive compartment deformation that can cause fatal injuries. To prevent collision-related occupant fatalities, roadside hardware, such as utility poles and ground-level sign posts, are designed to yield or break away under vehicle impact. That is, posts are designed to fail in a specific manner and allow a vehicle to pass through without abrupt deceleration. Most utility poles, such as light-poles or small sign structures, can incorporate breakaway features without significantly affecting functionality. Large ground signs, however, present a challenging engineering problem in that the sign supports must be structurally strong under hurricane wind loading yet weak under low-speed vehicle impact loading. Due to the large surface area on which wind loading will act, moderate to large sign structures usually require large post sizes and rigid foundation connections to transfer wind loads to the ground. Such features, however, tend to work against the goal of providing a system that breaks away at low impact load during a vehicle impact.

1.2 Motivation

To prevent fatal injuries to vehicle occupants, breakaway support design concepts have been applied for most types of objects that are located adjacent to roadways. In many states, including Florida, multi-post ground signs typically utilize a breakaway slip-base connection to minimize the potential collision hazards. The slip-base connection is designed so that under vehicle impact the post detaches at the slip surface between base plates and rotates about a hinge on the post near the bottom of the sign panel. Conversely, wind loading is transferred to the foundation through base plates, clamping bolts, and friction force that is developed at the slipping surface. However, there is a need to improve the performance of the breakaway slip-base connection that is widely used in the state of Florida because several large ground signs incorporating this slip-base connection collapsed (Figure 1-1) during hurricane events in 2004 and 2005.

Figure 1-1. Failure of sign structure with slip-base connection under hurricane wind loading

Furthermore, the effectiveness of the breakaway features of the present slip-base connection under vehicle impact has been determined to be disadvantageously sensitive to both installation and maintenance procedures. Since the post is joined to its stub by clamping bolts at the slipping surface, the design shear resistance, under impact loading, is obtained by pre-tensioning the bolts to a predetermined level. Bolt tension therefore becomes an important parameter affecting the breakaway performance of the sign support structure. Unfortunately, breakaway performance and structural resistance of a sign structure have opposite requirements on bolt tension levels. As a result, the range of acceptable bolt tension levels is quite narrow. It is therefore a challenging task to achieve and maintain the designed bolt tension level during installation and service life of sign structures. Instead, it is very likely that bolts will be pretensioned outside the target range since the relationship between bolt torque and axial tension is highly sensitive to friction. According to Bickford (2008), most torque energy is used to overcome friction losses between the surface of the nut and base plate (~ 50%), and between the surface of male and female threads (~40%). Only about 10% of torque energy is converted to bolt pretension (Bickford 2008). It follows that a 10% variation in friction, which is common between nuts and joint surfaces, can cause a 5% change in required torque and therefore a 50% change in bolt tension (Bickford 2008). If bolts are tensioned below the required level, the shear capacity of sign posts is decreased and bolt loosening may occur. If such loosening occurs, a ground sign post can walk off the stub column and collapse under wind loading levels well below the design level. Conversely, if the bolts are over-tightened, undesirable shear capacity of the sign posts will be added. The increased shear capacity will prevent the breakaway feature of the slip-base connection from working correctly and can cause fatal injuries to vehicle occupants during collision.

1.3 Objectives

A primary objective of this research was to develop an alternative breakaway connection for multi-post ground signs that presently utilize slip-base connections. Key design characteristics of the newly developed connection are: 1) structural resistance to hurricane wind loading, 2) breakaway behavior under vehicle impact loading, 3) breakaway behavior that is relatively insensitive to installation and maintenance procedures, and 4) applicability to ground signs with large panel sizes.

1.4 Scope of Work

Develop and evaluate breakaway connection concepts using numerical simulation: Using the targeted characteristics of the new connection, design wind loading, and sign configuration, an improved breakaway connection was developed and evaluated using structural impact modeling and analysis techniques. LS-DYNA (LSTC 2006), a general purpose finite element program, was used as the primary tool in the conceptual development. The breakaway connection concept was refined by iterating between structural calculations, equivalent-static wind load analyses, impact analyses, consideration of practical aspects of fabrication, installation, and maintenance. In addition to refining the breakaway connection design, data from finite element analyses were used to aid in planning physical tests.

Conduct static testing of breakaway connection and post: Static laboratory testing was used to evaluate the structural capacity (shear and moment) under equivalent-static design hurricane wind loading and frangibility under static shear loading. Additionally, static tension tests were conducted on connector bolts to aid in numerical simulation and facilitate connection development.

Impact pendulum test facility development: For dynamic impact testing of the newly developed breakaway connection, an impact pendulum test facility was analyzed, designed, and constructed. The pendulum structure employs three free standing 50-ft. tall pylons (also referred to as towers) and has the capacity to swing an impact mass of up to 9020 lbf (4090 kg; equivalent to two full-size pickup trucks) dropped through a vertical swing height of 35 ft.

Conduct dynamic pendulum impact testing of breakaway connection and post: A total of four (4) dynamic pendulum impact tests were conducted on breakaway post and connection test articles with an 1100 kg impactor, striking at a speed of 30 kph, and at angles of 0-deg. (head-on) and 25-deg. (oblique). Data obtained from the tests were processed and compared to corresponding finite element simulation results.

CHAPTER 2
LITERATURE REVIEW

2.1 Breakaway Systems

Since the introduction of the breakaway design concept more than 35 years ago, breakaway supports have been widely used across the United States for roadside devices, such as highway signs, luminaires, call boxes, traffic signals, and warning devices. To reduce impact severity to vehicle occupants and vehicle damage, roadside devices located within clear zone widths on highways must yield, fracture or separate when struck by a vehicle (AASHTO 2001).

For ground signs, breakaway mechanisms and configurations may be categorized as either large roadside signs or small roadside signs. The American Association of State Highway and Transportation Officials (AASHTO) *Standard Specifications for Structural Supports for Highway Signs, Luminaires and Traffic Signals* (AASHTO 2001) classifies small roadside signs as those having a panel area less than or equal to 54 ft^2 and large signs as those having a panel area greater than 54 ft^2.

For large roadside signs, fracture or slip-base breakaway supports are frequently used. Although steel sign support posts are most commonly used, wood supports are also used in some states for sign-panel configurations with large widths but areas less than 75ft^2 (Andrle et al. 2001). The challenging requirement for sign supports is that they must not only be capable of breaking away under impact loading by errant vehicles but must also be structurally strong enough to resist severe wind loading conditions (e.g., hurricanes). Figure 2-1 shows the loading conditions that control the design of breakaway sign supports in Florida.

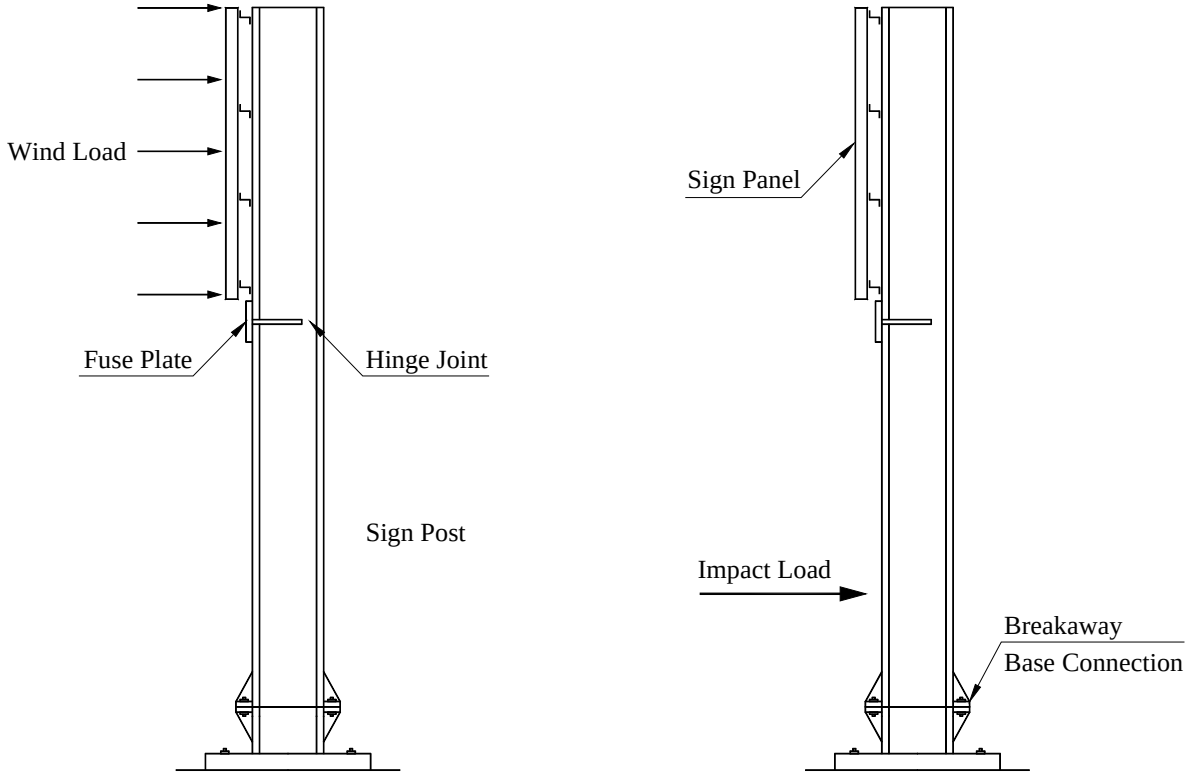

Figure 2-1. Loading conditions for sign supports

Both fracture and slip-base connection types function by having the sign support release when struck by a vehicle. At a location near the bottom of the sign panel, a hinge then activates and allows the support post to swing up and out of the path of the vehicle (Figure 2-2). Hinges are generally located at least 84 in. (AASHTO 2001) above the ground plane to prevent sign components or the upper section of the support from penetrating the windshield of the impacting vehicle. Furthermore, to ensure the desired performance, the total weight of post above the base plate and below the hinge is limited to 600 lbf (AASHTO 2001).

Under impact loading by a vehicle, a slip-base mechanism is activated when bolts clamping slip-base plates together are displaced. Slip-base connections may be of either unidirectional or multidirectional types. Figure 2-3 shows a unidirectional slip-base using four bolts. This type of connection is designed to break away when loaded from the front or back only. Where side impact is likely to occur, however, such as at intersections, this type of breakaway connection should not be used.

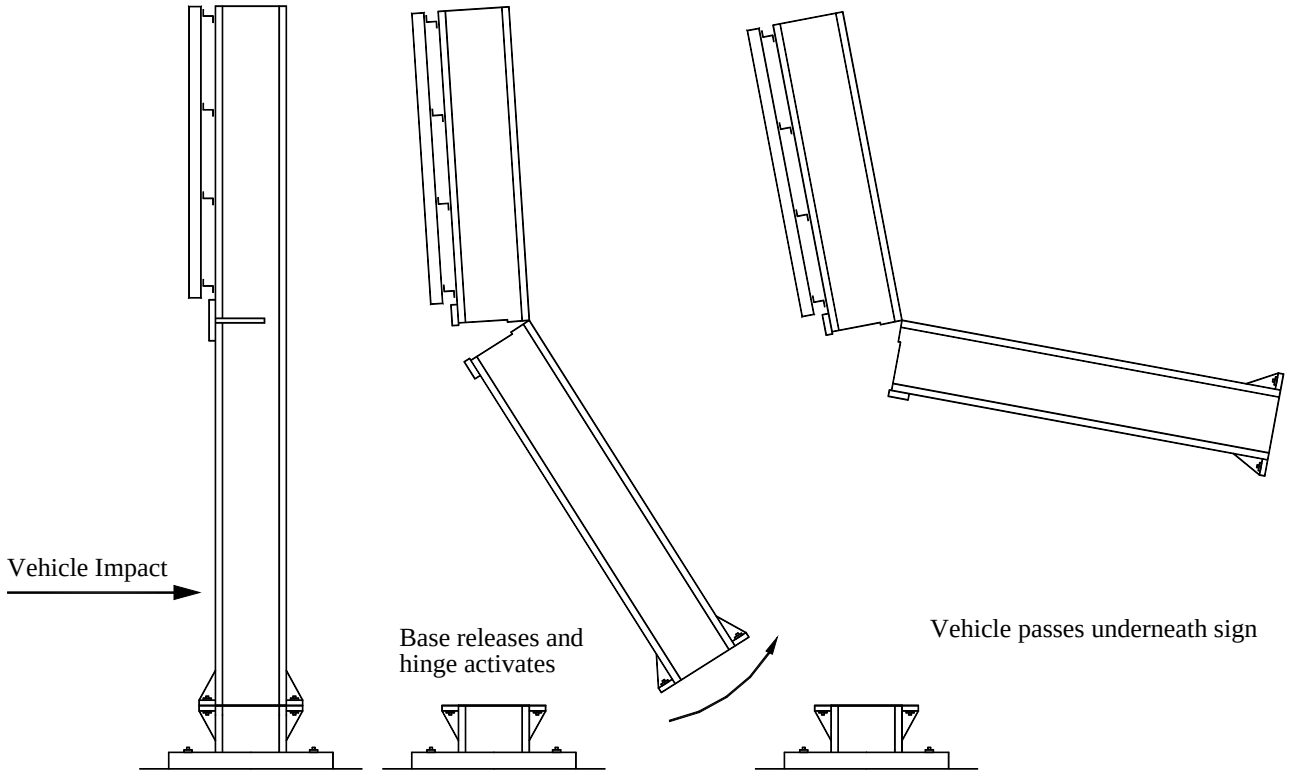

Figure 2-2. Breakaway behavior of sign supports

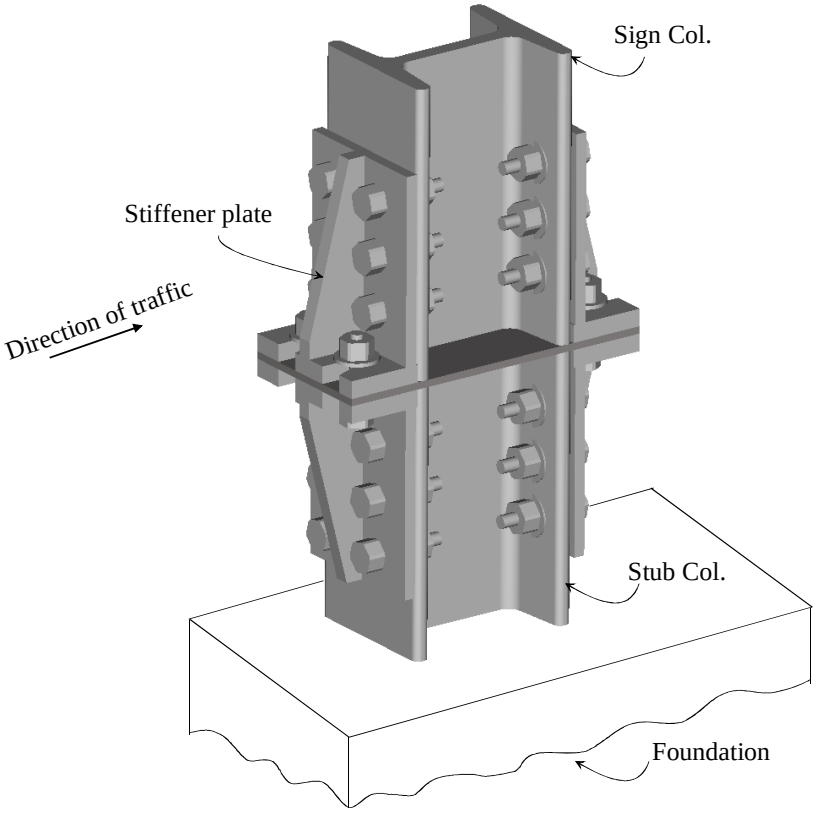

Figure 2-3. Unidirectional slip-base

Figure 2-4 shows a typical multidirectional triangular slip-base connection. Key connection components include a post base plate, a stub base plate, three connector bolts, and a bolt keeper. To allow the post to rotate out of the path of an impacting vehicle, a hinged joint (Figure 2-5) must be used in conjunction with the slip base. At the hinge joint, the post may be saw cut through the web to the rear flange and caulked with sealing compound. The rear flange then acts as a hinge when rotation of the post occurs. An alternate hinge design uses a hinge plate and the post is cut through the rear flange. A perforated fuse plate is used on the impact side of the post, however if a post is likely to be hit from either direction (front or back) fuse plates can be used on both sides of the post.

In a study aimed at improving the wind resistance of fuse plates, Reid (1996) proposed using A572 Grade 50 steel for the fuse plates rather than A36 steel. The study involved dynamic tests of fuse plates made from four different steel materials and full-scale tests of dual-support breakaway sign posts with a multidirectional slip base. As tested, the sign was composed of W6x9 wide flange posts 189 in. in height with a sign panel 120 in. wide by 96 in. high. The change from A36 to A572 Grade 50 steel increased the wind resistance capacity up to 60% and the breakaway force also increased up to 20%. Despite the increase in the breakaway force, full-scale tests performed at an impact angle of 25 degrees satisfied the basic requirements set forth in NCHRP Report 350: *Recommended Procedures for the Safety Performance Evaluation of Highway Features* (NCHRP 350) (Ross et al. 1993).

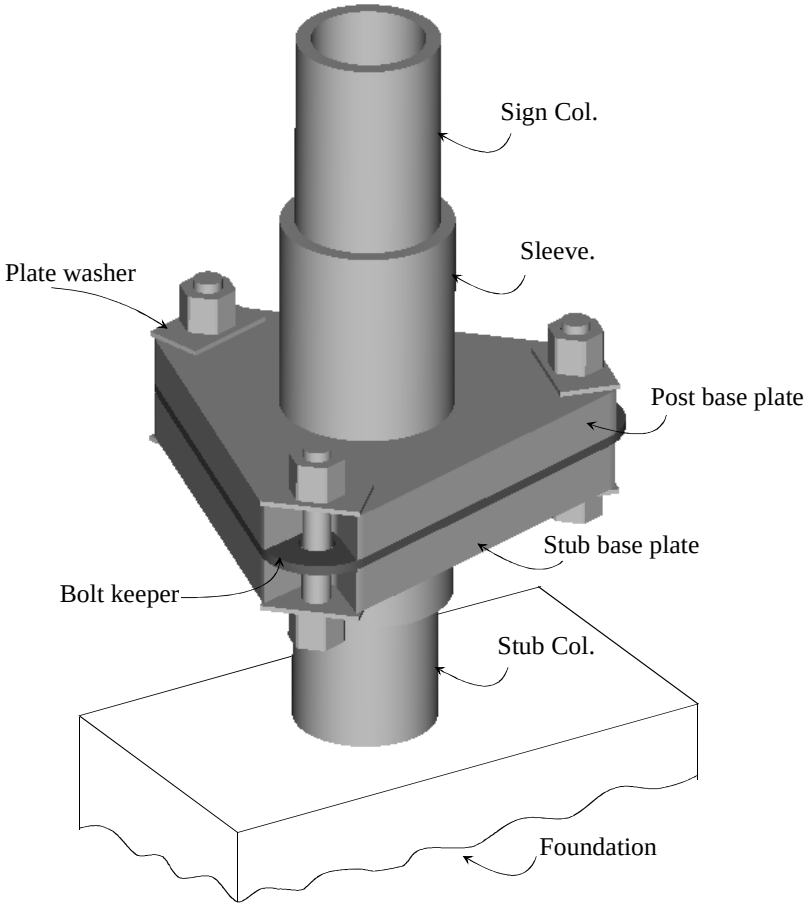

Figure 2-4. Multidirectional triangular slip-base

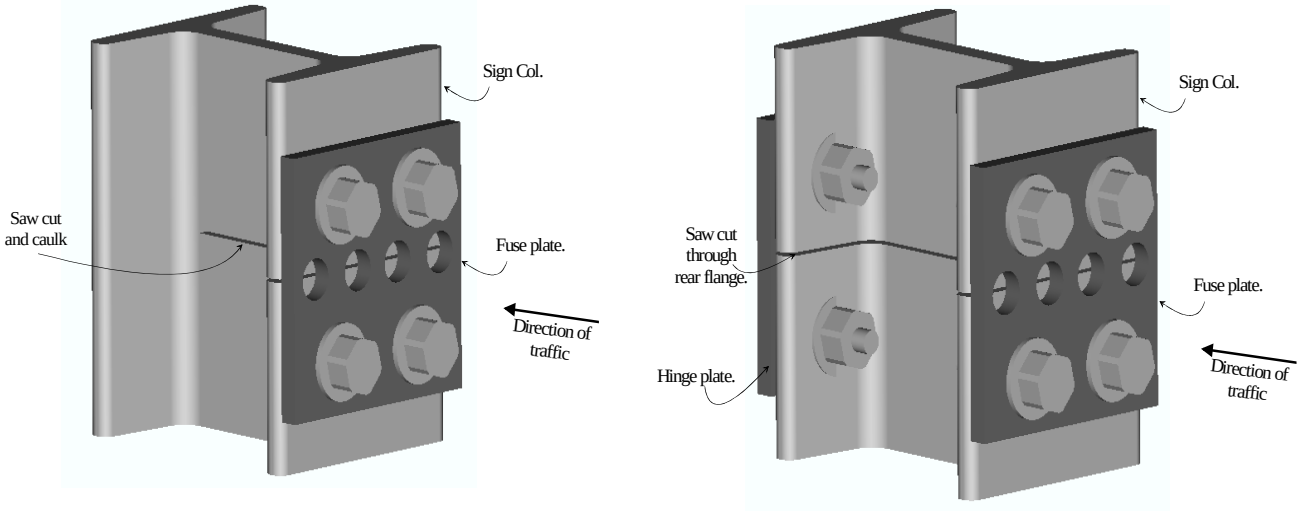

Figure 2-5. Typical hinge details

Subsequently, Reid and Paulsen (1998) presented a study on the use of a balanced hinge design using numerical simulations. The primary purpose of the study was to improve the wind load capacity on large-sign systems. The approach taken was to reduce moment acting on the hinge and fuse plates by locating the hinge point in line with the wind load resultant on the sign instead of locating it below the bottom of the sign (Figure 2-6). Unfortunately, high-speed (57.2 mph in this study) finite element impact simulation predicted a crushing deformation of 8 in. on the car model and the occupant impact velocity was 5.2 m/s (17 ft/s), which is higher than the maximum permissible value of 5.0 m/s specified in NCHRP Report 350.

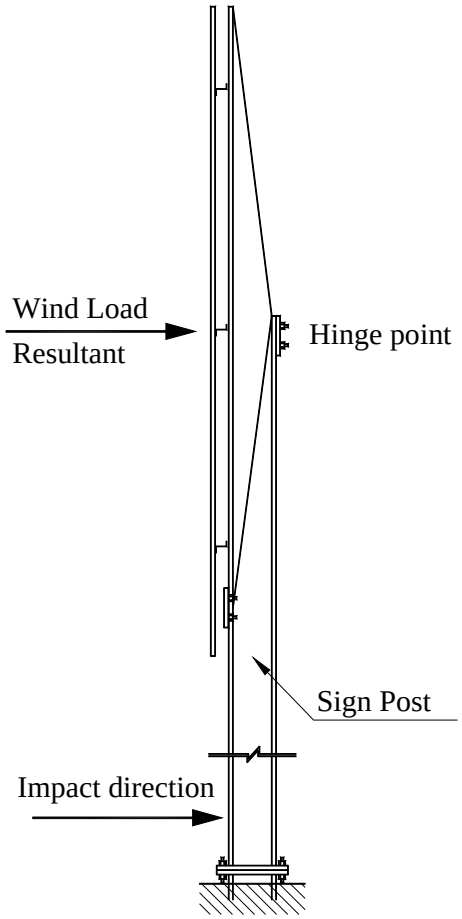

Figure 2-6. Balanced-hinge point design

Since slip-base performance depends greatly on friction between the post base plate and stub base plate, the requirement of specific bolt torque (indirect tension) level must be strictly followed. Moreover, the slip-base connection requires careful maintenance procedures, since, under wind vibration, bolts may loosen thus leading to sign collapse.

Fracture-based breakaway supports are commonly designed with reduced cross section couplers. For wood posts, cross-sectional properties are reduced by drilling holes in the post sides that are oriented transverse to the traffic direction. A fracture-based design approach typically allows the support to break away when hit from any direction. A beneficial feature of fracture-based design is that there is no specific bolt torque requirement. A proprietary fracture-based breakaway base connection, using multidirectional couplers, is illustrated in Figure 2-7.

Figure 2-7. Multidirectional coupler (Transpo Industries, Inc.)

For small roadside signs, breakaway supports are generally designed with either slip-base or bending-fracture mechanisms. Steel or wood can be used for sign supports. U-channel, square tube or round pipe steel posts typically function through bending or yielding mechanisms. Typically, near the impact region, the post is weakened by reducing the cross-sectional area. Figure 2-8 shows a round pipe support utilizing a threaded pipe coupling feature. This small sign breakaway connection is simple to install and easy to replace. When hit by a vehicle, the coupling usually breaks and the post may be reused.

For unidirectional breakaway supports, in addition to horizontal slip-base connections used for large sign supports, inclined slip-base connections are also used. An inclined slip-base connection used for small signs is shown in Figure 2-9. The slip-base is inclined in the direction of traffic flow at an angle (measured from horizontal) that varies from approximately 10 to 20 degrees (AASHTO 1996). Using an inclined angle ensures upward movement (velocity) of the sign support post during impact and thereby prevents the support from striking the car windshield. Hinges are not needed for small sign supports using inclined slip-base connections, however, such designs only work when struck from one direction. Where several impact directions are possible, multidirectional slip-bases are used instead of inclined slip-bases. The multidirectional slip-base concept for small sign supports is similar to that of large sign supports.

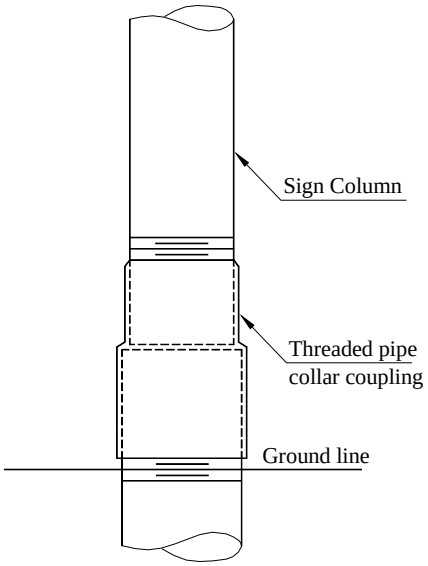

Figure 2-8. Threaded coupling breakaway connection

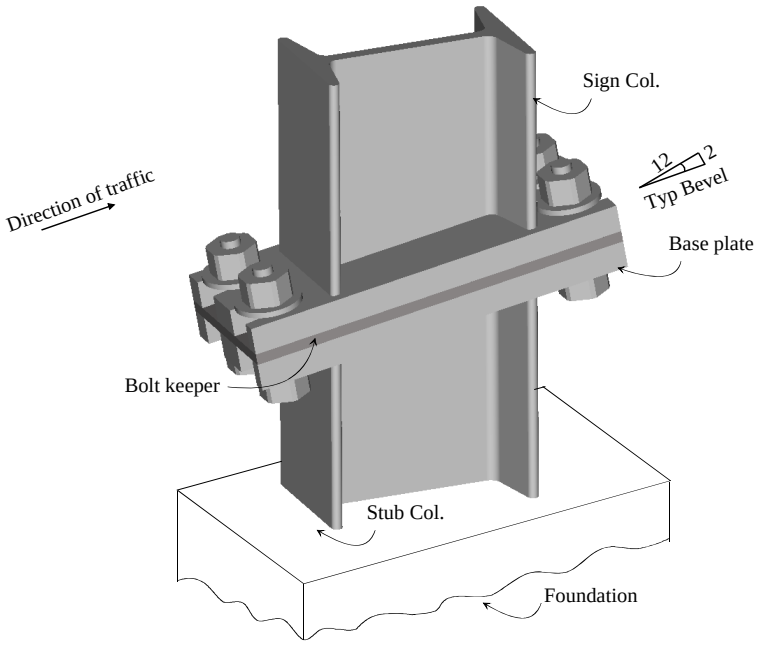

Figure 2-9. Inclined slip-base

Breakaway connections based on the concept of post pullout have also been applied to small signs. Figure 2-10 shows a universal anchor breakaway sign support system developed by HWYCOM Universal Systems. The system consists of a 3 in.-diameter fiberglass reinforced plastic (FRP) recyclable post inserted 10 in. into a universal anchor system (UAS). The UAS consists of a 3 in.-diameter anchor sleeve and steel ring that keeps the FRP tube in place. When struck by a vehicle, the FRP support fails by pulling out of the base. Single and dual support post systems are used for 16 ft^2 signs and 32 ft^2 signs, respectively.

Figure 2-10. Universal anchor breakaway sign support system (HWYCOM)

In an effort to improve installation and performance of slip-base breakaway connections, Pinelli et al. (2002) presented a new method to ensure correct bolt tension at the time of installation by using spring washers that consist of disk springs, the deflection of which indicates the tension load in the bolt. Field tests have shown that over the long term, and under wind and traffic induced vibrations, bolts installed with spring washers can maintain correct bolt tension within an acceptable range more consistently than bolts installed with traditional flat washers. However, accuracy of the deflection measurement of a stack of spring washers is still an important issue and requires a special tool to measure the deflection in the field (Pinelli et al. 2002).

Breakaway designs utilizing FRP composite materials have also been applied to luminaire supports. To achieve predictable breakaway performance of luminaire support poles, the FRP laminate must be weakened near the impact zone and strengthened above and below this zone. A typical method for weakening layers involves staggered-cutting of the FRP laminate and placing a layer of polyethylene foil between the layers within the impact zone. The polyethylene foil is used to delaminate the pole in the impact zone; thereby leading to a reduction of shearing capacity of the pole. However, this procedure also decreases the flexural capacity of the pole. To strengthen the pole above and below of the impact zone, additional fiber reinforcement is provided. This procedure is used to confine failure within the weakened zone and prevent failure from propagating to other regions of the pole.

2.2 Design Criteria Requirements for Breakaway Supports

Design of breakaway support devices is governed in part by the *AASHTO Standard Specifications for Structural Supports for Highway Signs, Luminaires and Traffic Signals* (AASHTO 2001) and *NCHRP Report 350 Recommended Procedures for the Safety Performance Evaluation of Highway Features* (NCHRP 350) (Ross et al. 1993). The AASHTO specifications require that breakaway supports be designed to meet both structural and dynamic performance requirements. For sign structures located in Florida, breakaway supports must be structurally capable of carrying dead load, wind load, and combinations of dead and wind loads. Load tests are required if the structural capacity of the support structure is potentially diminished by introduction of breakaway features.

NCHRP 350 provides guidelines for crash testing of highway safety features and performance criteria to evaluate test results. The report provides roadside safety hardware

developers and user-agencies a basis to compare the impact performance of proposed safety features. With the goal of providing uniform guidelines, NCHRP 350 covers standardized test parameters, such as test facility, test article, test vehicles and surrogate occupants. In addition to test parameters, test conditions for different roadside safety devices are assigned with suitable test levels. Test levels are further divided into different test designations in which vehicle type, nominal speed, nominal angle, impact point and evaluation criteria are specified. Recommended data acquisition systems and parameters that need to be determined during different phases of the testing process are also included. NCHRP 350 evaluation and testing criteria have been implemented by the Federal Highway Administration (FHWA) for breakaway hardware for use on the National Highway System (NHS) since 1998. The breakaway connection developed in this study conforms to the criteria set forth in NCHRP 350.

Recently, however, the AASHTO (2009) *Manual for Assessing Safety Hardware* (MASH), an update to NCHRP 350, has been officially adopted by AASHTO. Primary changes that affect assessment criteria for breakaway sign support structures are vehicle masses and impact conditions. Since publication of NCHRP 350, masses of all classes of passenger vehicles being sold in the U.S. have increased considerably. Therefore, to account for the change, the small car test vehicle mass has been increased from 820 kg (NCHRP 350) to 1,100 kg (MASH) and the pickup truck test vehicle mass has been increased from 2,000 kg (NCHRP 350) to 2,270 kg (MASH). In low-speed tests of support structures to evaluate breakaway, fracture, or yielding mechanisms, vehicle impact speed has been reduced from to 35 km/h to 30 km/h. Acceptable kinetic energy ranges for both low-speed and high-speed tests have been included in MASH to ensure consistent impact severities across tests at each test level. For support structures outside of divided highways, the critical angle range was also updated from 0-to-20-degrees to 0-to-25-degrees.

Evaluation criteria for dynamic performance of breakaway supports are found in NCHRP Report 350 and include: structural adequacy; occupant risk; and post-impact vehicular response. Structural adequacy under impact conditions requires that the breakaway support shall readily fail in a predictable manner by breaking away, fracturing, or yielding when struck head-on by a standard vehicle which has a mass of 820 kg (1800 lbf.), or its equivalent, at nominal speeds of 35 km/h (21.7 mph) and 100 km/h (62.1 mph) at test level 3 for high-speed arterial highways. For local roads and collector roads at test level 2, nominal speeds are designated at 35 km/h (21.7 mph) and 70 km/h (43.5 mph). Each of these speed levels is recommended for a different evaluation purpose. The mass of 820 kg specified by NCHRP 350 is equivalent to that of a small car. It is often more critical to evaluate breakaway performance using a small car since smaller mass leads to higher occupant decelerations which can increase the risks posed to vehicle occupants. Although an additional vehicle with a mass of 700 kg (1,550 lbf) is included in NCHRP Report 350, for tests with stricter performance criteria, it is optional because it represents a very small proportion of available light weight cars. For most sign supports, for the purpose of evaluating the breakaway mechanism and occupant risk measures, the low-speed test is more critical than the high-speed test since less kinetic energy is available to break the post. However, to evaluate post-impact vehicle and test article trajectories, the high-speed test can be more critical.

In regard to occupant risk factors and evaluation, NCHRP 350 limits the longitudinal component of occupant impact velocity (with respect to the interior surface of the passenger compartment) to no greater than 5.0 m/s (16.4 ft/s) with values less than 3.0 m/s (9.84 ft/s) being preferred. Maximum allowable longitudinal and lateral components of occupant deceleration are

limited to 20 g and preferably should not exceed 15 g. In addition to limits on velocity and deceleration at impact, detached elements (debris) from the breakaway support are not permitted to penetrate, or show potential for penetrating, the vehicle occupant compartment or present an undue hazard to other traffic, pedestrians or personnel in a nearby work zone. Potential for serious injuries to vehicle occupants due to deformation of the occupant compartment is also not acceptable. Satisfactory performance of the support requires that, after striking the breakaway support, the vehicle remain upright, although the criteria allows moderate roll, pitch, and yaw rotations of the vehicle to occur. The post-impact vehicular response evaluation criteria also require that after impact, the trajectory of the vehicle should not excessively intrude into an adjacent traffic lane.

In addition to the NCHRP 350 evaluation criteria cited above, AASHTO (2001) also provides additional requirements to ensure predictable and safe performance of breakaway supports. If full-scale crash testing is not performed, the combined mass of the post and fixtures attached to breakaway supports is limited to a maximum of 450 kg (992 lbf). To prevent a vehicle from snagging after breaking a support away from its base, AASHTO (2001) limits the maximum stub height to 4 in. This specified limit also helps to prevent instability of the vehicle should a wheel of the vehicle strike the stub. For multi-post breakaway sign supports, the hinge must be located at least 2.1 m (84 in) above ground level to prevent penetration of the sign into the windshield of the impacting vehicle.

For testing of a sign support system, NCHRP Report 350 recommends that the test be conducted with the panel that has the largest area among sign panels to be used on the support system, and that the aspect ratio of the sign should be typical of the largest panel. The sign panel material should also be that normally used in the support system.

CHAPTER 3
LOADING CONDITIONS

3.1 Selection of Sign Configuration

The primary objective of this research project was to develop a new breakaway base connection for multi-post ground signs. Multi-post systems are usually used for large roadside signs. As sign panel area and clearance height increase, it becomes more difficult to satisfy both of the 'conflicting' requirements of being wind resistant and being able to break away during impact. Consequently, the sign panel size used in developing the new breakaway connection was selected so that it was representative of large signs used in Florida. In a study involving field-testing of a new method for installing breakaway slip-base connections with spring washers, Pinelli and Subramanian (1999) selected seven signs along central Florida highways. Those typical signs had panel depths varying from 5 ft to 12 ft; panel widths varying from 10 ft to 20 ft; and clearance heights varying from 9 ft to 15 ft. Sign panel areas and first moments of area with respect to ground surface are computed and presented in Table 3-1.

Table 3-1. Central Florida signs selected for "Study of Break-away Sign Base Connections, II" project (Pinelli and Subramanian 1999)

Sign No.	Panel Width (ft)	Panel Height (ft)	Clearance Height (ft)	Sign Area (ft^2)	First Moment of Area (ft^3)
1	12	8	12	96	1536
2	20	12	11	240	4080
3	12	8	15	96	1824
4	19.5	6	13	117	1872
5	15.5	5	9	77.5	891
6	14	5.5	10	77	982
7	10	10	12	100	1700

For use in the present study, a sign system with panel dimensions of 12 ft x 20 ft (depth x width) was selected. An overview of the sign structure configuration for breakaway connection development is presented in (Figure 3-1). It should be noted that the selected sign size has a panel area of 240 ft^2, which is much greater than the 54 ft^2 that is required to be classified as a large road sign according to AASHTO.

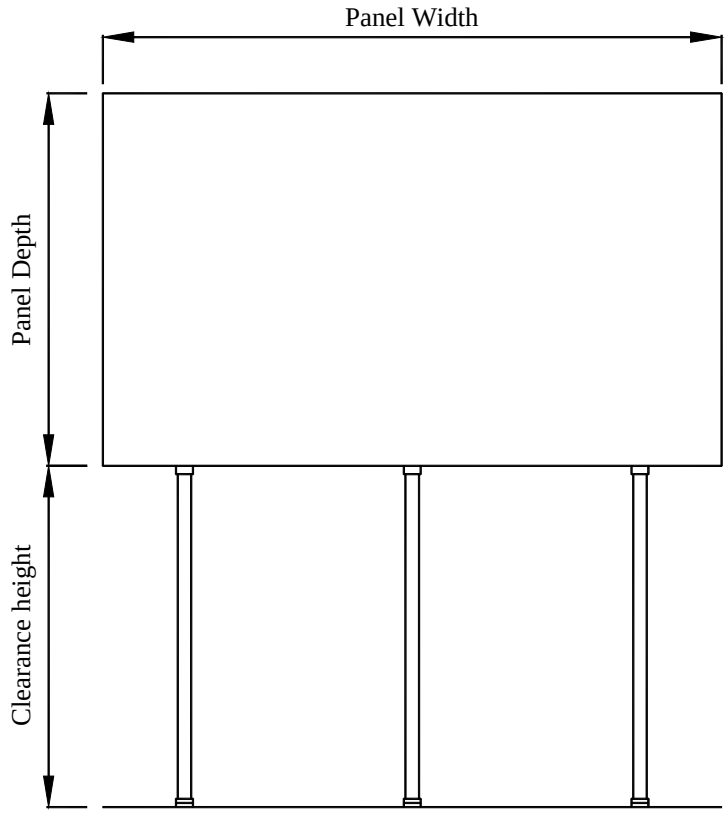

Figure 3-1. Panel dimensions and clearance height of selected sign

3.2 Structural Design Loading

A sign support structure must be designed to resist dead load, wind load and combinations of dead and wind that act on the structure during its service life. Designs of multi-post ground signs are required to conform to the AASHTO *Standard Specification for Structural Supports for Highway Signs, Luminaires and Traffic Signals* (AASHTO 2001). Multi-post ground signs in Florida must also be designed to meet the requirements specified in the *FDOT Modifications to Standard Specifications for Structural Supports for Highway Signs, Luminaires and Traffic Signals, 4th Edition* (FDOT Modifications to AASHTO 2001), Florida Department of Transportation Structures Manual, Vol. 9 (FDOT 2009). Note that ice loading is not applicable to the design of signs in the state of Florida, thus, the loads acting on the sign structure are wind loading and self-weight.

The first step in determining wind loading is to select the basic wind speed. AASHTO (2001) provides a design wind speed, which is derived from the ASCE 7-05 wind speed maps, for each county in the state of Florida. The design wind pressure at any point of the sign structure is then calculated as follows:

$$P = 0.00256 K_z G V^2 I_r C_d \tag{3-1}$$

where P is design wind pressure (psf), K_z is a height and exposure factor, and G is gust effect factor used to correct the effective velocity pressure for the dynamic interaction of the structure with the gust characteristics of the wind. AASHTO permits the gust effect factor to be taken as a

minimum of 1.14. V is design wind speed and I_r is the importance factor included to convert wind pressures associated with a 50-year mean recurrence interval to wind pressures associated with other mean recurrence intervals. C_d is the wind drag coefficient used to account for the effects of geometry of the element and the Reynolds number of the flow.

According to AASHTO (2001), for a height above ground z, or 16.4 ft, (whichever is greater) K_z is computed by the following equation:

$$K_z = 2.01\left(\frac{z}{z_g}\right)^{\frac{2}{\alpha}} \tag{3-2}$$

where z is the height above the ground at which the wind pressure is computed, z_g and α are constants that vary with exposure condition. AASHTO adopted exposure C for use in designing sign structural supports since it is considered to provide an accurate and conservative approach for such structures. Exposure C represents open terrain with scattered obstructions having heights less than 30 ft. For exposure C, z_g and α are taken as 9.5 and 900 ft correspondingly.

Wind loading analysis is conducted by multiplying wind pressures by corresponding projected areas and then applying the resulting loads statically and horizontally on the sign structure of interest. From sign size, material, configuration and preliminary post section selection, self-weight of the sign structure can be determined and combined with wind load for structural design. Combined effects of axial, bending and shear due to self-weight and wind loading are then analyzed. However, for most large multi-post ground sign structures, structural design is controlled primarily by wind loading.

3.3 Impact Loading

The typical design process for most structures begins with the determination of loads and load combinations that will act on the structure. Loads acting on a sign structure in Florida can be dead load, wind load, and impact load. Load determination procedures for each type of loading can be found in appropriate design provisions, guidelines, and design manuals. Static or dynamic analysis can then be performed using the determined loads to quantify member-level structural design forces (e.g., axial, shear, moment). As presented in the previous section, sign structure wind loads in Florida can be determined from the AASHTO provisions and the FDOT Structures Manual. Quantifying vehicle impact loads on a sign support structure, however, is not described prescriptively by the relevant codes. In fact, sign structures are not designed to resist vehicle impact loading, but rather to break away or yield under such loading conditions. As such, quantifying impact load is not a design requirement. Instead, primary focus is the safety of vehicle occupants should a collision occur. Hence, dynamic performance criteria are employed to address the vehicle impact loading condition. AASHTO requires sign support structures to be designed to meet the dynamic performance criteria specified in NCHRP 350. The evaluation criteria consist of three primary aspects: structural adequacy, occupant risk, and vehicle trajectory after collision.

3.4 Integrated Use of Finite Element Analysis (FEA) and Experimental Testing

Development of new roadside safety hardware typically includes three main phases: a research and development phase, an implementation phase, and an operational (in-service) phase. The research and development phase of safety hardware usually requires many iterations between different stages including preliminary design, laboratory testing, and impact (crash)

testing. Each stage can involve analysis, experimental testing or both. In past decades, experimental testing was the primary tool used in the process of developing new roadside safety devices. Unfortunately, such development is not a straightforward process and usually requires parametric analysis. Any new proposed safety feature is subjected to physical tests, design refinement, and repeated testing. Using such an approach, it is very difficult to successfully pass the testing criteria in one iteration.

Therefore, relying primarily on experimental testing is a very costly and time consuming means of getting a new device to meet the NCHRP 350 requirements and then moving on to the implementation and in-service phases. However, with the advancement of computing technology and reductions in computer costs, finite element analysis (FEA) has been increasingly used in all stages of the research and development phase. FEA is a numerical simulation method that can be used to solve many types of engineering problems. The method is very suitable for use in nonlinear dynamic contact impact problems, such as a vehicle impacting a breakaway support. A variety of material models and friction effects between contact surfaces can be represented and simulated using the FEA method. The availability of high-speed computers allows high resolution models of both breakaway support structures and vehicles to be included in the analysis. Moreover, the interaction between vehicle and structure can be accurately predicted and localized deformation can be quantified. FEA simulation can provide valuable insights into the complex mechanics of roadside safety hardware and can play a key role in refining the design of new safety hardware. Therefore, passing the required crash testing criteria, without multiple iterations of design modification and re-testing, becomes feasible with the use of FEA.

During the preliminary design stage, FEA usually serves as a primary design tool. Design of a sign support structure for loads, such as wind, can generally be accomplished by following well-established calculation procedures or relevant codes, and applying principles of mechanics in the calculations. However, the design of breakaway features is not as straightforward. For example, AASHTO requires load tests be conducted if there is a potential reduction of structural capacity due to the introduction of breakaway features. In such cases, FEA becomes a cost-effective means of assessing structural capacity of candidate breakaway support structures without requiring that physical load tests be conducted during the preliminary design stage. As a result, FEA is now regularly used as a primary tool in the process of developing and evaluating design alternatives.

During the laboratory testing stage, both finite element analysis and experimental testing are used to assess structural capacity and dynamic performance of new breakaway features. A promising design selected from the previously described numerical simulation stage can be subjected to experimental testing to evaluate and confirm structural strength (e.g., to wind load). Data from such testing can then be used to improve the finite element model of the system being developed.

Before conducting crash tests using full-scale production vehicles, laboratory dynamic impact testing usually involves the use of one of two main types of surrogate vehicle impact devices: gravitational pendulums and bogie vehicles. Surrogates are designed to possess properties, such as mass and crush characteristics, which are similar to production test vehicles and are used to minimize the costs associated with conducting tests with production vehicles. A gravitational pendulum testing facility typically includes a mass suspended from a support structure by steel cables or rigid arms. The pendulum mass is raised to a height so as to achieve the desired impact speed (and kinetic energy) when the mass swings through the lowest potential energy position and strikes the test article.

Bogie vehicles, in contrast, are rigid structures equipped with four wheels instead of suspension cables/arms (as are used in pendulums). During impact testing, the bogie vehicle is accelerated to the desired speed and aligned at a predetermined impact angle with the test object. Both gravitational pendulums and bogie vehicles can be installed with rigid or crushable impact noses to investigate the dynamic performance of breakaway. Crush characteristics of the nose are calibrated to represent frontal stiffness of specific test vehicles (e.g., a small car).

Gravitational pendulums are primarily applicable to low-speed impact tests since high-speed tests would require drop heights that are not feasible from a construction point of view. Bogie vehicles, however, can be used for both low- and high-speed impact tests. Pendulums and bogie vehicles are both widely used in lieu of production model test vehicles for the purpose of evaluating breakaway support performance. Some breakaway systems have even been put into service based solely on pendulum impact testing without production vehicle crash testing (NCHRP 350). With the advanced crashworthiness-analysis capabilities of current FEA programs, detailed models of such surrogates have also been developed and extensively used to evaluate the dynamic performance of breakaway systems under impact loading conditions.

Even though the above mentioned cost-effective experimental and numerical simulation tools have been commonly employed in the development of roadside safety devices, full-scale crash testing is still often required and desirable for roadside hardware for several critical reasons. First, full-scale crash testing can accurately reproduce the impact conditions that a roadside safety device will be subjected to in the field. Second, a limited number of full-scale tests can serve as a good baseline for calibration and validation of finite element models and surrogate vehicles, and therefore, can improve significantly the reliability of the numerical simulation techniques and the simplified experimental methods. Third, the use of surrogate vehicles is limited to certain types of test conditions. For example, gravitational pendulums cannot be used for tests where determining the vehicle trajectory after impact is of interest. Also, neither pendulums nor bogies can provide information regarding test article penetration into the vehicle compartment. Moreover, bogie suspension systems do not exactly match the suspension systems of production vehicles, and therefore production vehicle behaviors, such as snagging and rollover, cannot be accurately evaluated with bogies.

3.5 Occupant Risk Determination Procedure

The NCHRP 350 occupant risk criteria are constructed based on a simplified point mass, flail space model. This model assumes that the occupant can be approximated as a point mass that is able to flail inside an idealized vehicle compartment. The occupant is allowed to move longitudinally (forward) 0.6 m and laterally 0.3 m before impact with the inside of the vehicle compartment. It is assumed that motion of the vehicle and occupant are planar and yaw motions of the vehicle are ignored. These assumptions are warranted by the fact that in a majority of tests, including those on breakaway sign posts, the impacting vehicle is required to remain upright during and after collision, although moderate rolling, pitching, and yawing are acceptable (NCHRP 350). Two criteria related to occupant impact risk are typically used: occupant impact velocity; and ridedown acceleration. Occupant impact velocity is the velocity at which a hypothetical occupant impacts the idealized interior surface of the vehicle. Ridedown acceleration is defined as the maximum deceleration that the occupant experiences after contacting the interior surface of the vehicle. The process used to quantify occupant impact velocity and ridedown acceleration treats the motions of the occupant in the longitudinal and lateral directions independently. Calculation of the occupant risk measures involves the following steps:

1. From vehicular accelerations, quantified either from FEA simulation results or measured experimentally with accelerometers, the longitudinal (x-direction) and lateral (y-direction) occupant impact velocities relative to the vehicle frame are determined as:

$$V_x(t) = \int_0^t a_x(t)dt \quad with \quad V_x(t=0) = 0 \tag{3-3}$$

$$V_y(t) = \int_0^t a_y(t)dt \quad with \quad V_y(t=0) = 0 \tag{3-4}$$

where Vx and Vy are occupant impact velocities relative to the vehicle in the x- and y-direction, respectively; and a_x and a_y are vehicular accelerations in x- and y-direction, respectively. At the instant right before impact with a test article (e.g., a sign post), the occupant and the vehicle are assumed to have the same longitudinal and lateral velocities.

2. Occupant displacements with respect to (i.e., relative to) the vehicle compartment are obtained from time-integration of velocity data as follows:

$$X(t) = \int_0^t V_x(t)dt \quad with \quad X(t=0) = 0m \tag{3-5}$$

$$Y(t) = \int_0^t V_y(t)dt \quad with \quad Y(t=0) = 0\,m \tag{3-6}$$

where X, Y are the occupant movements relative to the vehicle in x- and y-direction, respectively; and V_x, V_y are the occupant-car interior impact velocities (relative to the vehicle), computed using Eqs. 3-3 and 3-4, in the x- and y-direction, respectively.

3. When the occupant has traveled either 0.6 m longitudinally or 0.3 m laterally, whichever occurs first, impact with the interior surface of the car is deemed to have occurred. Time of flight t^*, the time at which the occupant impacts with interior vehicle surface, is the shorter of times t_x^* and t_y^*, determined as follows:

$$X(t^*_x) = 0.6m \tag{3-7}$$

$$Y(t^*_y) = \pm 0.3m \tag{3-8}$$

4. Longitudinal and lateral occupant impact velocities are then determined by evaluating occupant velocities with respect to the vehicle obtained from Eqs. (3-3) and (3-4) at time t^*. Occupant risk evaluation criteria per NCHRP 350 for support structures require longitudinal occupant impact velocity below 5 m/s, with values less than 3 m/s preferred.

5. According to NCHRP 350, since vehicular acceleration spikes having durations less than 0.007 sec are not considered to cause occupant injury, vehicular accelerations computed using a 10-ms moving average are selected for occupant risk assessment. Ridedown accelerations in the longitudinal and lateral directions are determined by finding maximum magnitudes of the corresponding 10-ms averaged vehicular accelerations subsequent to t^*.

3.6 Comparison of Wind and Impact Design Forces

Wind load and vehicle impact loads have a common characteristic in that both types of load act horizontally on sign support systems. Before developing new breakaway connection concepts, preliminary analyses of a simplified system were conducted to determine the relative magnitudes of design wind load (carried by each post) and the estimated impact force that a small vehicle imparts to a post during a collision in which the breakaway performance criteria are not violated.

3.6.1 Wind Shearing Force

Since the goal of this study was to develop a hurricane-resistant, impact breakaway connection that can survive hurricane-force wind loads, a design wind speed of 150 mph—the highest design wind speed in Florida counties—was selected. Furthermore, while both AASHTO and FDOT Modifications to AASHTO recommend a minimum 10 year design life for roadside sign structures, at the request of FDOT, a design life of 50 years was selected for the design of the new connection system. Selection of the more conservative 50 year design life was based on the desire to ensure that important roadside signage (e.g. signage indicating exit numbers) remain intact, and undamaged, to guide emergency-responders during post-hurricane recovery periods.

Design wind pressures at the center of the sign panel were calculated based on Eq. 3-1. AASHTO provides drag coefficients for different ratios of width to depth of sign panels. The wind drag coefficient generally increases when the ratio of width to depth increases. For the selected sign panel, with an aspect ratio of 1.67, the wind drag coefficient was conservatively taken as 1.19 which corresponds to an aspect ratio of 2.0. Exposure C, accepted by AASHTO for structural design of sign supports, was used in wind load determination. For the selected design life of 50 years and hurricane wind loading, the importance factor is 1.0 corresponding to the 50-year recurrence interval. It should be noted that changing the design life from 10 years to 50 years increases the design wind load by 85% since the hurricane wind load importance factor for 10-year design life is only 0.54.

Once the design pressure was calculated, the total design wind load on the sign system was determined to be 17.1 kip. Acting on a three-post system, this total load would generate a shear force, per post, of approximately (17.1 / 3) + 1 = 6.70 kip, in which a conservative 1 kip estimate of wind load acting directly on the post surface is included. Acting on a two-post system, the 17.1 kip total wind load would generate a shear force per post of (17.1 / 2) + 1 = 9.55 kip. Of interest here was determining whether a small car, moving at low-velocity, would generate a post shear force substantially larger than the post shear force caused by wind loading. If the post shear force caused by vehicle collision substantially exceeded the wind induced shear force, then a connection system could be designed with adequate shear strength to resist hurricane wind loading, but which would also break away under direct vehicle impact loading. Therefore, to conservatively make this assessment, the larger two-post wind induced shear force of 9.55 kip was adopted for comparison to vehicle impact loads.

Currently, FDOT has adopted AASHTO (2001) for design of sign support structures. For comparison with ASCE7-05, should FDOT adopt the specification, determination of the total design wind load on the sign system according to ASCE7-05 is presented in Appendix A.

3.6.2 Simplified Post and Pendulum Impact Head Finite Element Models

The simplified post configuration used to preliminarily quantify shear force associated with vehicle impact was determined based on the maximum sign size of 12 ft x 20 ft and the maximum clearance height of 15 ft from the Table 3-1. The simplified post model was intended to represent a single post from a two-post sign support structure and consisted of a single W8x18 post fixed at the ground level (Figure 3-2). Mesh separations (discontinuities) were introduced at elevations 4 in. above and 15 ft above ground level to represent saw cuts through the steel section. Upper and lower portions of the post were joined together by dual fuse plates (at front and back of the post) at an elevation of 4 in., and by a combination of fuse and hinge plates at an elevation of 15 ft (Figure 3-2).

Post and fuse plates were modeled using shell elements and an A36 steel material model (Figure 3-3) with a yield strength of 36 ksi, an elastic modulus of 29000 ksi, a yield strain of 0.0012, and a plastic failure strain of 0.2. The A36 steel material was implemented in LS-DYNA by using material type 24 (`*MAT_PIECEWISE_LINEAR_PLASTICITY`) using an effective stress versus effective plastic strain curve. In the lower portion of the post model, a standard steel mass density of 7,850 kg/m^3 (15.232 (lbf/ft^3)/(ft/sec^2)) was specified for all components. In the upper 12 ft portion of the post, however, the mass density was artificially increased to account for the added mass of one half of the sign panel.

To simulate the effect of a small car impacting the simplified post model, a finite element model [developed at the National Crash Analysis Center (NCAC) for the Federal Highway Administration (FHWA) and the National Highway Traffic Safety Administration (NHTSA)] of a pendulum impactor was used. The NCAC model (Figure 3-4) was developed to represent the pendulum impactor used at the Federal Outdoor Impact Laboratory (FOIL).

The impactor consisted of 2,100 solid elements with 3,800 nodes and included a crushable nose assembly and a bumper block with front-end plates. The crushable nose assembly was made up of ten aluminum honeycomb cartridges, modeled with four different honeycomb material models such that the crush characteristics of the impactor reasonably approximates the stiffness of the front of a small car. Up to the point of full honeycomb wall buckling, the behavior of the honeycomb material was orthotropic. After full honeycomb wall buckling occurred, the material behavior was perfectly plastic. Cartridges in the impactor nose were separated by 0.5 in.-thick fiberglass plates. The honeycomb cartridges and fiberglass plates were attached to two steel pipes, which were rigidly connected to the impactor at one end. The two steel pipes were guided to slide through larger diameter steel pipes embedded in the bumper block. For computational efficiency, the bumper block, front-end plates, and steel pipes were modeled using the LS-DYNA `*MAT_RIGID` material model which maintains correct mass density but employs an infinite elastic modulus. All elements that made use of this material model were treated as being part of a single rigid body.

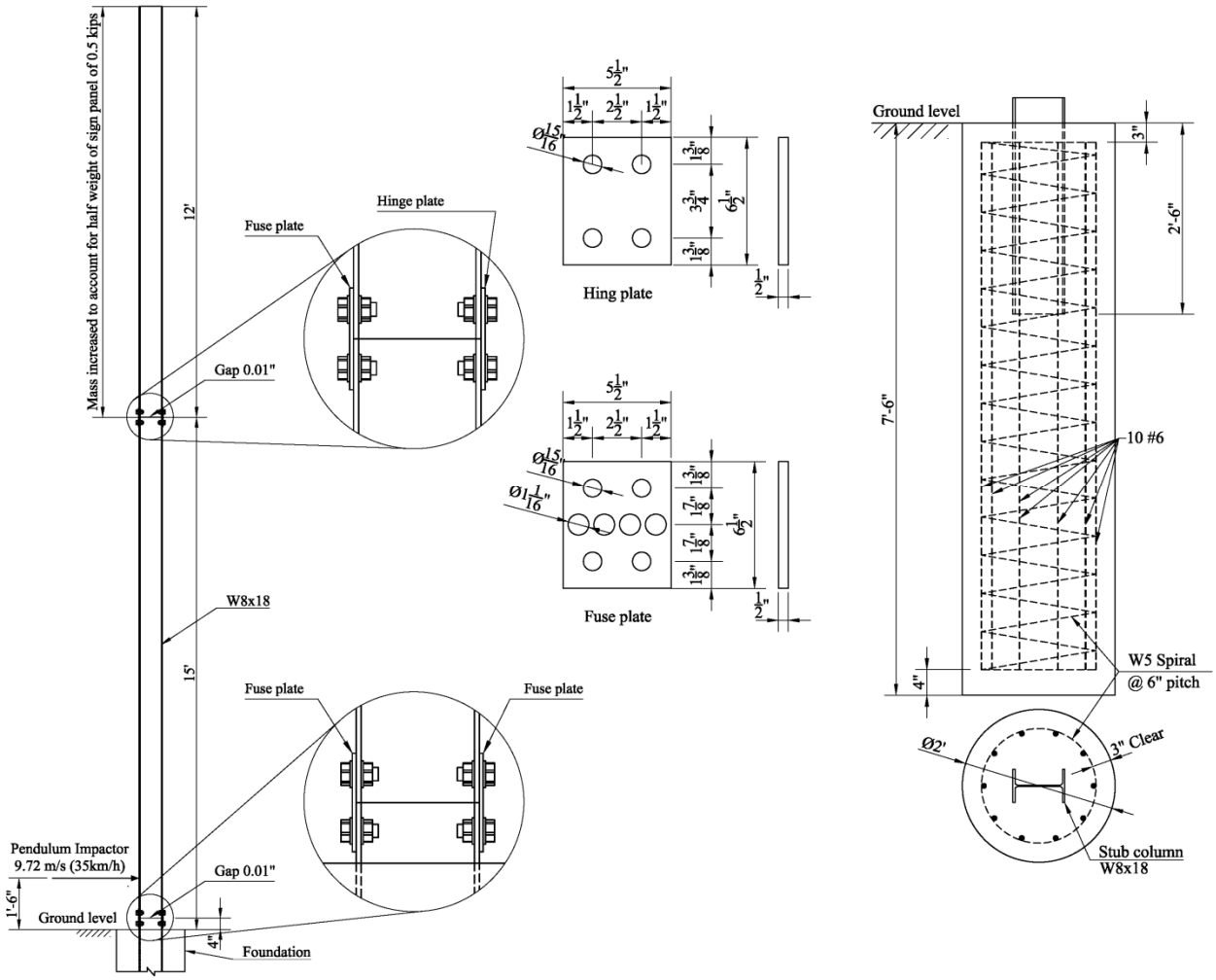

Figure 3-2. Schematic of the simplified model

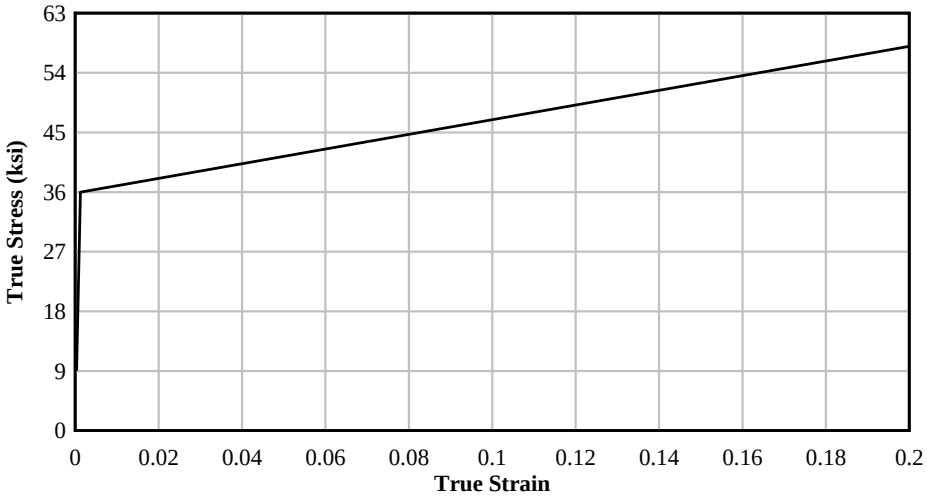

Figure 3-3. Steel material model of post and plates

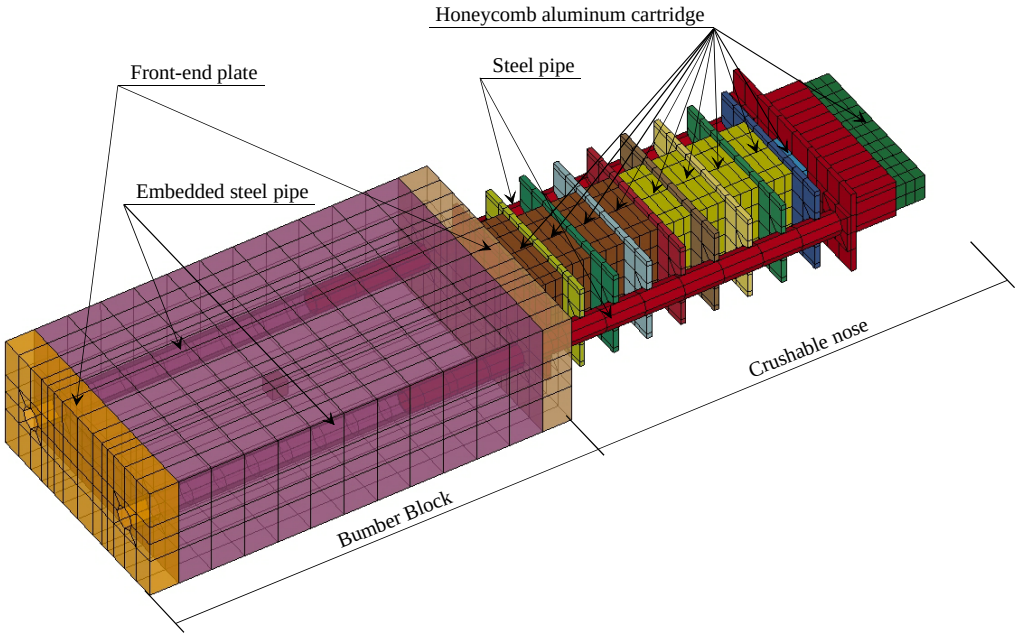

Figure 3-4. NCAC finite element model of pendulum impactor

An impact finite element analysis of the simplified post was conducted by imposing an initial velocity of 35 km/h (21.7 mph) on the crushable nose pendulum impactor and permitting the nose of the impactor to strike the post model. Since the sign panel elements were not modeled explicitly, the stiffness contribution of the sign panel was not included; therefore, two-post configurations were simulated to represent the upper and lower bound limits of the sign panel stiffness. A sign panel, in this context, consists of an aluminum panel, wind beams and related accessories. In the upper limit stiffness configuration, i.e., a rigid sign panel, the node at the intersection of post flange and post web and at the elevation of sign panel mid-height was fixed against translation and rotation motions. In the lower limit stiffness configuration, i.e., a zero-stiffness sign panel, added mass from the sign panel was included, but no springs or boundary conditions were used to represent sign panel stiffness.

3.6.3 Impact and Wind Shearing Force Comparison

In Figure 3-5, typical rupture of the simplified post model, as predicted by finite element simulations of the upper stiffness limit and lower stiffness limit model configurations, is illustrated. Post rupture was characterized by a progressive failure of the base connection followed by failure of the fuse plate. It should be noted that for the head-on, symmetric impact condition, lateral motion was negligible therefore only impact simulation results in the longitudinal direction are presented here (impacts occurring at oblique angles are addressed later in this report).

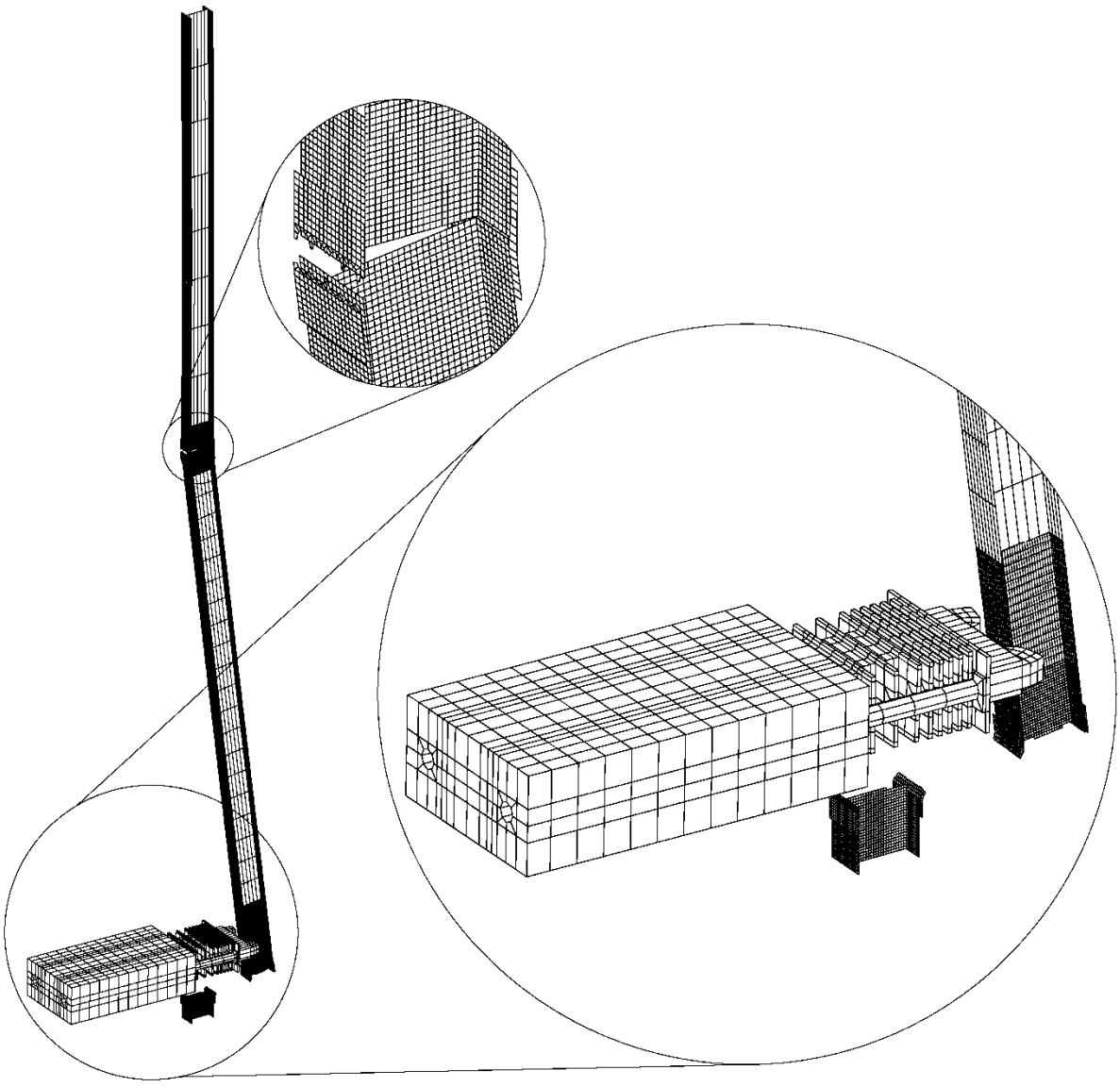

Figure 3-5. Rupture (break away) of post connection during impact

Figure 3-6 indicates that impact forces imparted to the post, in both the upper and lower limit panel stiffness configurations, maximize at approximately 20 kip. Comparing an impact load causing post rupture at 20 kip to the 9.55 kip wind load shear carried by each post in a two-post support system reveals that the post shear strength can be designed to resist severe wind loading while still permitting breakaway behavior under vehicle impact loading. This same conclusion holds true for a three-post sign support system since each post in that system will carry wind load that is less than that of the two-post system.

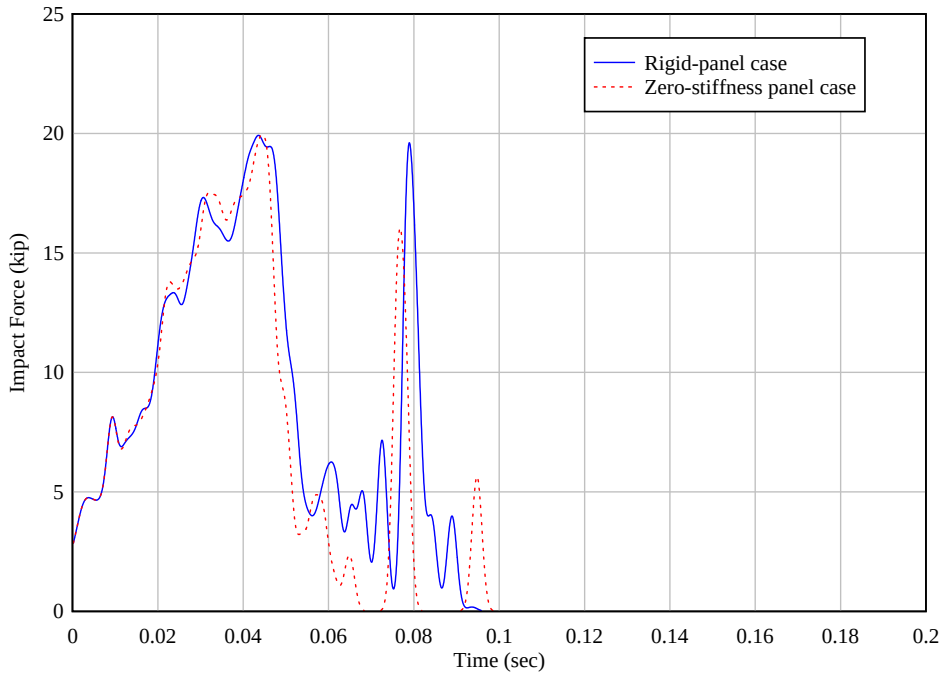

Figure 3-6. Impact force imparted to post

As discussed earlier, occupant risks were determined based on acceleration data measured at the center of gravity (CG) of a vehicle. Since the impact simulations were conducted using a pendulum impactor model instead of a vehicle model, acceleration and velocity data from the CG of the pendulum impactor were used. From impactor velocity and occupant velocity, which were assumed to be constant and equal to the pendulum velocity at the very beginning of impact, the time history of occupant velocity relative to pendulum was determined (Figure 3-7). Velocity data were integrated to obtain occupant displacements relative to the pendulum impactor (Figure 3-8). The travel time (time of flight) at which the occupant displacements reached 0.6 m were 0.197 sec and 0.18 sec for the rigid-panel case and zero-stiffness panel case, respectively. At these travel times, occupant impact velocities for the two cases were 3.86 m/s and 4.46 m/s—smaller than the permissible limit of 5 m/s specified in NCHRP Report 350. Since, in both cases, occupant impact occurred approximately 0.1 sec after the post and pendulum had separated from each other, pendulum decelerations are diminished and therefore the occupant ridedown accelerations meet the criteria set forth in NCHRP Report 350 (Figures 3-9).

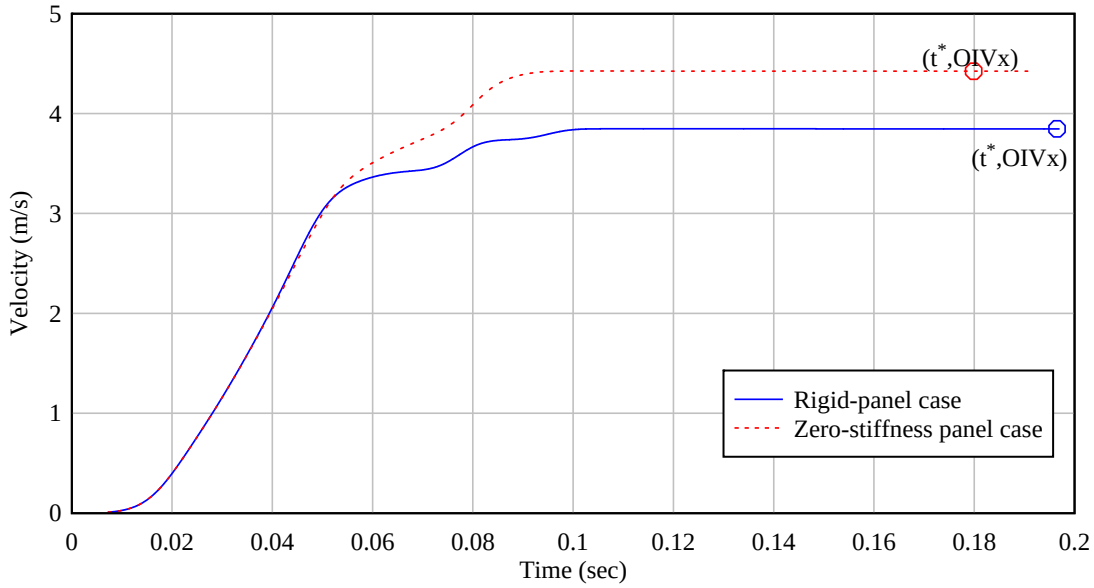

Figure 3-7. Longitudinal occupant velocity (OIV) relative to pendulum and longitudinal occupant impact velocity

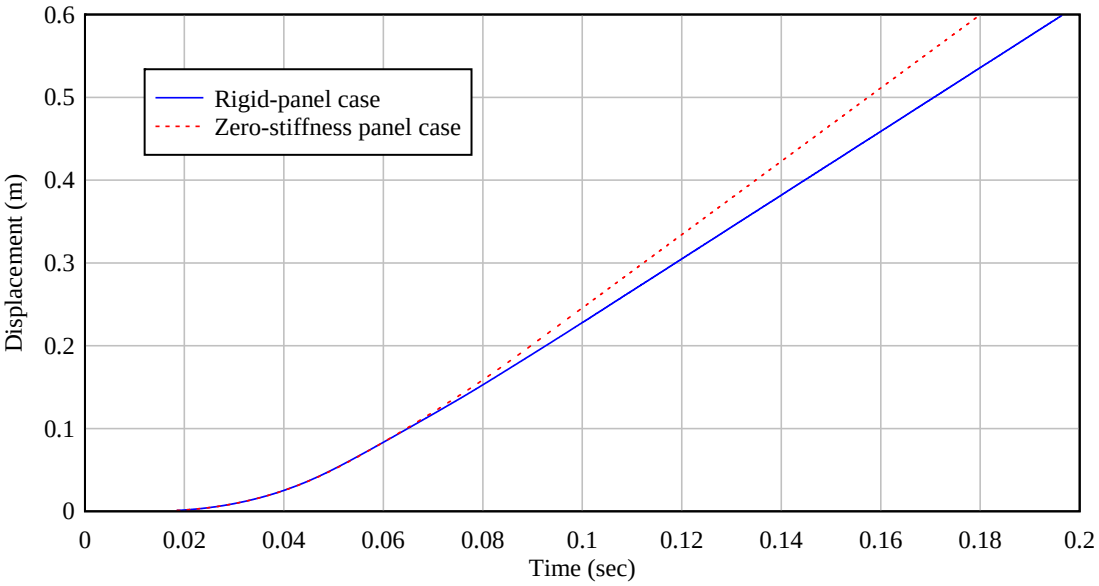

Figure 3-8. Longitudinal occupant displacement relative to pendulum

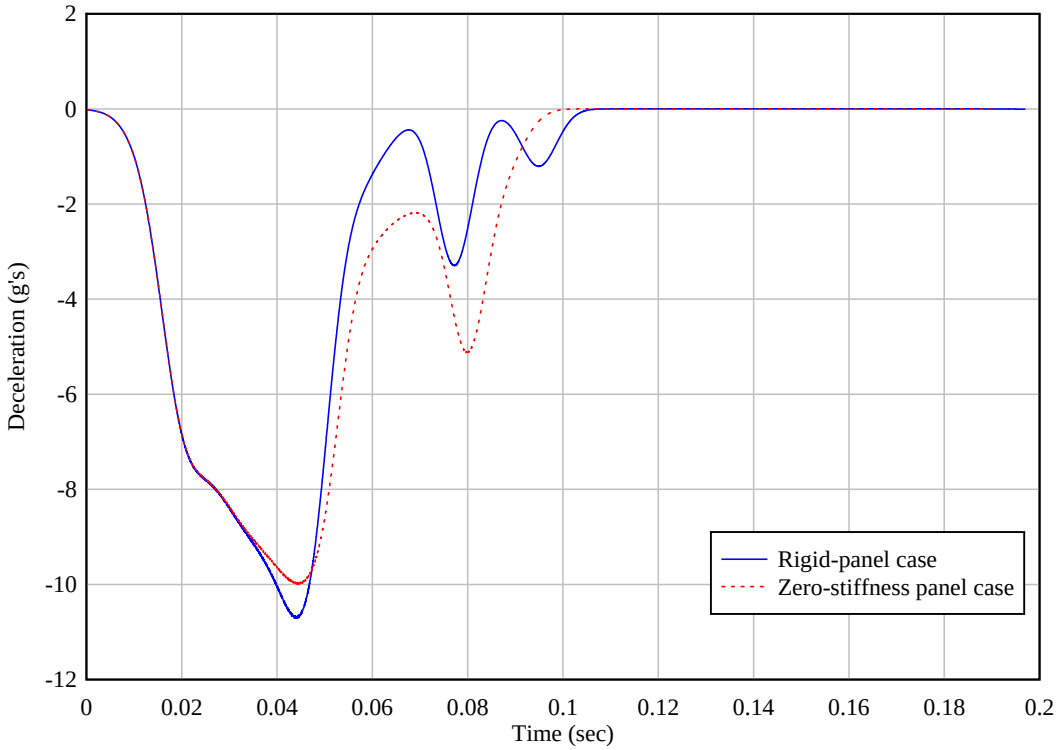

Figure 3-9. Longitudinal pendulum deceleration

3.7 Selection of Sign Panel Size and Configuration for Breakaway Connection Development

The simplified model above corresponded to the maximum panel size from Pinelli's study (Pinelli and Subramanian 1999) and, simultaneously, the maximum clearance height. However, using the maximum parameters is overly conservative and is not representative of sign configurations commonly used in the state of Florida. Moreover, occupant impact velocities from the simplified analyses were close to the upper limit and higher than the preferable limit set by NCHRP 350. Therefore, in the design of the breakaway connection that is the focus of the remainder of this study, a more realistic sign configuration was selected. Specifically, the sign from the Pinelli and Subramanian study (1999) that had the largest *moment of area* was selected: a 12 ft x 20 ft sign panel with an 11 ft clearance height. For the design wind loading condition and selected sign configuration, each post in a three-post support system was subjected to a wind load of 6.5 kip acting at 189 in. from ground level. This loading produces a post shear of 6.5 kip and the ground level and a base moment of 1,231 kip-in (102.6 kip-ft) (calculation of the design wind load and post forces can be found in Appendix A).

CHAPTER 4
PENDULUM TEST FACILITY

4.1 Introduction

Traditionally, full-scale vehicle impact tests are performed to evaluate newly developed roadside safety devices. However, due to the various numbers of required tests under different impact conditions (e.g., impact angle, vehicle class, vehicle frontal crush characteristic), a significant cost is associated with full vehicle crash tests. For this reason, to reduce development costs, surrogate test vehicles, such as four-wheeled bogies or impact pendulums, may be used to evaluate breakaway supports for signs and luminaires. In this research, an impact pendulum was selected to use as a surrogate for the small car.

According to NCHRP Report 350, a pendulum can be used as a surrogate for a small car in a low-speed impact test of a breakaway connection. In order to physically test the connection designs developed in this research, a new pendulum test facility was designed and constructed at the Florida Department of Transportation (FDOT) Structures Research Center. The minimum capacity requirement of the pendulum structure was to be capable of supporting a free-swinging impact mass of 820 kg at a maximum velocity of 35 km/h. However, future impact tests making use of the pendulum were envisioned to involve higher levels of impact kinetic energy. Therefore, it was determined that the pendulum support structure would be designed to swing a maximum mass of 4,090 kg (9,020 lbf.; equivalent to two full-size pickup trucks) dropped through a vertical height of 35 feet.

The pendulum support structure that was designed and constructed to meet this impact energy requirement, shown in Figure 4-1, consists of three 50 ft tall pylons (also referred to as towers). Each pylon is a space truss structure made up of three steel pipes 12 in. in diameter with steel angles L5x5x5/16, and is supported on a drilled shaft foundation. The pendulum structure was designed so that three separate test article installation areas can be accommodated. That is, the impact mass may be swung at target test articles installed in either of three different areas. Frequently, it is required that impact tests on soil-embedded test articles be conducted in both strong and weak soil installation conditions. By providing three separate test areas, articles to be tested can be installed in strong soil, weak soil, and rigid-foundation conditions independently of each other. This feature of the pendulum will minimize delays that would otherwise occur if the need arose to switch from one soil installation condition to another and only a single test pit were available.

Pulley hangers are attached to each of the three pylons. Steel cables wound around the pulleys are used to pull back, raise, and lower the pendulum impact mass to the desired drop height. At the top of each pylon is a cable hanger assembly that can be used in two different swinging directions of the impacting mass. Details of the structural design of the pendulum structure can be found in Appendix B.

The pendulum support structure was analyzed and designed for two load cases. Load case 1 (wind loading) consisted of factored structure dead load and factored wind load (1.2D+1.6W). Load case 2 (live loading) included factored structure dead load and factored live load of the impactor (1.2D+1.6L). In the following sections, the analysis procedure and results for the wind loading and live loading of the swinging impactor are presented.

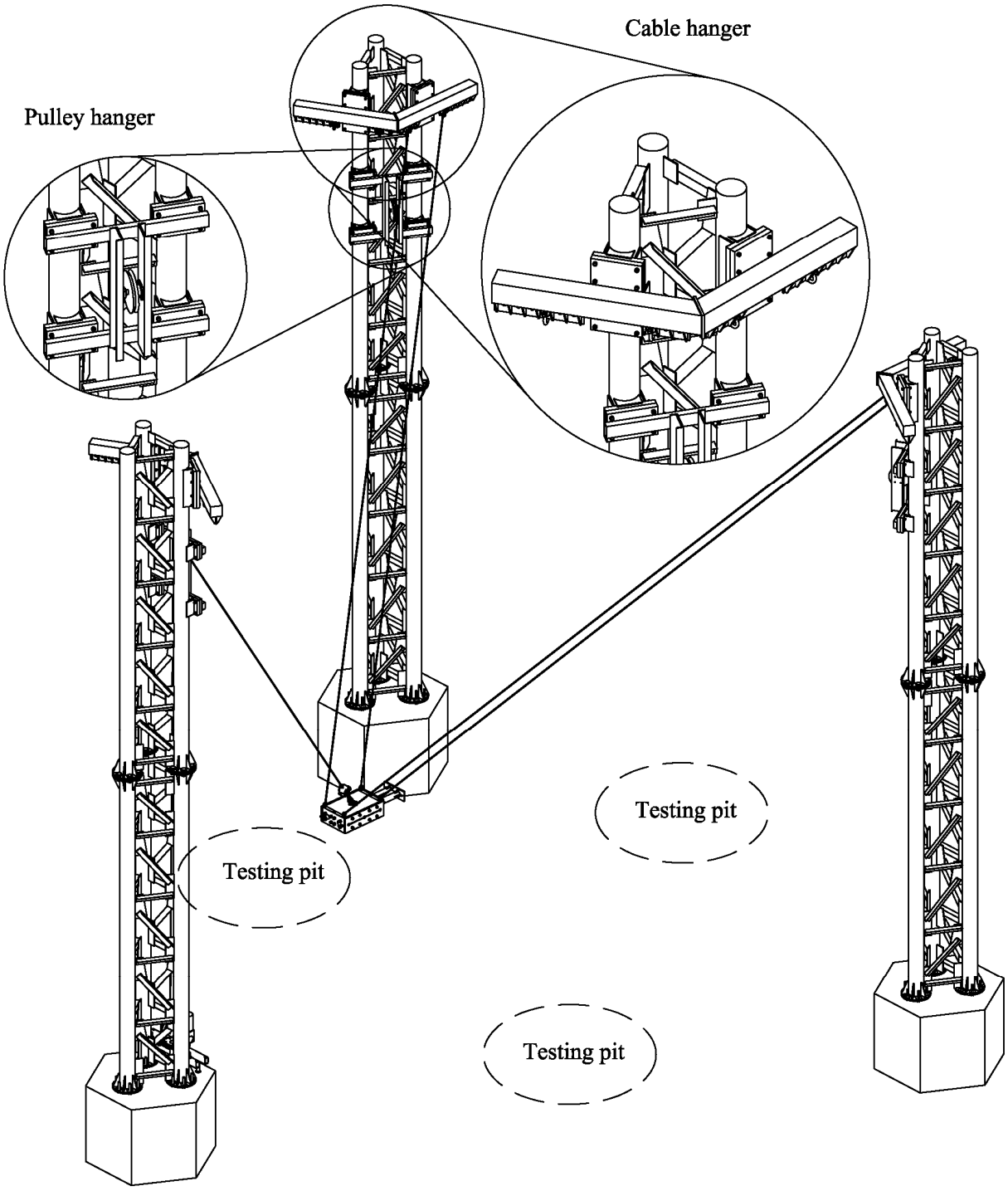

Figure 4-1. Pendulum support structure

4.2 Wind Loading

In the wind load case, wind load and dead load of structure were factored by 1.6 and 1.2, respectively. The wind load calculation conforms to ASCE (2005) "*Minimum design loads for*

buildings and other structures". The structure was design for a wind speed of 110 mph and Exposure C. Wind loads on structural components are conservatively computed based on their maximum projected area. Although wind load pressure on the structure varies with height, it is conservatively assumed that all structural components are subjected to pressures computed at the highest point on the pylons (at an elevation of 50 ft). LS-DYNA was used to perform wind loading analysis. A finite element model of a pylon subjected to wind loading is shown in Figure 4-2.

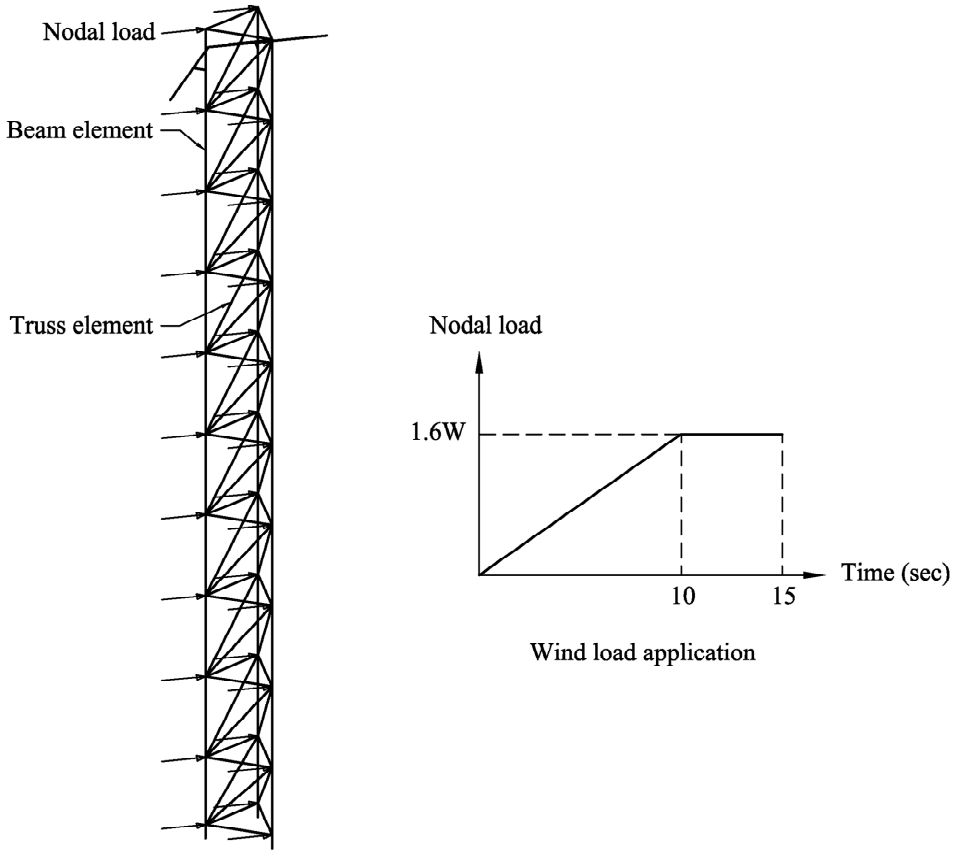

Figure 4-2. Finite element model of a pylon and wind load application

Structural pipes and web angles of the pylon were modeled by resultant beam elements and truss elements respectively. Pylon nodes were fixed (all 6 degrees of freedom) at the base. Wind loads on each element were lumped at the nodal points. At the intersection of structural members, nodal loads were computed by summing the individual loads contributed by the connected members. A quasi-static analysis method was utilized for the wind analysis by gradually increasing nodal loads on the pendulum support structure to the factored wind load at each node (Figure 4-2). It should be noted that the load-ramping period of 10 seconds is much longer than the first mode natural period of the pylon (approximately 0.3 sec; determined in a separate analysis). Thus, inertial effects of the pylon in the quasi-static analysis were negligible.

4.3 Live Loading

In the live load case, the mass of the impactor (4090 kg, 9,020 lbf) and self-weight of the structural components were factored by 1.6 and 1.2, respectively. Two analysis methods—

dynamic and simplified dynamic—were used. The former method involved time history analysis of the structural response related to the swinging impactor. In the latter analysis, cable forces were computed at various locations of the impactor with respect to the pendulum support structure in which the inertial effects of the impactor were taken into account. The forces were then applied to the structure in a static manner.

4.3.1 Dynamic Analysis

Dynamic analysis of the pendulum support structure involved simulating the drop of an impactor, supported by four (4) cables mounted on two pylons, from a 35 ft initial height. The pendulum impactor was allowed to swing a full cycle to capture the most severe loading condition for each structural member. The finite element model of the pendulum support structure is presented in Figure 4-3.

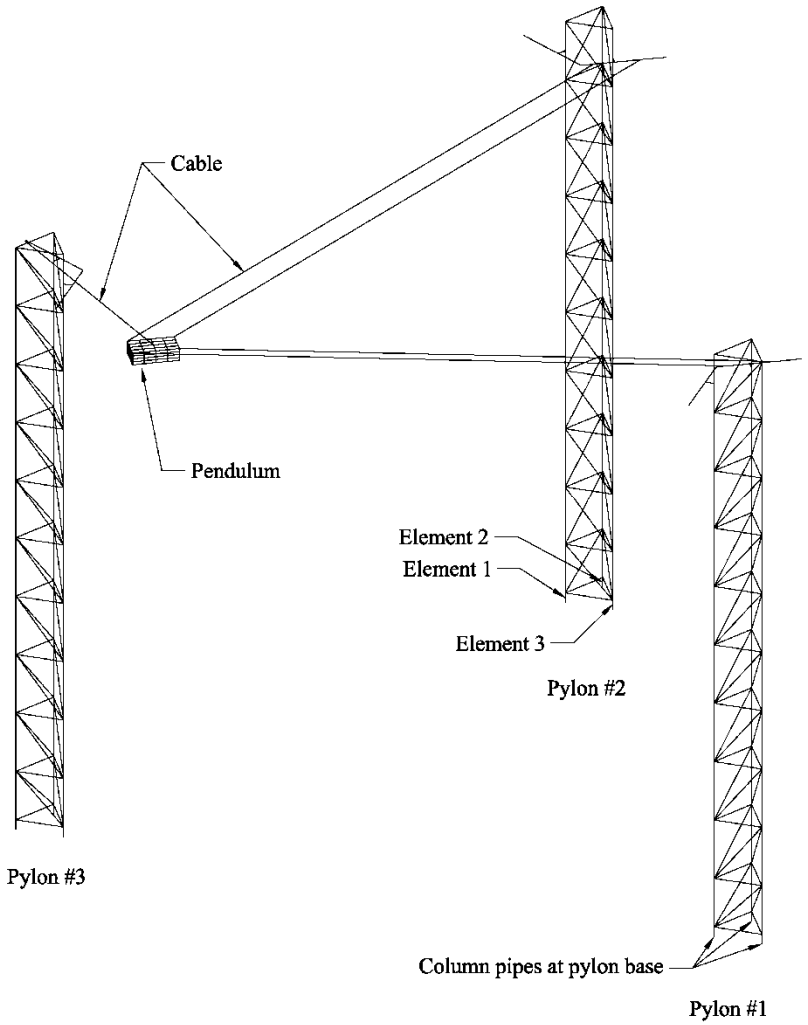

Figure 4-3. Finite element model of the pendulum support structure

Solid elements were used to model the pendulum impactor. Mass density of the solid elements was specified such that the total mass of the impactor was equal to the factored mass

(1.6 x 4090 kg). Cables used to hang the impactor and pull it to the initial position were modeled using beam elements with a cable element formulation and a cable material model. At the beginning of the analysis, the pull back cable was fixed at one end and the gravity load acting on the impactor was carried by five cables (four support cables; one pull back). The pendulum impactor was then dropped by removing the fixed boundary condition of the pull back cable. Time histories of internal forces of beam elements representing the steel pipes were checked by the American Institute of Steel Construction (AISC) axial-moment interaction equations:

$$\begin{cases} \dfrac{P_u}{2\phi_c P_n} + \dfrac{M_u}{\phi_b M_n} < 1.0 \quad if \quad \dfrac{P_u}{\phi_c P_n} < 0.2 \\ \dfrac{P_u}{\phi_c P_n} + \dfrac{8}{9}\dfrac{M_u}{\phi_b M_n} < 1.0 \quad if \quad \dfrac{P_u}{\phi_c P_n} \geq 0.2 \end{cases} \tag{4-1}$$

where P_u is the axial force determined by the analysis for the factored loads, ϕ_c is the resistance factor for columns (0.85 for compression and 0.9 for tension), P_n is nominal axial capacity, M_u is moment determined by the analysis for the factored loads, ϕ_b is the resistance factor in bending, and M_n is nominal bending capacity.

For convenience when interpreting the results, the projected angle is defined as the angle between a hanging cable and its vertical position projected on the plane of the impactor motion (Figure 4-4). Figures 4-5 and 4-6 show internal axial force and moment versus the projected angle of the three elements representing pipe members at the base of the pylon. It should be noted that only results of the first half cycle of the impactor motion are plotted since response differences of the elements in each half cycle were negligible. Figure 4-5 indicates that the elements had similar magnitudes of maximum axial force however they had different responses of internal forces depending on their footprint locations, connected angle directions, and the position of the impactor. There was a larger variation between moment magnitudes of the elements (Figure 4-6), which indicates the higher sensitivity of the moments with respect to the positions of the pylon pipes in the pendulum system.

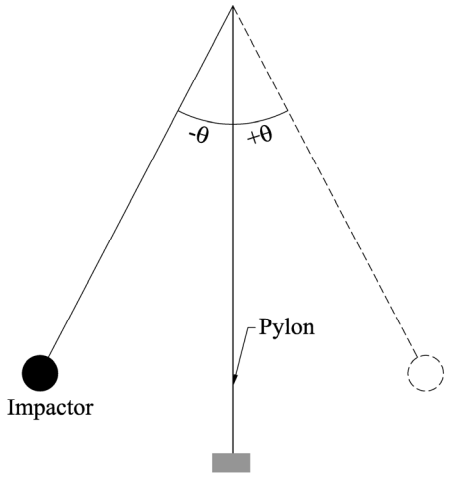

Figure 4-4. Projected angle sign convention

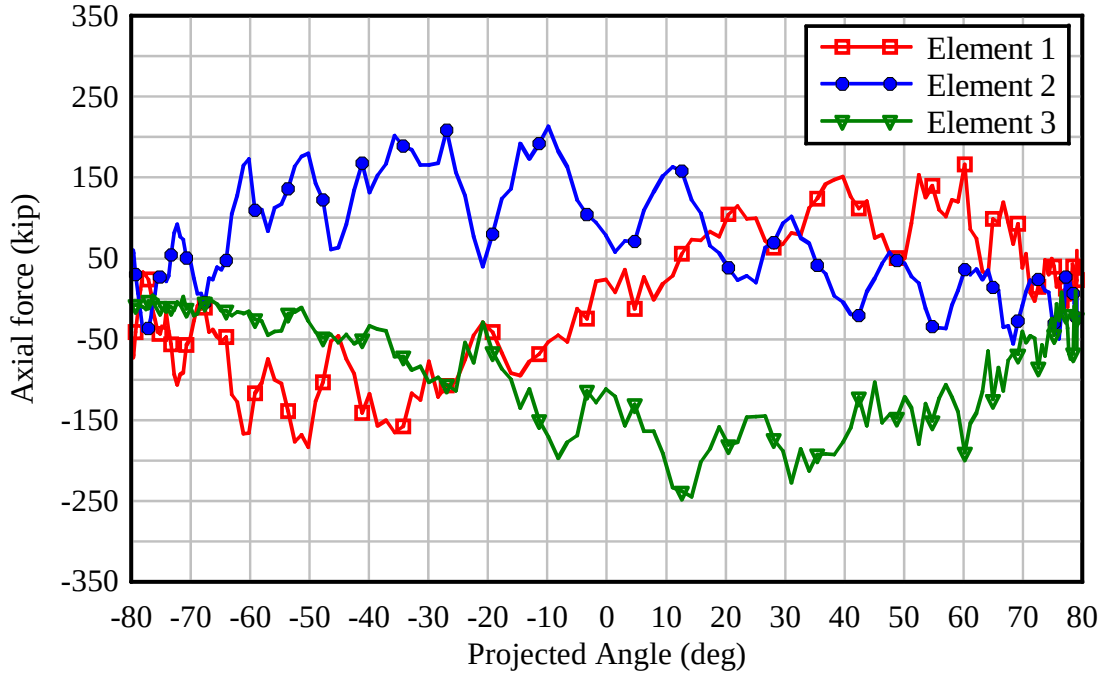

Figure 4-5. Axial forces of three column pipes at the pylon base

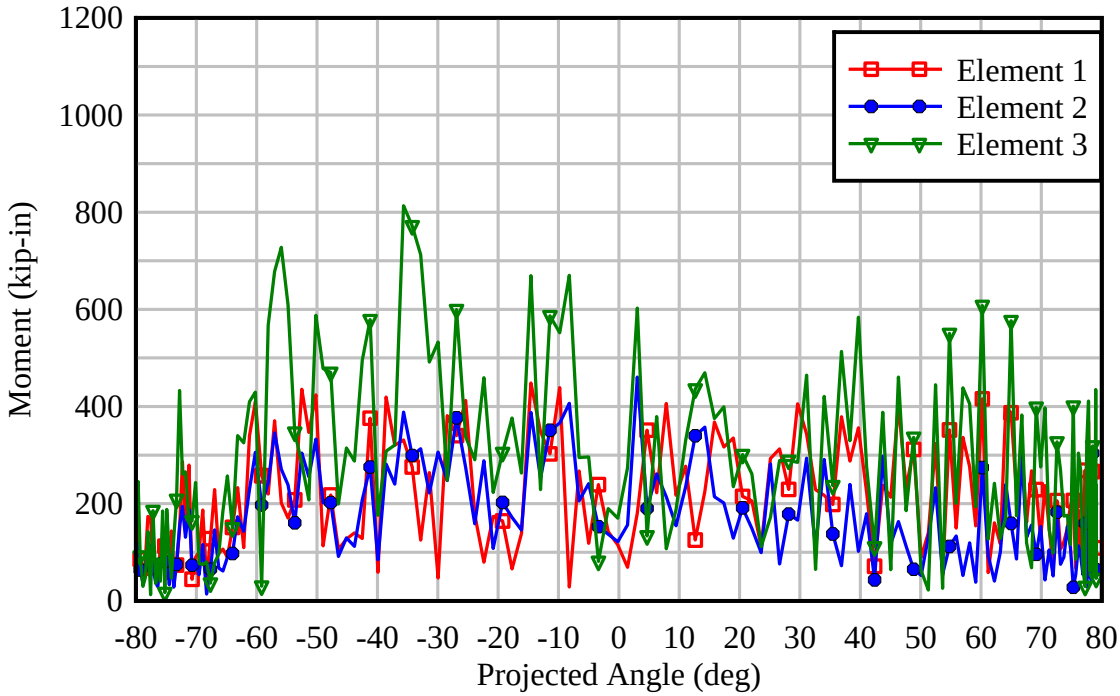

Figure 4-6. Moments of three column pipes at the pylon base

In Figure 4-7, the left hand side (LHS) terms of the AISC interaction equations and the projected angle are plotted against each other. The fact that values of the LHS terms are well below 1.0 indicates structural adequacy of the selected pipes. In addition, it can be seen that the

elements experienced a similar level of loading severity, indicated by LHS term magnitude. Although element 1 had a considerably larger internal moment than elements 2 or 3, its corresponding axial force at the same projected angle is small.

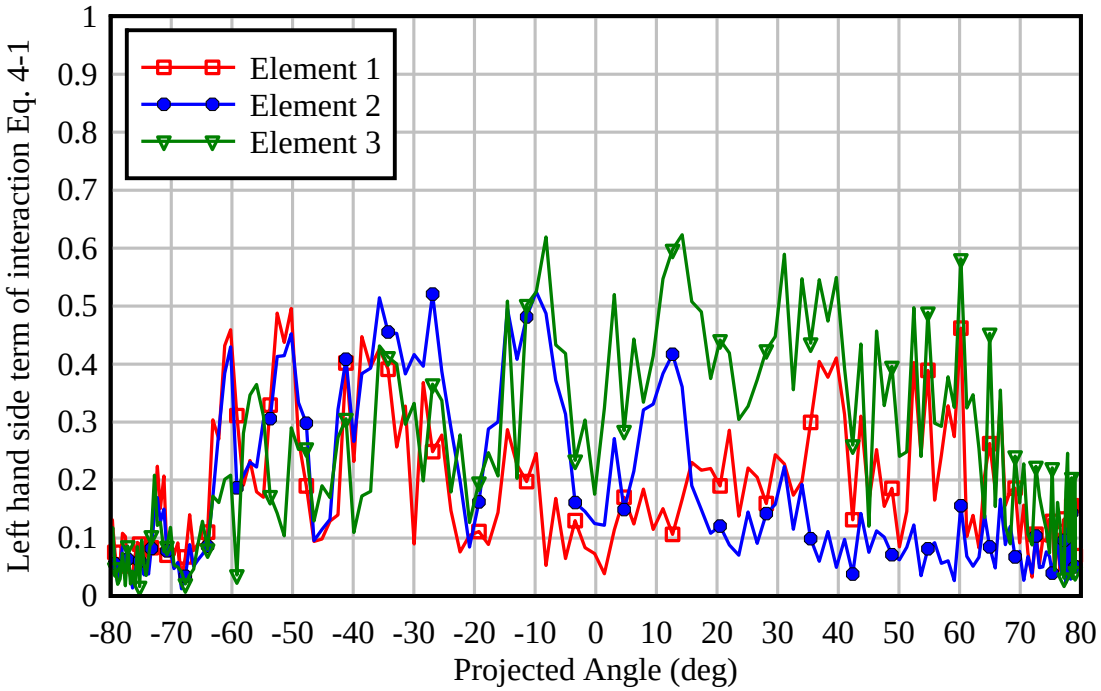

Figure 4-7. Lefthand side terms of AISC interaction equations for three column pipes at base of pylon

4.3.2 Simplified Dynamic Analysis

In addition to the time history dynamic analysis of the live loading (load case 2), the structure was also analyzed by a simplified dynamic analysis method to provide further confidence in the dynamic analysis results. In the simplified analysis method, the inertial effects of the pylons during the swinging motion of the impactor were neglected, thus, the dynamic interaction between impactor and pylons was eliminated from the analysis. Implementation of this analysis approach was carried out by computing forces in the impactor hanger cables at several critical positions during the impactor swing. Detailed calculation of the cable forces can be found in Appendix C. The forces represent dynamic loads induced by the impactor to the cables. The pylon structure was then statically analyzed by applying these forces at the cable hanger locations in conjunction with structural self-weight. Figure 4-8 shows a finite element model of a pylon with applied cable forces illustrated. At each cable hanger location, three force components were applied. Magnitudes and directions of the forces varied with respect to the impactor position being studied (as defined by the projected angle).

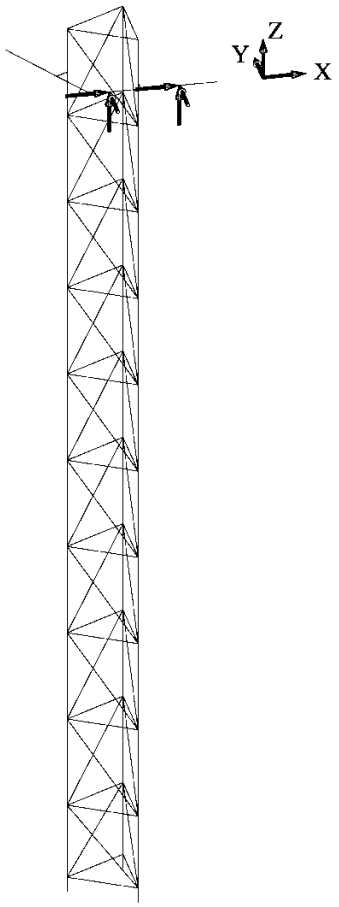

Figure 4-8. Cable forces applied to a pylon

Two analysis programs, ADINA (2005, version 8.3.1) and LS-DYNA (LSTC 2006), were used to conduct static analyses of the pylon. In order to achieve static analysis using the explicit-dynamic LS-DYNA program, a quasi-static analysis was performed by gradually ramping applied loads to the target values. Figure 4-9 shows axial force results for the three elements at the base of a pylon (Figure 4-3) with respect to the projected hanger cable angle, as computed using three different analysis approaches: dynamic analysis by LS-DYNA, quasi-static analysis by LS-DYNA, and static analysis by ADINA (simplified dynamic analysis). It can be seen that quasi-static and static results computed by the two different programs agree very well. The agreement suggests that the LS-DYNA finite element model of the pylon was a reliable means of computing design forces. The trends of the static and quasi-static axial forces of the elements also match the corresponding dynamic responses indicating reliable dynamic analysis results.

Magnitudes predicted by the dynamic analysis method, however, were (as expected) larger than those predicted by simplified dynamic analysis due to dynamic response of the pylon. Similarly, moment results computed using the various analysis approaches are plotted against the projected hanger cable angle in Figure 4-10. Moments from quasi-static and static analyses by LS-DYNA and ADINA closely match. The trends of moments with respect to projected angle from the three approaches are similar. The figure indicates that simplified dynamic analysis

(static and quasi-static) considerably underestimates maximum moments carried by the elements. Dynamically predicted axial and moment results for each element were greater than the statically predicted values, therefore, dynamic analysis results were used in design of the pendulum structure.

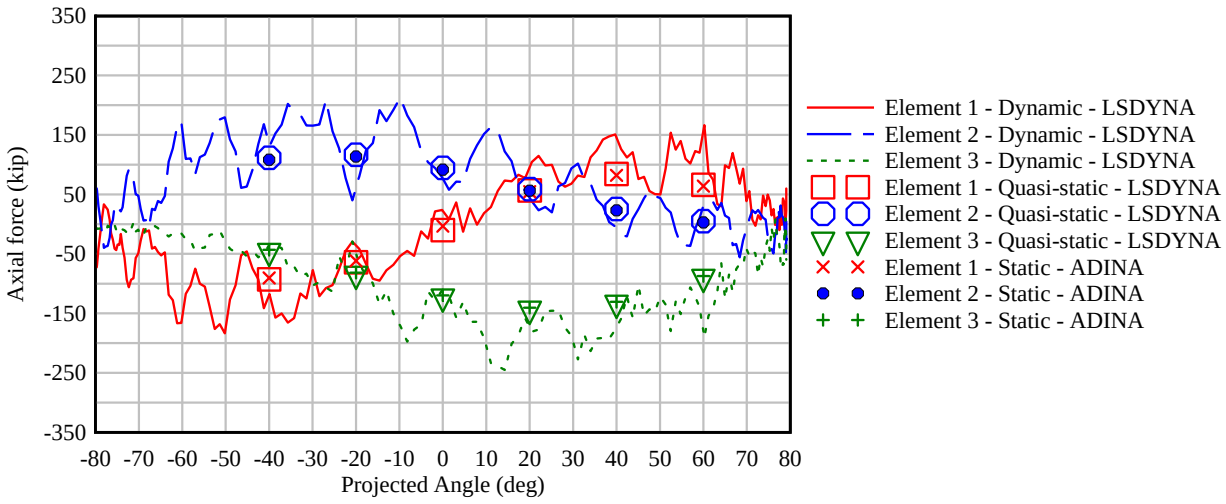

Figure 4-9. Result comparison of axial forces between dynamic and simplified dynamic analysis methods

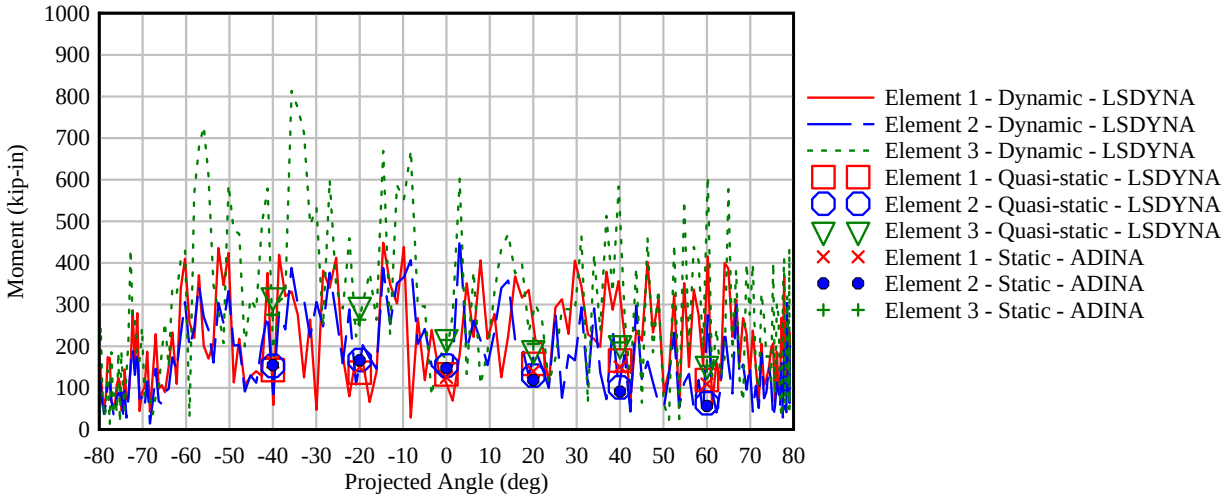

Figure 4-10. Result comparison of moments between dynamic and simplified dynamic analysis methods

4.4 Column Punching Check

A detailed stress analysis of column pipes at the base of the pylons was also conducted to ensure adequate stability and strength against punching caused by stiffeners. A quasi-static analysis using LS-DYNA was utilized to perform the design check. In order to accurately capture the localized deformation and possible buckling of pipes and stiffener plates, a high

resolution model of the components with solid or shell elements was needed instead of resultant beams. However, modeling the whole pendulum support structure with this approach was computationally infeasible. Therefore, only the column pipe, base plate and associated stiffeners in the vicinity of the ground level (collectively referred to as pipe stubs) were included in the finite element model for punching analysis. Internal forces of the pipe components obtained from the dynamic analysis were used as applied loads in the punching analysis model. Generally, critical loading conditions for punching analysis were obtained when column pipes reached the maximum axial load, maximum moment, and maximum left hand side (LHS) term of the AISC interaction equations. These maximum values were quantified from the dynamic analysis of all elements that modeled the column pipes.

From dynamic analysis of the structure, maximum moment condition and maximum LHS condition occurred simultaneously. Therefore, two critical conditions were identified and used for punching analyses of pipe members. The first condition consisted of internal forces of the pipe stub at the pylon base at the time the maximum moment and maximum LHS (axial force of 148.9 kip, moment of 1072 kip-in, and shear of 33 kip) were reached. The second condition was determined by internal forces of the critical column pipe at the time that maximum axial force occurred (axial force of 230 kip, moment of 378 kip-in, and shear of 3.2 kip). Figure 4-11 shows a schematic of the column pipe at pylon base under the two critical loading conditions. A pipe length of 24.5 in. from the ground level was chosen to ensure that the applied load representation did not affect the stress state of the pipe at the junction between stiffener and pipe wall. From the internal forces of the column pipe at the base, obtained from the dynamic system analysis, loads applied at the *top* of the punching analysis model were calculated such that the correct resultant internal forces at the base were achieved.

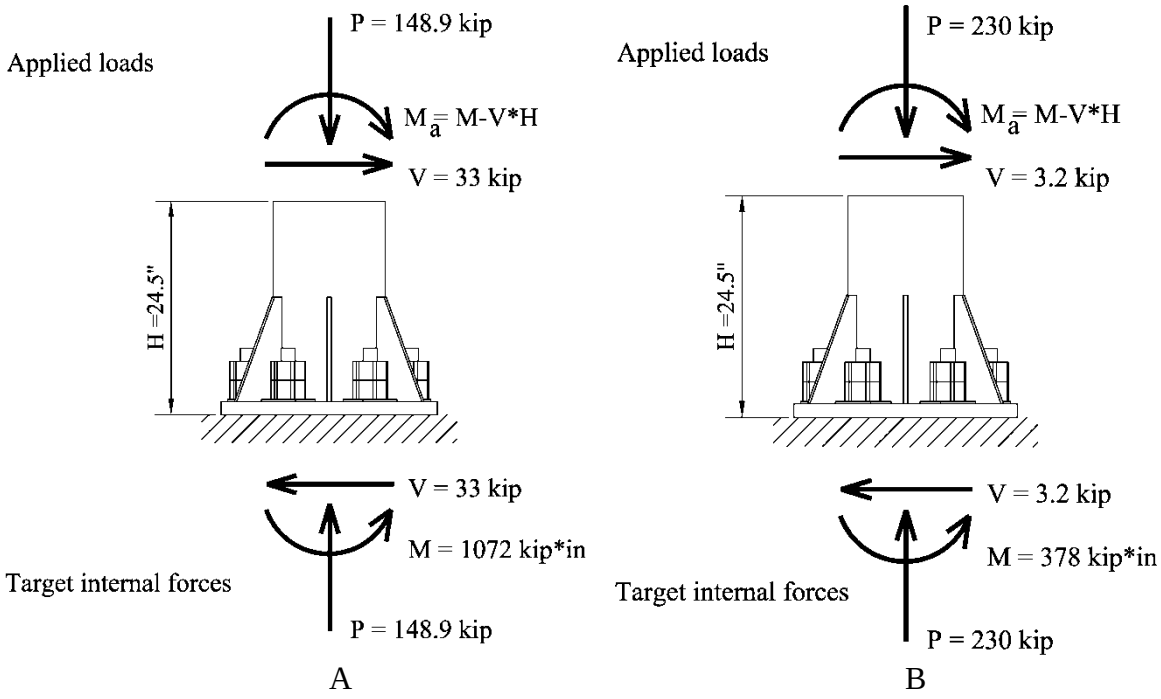

Figure 4-11. Schematic of two critical loading conditions for punching analysis: A) Maximum moment and maximum LHS term of interaction equation; B) Maximum axial force

As shown in Figure 4-12, all components were modeled using eight-node solid elements. Fillet welds between the column pipe, stiffeners and base plate were approximated by nodal merging at interfaces between the various parts. A piecewise linear plasticity material model was used for all steel components. The steel material had an elastic modulus of 29000 ksi, a Poisson ratio of 0.33, a yield stress of 36 ksi, and a failure strain of 0.2 (see Figure 3-3). The grout base was modeled using a linear elastic material model with an elastic modulus of 5,000 ksi and a Poisson ratio of 0.19. Nodes at the bottom surface of the grout base were fixed against translation and rotation. The grout base was included in the model to properly represent contact between the base plate and the foundation. This contact interaction is characterized by defining a pair of contact surfaces at the bearing surface. A nodal rigid body definition was utilized to represent the effect of anchor bolts connecting to the base plate. That is, base plate nodes at each bolt location were included in a nodal rigid body and all six degrees of freedom of a center node of the rigid body at bottom were fixed. In order to prevent unrealistic local deformation and stress concentration at the top of column pipe due to applied loads, all pipe nodes at the top pipe surface were grouped into a rigid body. Loads applied on the rigid body, therefore, acted as resultant forces and were distributed over the entire cross section.

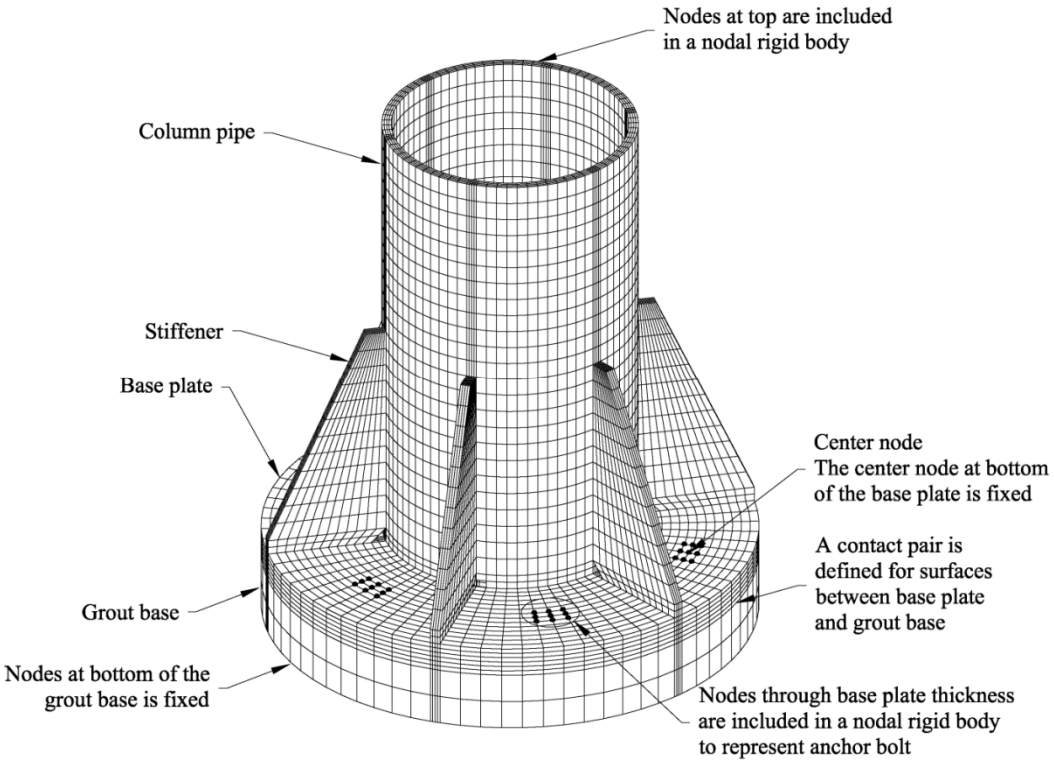

Figure 4-12. Finite element model of column pipe for punching analysis

Von Mises stress contours of the analyzed components under the two critical loading conditions are shown in Figure 4-13 and 4-14. The figures indicate that the maximum effective stresses in the pipe wall occurred at the connection with the tip of stiffeners on the compression side. Magnitudes of maximum stresses in both cases (33 ksi and 30 ksi) are approximately equal to each other and below the minimum yield stress of 36 ksi of the column pipe steel. Therefore, the pipe and stiffener design was deemed to be structurally adequate for use at the base of the pendulum structure.

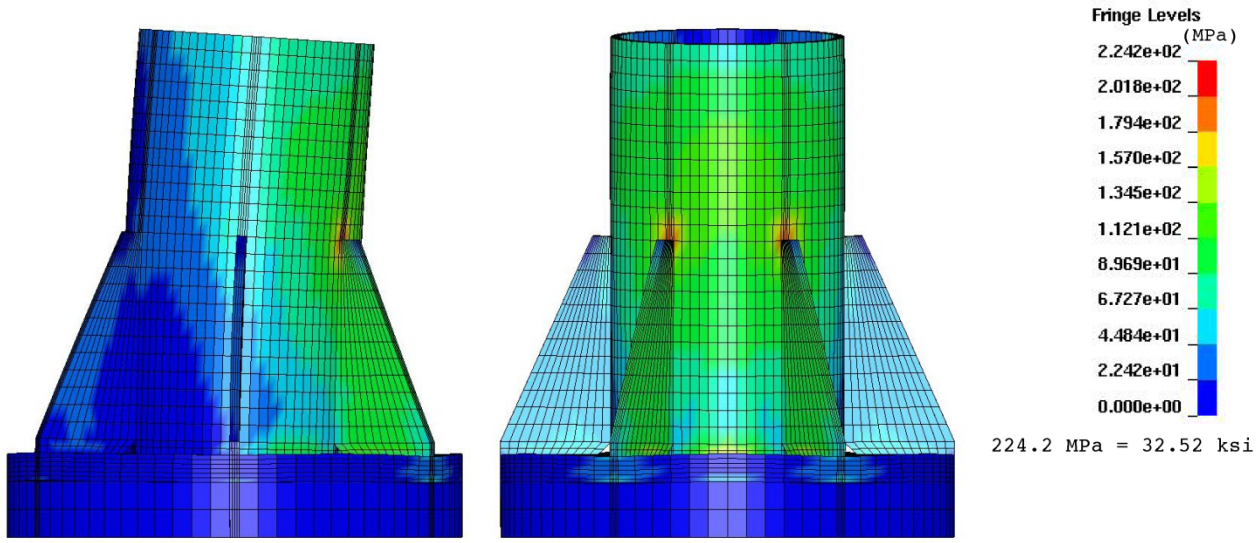

Figure 4-13. Von Mises stress contour plot under the loading condition shown in Figure 4-11A

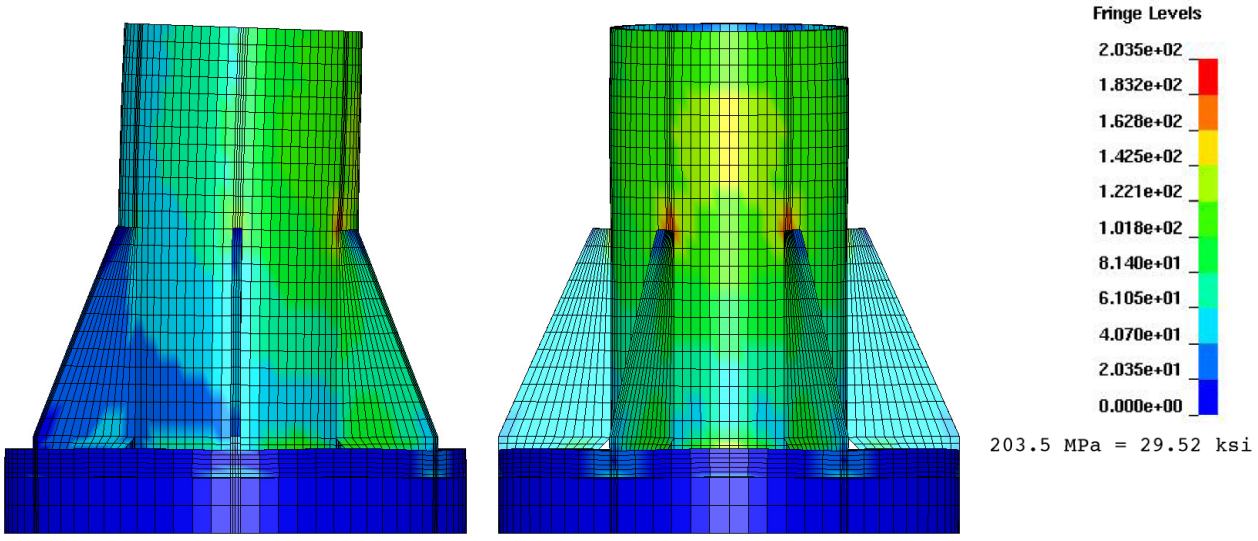

Figure 4-14. Von Mises stress contour plot under the loading condition shown in Figure 4-11B

4.5 Constructed Pendulum Facility

The pendulum impact facility was fabricated and constructed, by FDOT personnel, at the FDOT Structures Research Center (Figure 4-15). After fabrication, each of the three steel pylons was galvanized prior to erection. The pylons were supported on drilled shaft foundations that are 19 ft. long with a diameter of 4 ft.

Figure 4-15. Completed pendulum impact test facility at the FDOT Structures Research Center

CHAPTER 5
FRICTION TESTS

5.1 Introduction

Breakaway connections generally involve contact between various components. Therefore, development of a breakaway connection requires the determination of material friction coefficients of the components. Since multi-column ground signs are currently designed conforming to FDOT standards which requires steel components to be galvanized in accordance with Standard Specifications 962-7, the friction coefficient of galvanized steel needed to be quantified. Moreover, preliminary analyses of breakaway connection concepts, conducted using computer simulation, indicated sensitivity of breakaway performance to friction. Generally, low friction is desirable for breakaway connections since it reduces the load required to separate a sign post from the stub base. Consequently, the likelihood of injury to vehicle occupants upon impact is decreased with decreased friction. In this study, two different friction reducing products—an anti-friction coating called the Molykote-7409 and a Teflon PTFE (polytetrafluoroethylene) sheet—were explored. Based on the product specifications, these materials appeared to hold promise in lowering the friction between contacting steel surfaces. However, instead of directly using friction coefficients obtained from the product specifications, experimental tests were conducted to quantify frictional values for the materials when used with structural steel. In addition to friction reducing materials, the friction coefficient for plain (untreated) steel on steel condition was also quantified.

5.2 Friction Test Setup Description and Test Results

Tests were conducted for four friction conditions: plain steel on plain steel, galvanized steel on galvanized steel, Molykote coated plain steel on Molykote coated plain steel, and a Teflon sheet inserted between galvanized steel components. An overview of the experimental test setup used to quantify static friction coefficients is illustrated in Figure 5-1. Each test involved vertically pulling a slip plate using a loading frame and a 30-kip Instron testing machine (see Figure 5-2). Motion of the slip plate was restrained through frictional resistance at the grip surfaces as a result of the compression load (normal force) exerted by a hydraulic jack. A jack compression load of 18.6 kip was applied to the angles through ½ in.-thick bearing plates and kept constant during each test. The jack load was applied concentrically at the center of the grip area to achieve an approximately uniform pressure on the slip plate. A built-in load cell of the Instron testing machine was used to record the tension load applied to the slip plate. The tension load was applied at a rate of 10 lbf/sec until the plate slipped out of the holding angles. For each test condition, the friction coefficient was determined as the ratio of the maximum tension load to the compression jack load (i.e., normal force).

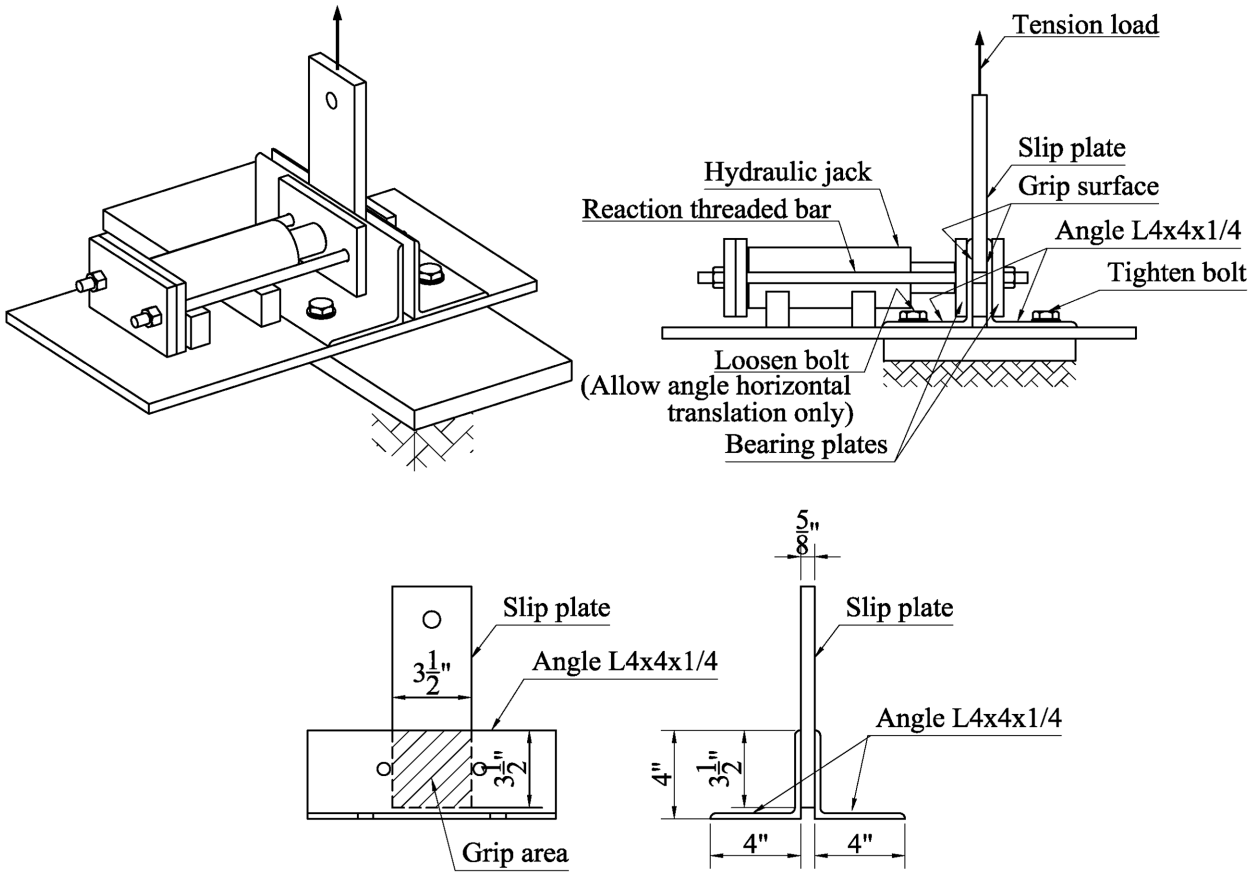

Figure 5-1. Experimental test setup used to quantify static friction coefficients

Figure 5-2 shows the plain steel on plain steel friction condition that was tested in which the specimens, slip plate, and angles, were constructed from A36 structural steel. Hot-dip galvanized steel specimens for the galvanized steel on galvanized steel friction coefficient determination are shown in Figure 5-3. For the steel friction condition between the Molykote coated steel components, all grip areas of the plain steel specimens were coated with a thin film of the Molykote-7409 lubricant and cured prior to testing (see Figure 5-4). The test setup used for evaluation of the Teflon sheet friction condition is presented in Figure 5-5. Two Teflon sheets, each 0.02 in. in thickness, were placed between the galvanized steel tension plate and the galvanized steel angles to cover the grip areas.

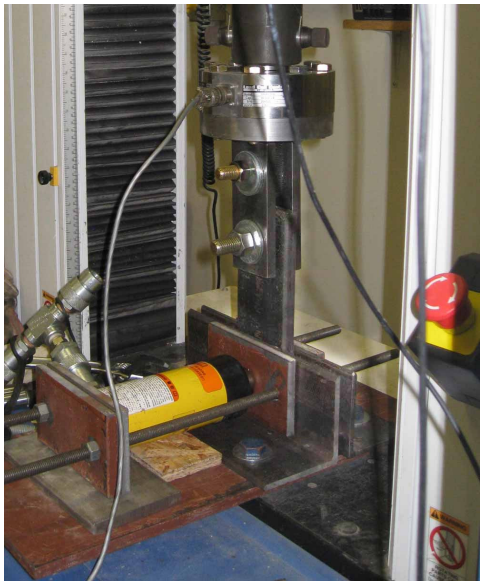

Figure 5-2. Experimental setup used to quantify static friction coefficients

Figure 5-3. Galvanized steel specimens

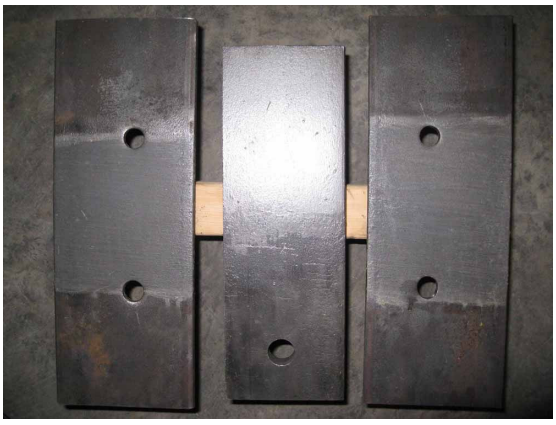

Figure 5-4. Steel specimens coated with Molykote-7409 anti-friction lubricant at grip areas

Figure 5-5. Experimental setup with Teflon sheets installed

In Table 5-1, static friction coefficients obtained from the experimental tests are presented. The results indicate that galvanization of steel components provided a lower friction condition than plain steel. However, the friction coefficient of galvanized steel on galvanized steel of 0.45 is still relatively high. The Molykote-7409 friction-reducing coating and the Teflon sheet both considerably reduced friction conditions between contacting steel parts. It is noted that the experimentally determined frictional coefficient of the Molykote coated steel on Molykote coated steel was 0.35, which is higher than that of 0.1 cited in the material specifications. However, this difference is likely due to the fact that a thin film of Molykote is not as effective on the surface of textured, untreated steel components as it would be on machined (smooth) steel surfaces. Conversely, test results obtained from the use of 0.02 in.-thick Teflon sheets indicated insensitivity to surface texture of contacting parts. The Teflon sheet friction coefficient of 0.2 obtained from the experimental test agreed well with that from the Teflon product specifications. Since the use of the Teflon sheets was found to effectively reduce friction between contacting steel parts, even with surface texture present, Teflon was used in the design of the breakaway connection that was developed in this study.

Table 5-1. Friction coefficients determined from experimental tests

Friction condition	Friction coefficient
Plain steel on plain steel	0.55
Galvanized steel on galvanized steel	0.45
Molykote coated steel on Molykote coated steel	0.35
Teflon sheet (with galvanized steel)	0.20

CHAPTER 6
NUMERICAL DEVELOPMENT OF SHEAR-CONTROLLED MOMENT COLLAR BREAKAWAY CONNECTION

6.1 Introduction

With the goal of finding a new solution to improve the current designs of breakaway sign support structures, so that a sign support structure is capable of resisting the selected hurricane wind load of 150 mph but will break away under vehicle impact, a new shear-controlled moment collar connection was developed. This chapter presents and discusses the development of the new breakaway connection using numerical simulations. Possessing robust capabilities in large-deformation dynamic impact contact analysis and a variety of nonlinear material models and element types, the finite element analysis program LS-DYNA (LSTC 2006) was used as the primary tool in the numerical development of the breakaway connection.

6.2 Numerical Development Procedure of the Connection

The numerical procedure used for the breakaway connection development in this research included the following major steps:

Step 1: From the functional design goals, sign configuration, design wind load, and targeted breakaway performance, conceptual breakaway sign support systems were proposed.

Step 2: The conceptual breakaway sign support systems were transformed into preliminary designs with sufficient detail for finite element modeling. This step involved structural calculations conforming to standard design requirements and sizing structural components with consideration of the feasibility of fabrication and installation, as well as the service condition of the system.

Step 3: The preliminary designs were then evaluated using computer simulation techniques. In this step, finite element models of the proposed sign support structures with breakaway connection features were developed and analyzed for structural adequacy and breakaway dynamic performance. Analyses for moment capacity were conducted to ensure adequate functional capacity of the structure under the design wind load, since new breakaway features generally introduce “non-standard” components that requires the structure to be analyzed as a whole. Impact simulations were performed to predict and evaluate dynamic performance of the structure. AASHTO requires support structures to be tested at test level 3 specified in NCHRP 350 for use on high-speed arterial highways. At this test level, sign support structures are impacted by a 820-kg standard vehicle at a low-speed of 35 km/h (21.7 mph) and a high-speed of 100 km/h (62.1 mph). Impact angle ranges from 0 degree to 20 degrees. However, according to NCHRP 350, low-speed tests are generally conducted to evaluate breakaway, fracture, or yielding mechanisms. Therefore, during the preliminary design evaluation step of this study, low-speed impact simulations with the 820-kg test vehicle were conducted.

Step 4: By comparing breakaway performance from impact simulation results of the preliminary designs and taking fabrication, installation, and maintenance issues into account, the most promising preliminary design was selected.

Step 5: At this step, extensive computer simulations were conducted to refine the selected design. A range of friction conditions were included in the simulations to investigate the effect of friction on the breakaway performance. Experimental tests were also conducted at this stage to explore friction-reducing materials in order to produce a breakaway connection design that was not sensitive to friction. Concerns regarding penetration of the breakaway sign support structure parts into the vehicle occupant compartment were investigated using a 2000-kg pickup truck in

impact simulations. High-speed impact simulations were also conducted to evaluate the vehicle and test article trajectory.

6.3 Conceptual Development of Shear-Controlled Moment Collar Connection

From design wind load, as well as functional and breakaway requirements of sign support structures, a breakaway connection concept was developed in this study that is referred to as a "shear-controlled moment collar". The underlying principle of the shear-controlled moment-collar connection is that a large moment capacity of the post be maintained while dramatically reducing the shear capacity. Key aspects in the development of this connection concept were:

1. Difference of the load application point on the structure: A vehicle impacts at a low elevation near the ground level while wind load acts at much higher elevation.

2. The design wind load on a post associated with the selected large sign is less than the impact load that a vehicle is capable of generating.

3. For a given design wind load on a sign panel, increasing the elevation of the center of gravity of the sign panel increases the ground moment linearly but the shear at the ground level is constant. Shear is also essentially constant over the post length because wind loads applied directly on the projected area of the post are insignificant in comparison to that applied to the sign panel.

Key point 1 above relates to the difference of post internal forces at the breakaway plane. Both moment and shear act at the breakaway plane of a post when wind load is applied to the system, while primarily shear acts at the plane when a vehicle collides with the post. From the standpoint of wind resistance, the post must be able to transfer both moment and shear to the foundation. However, from the standpoint of the breakaway requirement, the post should have shear and moment capacities that are as small as possible. Fortunately, key point 2 indicates that the breakaway connection can be designed for shear capacity up to that required for wind resistance but can still be frangible under vehicle impact. The remaining issue involves transferring the post base moment to the foundation without preventing the post from breaking away under vehicle impact.

Key point 3 suggests that for a very low clearance height, a post designed solely on the shear capacity requirement may have sufficient required moment capacity. However, ground signs must have the minimum clearance of 7 ft. Moreover, to ensure that the connection concept developed in this study is applicable to a variety of different ground sign configurations, a more conservative clearance height of 11 ft has been selected. This choice results in a very large moment at the base of the post. Consequently, design of the post based solely on the shear requirement does not guarantee that the post has sufficient moment capacity. Therefore, there is a need to be able to increase the moment capacity of the post connection without correspondingly increasing the shear capacity.

From the goals and keys identified above, a conceptual shear-controlled moment collar connection used in a three-post support structure was developed. The conceptual connection is shown in Figure 6-1. The webs and flanges of the posts and post stubs are thickened on both sides in the vicinity of the slipping plane. The post and post stub are joined by two U-shaped collar halves. Webs of the collar halves are recessed in the middle region to accommodate the

thickened parts of the posts and post stubs. The collar halves are then joined to each other by two connector bolts on two sides. A schematic diagram of load transfer from the upper post to the post stub through the conceptual connection is shown in Figure 6-2. Moment is transferred to the post stub through the thickened flanges and collar halves. Therefore, transferring full moment capacity of the post, required by the design wind load through the connection, can be maintained by sizing appropriate thickness and height of the thickened parts of the post and collar halves. Shear is transferred to the post stub through connector bolts and collar halves. Shear capacity required to resist the computed wind load is achieved by selecting suitable bolt tension capacity. It should be noted that the idealized load transfer mechanism described above corresponds to the condition where deformation of connection parts are negligible and connector bolts are equally loaded.

The advantage of this conceptual connection is that the shear and moment capacities of the connection are designed independently. Therefore, satisfying the large moment capacity requirement will not affect the frangibility feature of the connection under vehicle impact. Instead, shear capacity of the connection can be designed in a controlled manner to resist the shear force due to wind load. Another feature of this connection concept is that under the effects of wind load, and with frictional effects included, the moment component helps to increase shear capacity of the connection (due to friction) at the shearing plane on the compression side and at the contact surfaces between the post and the collar on the tension side of the connection. However, under vehicle impact, in which the friction is not desired, the moment component at the breakaway plane is much smaller than that of the wind load (since impact location is close to the plane). The advantage of this conceptual shear-controlled moment collar connection over the slip-base connection currently used in Florida is that it overcomes the problems of sensitivity to bolt pre-tension. Therefore impact frangibility of the new connection is not sensitive to installation and maintenance procedures.

6.4 Structural Design of Sign Support Structure with Shear-Controlled Moment Collar Connection

Based on the preliminary conceptual design discussed above, various connection prototypes were explored utilizing finite element impact simulation. For each prototype considered, a moment capacity analysis and four low-speed impact analyses were performed to quantify the system moment capacity and to evaluate performance of the breakaway mechanism. This section presents a shear-controlled moment collar connection that met the structural adequacy requirement for the design wind load and occupant risk criteria under the low-speed 0-degree impact angle simulated conditions. The connection was fabricated and experimentally tested (described in the next chapter) to evaluate its frangibility under static equivalent impact load and moment capacity as is required for wind resistance. An overview of the sign support structure with the shear-controlled moment collar connection is presented in Figures 6-3 and 6-4.

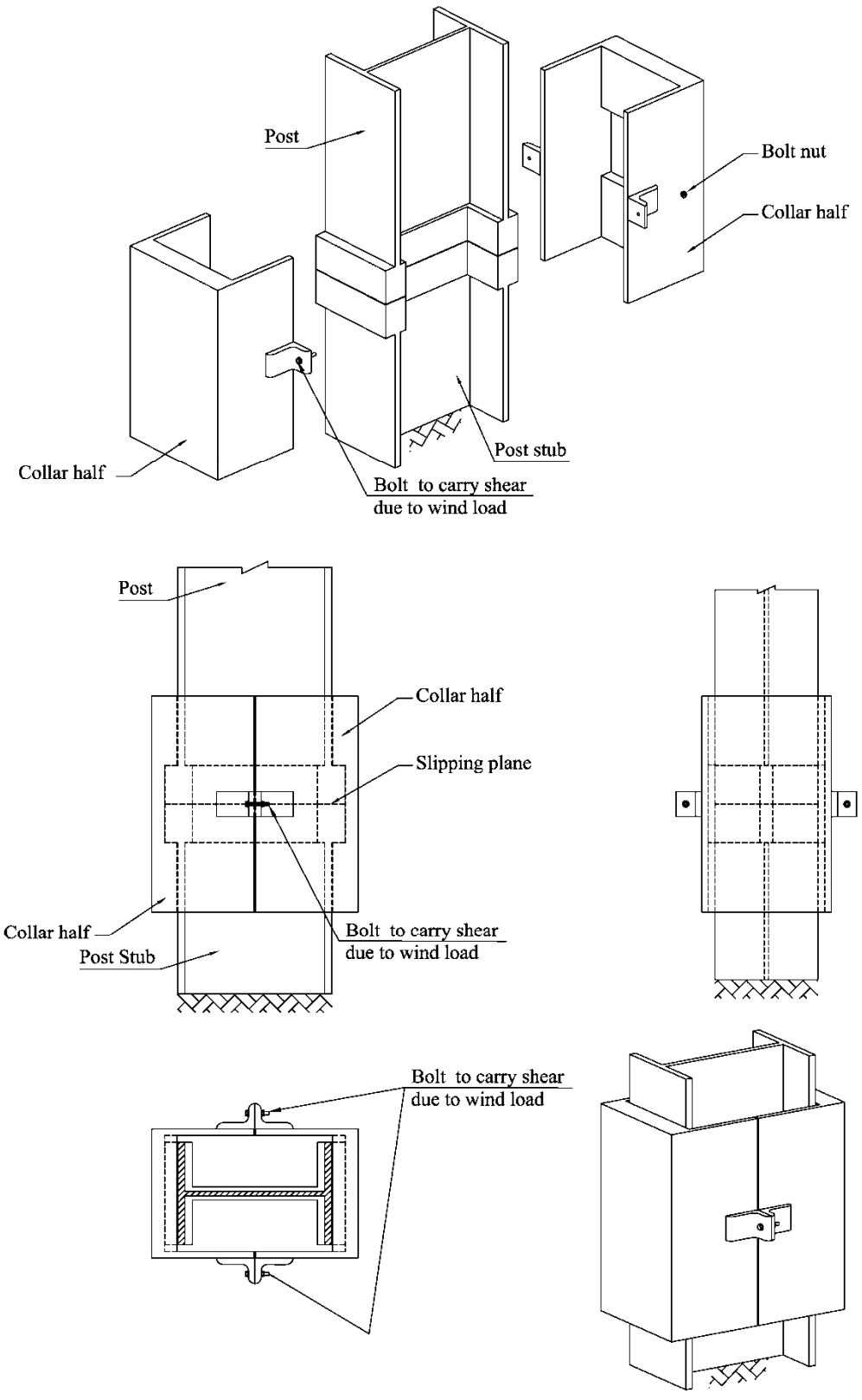

Figure 6-1. Preliminary concept of the shear-controlled moment collar connection

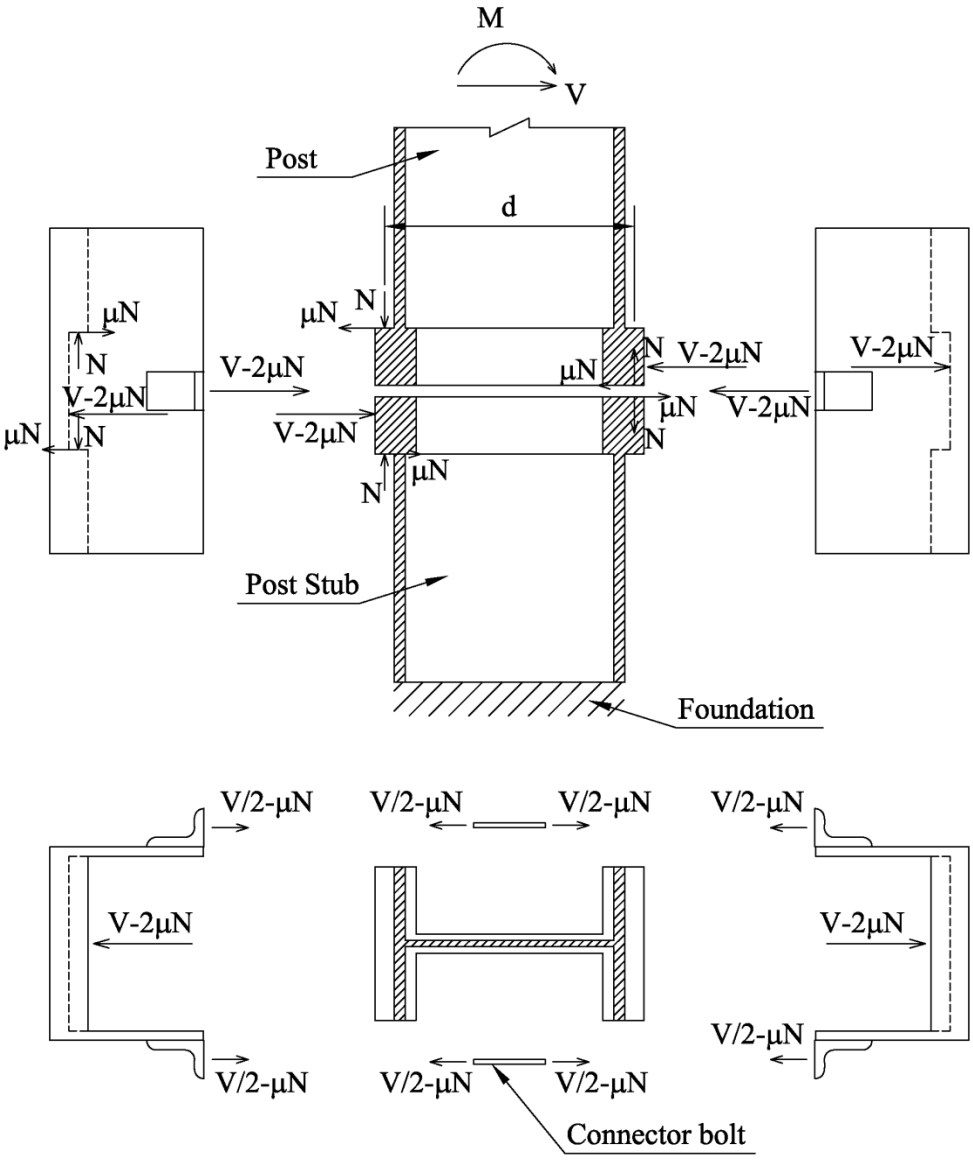

Figure 6-2. Schematic of load transfer through the preliminary concept shear-controlled moment collar connection

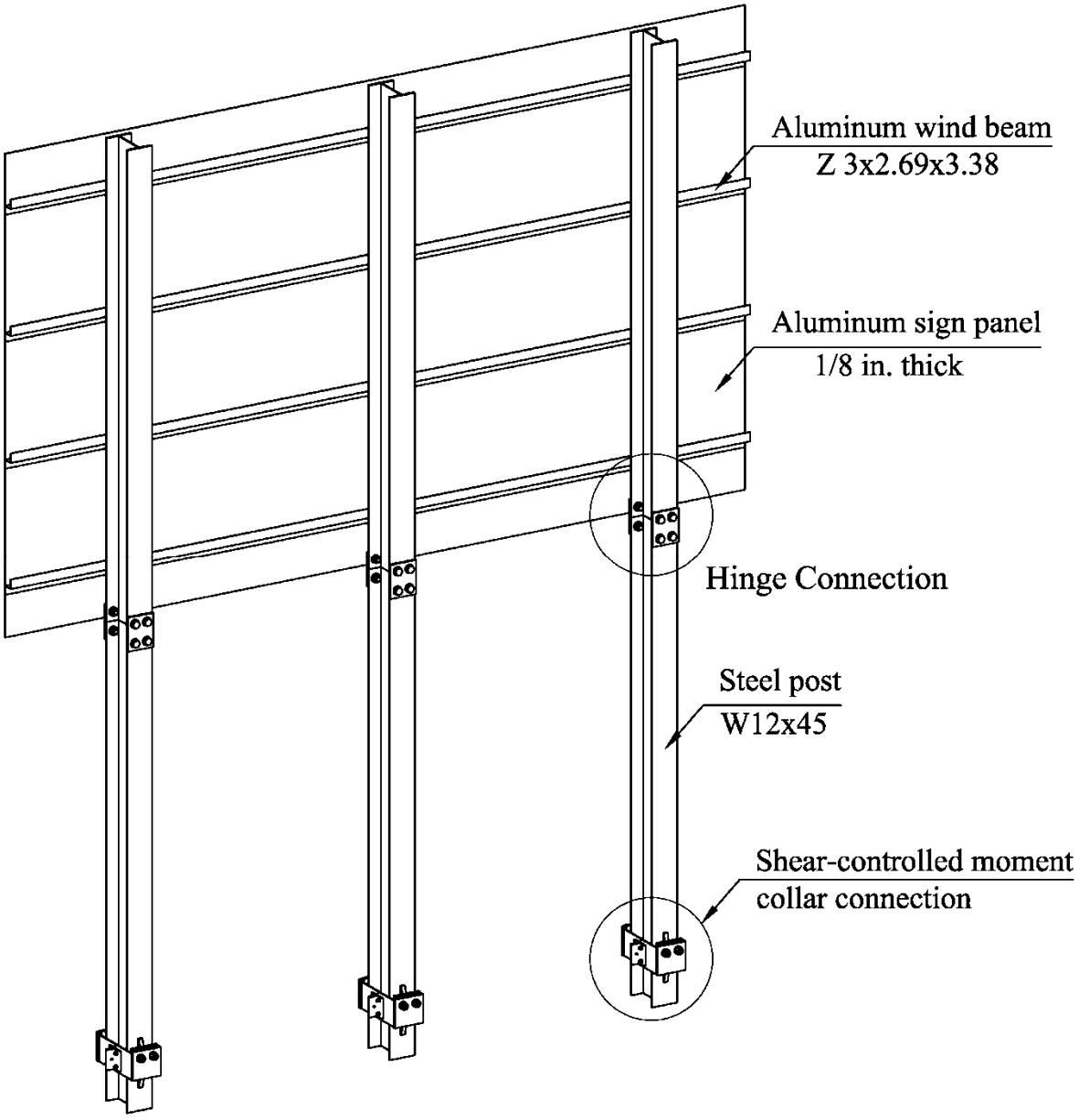

Figure 6-3. Isometric view of sign support structures with shear-controlled moment collar connection.

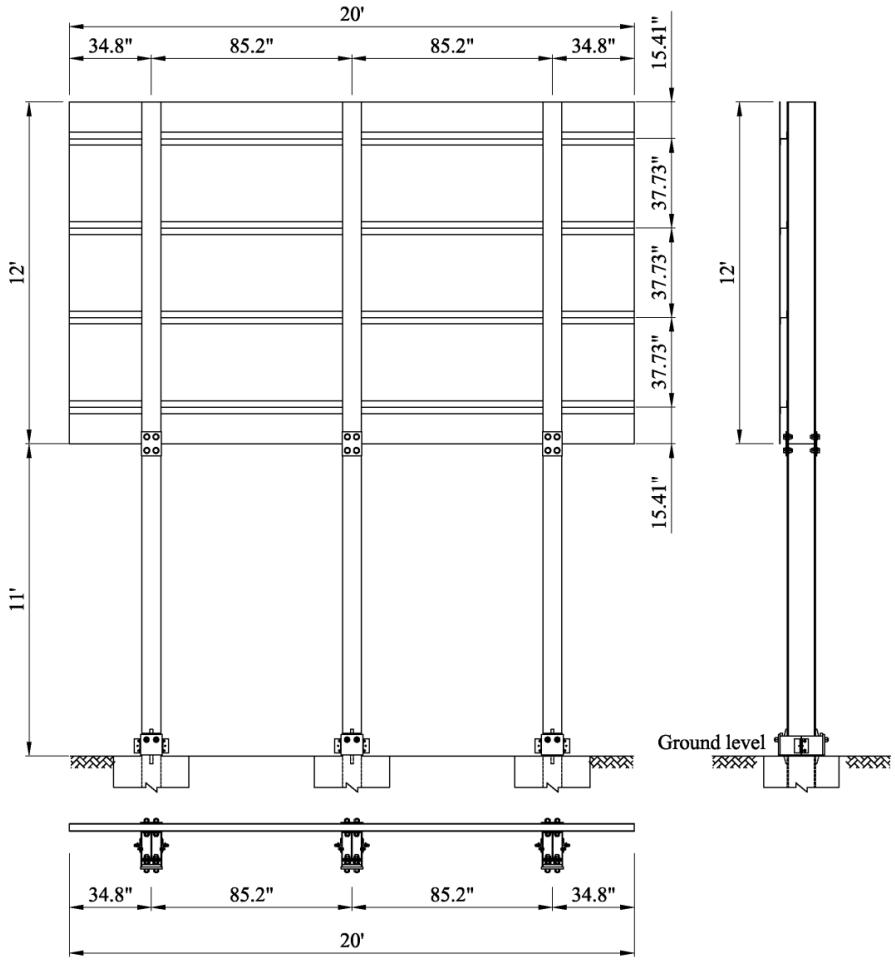

A

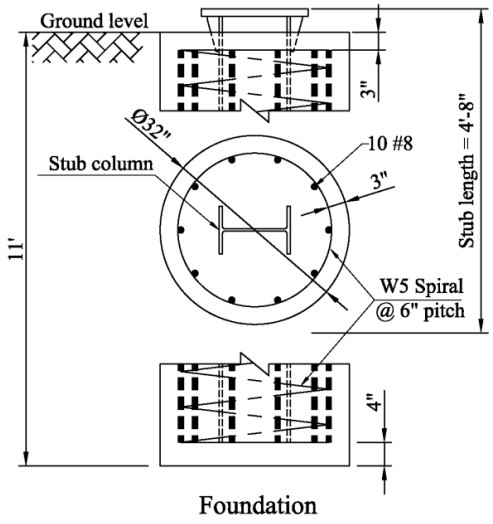

B

Figure 6-4. Sign support structures with shear-controlled moment collar connection: A) Elevation and plan views; B) Foundation

The sign structure includes a sign panel and three wide-flange steel posts arranged in a single row. The sign panel, the configuration of which is based on Index drawing 11200 of the FDOT (2008) design standards, consists of a 1/8 in.-thick aluminum sheet and four Z3x2.69x3.38 aluminum wind beams at 37.73 in. apart. Steel post size selection for wind load and self-weight conformed to AASHTO (2001) and FDOT (2008) design standards. For the selected sign structure configuration and design wind load, a steel W12x45 post was selected. (Detailed post design calculations are provided in Appendix A.) Each post is separated near the ground level and at the bottom of the sign panel. The separated parts are then joined together by the shear-controlled moment collar connections and a hinge connection, respectively.

Figure 6-5 and 6-6 show overviews of the developed shear-controlled moment collar connection. Detailed fabrication drawings of the connection are provided in Appendix D.

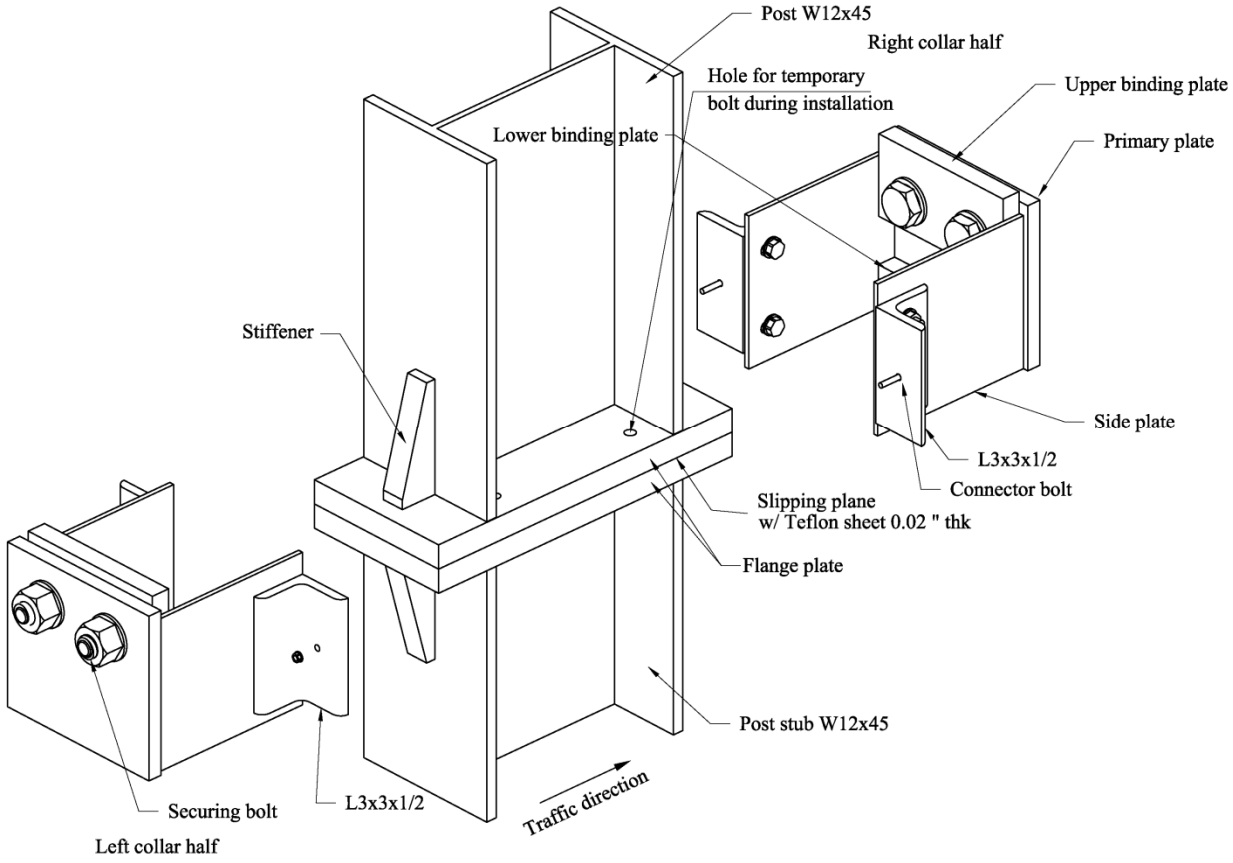

Figure 6-5. Exploded view of the shear-controlled moment collar connection

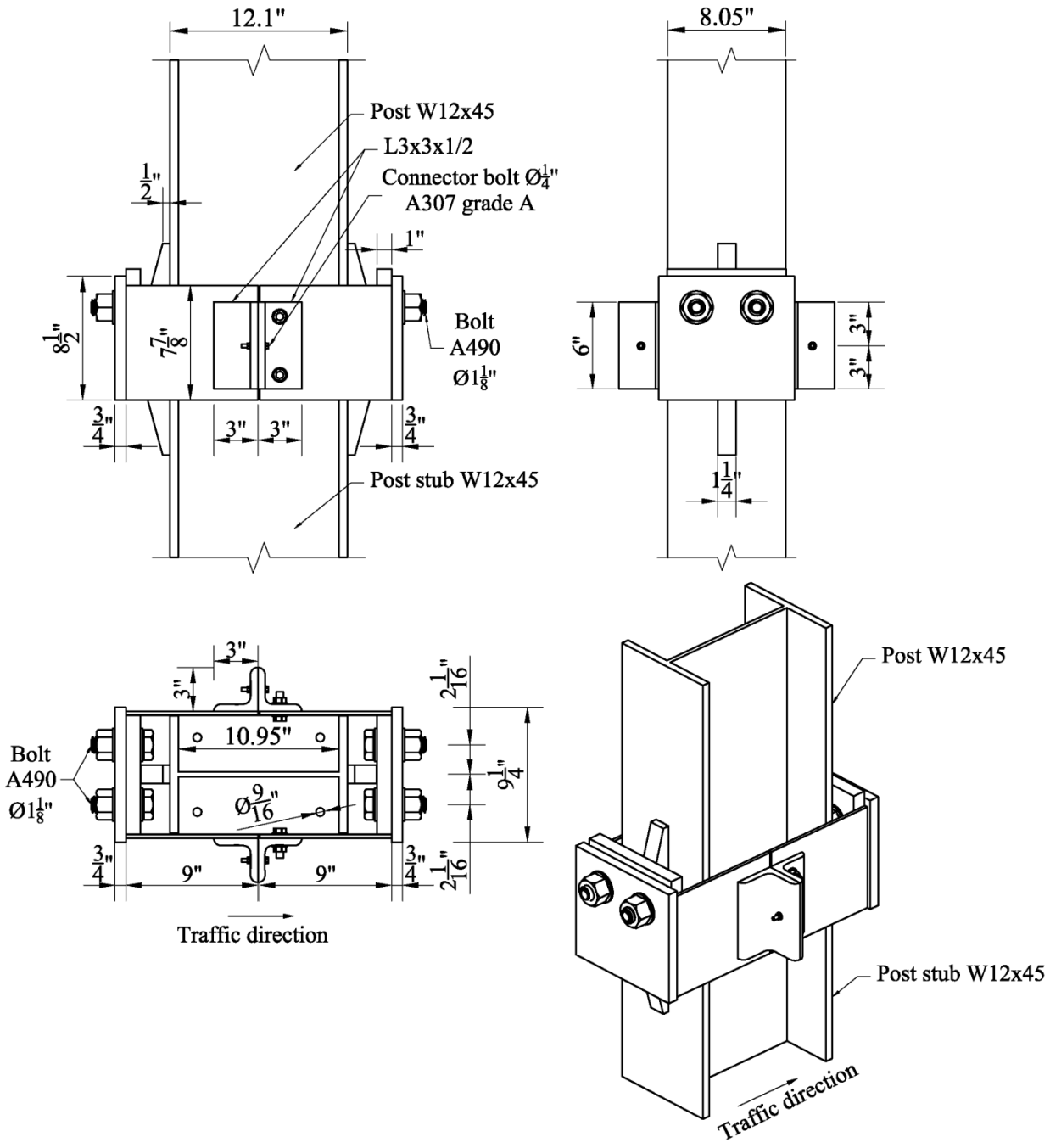

Figure 6-6. Detail of the shear-controlled moment collar connection

The connection has two 1-1/4 in.-thick steel flange plates. One plate is welded to the post, and the other is welded to the post stub to create a slipping surface between them. Four steel stiffeners of 1-1/4 in.-thickness are welded to the flanges and flange plates. Loads are transferred from the post and post stub through a collar which consists of two halves joined by two connector bolts that have a design tension strength of 3.25 kip each. Each half of the collar consists of a primary plate, binding plates, side plates, and angles. The lower binding plate is

welded to the primary plate, whereas the upper binding plate is secured to the plate by two 1-1/8 in.-diameter bolts. Bolt holes in the primary plates are slotted so that the position of the upper binding plate can be adjusted. Such adjustment may be necessary to eliminate gaps between the collar binding plates and flange plates that may result from fabrication tolerances. A 0.02 in.-thick Teflon sheet with a friction coefficient of 0.2 is used to reduce the frictional resistance at the slipping plane. Side plates are welded to the primary plate and connected by angles. Side plates on one half of the collar are slotted so that the bolted angles are adjustable to accommodate fabrication tolerances. However, angles are welded to the side plates of the opposite collar half, because the use of bolts on this side could cause snagging between the collar and post flange and therefore degrade the breakaway performance of the connection. Specific roles played by each component in the breakaway connection will be discussed in more detail later.

In addition to the shear-controlled moment collar connection, a hinge connection is also used at the elevation of the bottom of the sign panel. Figure 6-7 shows detailed views of the hinge connection which includes a hinge plate and a fuse plate, each 0.5 in. in thickness. The plates connect to separate parts of the post by 1-1/4 in.-diameter bolts. The fuse plate is perforated by four 1-11/16 in.-diameter holes to weaken the tensile strength of the plate and initiate formation of a hinged connection under vehicle impact loading. However, the fuse plate still provides adequate strength to resist the design wind load. (Structural design calculations of the hinge connection can be found in Appendix A.)

6.5 Finite Element Modeling of the Sign Support Structure with the Shear-Controlled Moment Collar Connection

During the development process of the connection, a variety of connection designs were modeled, analyzed, and modified. However, similar techniques were used for all designs in terms of material models, element types, contact definitions, and modeling approach. Moreover, design of the support structure parts above the connection did not change throughout the connection development process. Therefore, finite element modeling of the sign support structure with shear-controlled moment collar connection, presented above, is selected for discussion in this section.

A key objective in modeling a structural system is obtaining a reliable finite element model with minimum computational cost. With this in mind, modeling schemes were selected for the structural components after carefully examining and predicting the behavior of the structure. All assumptions were checked after simulations were performed. Since the sign structure was 23 ft high with three posts each incorporating a breakaway connection, modeling the entire structure with a uniform resolution would require a significant amount of computational time and resources. Therefore, different finite element meshing density levels were applied for different regions and components. The sign support posts and panel were discretized using 80,000 eight-node solid elements, 5,000 four-node shell elements and 32 resultant beam elements, resulting in more than 110,000 nodes. Shell and solid elements of the structure were assigned a fully-integrated finite element formulation to prevent hourglass modes, which may lead to unreliable predictions of the structural response.

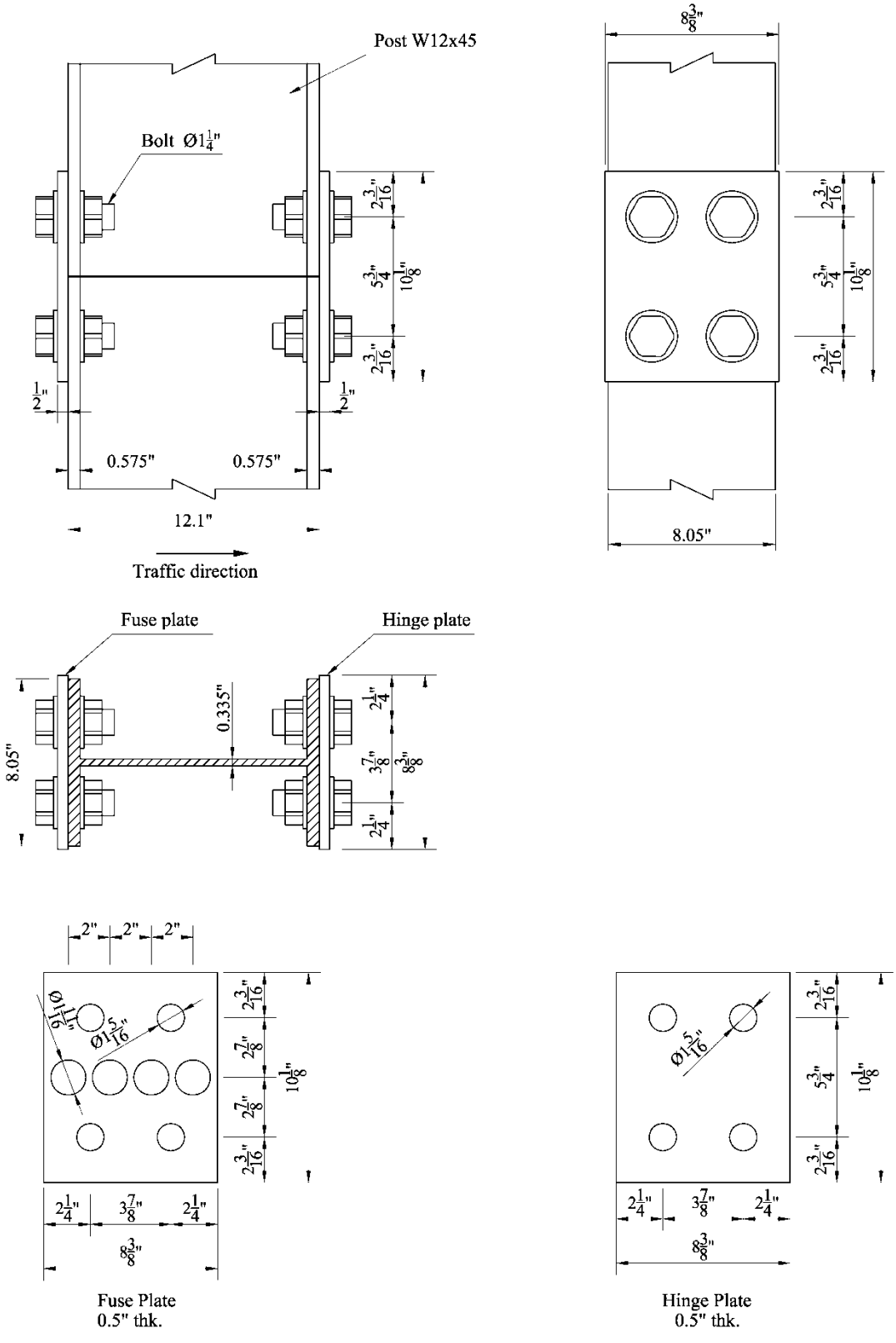

Figure 6-7. Hinge connection detail

The structure was divided into four regions for meshing purposes, as shown in the Figure 6-8. Region 1 included the post stubs, shear-controlled moment collar connections, and post parts below an elevation of 42 in. and 22 in., from the ground level, for the impacted post and non-impacted posts respectively. Region 2 consisted of the post portion above Region 1 and below the hinge connection. Region 3 contained the post portion in the vicinity of the cut plane at the sign bottom level, hinge plate, and fuse plate that made up the hinge connection. The remaining post portion and the sign panel were designated as Region 4.

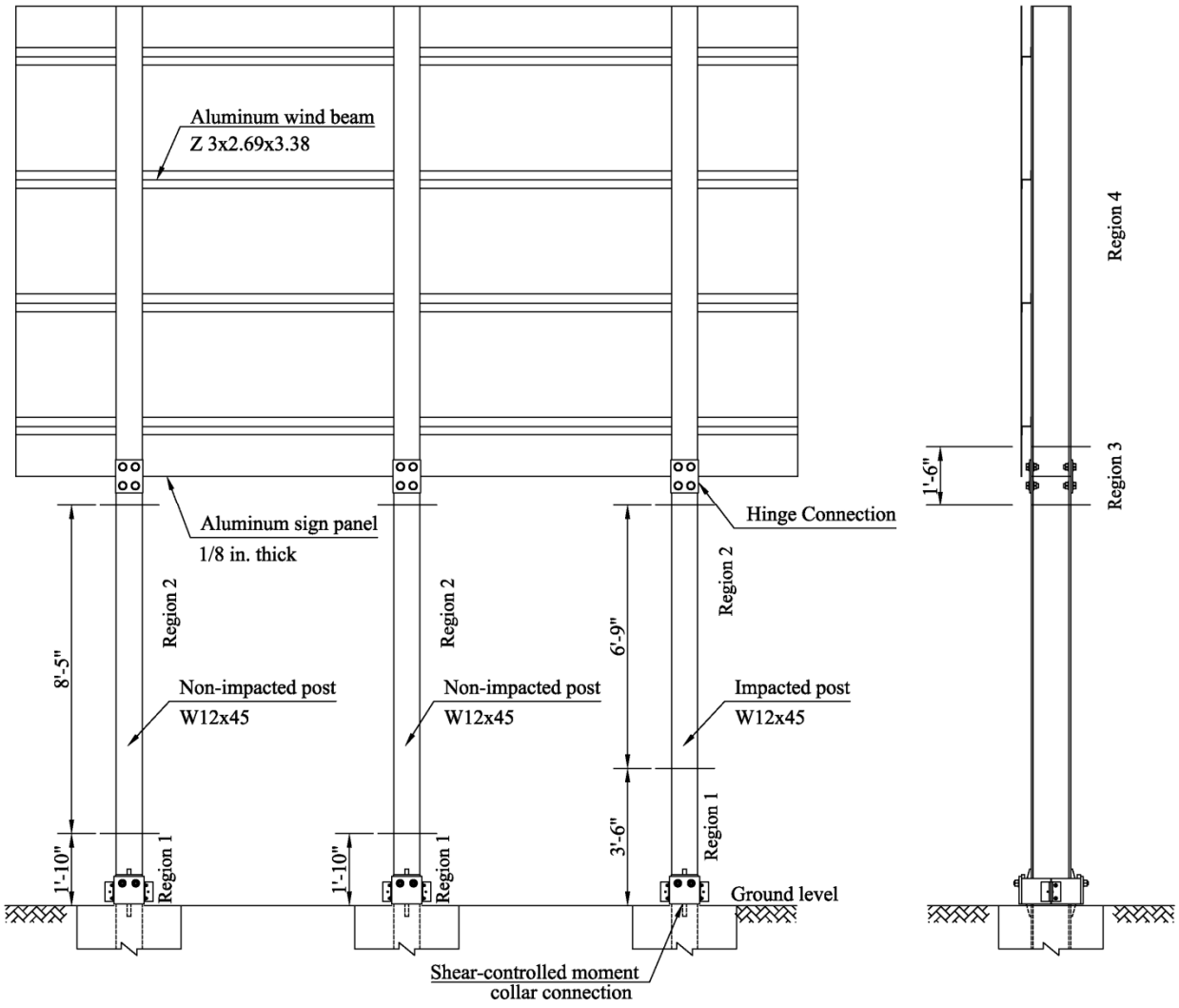

Figure 6-8. Post region divisions for finite element meshing

6.5.1 Region 1 – Connection and Impact Region

Figure 6-9 shows the finite element meshes of the impacted post and non-impacted post at Region 1. Due to the complex behavior of the breakaway connection and its significant effect on the overall performance of the system, all components within this region of the post, to be impacted by test vehicles, were modeled with a high resolution mesh since they were subjected to the most severe loading condition under vehicle impact. This loading condition has the potential to cause severe element deformation and, consequently, erroneous results if the mesh

resolution was not sufficient. Furthermore, a fine mesh resolution in this region provided a better representation of stress concentrations and therefore, better element failure predictions. A high level of mesh discretization was also applied for a single post model used in moment and shear test simulations to determine wind resistance capacity and static equivalent impact shear capacity of the support structure. Components of non-impacted posts in this region were modeled with a lower resolution than the impacted post but careful modeling consideration was still taken to ensure proper element shape and mesh compatibility between various contact components.

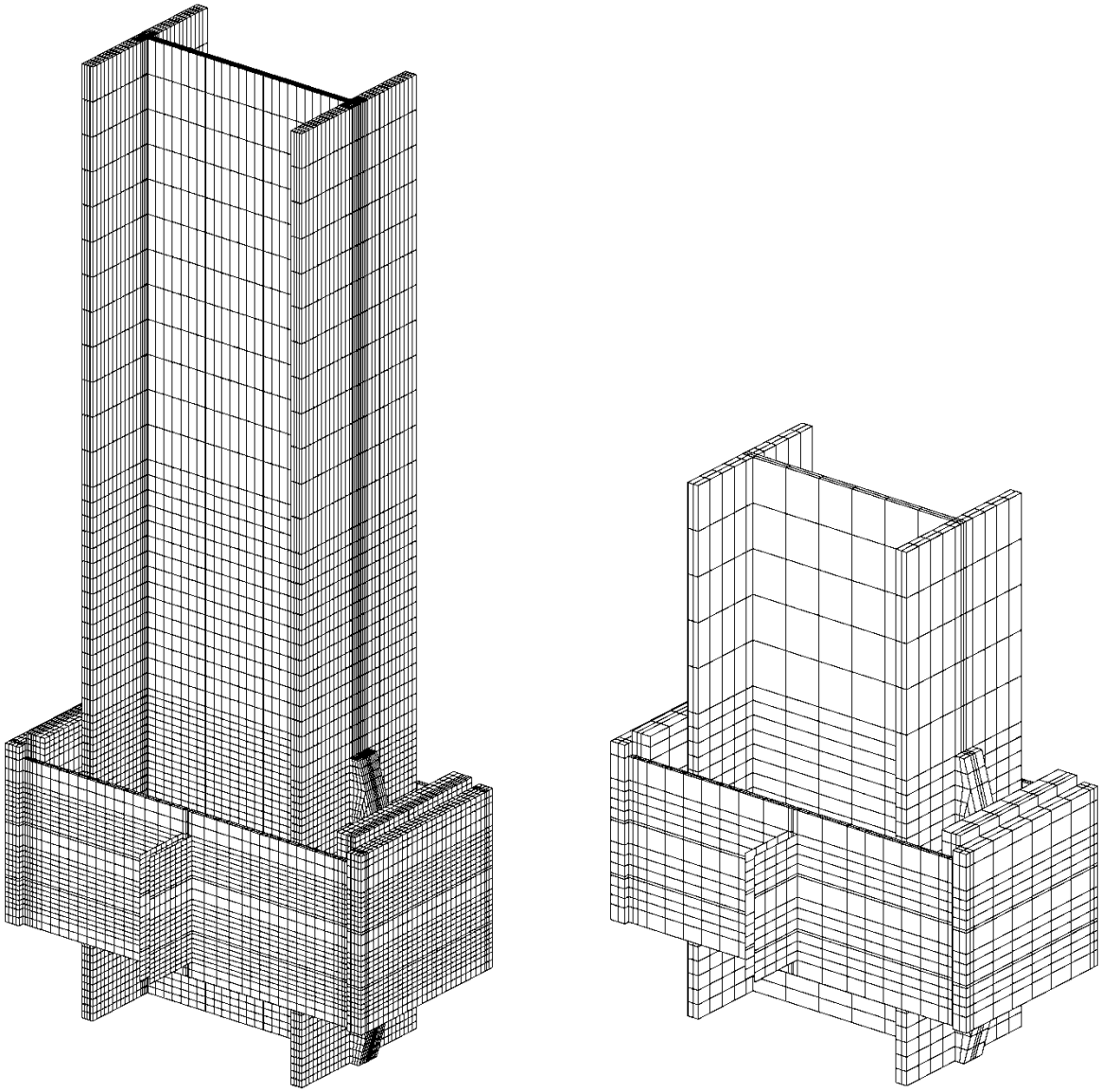

A B

Figure 6-9. Finite element meshing of post in Region 1: A) Impacted post; B) Non-impacted post

An exploded view of the shear-controlled moment collar connection is shown Figure 6-10. Solid elements were used to model the post, post stub, and the majority of collar

components. Collar angles were modeled with shell elements. Since the post and post stub were welded “all-around” to the flange plates, and no failure due to the weld connection or weld material was expected, the welded connections were approximated as if the flange plates were monolithic with the post and post stub. That is, finite element meshes of these components share common nodes at their interface. The same technique was used to model the full penetration welds that connected the stiffeners to the post, the post stub, and the flange plates. The post and the post stub were then put in contact at the slipping plane of flange plates. However, an extremely small gap of 1/320 in. was specified between the contact surfaces of the flange plate to prevent any initial stresses as a result of initial penetration. This gap was closed by allowing sufficient time for gravity load to be effective on the structure before vehicle impact or lateral wind load application. The post stub was attached to the foundation by applying fixed boundary conditions to all nodes below the ground level.

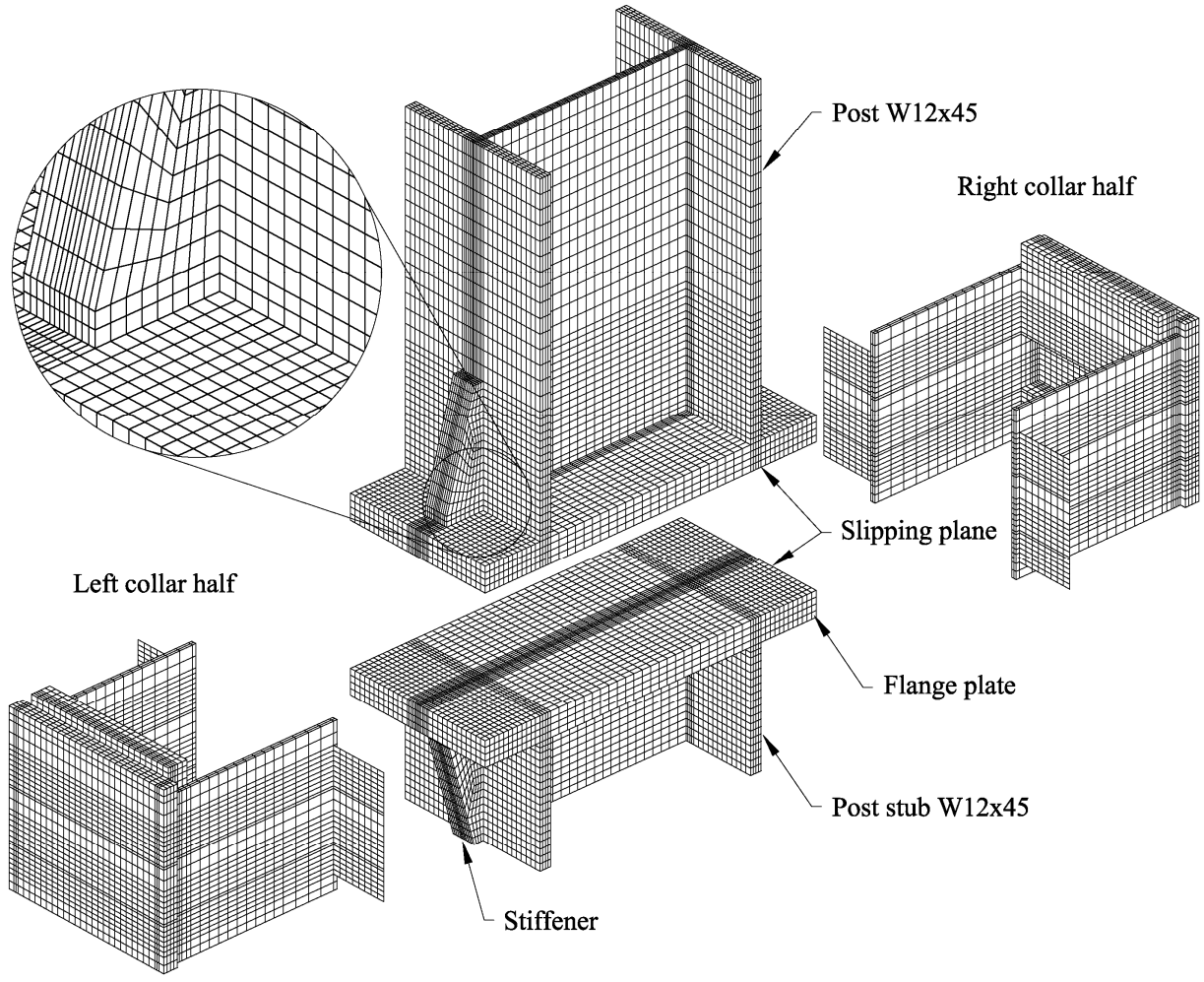

Figure 6-10. Exploded view of the finite element model of the shear-controlled moment collar connection

Although the two collar halves have a physical difference in the connection of the angles to the side plates, all other structural characteristics of the side plates with angles in both cases

are the same. Therefore, the same finite element representation is applied for both collar halves. Figure 6-11 presents the finite element model of a collar half.

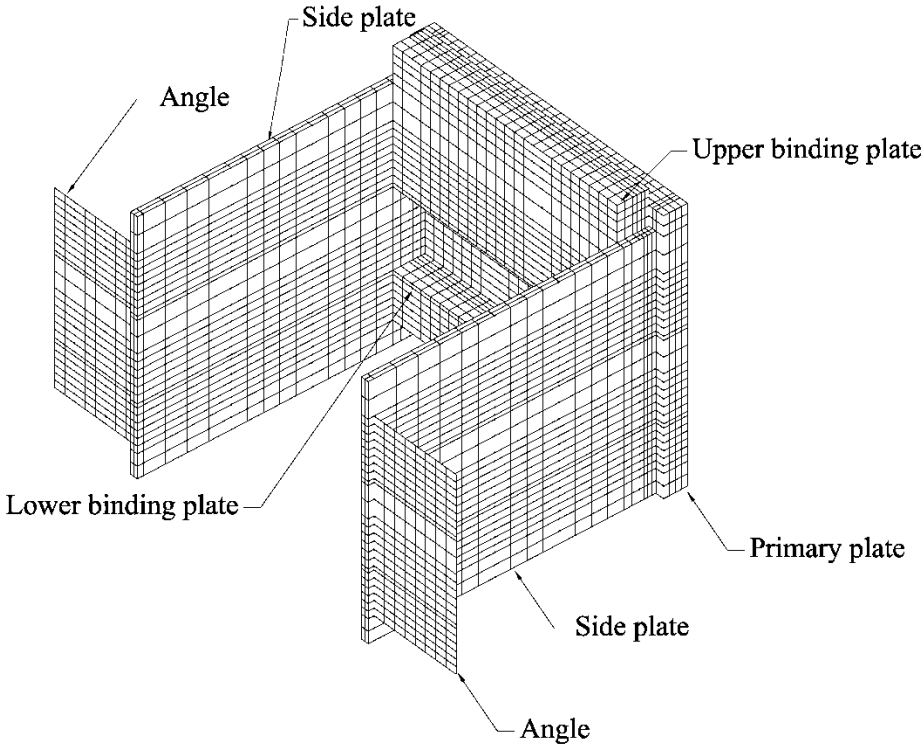

Figure 6-11. Finite element model of the collar half

It was assumed in the model that the upper binding plate was securely attached to the primary plate and that no sliding occurred between the two. This assumption was conservative for the impact conditions simulated since sliding would make the connection more frangible. Therefore, the attachment was modeled by ensuring all nodes at the interface were shared by both the upper binding plate and the primary plate. The technique of sharing nodes at the interface was also used to represent welded connections between other components of the collar halves, such as the lower binding plates to the primary plates, the side plates to the primary plates, and the angles to the side plates. Angle legs in contact with side plates were also modeled.

Models of the two collar halves were brought together to secure the post to the post stub. Each connector bolt joining the two collar halves was modeled by a spot weld constraint defined by `*CONSTRAINED_SPOTWELD` in LS-DYNA. A spot weld constraint couples the nodal rotations and displacements of the two nodes included in the constraint. Figure 6-12 shows the spot weld constraint that was used to represent each connector bolt in the connection. Two nodes on the collar angles at the bolt location were assigned the constraint with a failure criterion based on the connector bolt design strength and resultant forces of a hypothetical rigid beam between the two nodes. A connector bolt fails when the following criterion is met:

$$\left(\frac{T}{T_n}\right)^{5/3}+\left(\frac{V}{V_n}\right)^{5/3}\geq 1.0 \qquad (6\text{-}1)$$

where T and V are tensile and shear forces acting at the spot weld constraint. T_n is the design tension strength of the connector bolt specified as 3.25 kip such that two connector bolts had sufficient capacity to resist the design wind shear load of 6.5 kip. V_n is the design shear strength of a connector bolt, and was specified as $0.6T_n$.

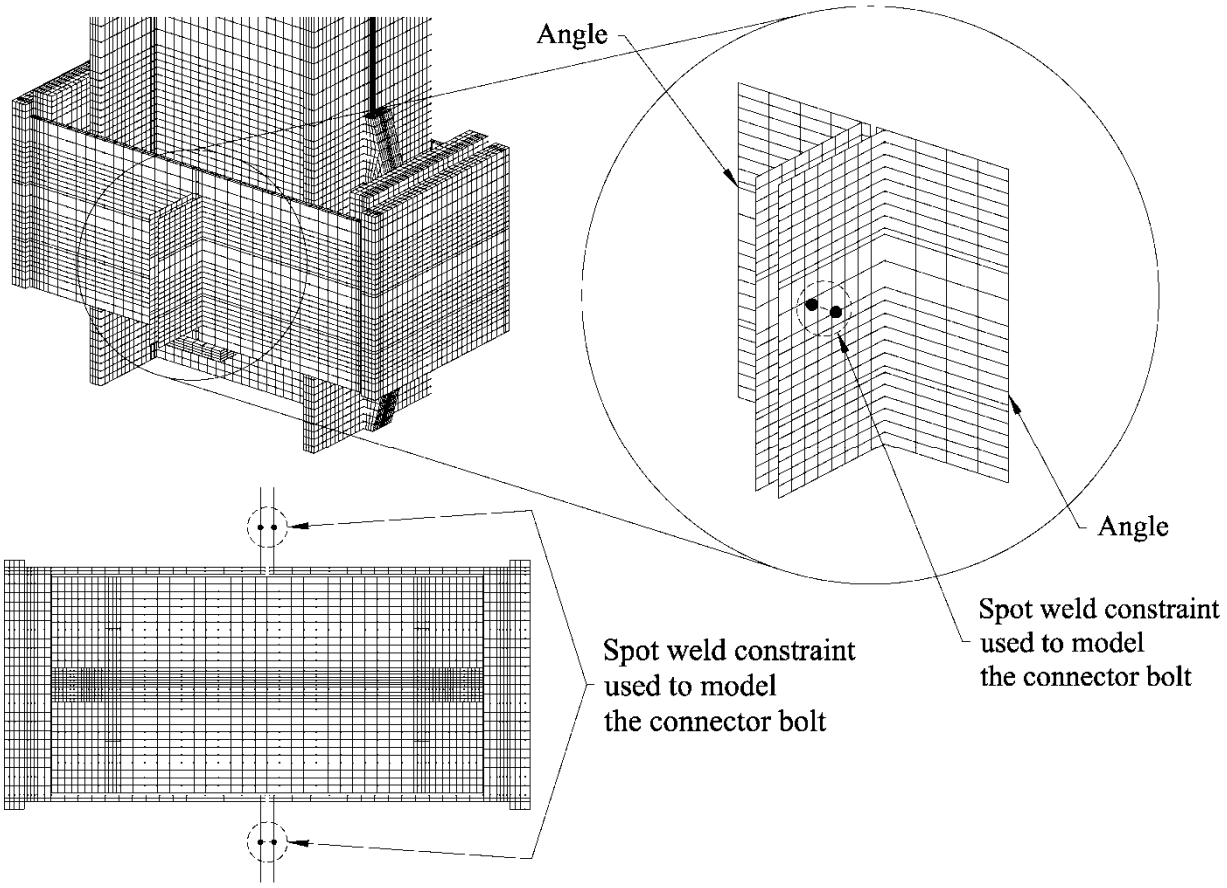

Figure 6-12. Spot weld constraint representation of connector bolts

Elements in this region were assigned an A36 steel, inelastic stress-strain relationship that was discussed previously in Section 3.6.2. Contact surfaces between structural components play an important role in load transfer within the shear-controlled moment collar connection and require proper contact representations. Shear force from each support post is primarily transferred to the post stub through a contact surface between the flange plates and collar primary plates. Another portion of shear load is transferred through the slipping contact surface between the two flange plates by friction resistance. Moment, on the other hand, is transferred to the post stub by normal contact force between flange plates and binding force between flange plates and collar binding plates. As such, without an appropriate contact detection scheme, structural characteristics of the system would be misrepresented. All possible contacts must be anticipated and predefined such that they will be detected and treated correctly, otherwise breakaway performance of the connection may be erroneously predicted.

Contact implementation in LS-DYNA is performed through a contact definition with a variety of available contact types. Each contact definition contains sets of element segments, or sets of nodes, or both, that are checked for contact during simulation. Contact detection can be defined for both 8-node solid and 4-node shell elements. For the solid element type, a segment is defined by four nodes on the "outer" surface of the element that may come into contact with other elements. For the shell element type, a segment is defined by four corner nodes of the element. Frictional coefficients used to compute the friction force (from the normal force) are specified to simulate the frictional effect between contact segments. LS-DYNA allows the frictional coefficient to be specified in a general form in which the sliding velocity between the contact surfaces can be taken into account. However, for the breakaway requirement of the connection, it is conservative to use the static friction coefficient since it is greater than the velocity-dependent sliding coefficient. A higher frictional coefficient means higher frictional resistance, therefore higher deceleration and occupant impact severity. Thus, constant friction coefficients equal to the static friction coefficients of the contact surfaces were used in the present study.

Originally, all elements of the components of the connection (post, post stub, stiffener, guide plate, flange plate, and collar components) that may come into contact with each other during simulation were included in a single segment set of a contact group defined by the contact type `*CONTACT_AUTOMATIC_SINGLE_SURFACE`. Using this contact type, the finite element model of the connection can be subjected to a variety of different loading conditions without redefining contact groups. A single friction coefficient was applied for all elements belonging to this contact group. Such a contact treatment method would be a good choice for a connection consisting of components having the same contact friction coefficient. However, during the development of the connection, Teflon sheets were introduced to improve the friction condition between critical contact surfaces. Therefore, the model was revised and four contact groups were defined for the connection in order to envelop all possible contact scenarios of the connection components. The first group included segments of elements at the slipping plane of the flange plates and was defined using the contact type `*CONTACT_AUTOMATIC_SINGLE_SURFACE`. Since Teflon sheets were placed at the contact surface, the friction coefficient of 0.2 obtained from the Teflon product specification (and friction tests presented in Chapter 5) was applied for this contact group.

The second group, the `*CONTACT_AUTOMATIC_SURFACE_TO_SURFACE` contact type, consisted of segments of elements at the contact surfaces between the flange plates and binding plates. This group was given a steel-to-steel friction coefficient of 0.55. This value was obtained from friction tests for the steel-to-steel condition presented in Chapter 5. However, for later refinement in which Teflon sheets were also inserted at these contact surfaces, a friction coefficient of 0.2 was specified.

The third group included segments of elements belonging to the flange plate and collar components, except those segments already included in the second group. The contact type `*CONTACT_AUTOMATIC_SURFACE_TO_SURFACE` was used to define the third contact group with a friction coefficient of 0.55.

The fourth group included all segments of post, post stub, stiffener, guide plate, and collar components and was assigned the `*CONTACT_AUTOMATIC_SINGLE_SURFACE` contact type. A friction coefficient of 0.55 was also used to represent the steel-to-steel friction coefficient of this contact group.

6.5.2 Region 2 – Post Middle

Region 2 was the post portion above Region 1 and below the hinge connection of three posts of the sign support structure. The post portion in this region was also modeled using 8-node solid elements but with a much lower mesh resolution. A lower level of mesh resolution was suitable for regions having low deformation and no stress concentrations. If meshed in high resolution, significant computational cost would have been required since this region accounts for approximately 11.7 ft and 12.4 ft lengths of the non-impacted post and the impacted post, respectively. Three nodal rigid body constraints were used to attach post portions in this region to the corresponding post portions in Region 1. The constraint type, defined by `*CONSTRAINED_NODAL_RIGID_BODY` in LS-DYNA, was utilized to join two finite element models of post portions having different mesh resolutions together at their common interfaces. All nodes at the common interfaces were included in a group having a single set of translational and rotational degrees of freedom (see Figure 6-13).

Material type 24 (`*MAT_PIECEWISE_LINEAR_PLASTICITY`) was also used to model the A36 steel material of the posts in this region. An explanation of the material model implementation was presented in Section 3.6.2.

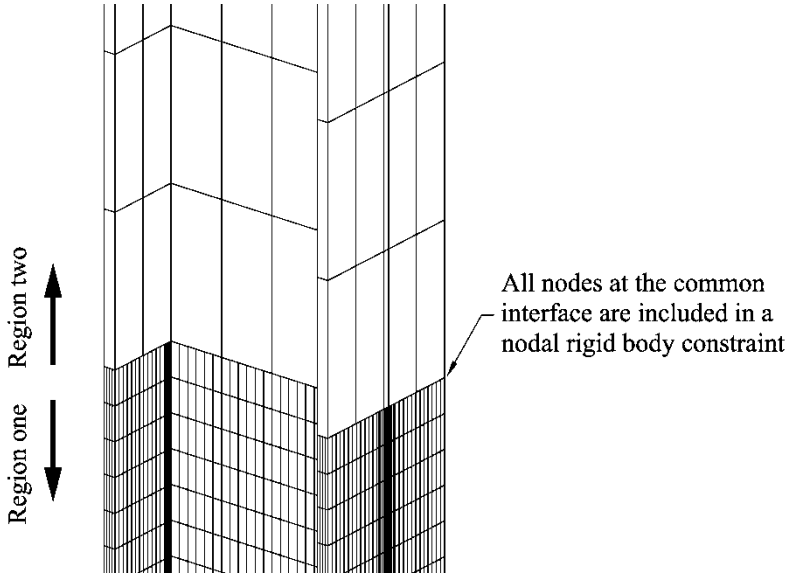

Figure 6-13. Nodal rigid body constraint at the interface of region one and region two of the post

6.5.3 Region 3 – Hinge Connection

Region 3 was an 18 in. segment of the support structure that consisted of three hinge connections at the sign bottom level. Each hinge connection was made up of two post segments modeled with 8-node solid elements joined by fuse and hinge plates modeled with 4-node shell elements (Figure 6-14). Gaps of 1/320 in. between post segments were included to represent cuts through the post section. Since hinge connection behavior directly affects the overall breakaway performance of the support structure, it was important to capture large deformation and material failure of the connection. As such, a high resolution mesh was implemented for this region, especially for the fuse plate where high stress concentrations and element failures were likely to occur. A refined finite element mesh of the fuse plate was essential to simulate progressive

failure of the plate. In the vicinity of the perforated holes of the fuse plate, special care was taken to generate elements with minimal distortion. It was necessary to eliminate highly distorted elements (e.g., those with severe skew or large aspect ratios) around the perforated holes because elements with such shape distortions might predict erroneous connection failure under vehicle impact loading.

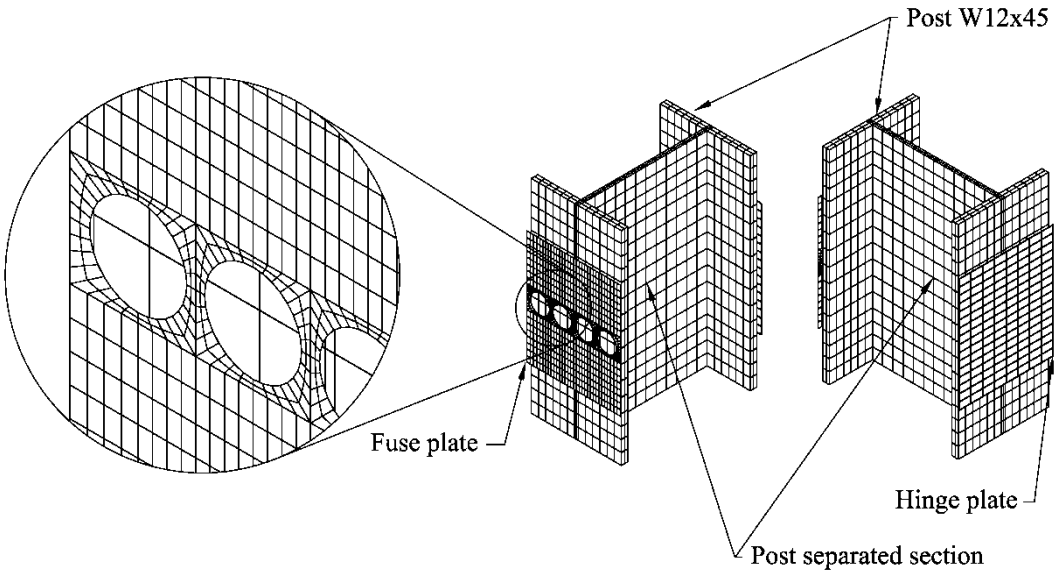

Figure 6-14. Hinge connection finite element model

Nodal rigid body constraints, `*CONSTRAINED_NODAL_RIGID_BODY`, were used to model the bolts that connect the fuse and hinge plates to the post segments. It was assumed that the effective clamping area of each bolt was a square area, the side-dimensions of which were three times the bolt diameter. Within this effective area, the fuse and hinge plates were fully tied to the post flange without slip or separation. Each nodal rigid body constraint included all nodes of the post flange and fuse plate, or hinge plate depending on the location, inside of the effective clamping area (Figure 6-15).

Due to the different mesh resolutions of the post in Region 2 and Region 3, a nodal rigid body constraint was also used to "glue" the hinge connection to the post in Region 2 by including nodes at the common interface of the constraint. During initial collision by a vehicle, but prior to fuse plate failure, the fuse plate area around perforated holes stretches, and bears and slides against the post flange. To represent these behaviors, a contact definition of type `*CONTACT_AUTOMATIC_SINGLE_SURFACE` was defined between the parts of the hinge connection and the post. A friction coefficient of 0.55 for steel-to-steel contact, determined in Chapter 5, was used for the contact between the hinge connection parts. An elasto-plastic material model for A36 steel, defined by `*MAT_PIECEWISE_LINEAR_PLASTICITY` in LS-DYNA, with failure strain of 0.2, was used for hinge connection material representation.

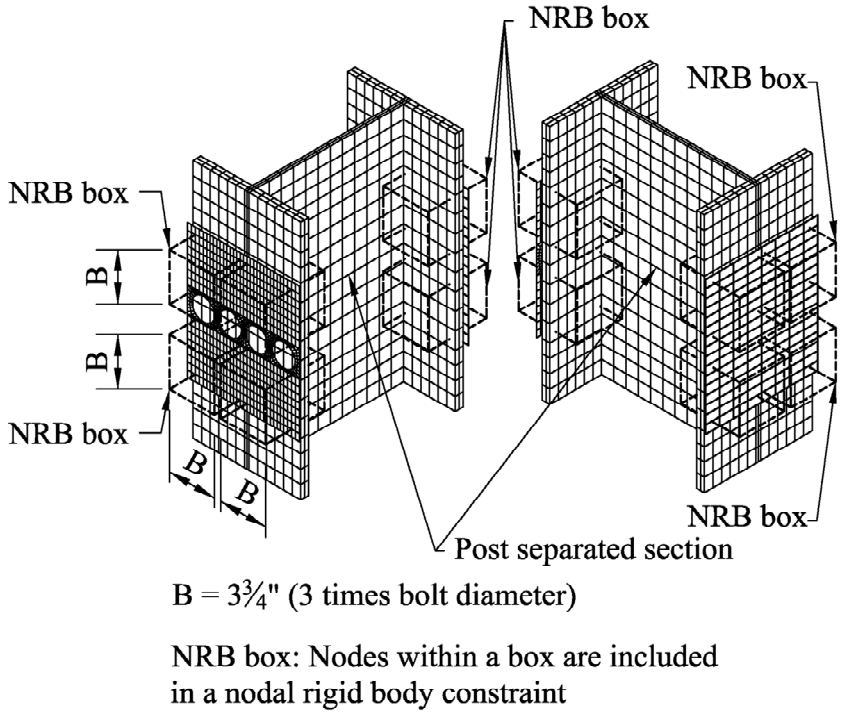

Figure 6-15. Nodal rigid body constraints to attach hinge and fuse plates to the separated post

6.5.4 Region 4 – Sign Panel

Region 4 consisted of a sign panel, wind beams, and the remaining length of the supporting posts. The finite element model of this region is presented in Figure 6-16. A low mesh resolution was applied for components in this region since it was anticipated that only moderate deformation would occur. Wide flange posts were modeled with the same modeling approach used for the posts in Region 2. However, the posts in Region 4 were meshed such that element nodes were created at the elevations of the wind beams. The Region 4 posts were then joined to the corresponding hinge connections of Region 3 by nodal rigid body constraints at common interfaces. Although a coarse finite element mesh was used, the stiffnesses of the sign panel and the wind beams were still accurately modeled so as to represent their influence on the behavior of the impacted post. If these stiffnesses were significantly overestimated, the hinge connection on the impacted post would tend to fail prematurely after rupture of the breakaway connection. Conversely, if these stiffnesses were significantly underestimated, the sign panel will experience significant twist before failure of the hinge connection. Both conditions could lead to an unrealistic representation of vehicle-structure interaction and thus the possibility of an incorrect prediction occupant risk. Consequently, the wind beams were modeled with resultant beam elements and the sign panel was modeled with shell elements for computational efficiency and accuracy. Screwed attachment of the sign panel to the wind beams was modeled by merging all nodes of the beam elements with the shell element nodes. Bolted connections between the wind beams and supporting posts were represented by nodal rigid body constraints. Each constraint consisted of a beam node and adjacent nodes in the post flange. A linear elastic material model, defined by `*MAT_ELASTIC`, of aluminum with a mass density of 5.252 lbf-sec^2/ft^4

(2,707 kg/m^3), an elastic modulus of 10,000 kip/in^2 (69 GPa), and a Poisson ratio of 0.33, was employed for the sign panel and wind beams.

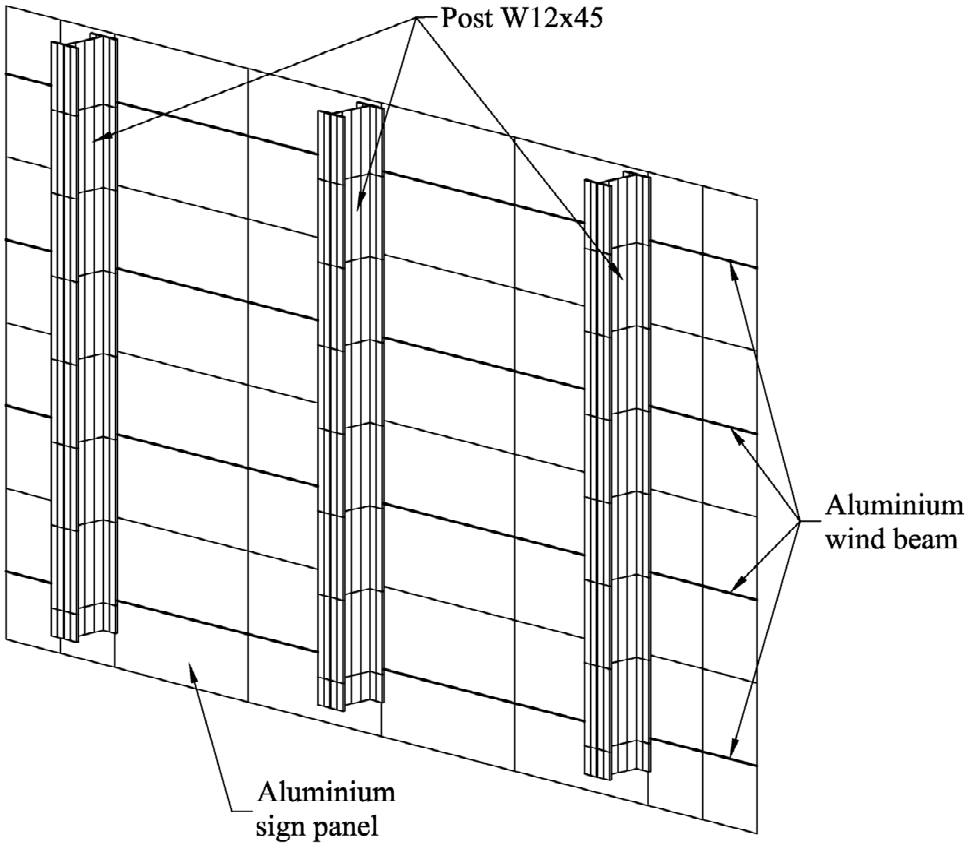

Figure 6-16. Sign panel finite element model

6.6 Test Vehicles and Impact Conditions

A finite element model of an 820 kg pendulum impactor, obtained from the National Crash Analysis Center (NCAC), was utilized to perform impact simulations in order to evaluate breakaway performance of candidate connection concepts. (Details of the pendulum model were presented in Section 3.6.2.) While the pendulum impactor was efficient in assessing the breakaway mechanism, it was unable to assess the effects of the impacted structure making contact with the vehicle roof or windshield (NCHRP 350). Also according to NCHRP 350, for primary concerns of the penetration of the impacted post and related components into the occupant compartment, a 2000 kg vehicle is preferred in lieu of, or in addition to, the 820 kg small car. Therefore, to investigate the potential for vehicle compartment deformation, a finite element model of a 2000-kg pickup truck (2000P) from the NCAC was also obtained for use in impact simulations. The vehicle model represented a Chevy C2500 pickup truck and contained approximately 66,000 nodes and 60,000 elements (Figure 6-17).

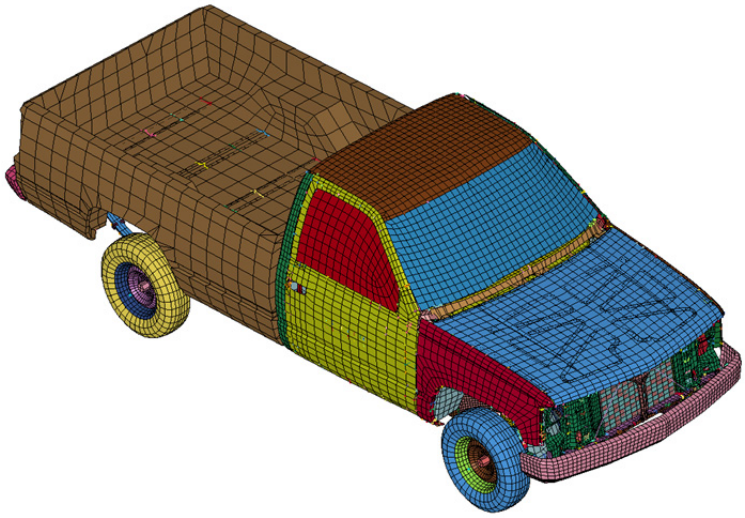

Figure 6-17. Finite element models 2000-kg pickup truck (2000P) by NCAC

Impact simulations conducted in the breakaway connection development involved a variety of parameters including the friction condition, impact vehicle type, impact vehicle velocity, and impact angle. However, the impact simulations conducted can be grouped into four types with different vehicle types and impact angles. For each simulation, a finite element model of the relevant test vehicle was merged with the model of the sign support system. The combined system was then modified such that both substructures could interact with each other under the desired impact conditions. Figure 6-18 shows the model of a pendulum and a sign structure in a head-on impact (0-degree impact angle). In Figure 6-19, a pendulum model corresponding to an oblique impact condition, with an impact angle of 20 degrees, is shown.

During physical impact testing, a pendulum impactor is suspended by cables and swung in a circular motion when dropped from a given height. The pendulum achieves its target velocity just prior to collision with a breakaway connection at the position of lowest elevation. However, the computational cost of simulating the entire swing process was expensive and was deemed unnecessary. Therefore, in both impact angle conditions, the pendulum model was aligned to impact the sign post in the horizontal direction and at an elevation 19 in. above ground level. An initial translational velocity corresponding the impact speed, either 35 km/h (21.7 mph) or 100 km/h (62.1 mph), was assigned to all nodes in the pendulum model. Since neither the pendulum support cables nor the swinging motion were modeled, vertical gravitational loading was not applied to the impactor.

A contact definition was defined between the sign structure and the front parts of the impactor that could potentially come into contact with each other. The contact definition allowed the time history of pendulum impact force imparted to the sign post to be recorded. In Figure 6-20 and 6-21, models of 2,000-kg pickup truck impacts against the sign structure are shown for impact angles of 0-degrees and 20-degrees, respectively. A contact definition was also established between the truck and sign structure to ensure that all possible contact scenarios and compartment penetration could be detected. Pickup truck speed prior to impact was applied by specifying an initial translational velocity to all nodes in the pickup truck model and an additional angular velocity to all nodes in the vehicle wheels. The angular velocity was determined from the translational velocity divided by the radius of the truck wheels. A concrete road was modeled to enable simulation of contact between the truck wheels and the roadway.

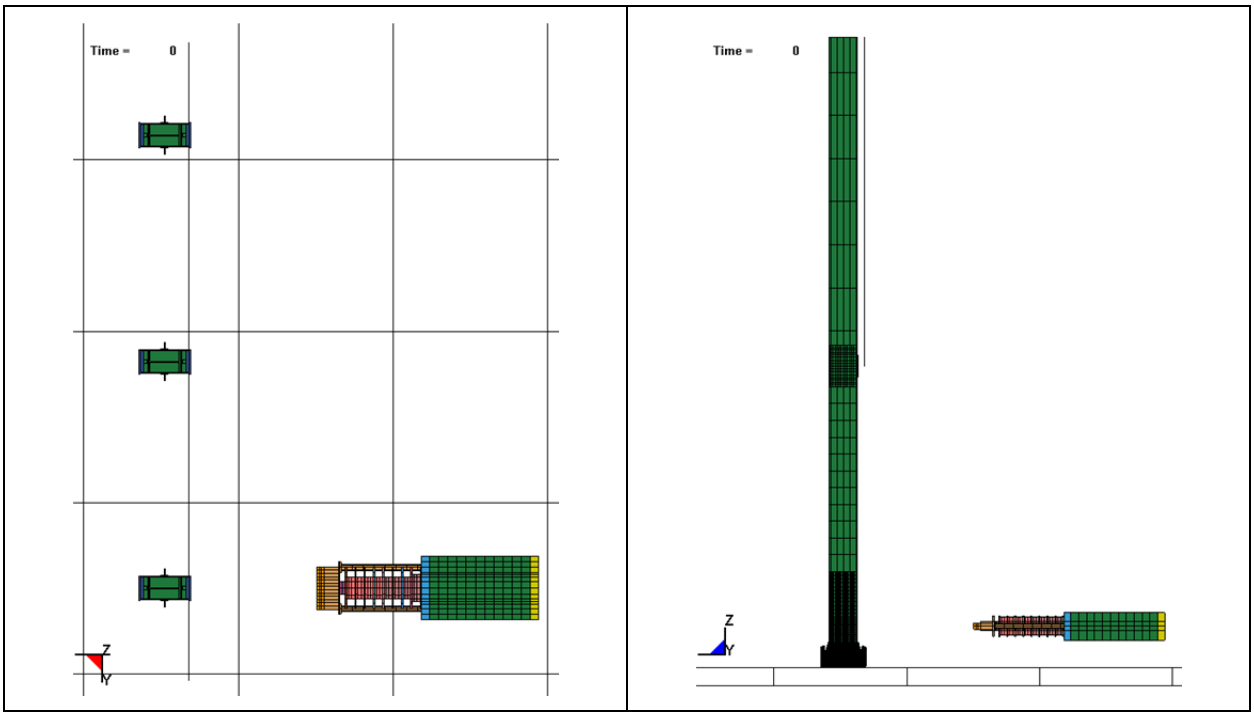

Figure 6-18. Pendulum at 0-degree simulated impact condition (820-kg pendulum, 0 degree impact angle)

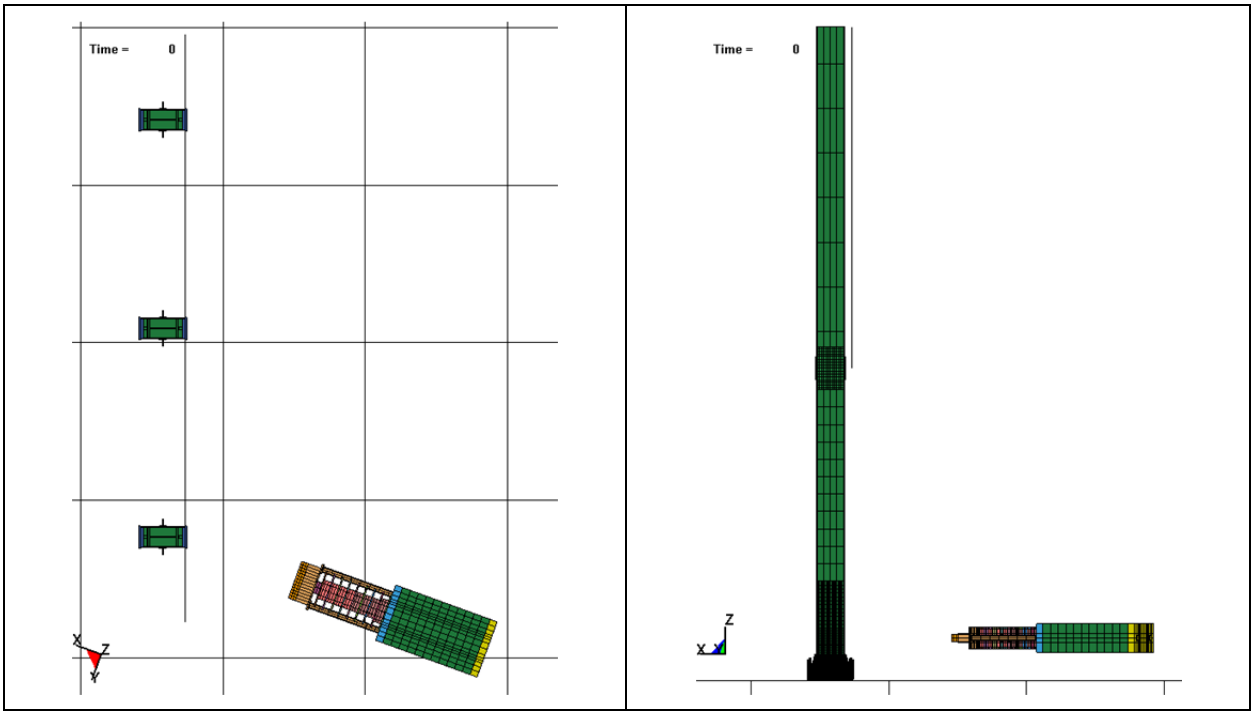

Figure 6-19. Pendulum at 20-degree simulated impact condition (820-kg pendulum, 20 degree impact angle)

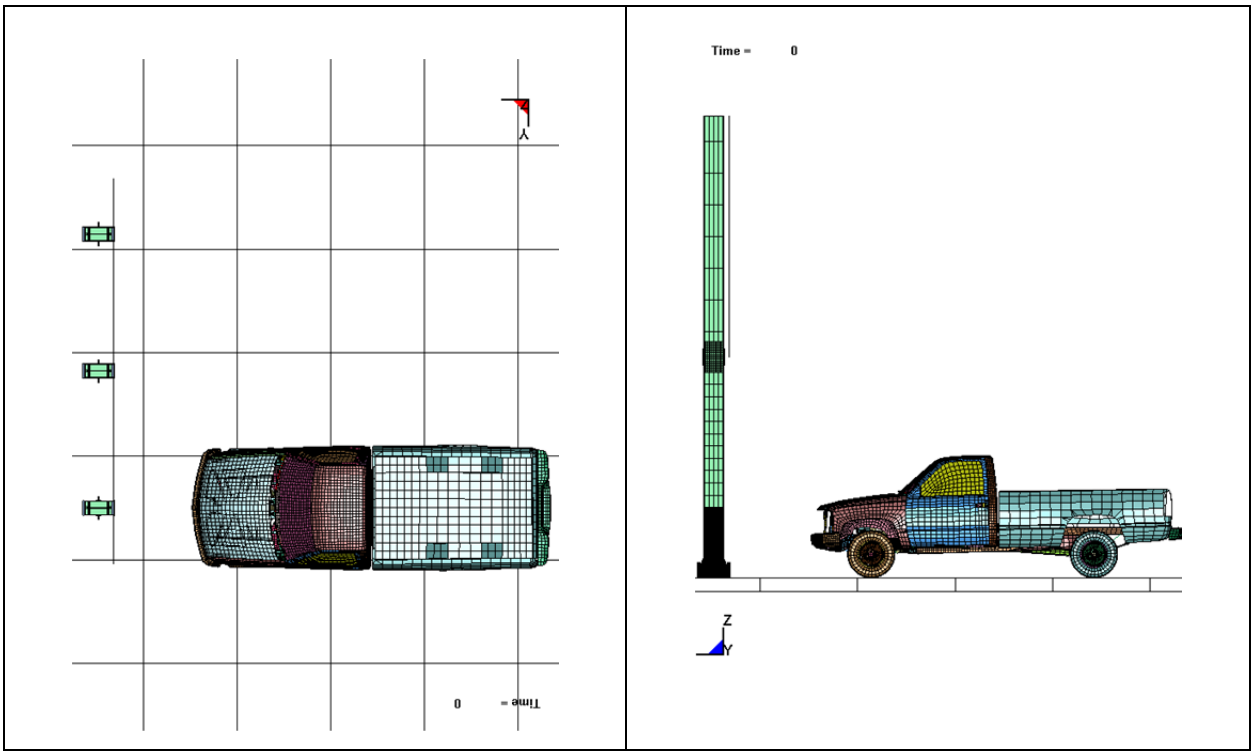

Figure 6-20. Truck at 0-degree simulated impact condition (2000-kg pickup truck, 0 degree impact angle)

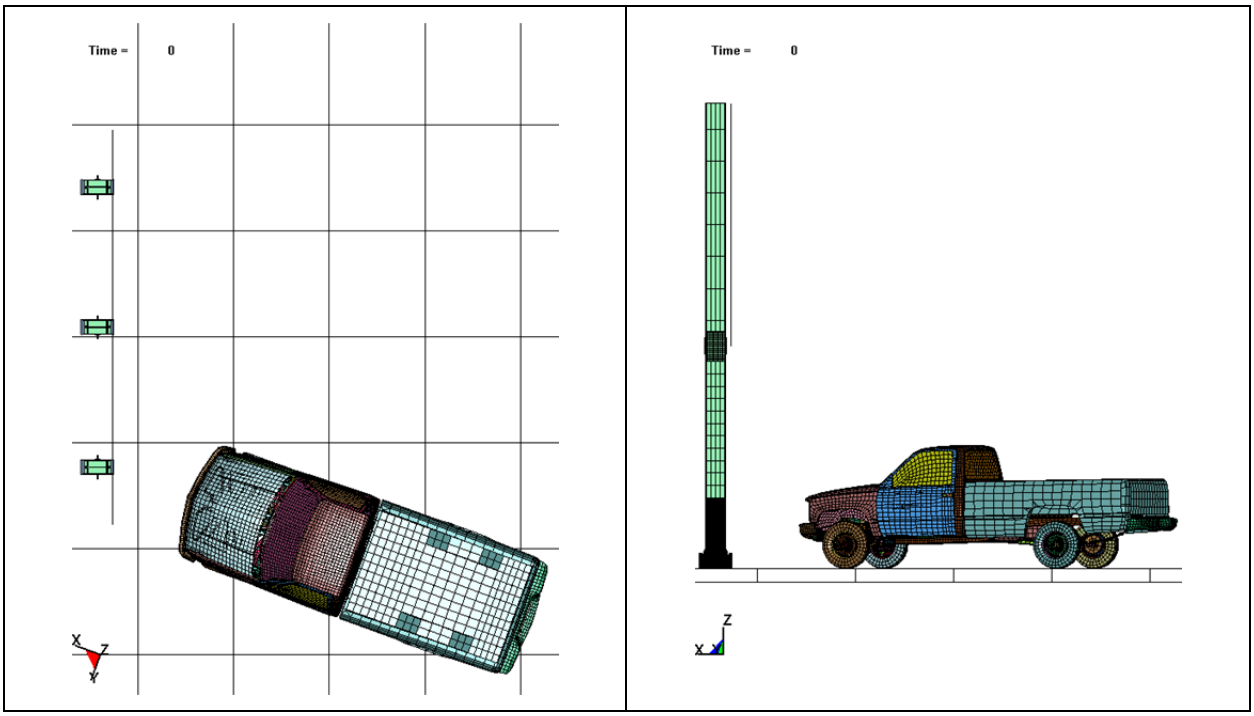

Figure 6-21. Truck at 20-degree simulated impact condition (2000-kg pickup truck, 20 degree impact angle)

6.7 Finite Element Model of the Shear-Controlled Moment Collar Connection for Determination of Moment Capacity

Breakaway features were introduced into the sign support connection to lessen the impact severity to occupants should a collision occur. However, such features must not reduce the strength of the sign support to a level below that required for design wind loading. Therefore, for each proposed connection design, in addition to the finite element model of the full sign support system (three posts and panel) that was used for impact analysis, a finite element model of a single post was also developed. Each single post model incorporated the breakaway connection and was developed for use in determining static equivalent wind resistance capacity, as represented by flexural (moment) strength quantified using a pull-over analysis. Each single post finite element model was approximately the same as the model of the impacted post of the full sign support structure. However, in the single post model, the hinge connection was removed and the post region above the breakaway connection was re-meshed such that loads could be applied to model nodes at desired positions.

Figure 6-22 shows a schematic of a post configured for pull-over analysis. A lateral load was applied to the post model at 188.8 in. above the ground level in a gradually increased (quasi-static) manner until post failure occurred. The location of the applied load corresponded to the location of the resultant wind force acting on the middle post of a three-post system (sign panel tributary loading as well as load directly applied to the post itself; see Appendix A for more detail). To represent the post self-weight and upper structure weight on the breakaway connection, a constant axial compressive load of 1.38 kip was applied during the lateral loading.

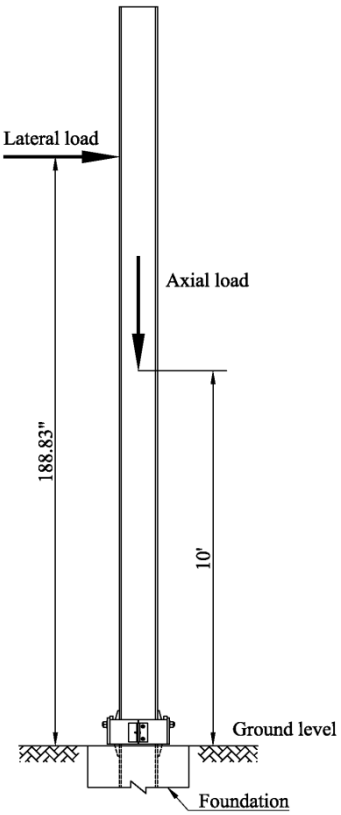

Figure 6-22. Schematic of loads applied for post moment capacity determination

6.8 Structural Adequacy and Dynamic Performance Evaluation of the Shear-Controlled Moment Collar Connection

6.8.1 Structural Adequacy Evaluation of Shear-Controlled Moment Collar Connection

A pull-over analysis was performed on the post, utilizing the shear-controlled moment collar connection, to evaluate structural adequacy for the design wind load. The analysis results indicated that the breakaway post was capable of resisting a base moment of 2099 kip-in (175 kip-ft) at the ground elevation before plastic failure. This means that the post, with incorporated shear-controlled moment collar, had a moment strength factor of safety of 1.71 for the design wind load and selected sign configuration (see section 3.7). It should be noted that the predicted moment capacity was based on a conservatively low value of friction coefficient of 0.1 for all contact surfaces. Greater frictional resistance between connection components would reduce post slip. As the post slips, the force applied by the displaced flange plate on the upper binding plate causes increasing eccentric moment on the primary plate which lowers the connection moment capacity. Therefore, a higher moment capacity can be achieved by reducing post slip.

In Figure 6-23, a plot of the effective plastic strain contours of the connection indicates that initial material failure occurred at the interface between the lower stiffener and the flange plates, where the largest effective plastic strain occurred. The majority of components, however, were still in elastic strain range. It is also noted that the connector bolts joining the two collar halves did not fail when the stiffener reached the failure strain. As plastically-failed elements in the stiffener model were removed, as the analysis progressed forward, the bending stiffness of the connection deteriorated. As a result, the flange plate experienced significant bending deformation which caused increasing rotation of the collar halves and eventually failure of the connector bolts.

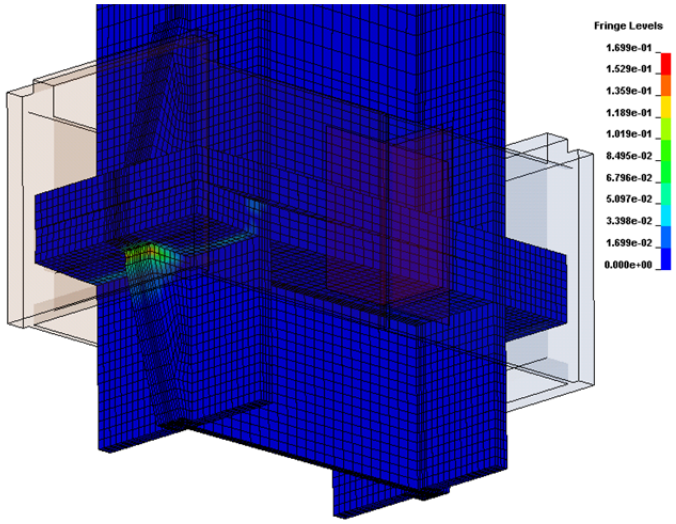

Figure 6-23. Effective plastic strain contours of the connection at incipient failure

6.8.2 Breakaway Performance of Moment Collar Connection under Low-Speed Impact

The breakaway connection, which met the flexural adequacy requirement (based on the simulation results presented above), was incorporated into the full sign support structure model and subjected to impact simulations for dynamic performance evaluation. Causing connection break away under low-speed (and therefore low kinetic energy) vehicle impacts is more challenging than in high-speed (high kinetic energy) impacts. Also, as recommended by NCHRP 350, low-speed impact tests are intended to evaluate the breakaway and yielding mechanisms of the support structure. Therefore, priority was given to low-speed impact simulations to ensure connection frangibility under the lowest vehicle kinetic energy condition.

Breakaway performance of the connection depended on many factors associated with the connection itself, such as geometry, component stiffness, connector bolt strength, post weight, possible contacts between parts, and corresponding contact frictional coefficients. To investigate the influence of friction, impact simulations of the sign structure were conducted at lower and upper frictional bounds. For each bound, it was assumed that all components involved in contact had the same friction condition. A frictional coefficient of 0.1 was specified as the lower bound, which was intended to explore the potential benefits to frangibility that could be achieved by reducing friction (e.g. by using Teflon, etc.). A conservative upper bound friction coefficient of 0.8 was selected to assess worst-scenario performance of the breakaway connection (without friction-reducing surface treatments) and to improve the design so that a broader range of friction coefficients could be accommodated.

In the *Guide to Design Criteria for Bolted and Riveted Joints* (Kulak et al. 1987), slip friction coefficients reported for tests on joints with hot-dip galvanized faying surfaces were between 0.08 and 0.36. In addition, the static friction coefficient for hot-dip galvanized samples was determined in the present study to be 0.45 (recall Table 5-1). Hence, the range of friction coefficients, 0.1 to 0.8, chosen for the friction investigation adequately spanned the range of measured values noted above.

In Figure 6-24, time histories of longitudinal velocity of the pendulum during impact with the breakaway structure at an angle of 0 degrees and a speed of 35 km/h (21.7 mph) are presented. With a friction coefficient of 0.1, the simulation indicated that the connection readily broke away without generating unacceptably high occupant risk measures. There were two notable phases of pendulum velocity reduction in this case. The first occurred shortly after impact initiation, and was due to base connection and post inertial resistances. The second phase occurred as a result of hinge connection resistance. Longitudinal occupant impact velocity (OIV) was determined to be 3.35 m/s, which satisfies the permissible limit of 5 m/s per NCHRP 350. The vehicle (pendulum impactor) experienced a maximum deceleration of 8 g, however the longitudinal occupant ridedown acceleration (ORA) was negligible since after the occupant impacted the hypothetical vehicle interior, the vehicle had separated from the post and maintained a virtually constant velocity.

Results from the simulation with a friction coefficient of 0.8 indicated that the vehicle came to a complete stop, and even rebounded. Although the connector bolts failed, the vehicle was not able to clear the post from the stub base. This was primarily attributed to the binding action of the collar on the post flange plates, and resulted from frictional resistance between the contact surfaces. In this case, a rapid decrease in vehicle velocity occurred between 0.015 sec. and 0.09 sec. and led to an unacceptably large value of OIV, exceeding the allowable limit.

An examination of the behavior of the collar during this impact simulation prompted a modification to the design, wherein guide plates was added (see Figure 6-25) to prevent the collar halves from rotating, thus alleviating the binding effect of the collar. Guide plates were affixed to the post stub by defining a nodal rigid body constraint. By creating the nodal rigid body constraint, using the LS-DYNA feature `*CONSTRAINED_NODAL_RIGID_BODY`, translational and rotational degrees of freedom of nodes included in the constraint were locked together. Impact analysis results of the connection both with and without the added guide plate are presented in Figure 6-26. Note that frangibility of the connection was considerably improved by introduction of the guide plate. In the modified (guide plate added) simulation, the vehicle was able to clear the post out of its pathway and maintain a constant velocity afterward. Consequently, the longitudinal occupant impact velocity was reduced from 10.32 m/s to 4.86 m/s, which was below the permissible limit set by NCHRP 350.

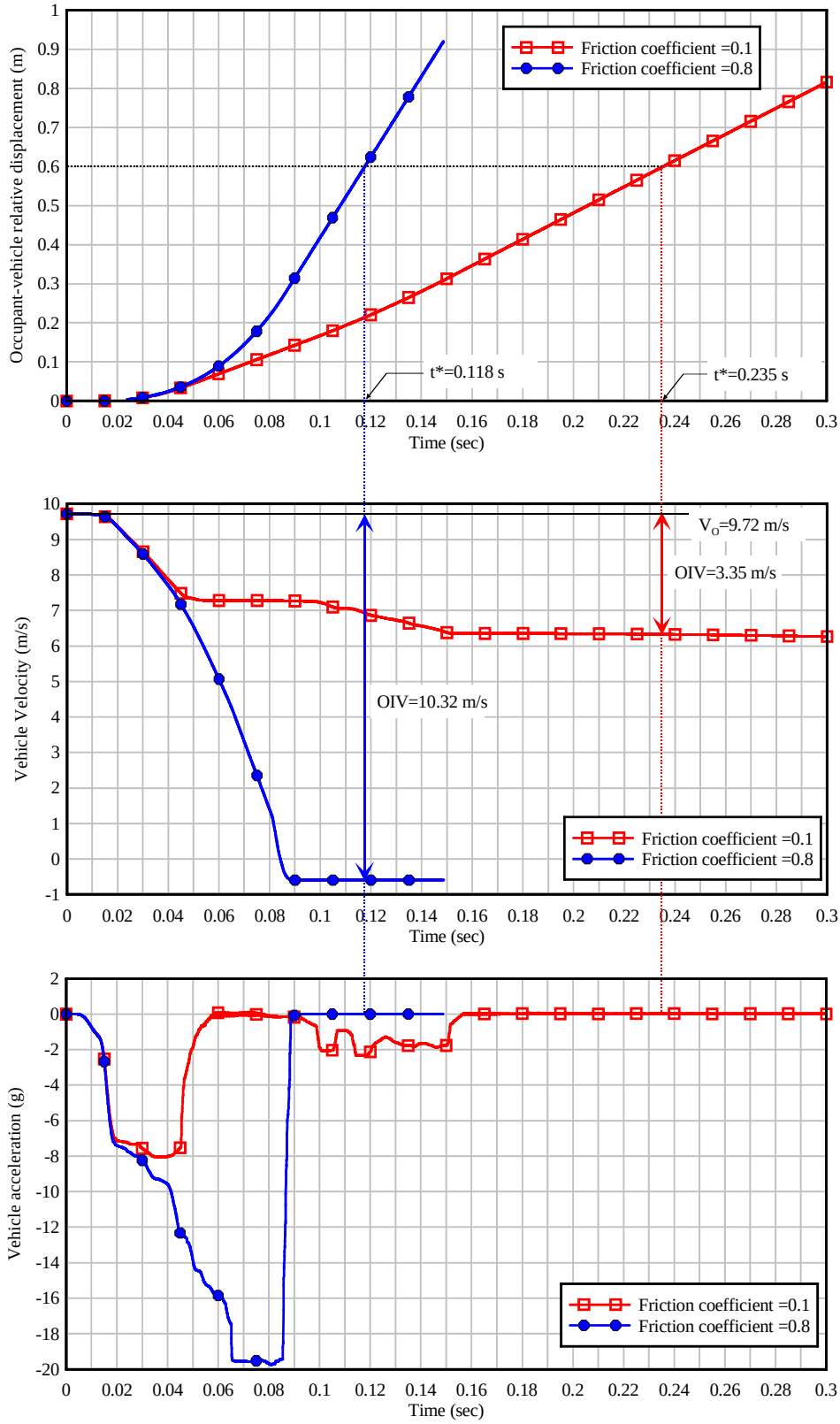

Figure 6-24. Simulation results for the connection under 0-deg, 35 km/h impact condition and two bounds of friction

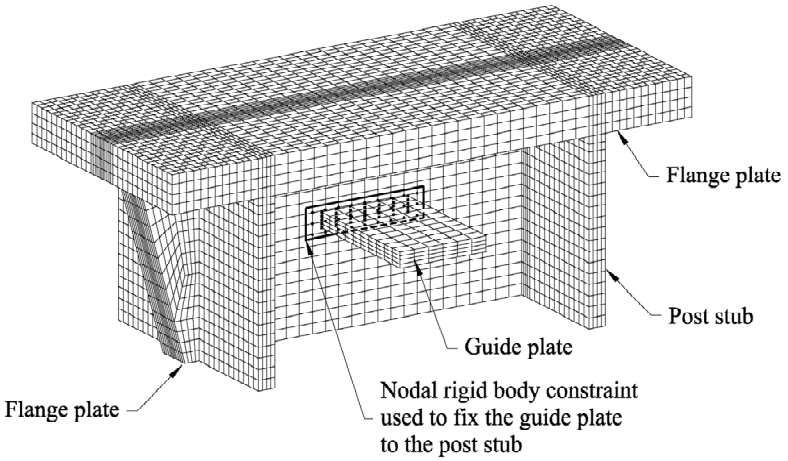

Figure 6-25. Nodal rigid body assignment between guide plate and post stub

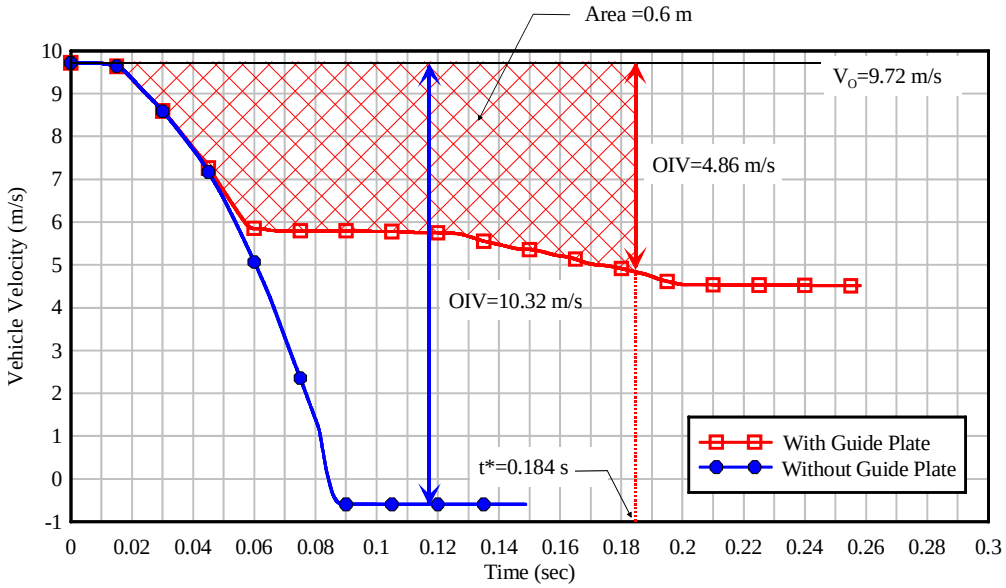

Figure 6-26. Simulation results for cases with and without guide plate in 0-deg, 35 km/h impact condition and friction coefficient of 0.8

CHAPTER 7
EXPERIMENTAL STATIC PROGRAM

7.1 Introduction

Experimental testing was an important component of the overall development process of the breakaway connection and was used both for design validation and numerical model improvement. Since it was important to ensure that the breakaway features of the connection did not adversely affect the structural performance of the system, static tests were conducted to evaluate the structural strength of the breakaway post under the design wind load and to determine the ultimate strength of the breakaway post. In addition to structural strength, post deflections under service load level were evaluated, and the load-deflection relationship was obtained through static testing. Furthermore, static tests provided insights into the system behavior and interaction of the components that constitute the breakaway feature of the sign post.

Equivalent static impact load testing allowed multiple tests to be performed to help in predicting the impact performance of the breakaway connection under a variety of system configurations, such as stiffness of the sign panel and hinge. Static testing also allowed an investigation of the sensitivity of the shear strength of the connection to friction and bolt strength. Data obtained from static tests were used to refine and calibrate the finite element model for subsequent simulations and to make revisions to the breakaway connection, where necessary, before dynamic impact tests were performed. Therefore, a wide-flange steel post approximately 21 ft in length, utilizing the developed shear-controlled moment collar breakaway connection, was selected for the experimental static program. The post and connection were fabricated at the Florida Department of Transportation (FDOT) Structures Research Center in Tallahassee, Florida, and transported to the University of Florida (UF) Civil & Coastal Engineering Structures Laboratory in Gainesville, Florida for static tests.

7.2 Test Setup and Results of Connector Bolt Tensile Capacity Determination

A key feature of the shear-controlled moment collar connection is that the design shear capacity of the breakaway sign post can be controlled by selecting proper tension strength of connector bolts joining the two collar halves. For the three-post sign support structure, the tributary design wind load on the middle post (which is the largest load) is 6.5 kip (Appendix A). Numerical simulations presented in Chapter 6 indicated that with a combined total tensile strength of two connector bolts of 6.5 kip, the connection was able to resist the design wind load with a factor of safety of 1.71. Since the AASHTO Highway Sign, Luminaire, and Traffic Signal Specifications require that the experimentally determined capacity be 1.5 times the nominally required capacity, the connection was estimated to have a reserve capacity for wind loading of 1.37 kip ((1.71-1.5) x 6.5 kip). However, simulations also indicated that the connector bolts can fail (break), as desired, under a low-energy impact condition as specified by NCHRP 350. Therefore, selection of connector bolts for use in the connection should be based on the criterion that each bolt should have a tension capacity close to 3.25 kip (half of the design wind load on the middle post). Simultaneously, however, the tensile capacity should not be significantly larger than 3.25 kip, otherwise it might adversely affect the breakaway performance of the connection. Commercially available bolts that have potential application in the breakaway connection are ¼ in. in diameter and have a tensile strength of 60 ksi. The connector bolt specification is shown in Table 7-1. In order to evaluate the applicability of this bolt type for the connection, 40 tensile tests were performed. An Instron testing machine at UF was used to conduct the connector bolt tests. The test setup is shown in Figure 7-1. In addition to a built-in Instron load cell, a pancake

load cell and a washer load cell were also used to measure connector bolt strength. Connector bolts were tested at a loading rate of 50 lbf/sec.

Table 7-1. Connector bolt specification

Material Type	Steel
Finish	Plain
Square Head Bolt Type	Low-Strength
Inch Thread Size	1/4"-20
Minimum Thread Length	3/4"
Length	2"
Head Height	11/64"
Head Width	3/8"
Rockwell Hardness	Minimum of B69
Minimum Tensile Strength	60,000 psi
Specifications Met	American Society for Testing and Materials (ASTM)
ASTM Specification	ASTM A307 Grade A

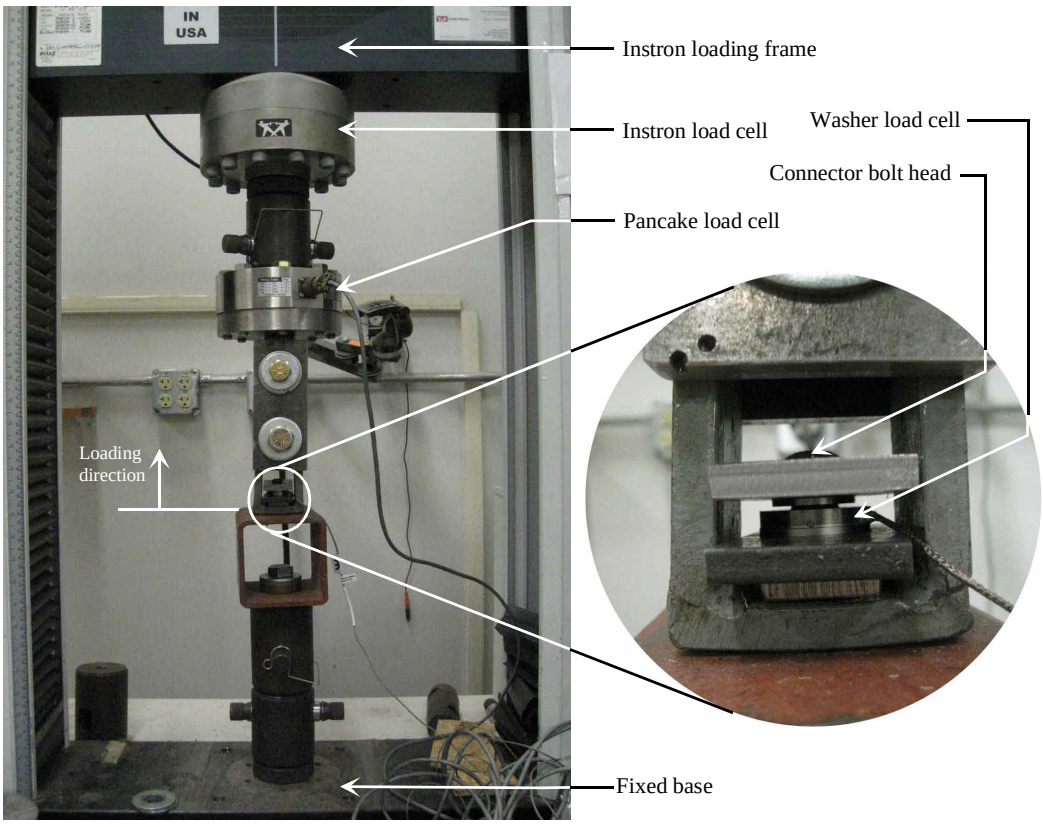

Figure 7-1. Connector bolt test setup

Failure loads from forty (40) tests, recorded by the three load cells, are plotted in Figure 7-2. More variation of bolt strength was obtained from the washer load cell reading than was observed in the other load sensors. This is due to the fact that the washer load cell was reinstalled after each test. Since the Instron load cell was least affected by the bolt installation process from test to test, the average bolt strength of 2.8 kip recorded by Instron load cell was taken as the nominal capacity of the connector bolts (see Figure 7-3).

Total strength of the two connector bolts was then found to be 5.6 kip, which is less than the required design wind shear load by 0.9 kip. However, pull-over analysis (presented in Chapter 6) showed that a post utilizing the shear-controlled moment collar connection with a total bolt tensile strength of 6.5 kip has the capability to resist the design wind load (6.5 kip) with a factor of safety (F.S.) of 1.71. Therefore, the breakaway system has a shear capacity of 1.37 kip in excess of that required by AASHTO: 1.71 x 6.5 kip – F.S. x 6.5 kip = 1.71 x 6.5 kip – 1.5 x 6.5 kip = 1.37 kip; where F.S.=1.5 per AASHTO. Since the excess capacity is greater than the difference between the total actual strength of the two bolts and that used in the pull-over analysis, the bolt type was deemed adequate to achieve a breakaway post capacity needed for the design wind load and a F.S. of 1.5. Therefore, the type of bolt tested (Table 7-1) was selected for use with the connection.

7.3 Static Test Setup

In order to mount the test post, a steel support fixture was designed, constructed, and installed in the Civil & Coastal Engineering Structures Laboratory at the University of Florida. A photograph of the fixture in the lab is shown in Figure 7-4. The fixture was bolted to the strong floor using six fully-threaded bars at two anchor points located 4 ft apart.

An overview of the setup for the static tests is shown in Figures 7-5 and 7-6. The total post length was 21 ft-1/2 in. The post length was selected based on the laboratory testing condition and the location of the force resultant of the wind loads acting on the tributary sign panel and along the post length below the sign panel.

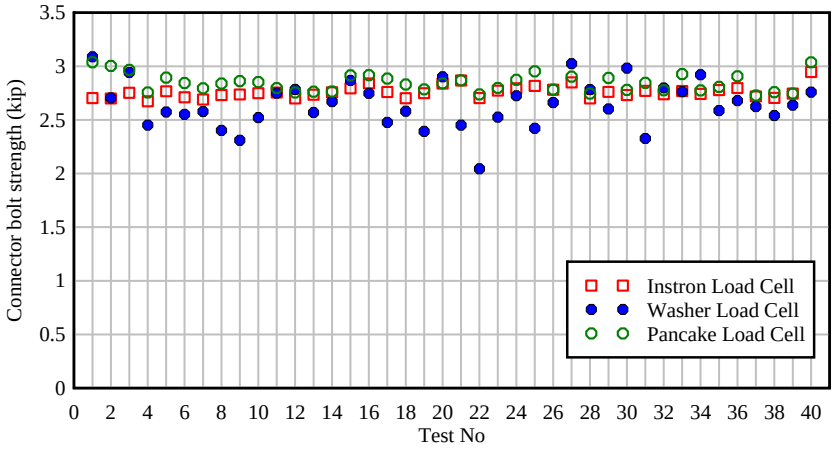

Figure 7-2. Connector bolt tensile strength from three load cells

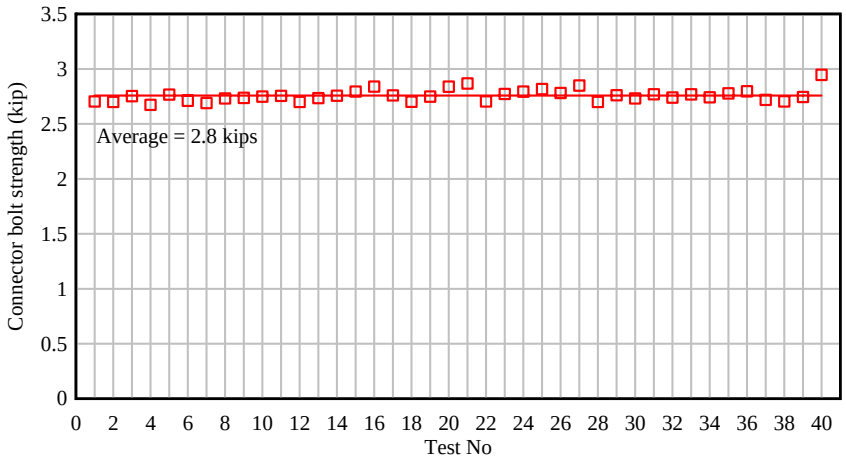

Figure 7-3. Average connector bolt strength by Instron testing machine

Figure 7-4. Steel support fixture in the UF Civil Eng. Structures Lab.

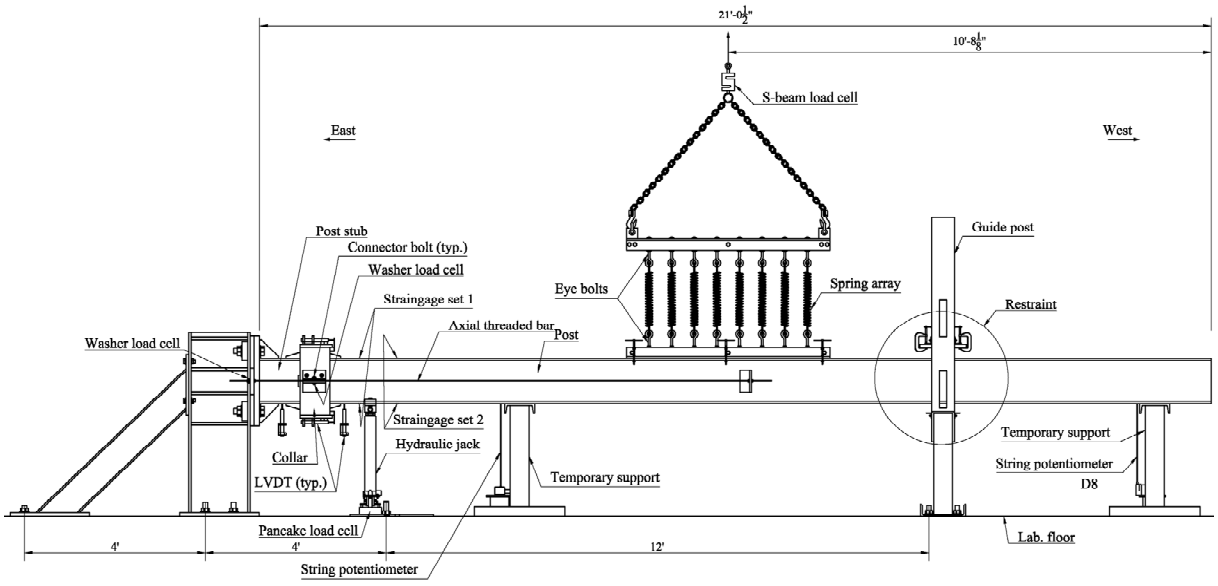

A

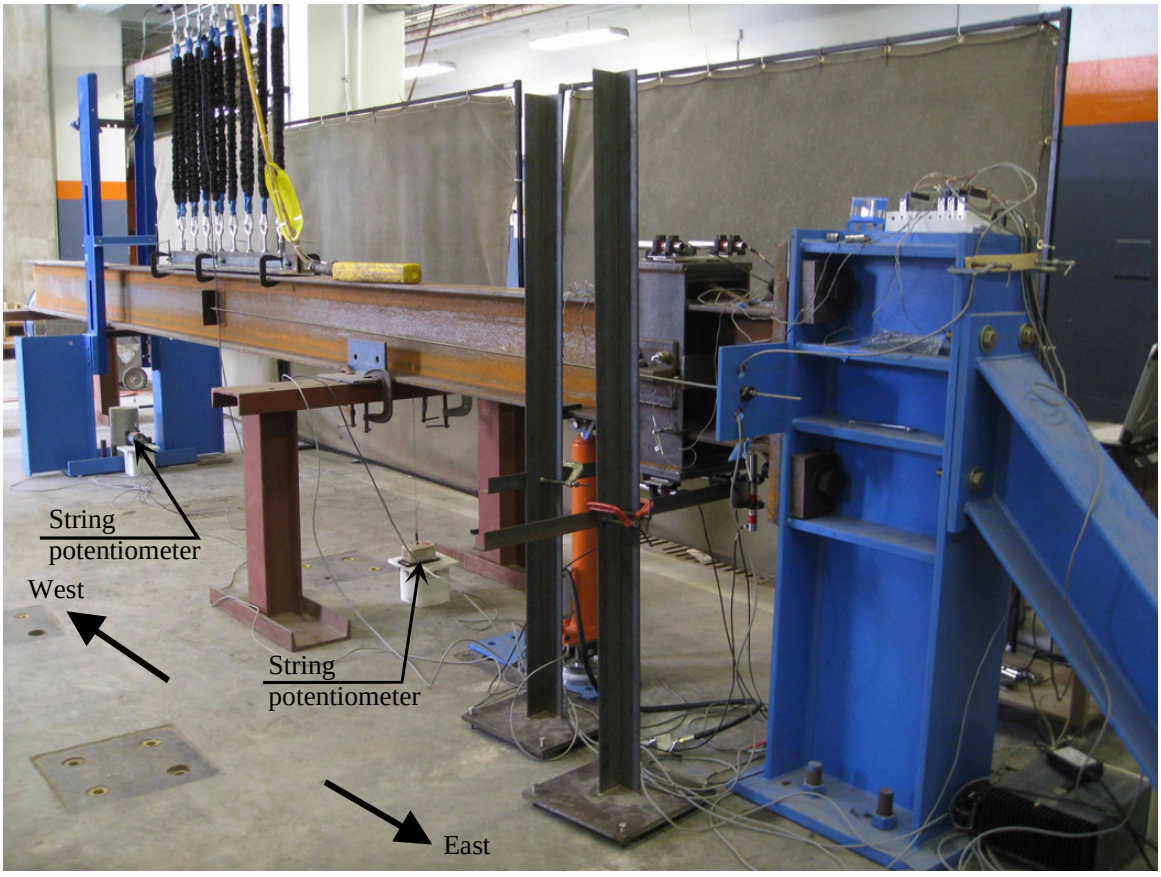

B

Figure 7-5. Static test setup overview: A) Elevation view illustration; B) View from east side

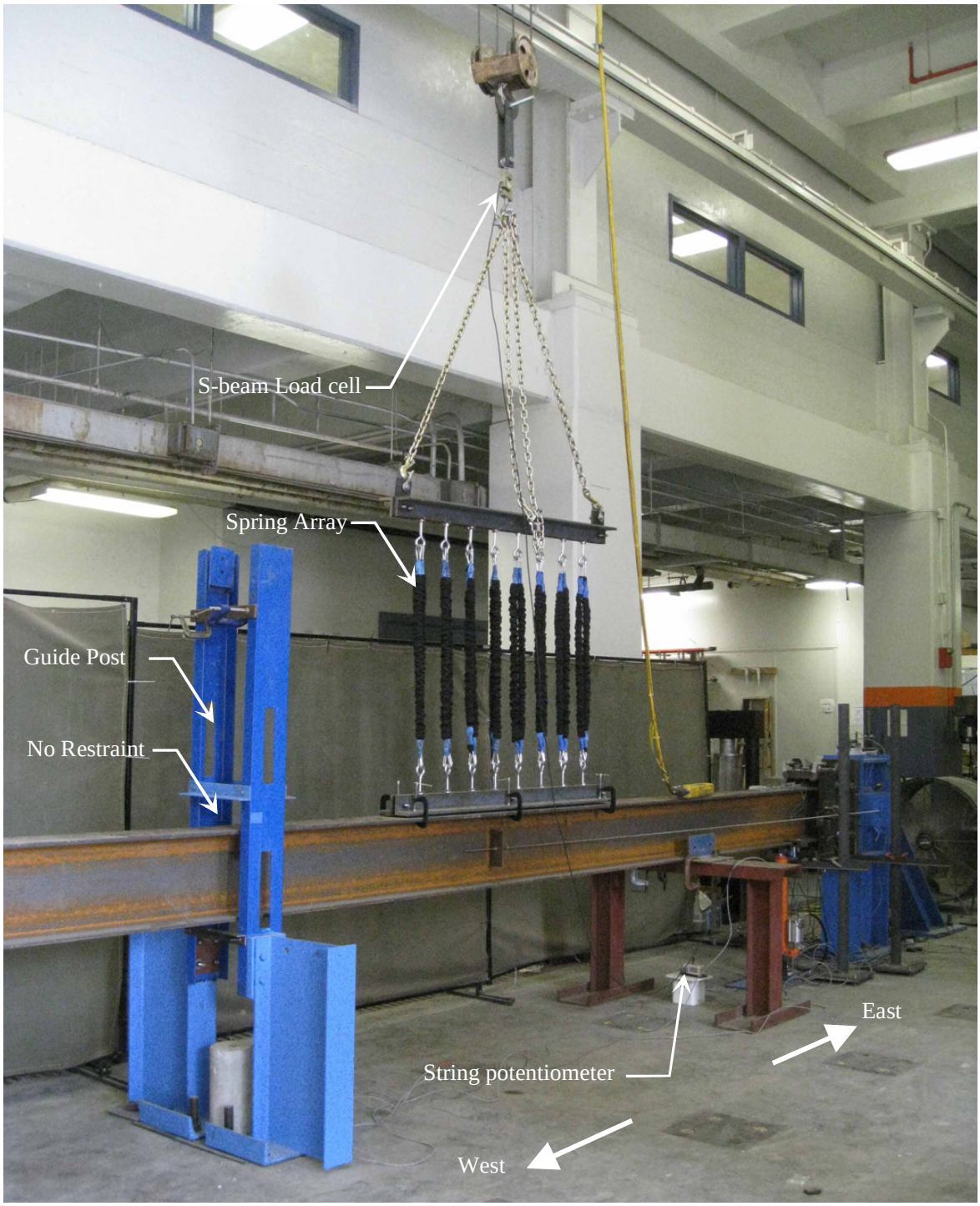

Figure 7-6. View from west side of the static test setup

The tested breakaway post essentially consisted of three main parts: a post stub, post, and a collar. The post stub was connected to the support fixture by four 1-1/2 in.-diameter bolts at the base plate. The post was aligned with the post stub at the slipping surface and supported by two temporary steel supports. Upon loading, the post lifted completely off the temporary supports. Once the post stub and the post were properly positioned, they were joined together by the two

breakaway collar halves and connector bolts. Connector bolts were lightly tensioned to 50 lbf to prevent any gaps that might cause free separation of collar angles. The two collar halves were aligned such that the primary plates were in flush contact with the flange plates. The bolts connecting the binding plates to the primary plates were installed using the following steps (see Figure 7-7). First, the binding plates were aligned flush to the primary plates. Second, a force of 300 lbf was applied to the binding plates to ensure full contact with the flange plates. Finally, the bolts were tightened with a torque of 250 lbf-ft to clamp the binding plates to the associated primary plates.

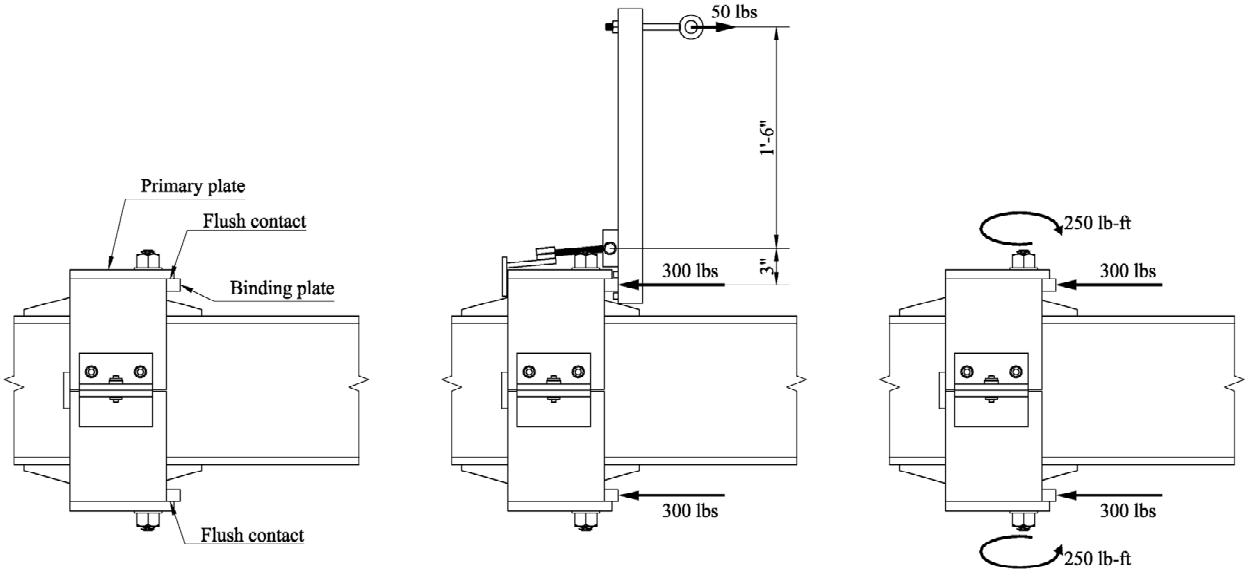

Figure 7-7. Installation of bolted connection between binding plates and primary plates

The tested post was restrained from lateral movement by a guide post rigidly bolted to the laboratory floor at 16 ft and 20 ft from the support fixture for shear tests and moment tests, respectively. The guide post was also utilized as a reaction support for shear tests that needed to restrain the post from upward movement at the guide post location. A detail of the pinned restraint at the guide post is shown in Figure 7-8. A ½ in. diameter bolt was screwed into the load cell, which was placed on the top flange of the tested post, to create a pinned restraint condition (since the bolt head was prevented from vertical translation).

Since the post was tested horizontally, which is different from the field (service) condition of sign posts, post self-weight was no longer axially oriented but perpendicular to the post axis. Therefore, two measures were applied to accommodate the testing condition. First, in order to account for the axial load due to the post self-weight and the tributary sign panel weight, a pair of ¼ in.-diameter axial threaded bars was used. Each bar was 12 ft long with one end connecting to the post web through a welded angle and the other end connecting to the support fixture through an extended plate inserted between base plate and the fixture. To apply the axial load, the threaded bars were pre-tensioned to 800 lbf by tightening the end nuts.

Figure 7-8. Pinned restraint

Second, the unwanted post gravity force was canceled out by applying to the post, through a spring array system, a lifting force equal to the post weight of 953 lbf. The spring array system consisted of sixteen extension springs connected to lower and upper cords made from double angles, which were 3 in. by 3 in. by ½ in. thick. Eye bolts were placed between the two angles and bolted to the double angle cords. The lower cord was securely clamped to the top flange of the post while the upper cord was lifted by a crane. The spring array was positioned so that the spring force resultant passed through the post center of gravity and was in the opposite direction to the post self-weight force. Correct positioning was achieved by iteration of clamping the spring array system at several locations near the post mid-span and lifting the post prior to collar installation until the post was horizontally balanced. Each spring had a stiffness of 3.21 lbf/in and maximum capacity of 77 lbf. Very low stiffness springs were selected so that post deflection during testing could be accommodated without causing a considerable change in the targeted lifting force. For test configurations in which zero moment was produced at the breakaway connection, the spring array was utilized to apply a controlled lateral load on the post.

Load was applied on the post using a vertical hydraulic jack through a ½ in.-thick bearing plate clamped by ½ in. diameter bolts onto the bottom flange of the post (Figure 7-9A). In order to accommodate post rotation during tests, a pin joint was used to connect the jack to the bearing plate (see Figure 7-9B). A 30-kip load cell was placed under the jack to measure applied loads. The jack and the load cell were also connected together by a pin joint to ensure that axial jack loading did not also cause bending moments. The load cell was secured by four ½ in. diameter bolts to a ½ in.-thick keeper plate bolted to the floor.

A

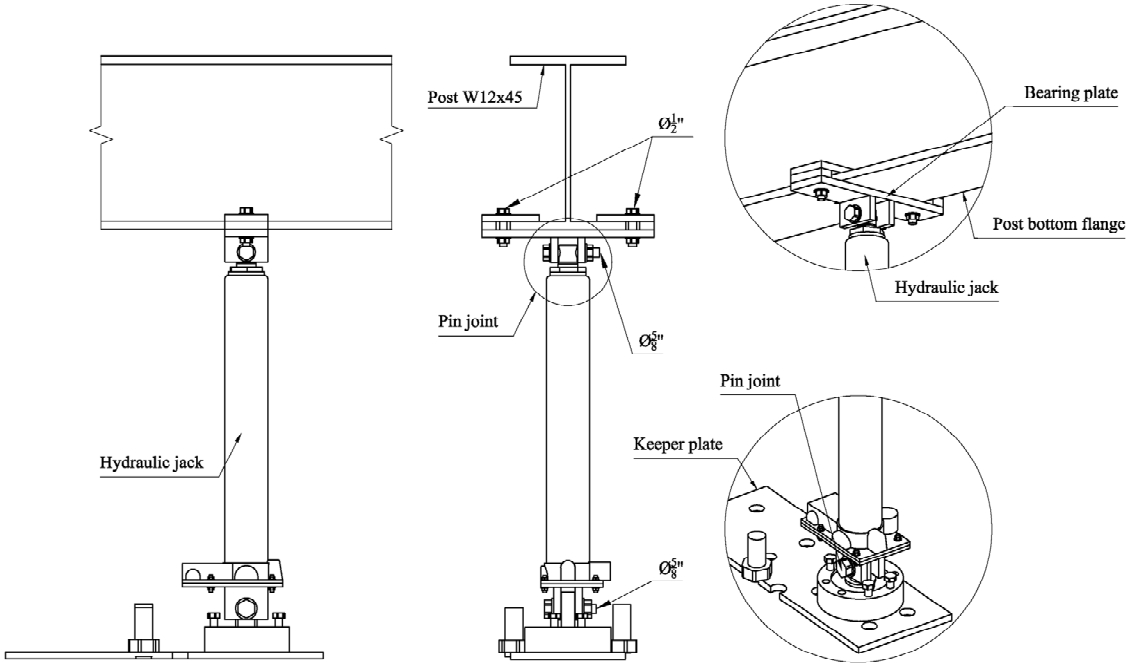

B

Figure 7-9. Loading system: A) Photo of the loading system; B) Illustration detail of the loading system

7.4 Instrumentation

There were two main types of static tests conducted in this study: a shear test and a moment test. To collect data from such tests, an instrumentation system was designed and installed. The instrumentation system included electrical resistance strain gauges, load cells, linear variable displacement transducers (LVDTs), string potentiometers, and a data acquisition (DAQ) system. This section presents detailed descriptions of the devices used.

7.4.1 Electrical Resistance Strain Gauges

The electrical resistance strain gauges used in this study were of type FLA-10-11-5L (Figure 7-10), manufactured by Tokyo Sokki Kenkyujo Co., Ltd. The gauges had a gauge length of 10 mm (0.4 in.), a gauge factor of 2.09, and a gauge resistance of 120 ohms. There were two strain gauge sets used to measure moment at two locations along the post length in the vicinity of the breakaway connection (Figure 7-11). Each strain gauge set consisted of two active strain gauges and two inactive (dummy) strain gauges. Active strain gauges were bonded to the outer surfaces of the top and bottom flanges of the post while the inactive strain gauges were left in the same thermal (lab) environment as the active ones, but not bonded to the post.

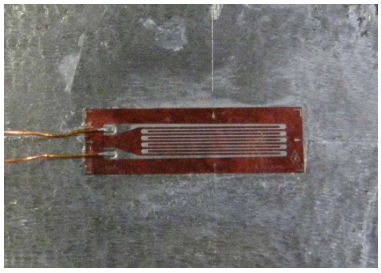

Figure 7-10. Electrical resistance strain gauge (FLA-10-11-5L)

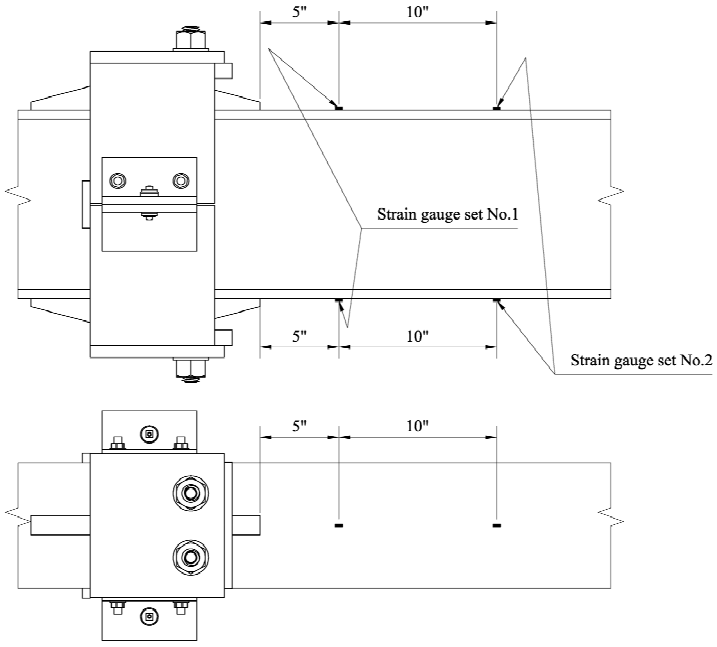

Figure 7-11. Strain gauge setup

A circuit diagram for each strain gauge set is illustrated in Figure 7-12. Since both active and inactive strain gauges were of the same type and had the same wire length, the circuit that was used eliminated the undesirable effect of temperature variation and lead resistance. Output

voltage was directly proportional to the moment at the location of interest and the strain was computed as follows:

$$\varepsilon = \frac{-2V_r}{GF} \tag{7-1}$$

where ε was the measured strain, GF was the gauge factor, V_r was the voltage ratio defined by the following equation:

$$V_r = \frac{V_{CH}^{(strained)} - V_{CH}^{(unstrained)}}{V_{EX}} \tag{7-2}$$

where V_{CH} was the measured signal voltage and V_{EX} was the excitation voltage.

Two sets of active strain gauges were positioned 10 in. apart to measure strain at two locations along the post length. The use of two strain gauge sets had two purposes. The first purpose was to obtain the shear force in the post, in addition to that determined from the applied load, since shear force could be determined from the moment gradient. The second purpose was to ensure that moment data from at least one position near the slip base was recorded in the event that one strain gauge set malfunctioned. Strain gauge set No. 1 was installed 5 in. from the edge of base connection stiffeners to ensure that at the strain gauge locations the maximum principal stress directions were parallel to the post axis and to avoid the region potentially becoming plastic at maximum bending capacity of the post.

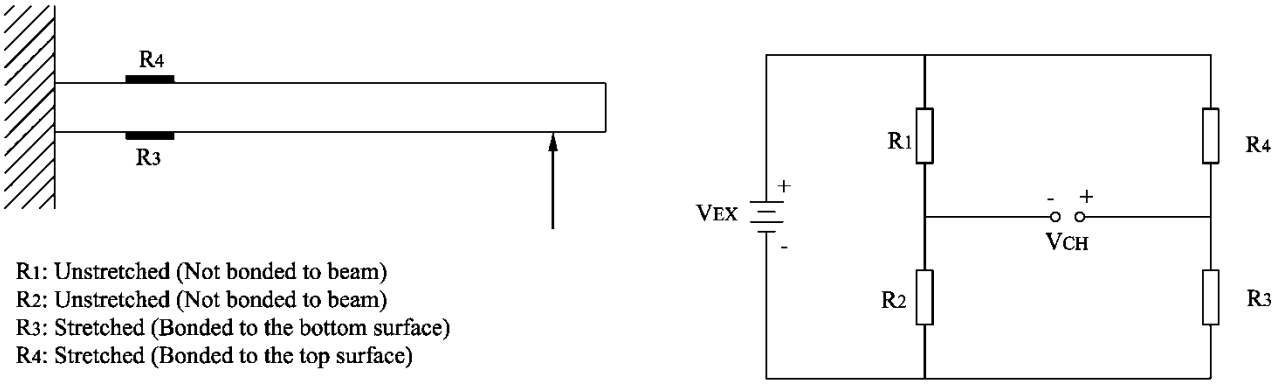

Figure 7-12. Circuit diagram of a strain gauge set

7.4.2 Pancake Load Cells

There were two types of pancake load cells used in this study to measure the applied load and reaction force. The load cells used to measure the applied load from the jack were manufactured by Load Cell Central (model SRP4-30k) with a capacity of 30 kip. Figure 7-13 shows the load cell pinned to the jack and bolted to the keeper plate. A load cell manufactured by Sensotec (model 41/572-05), which had a capacity of 5 kip, was used to measure the reaction force at the pinned restraint. Figure 7-14 shows the load cell as an individual unit. A ½ in.

diameter bolt was screwed into the center hole to transmit the reaction force to the load cell. The load cell installed at the pinned restraint is shown in Figure 7-8.

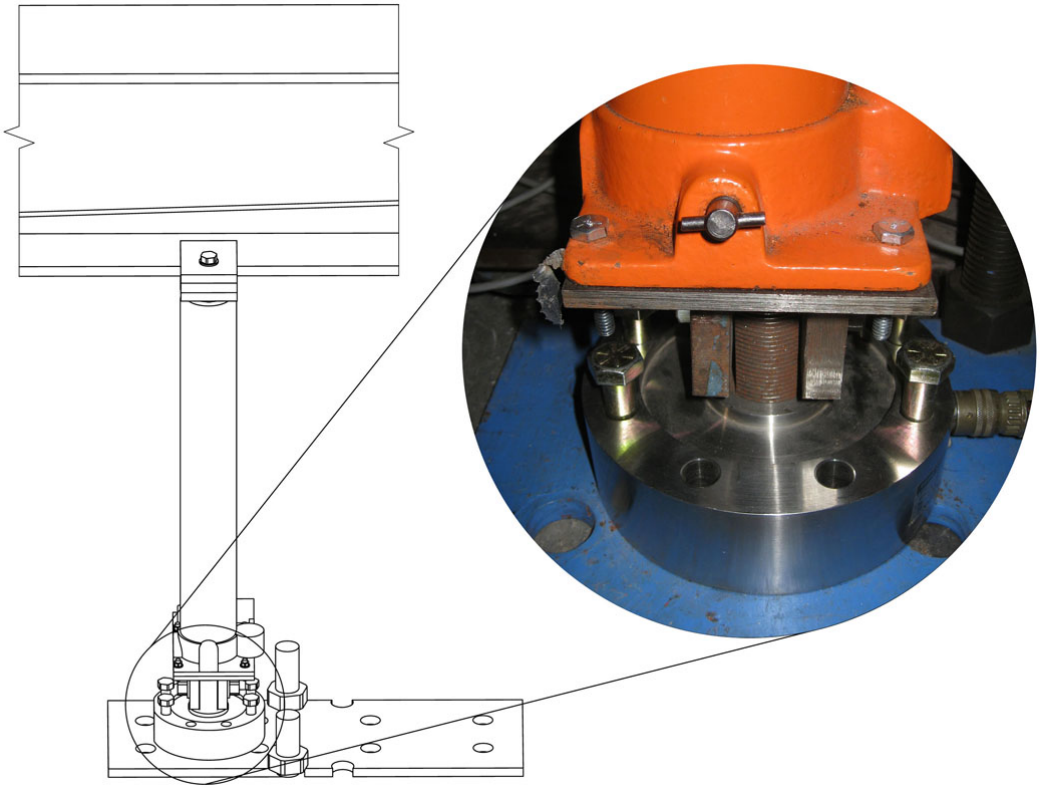

Figure 7-13. Pancake load cell SRP4-30k

Figure 7-14. 5-kip pancake load cell

7.4.3 Washer Load Cells

Two washer load cells were used to measure the magnitude of the axial forces in the connector bolts and two additional load cells were used to measure forces in the threaded bars. The four washer load cells used in this study were manufactured by Omega Engineering, Inc. (model LC901-1/4-5k), and were designed to measure axial force in a ¼ in.-diameter bolt. The layout and installation details of the washer load cells are shown in Figure 7-15.

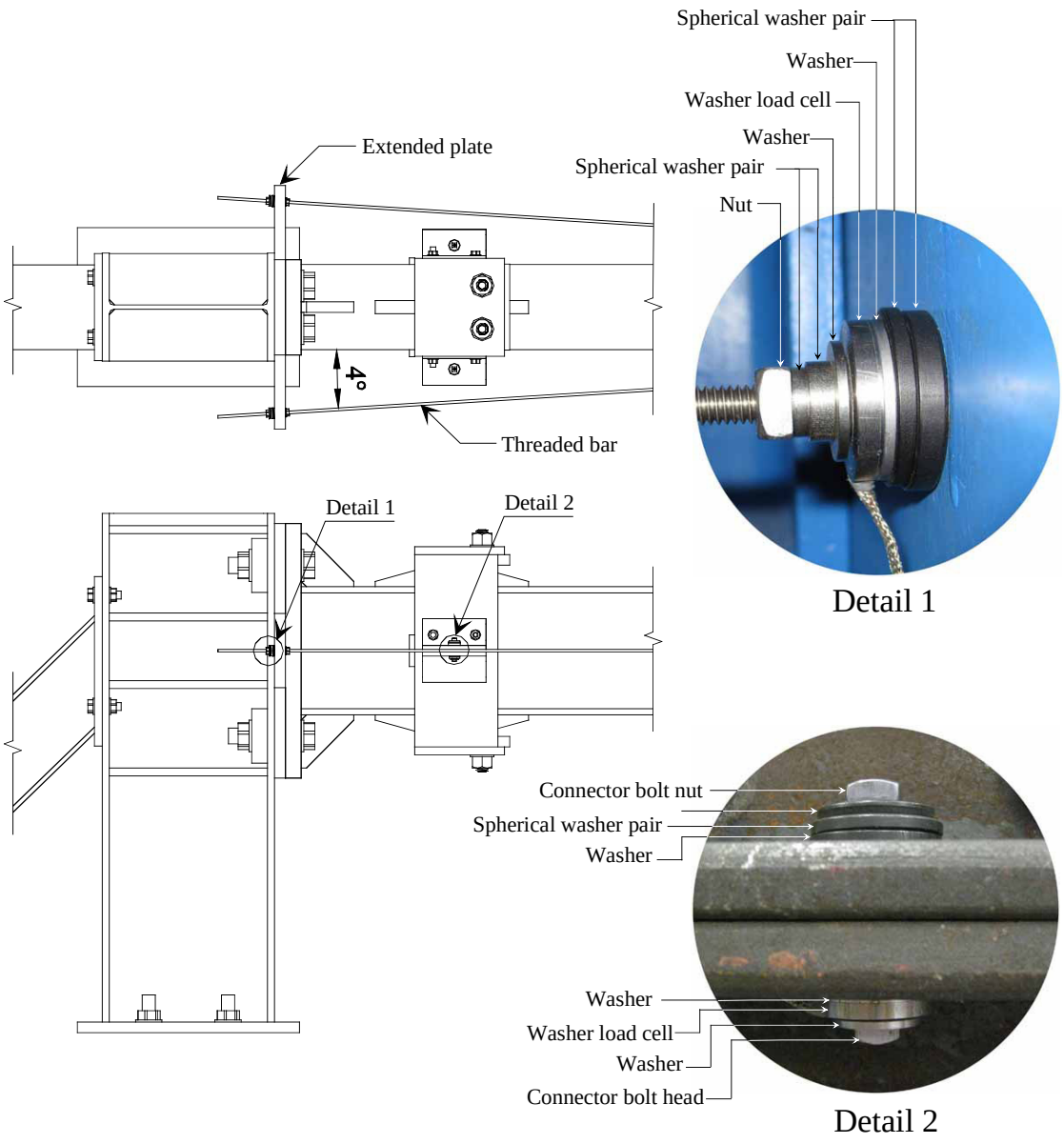

Figure 7-15. Washer load cells

Detail 1 in the figure shows the washer load cell used to measure the pre-tension force applied to the threaded bar. Since the threaded bars were at 4 degrees with respect to the normal surface of the extended plate, spherical washers were used to ensure that the threaded bar axial force reaction was aligned with the center of the washer load cells. This was an important requirement of the washer load cells to avoid obtaining an improper reading. Spherical washers act like a ball and socket joint and are generally used to compensate for small angle misalignments. Each washer load cell measuring threaded bar axial force was installed with two pairs of spherical washers to ensure complete compensation for the 4-degree angle. Detail 2 in Figure 7-15 shows the washer load cell used to measure connector bolt forces and another pair of spherical washers used to compensate for small rotations of the collar angles so that proper readings of the connector bolt forces were obtained.

7.4.4 S-Beam Load Cells

To measure the magnitude of the lifting force of the spring array on the post, an S-beam load cell manufactured by Omega Engineering Inc. (model LCCA-10k) was used. The load cell had a capacity of 10 kip. One end of the load cell was connected to an overhead crane and the other end was connected to the spring array system (Figure 7-16).

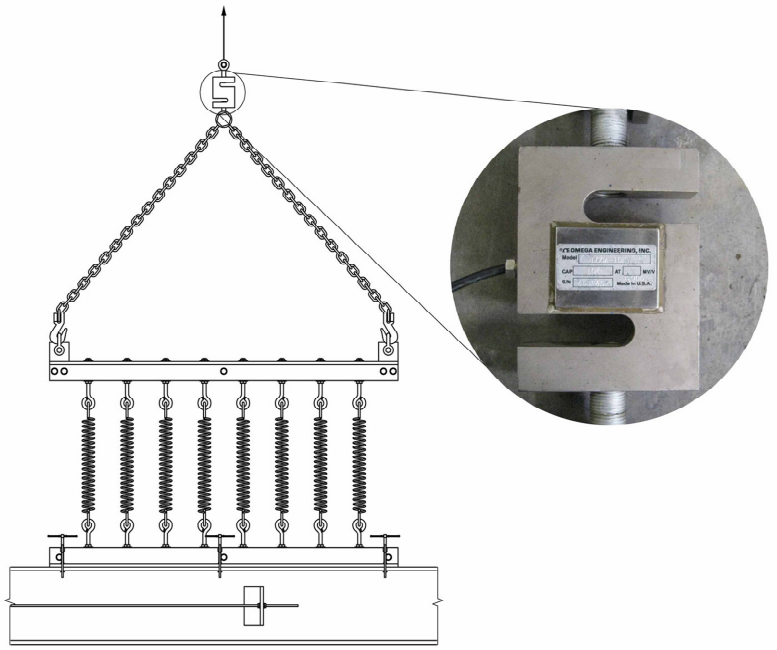

Figure 7-16. S-beam load cell

7.4.5 Position Transducers (String Potentiometer)

Two position transducers, an Ametek Rayelco Linear Motion Transducer P-2A and a UniMeasure HX-P1010-50, were used to measure post displacement in this study. The position transducer model P-2A had a range of 0-2 in. and was located at the temporary support close to the breakaway connection (see Figure 7-17). Maximum post displacement during the tests at the measured location was anticipated to be below 2 in. The position transducer model HX-P1010-50 had an adjustable measurement range up to 50 in. (Figure 7-18). For use in this study, the transducer was configured to measure in range from 0 in. to 20 in. The position transducer was typically placed close to the post end where the maximum post displacement was expected. For tests where the post was pinned at the guide post, the position transducer was placed at the pinned location to monitor the effectiveness of the translational restraint provided by the pinned support. Measurement accuracy required the position transducers to be anchored at a stationary position relative to the test post. Therefore, the position transducers were attached to two steel base anchors that were heavy enough to prevent any movement.

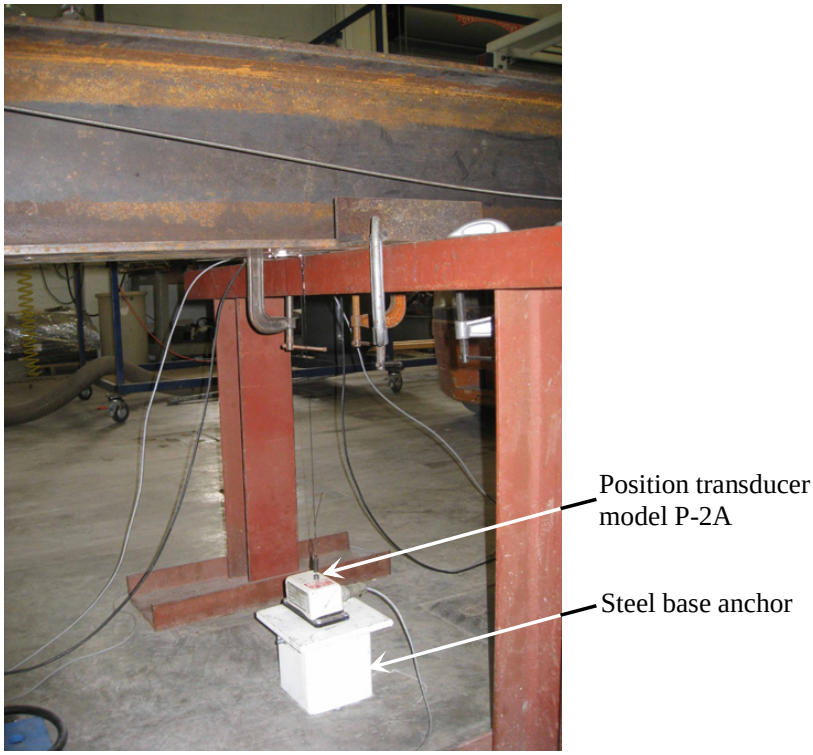

Figure 7-17. Position transducer model P-2A

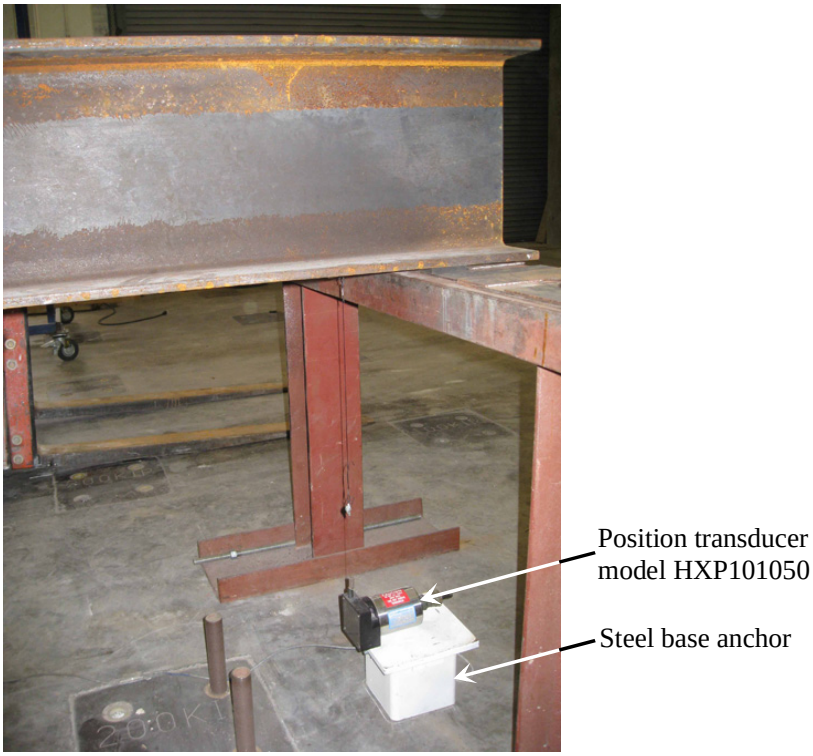

Figure 7-18. Position transducer model HX-P1010-50

7.4.6 Linear Variable Displacement Transducers (LVDT)

Post displacement near the breakaway connection and translation of the bolted collar plates were quantified by using DCTH Series LVDTs manufactured by RDP Electrosense. The LVDTs can measure displacement up to 1 in. Two LVDTs were used to measure relative displacement between post and post stub at the slipping surface (Figure 7-19). Two LVDTs were mounted on the top of the collar and other two were mounted on the bottom of the collar to monitor in-plane motion of the bolted collar plates (Figure 7-20).

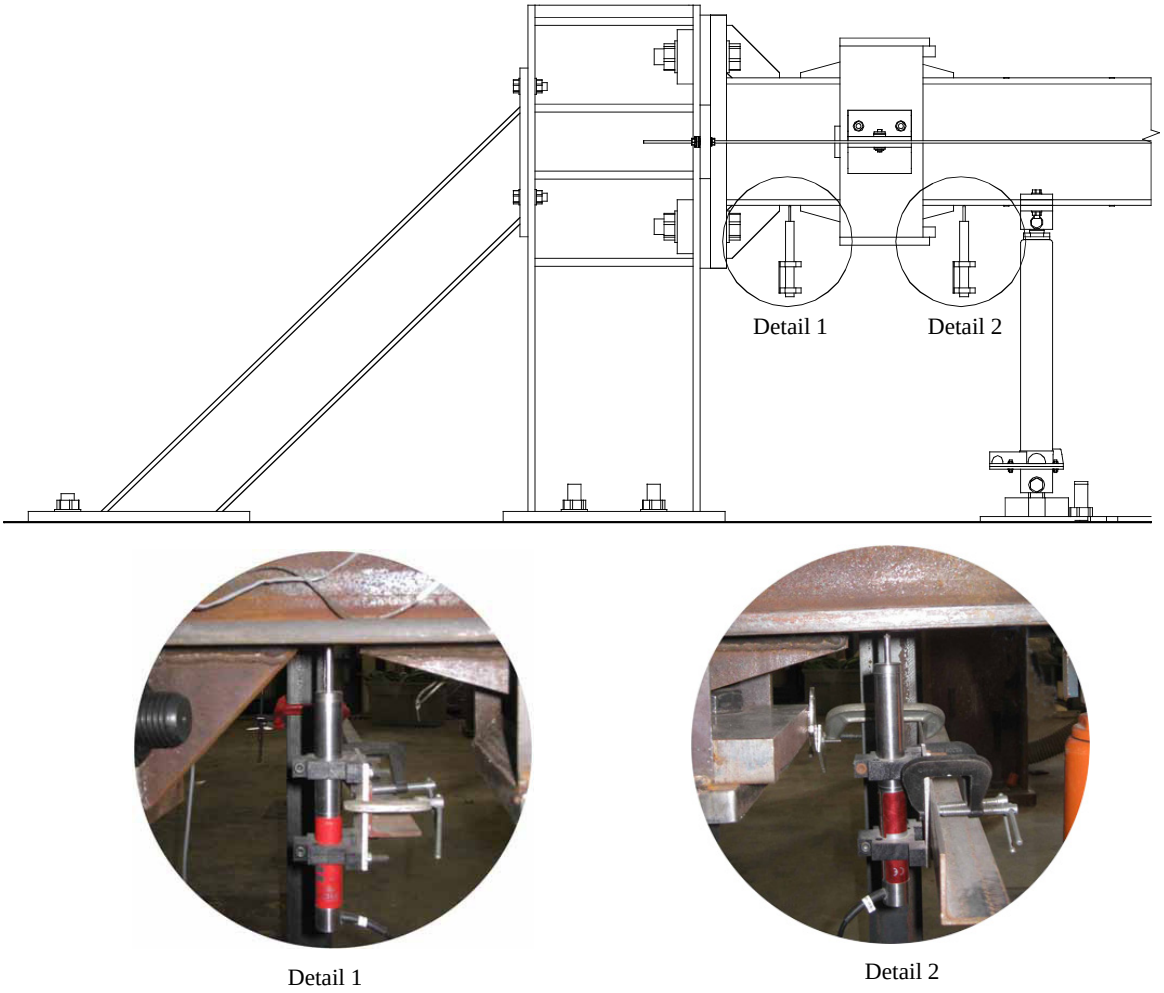

Figure 7-19. LVDTs for measuring relative displacement between post and post stub

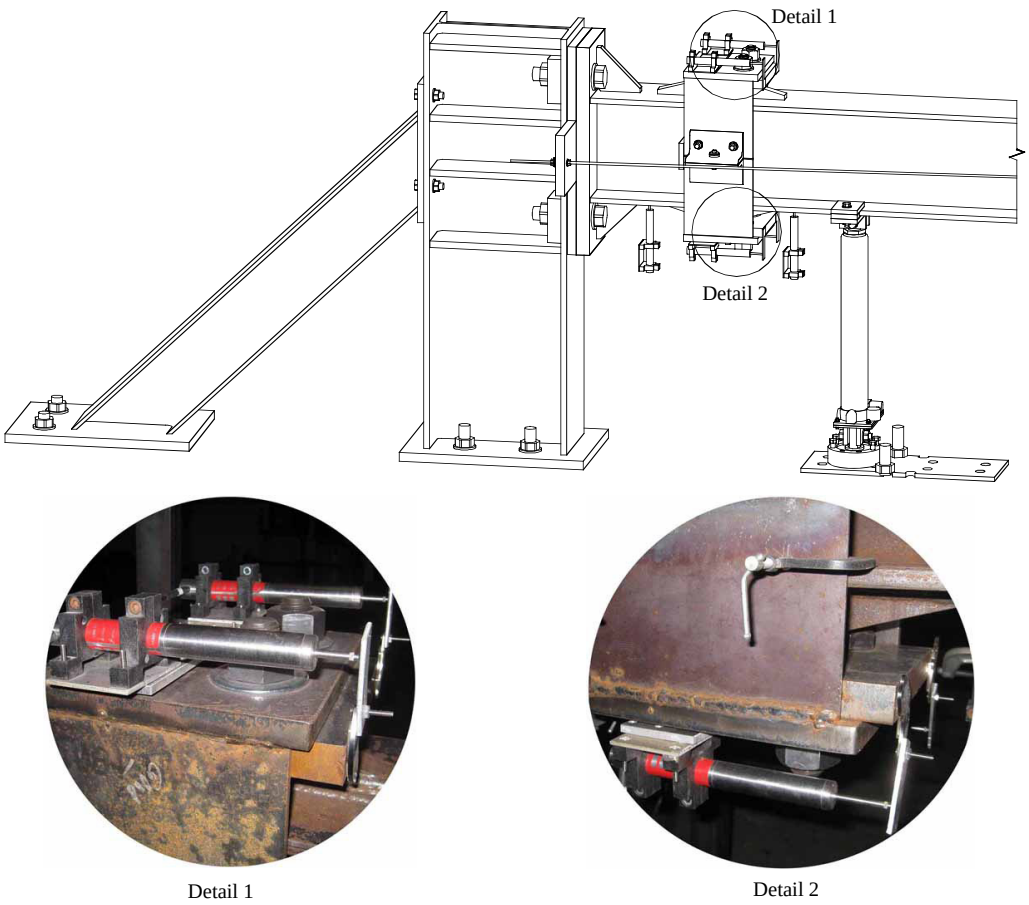

Figure 7-20. LVDTs for measuring in-plane motion of the bolted collar plates

7.4.7 Data Acquisition

A data acquisition system, which was used to collect data from the variety of instruments described above, included four main components: a NI cDAQ-9172 chassis, analog input modules, DC power supplies, and a notebook computer. Figure 7-21 shows the chassis with the four analog input modules installed. The NI cDAQ-9172 chassis had 8 slots for use with C Series I/O modules. The chassis was designed for measuring analog and digital I/O signals and sensors using a high-speed USB interface. The three types of analog input modules employed in this study were: NI 9201, NI 9219, and NI 9205. The NI 2019 module was able to acquire signals from eight analog input channels with a maximum aggregate sampling rate of 500,000 samples/second. The module had a built-in analog-to-digital converter (ADC) with 12-bit resolution. Two channels of the module were used to record signals from the two position transducers that were provided with excitation voltage by two external DC power supplies.

The NI 9219 module had four analog input channels with built-in 24-bit ADC as well as voltage and current excitation. NI 9219 modules were capable of a sampling rate of 100,000 samples/second. Two NI 9219 modules were used to provide eight connections for analog input channels from strain gauges and load cells (four washer load cells, one 30-kip pancake load cell and one S-beam load cell).

The NI 9205 module was used to acquire input voltage signals from six LVDTs and a 5-kip pancake load cell. The module was capable of providing connections for 32 single-ended or 16 differential analog input channels with 16-bit ADC resolution. External DC power supplies were also used to provide voltage excitation for sensors wired with the NI 9205 module. Labview software version 8.5, by National Instruments, was installed on a Panasonic Toughbook CF 28 notebook computer to control the data acquisition process. Input signals from sensors were scanned, buffered, conditioned, digitally sampled and transferred to the notebook computer for data storage, processing and display. The data acquisition (DAQ) system was set to acquire data at a sampling rate of 10 Hz.

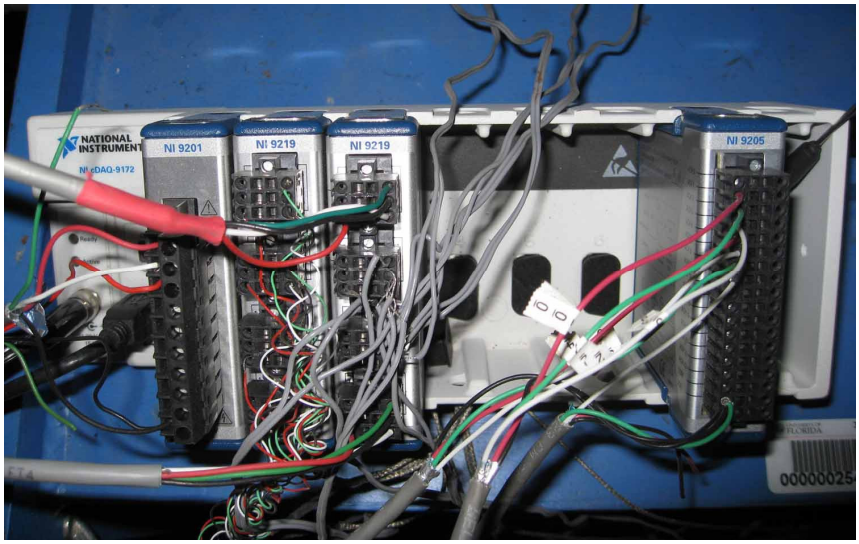

Figure 7-21. NI cDAQ-9172 chassis and four installed analog input modules

7.5 Static Shear Test Configurations and Results

7.5.1 Test Configurations

Shear tests were set up to determine the static equivalent impact shear capacity (SEISC) of the developed breakaway connection for sign post structures. The shear loading was applied at 19 in. from the hypothetical ground location on the post to replicate an impact condition by a 820-kg small car, except that the load was applied statically rather than dynamically. The static shear testing was non-destructive since all structural components were well below their plastic limit except for the connector bolts, which were designed to break. Therefore, multiple tests could be conducted on the same post for frangibility investigation. It was anticipated that improving the frangibility of the connection under the static shear loading condition would also improve the dynamic performance of the system. The matrix of shear tests conducted is presented in Table 7-2.

Table 7-2. Shear test matrix

Friction condition	Zero moment at breakaway connection	No post restraint	Post pinned at “fuse-plate”
Bare steel friction condition	3 tests	3 tests	3 tests
Teflon friction condition	3 tests	3 tests	3 tests

The matrix has six test types with two steel friction conditions and three-post configurations. A total of 18 shear tests, three tests for each test type, were conducted. The two steel friction conditions were a bare steel friction condition and a Teflon sheet friction condition. In the Teflon friction condition, a 0.02 in.-thick sheet of Teflon was cut to the size of 18-1/8 in. by 8-1/8 in. and placed between the flange plates at the slipping surface. Figure 7-22 shows the Teflon sheet in place prior to collar installation.

Figure 7-22. Teflon sheet placed between flange plates

The three shear test configurations conducted in this study were: no post restraint, post pinned at the fuse plate, and zero moment at the breakaway connection. These configurations were selected to serve as representative cases for multi-post ground sign systems with a variety of lateral stiffness contributions from the non-impact posts, the sign panel, and the wind beams (henceforth referred to as non-impact sign structural components).

The “post pinned at fuse plate” configuration represented the condition in which the non-impact structural components provide a relatively high lateral stiffness to the impacted post (at the fuse plate location) such that post translation in the loading direction is negligible. Figure 7-23A illustrates the schematic setup of the “post pinned at fuse plate” configuration. Prior to applying the jack load, the post was gradually lifted up by a crane using the spring array system until a force of 953 lbf, equal to the post self-weight, was reached. The lifting force was then

maintained constant throughout the testing process. The shear test setup and instrument plan for the “post pinned at fuse plate” configuration is presented in Figure 7-24.

The “no post restraint” configuration represented the condition in which the lateral stiffness contribution of the non-impact structural components is negligible. A schematic setup of the “no post restraint” configuration is shown in Figure 7-23B. For this configuration, a constant lifting force of 953 lbf was also maintained during the jack loading process. In addition to enabling the determination of the SEISC, shear tests utilizing this configuration provided useful information regarding the shear capacity of the connection under the wind loading condition. The “no post restraint” configuration shear test setup and instrumentation plan is presented in Figure 7-25.

The two configurations presented above have a common characteristic in that a resultant moment in the post (at the slipping surface) is always present and caused by lateral loads, such as: the jack load, lifting load, post gravity load, and reaction at pinned support (for the “post pinned at fuse plate” configuration). In each such case, the moment is balanced by the binding force couple that the collar and post stub produce on the post flange plate. The binding force couple leads to additional frictional resistance which increases the shear resistance of the post. Figure 7-26 shows the binding force couple acting on the flange plates. The magnitude of the binding force couple can be determined from the moment at the slipping surface and the moment arm of the binding force couple.

The load required to fail the connection, therefore, needs to overcome the tension strength of the two connector bolts, the frictional resistance due to axial load representing post and upper structure self-weight, and the lateral load dependent frictional resistance. Thus, shear strength depends on the friction coefficient between the collar and flange plate components. If there was no friction, post shear strength would depend only on connector bolt strength. However, under the normal friction condition of bare steel (friction coefficient of 0.55), the shear resistance associated with the binding force can be a primary source of resistance. Therefore, to quantify the unbound SEISC of the post, utilizing the developed shear-controlled moment collar breakaway connection, and to compare it with the design shear strength, a “zero moment at breakaway connection” configuration was used. Figure 7-23C shows the schematic setup for the “zero moment at breakaway connection” configuration. This test condition was achieved by continuously adjusting the lifting force during testing so that the moment at the slipping surface (due to the jack load, post self-weight and lifting force) was maintained at zero. The shear test setup and instrument plan for the “no post restraint” configuration and the “zero moment at breakaway connection” configuration are presented in Figure 7-25.

The shear test procedure started with alignment of the flange plates of the post and post stub. A Teflon sheet was placed between the plates for the Teflon friction condition tests. The axial threaded bars were then pre-tensioned by nut-tightening and were monitored using the installed washer load cells. Once each bar reached 800 lbf, the loads were kept constant and the collar halves were installed. The two collar halves were joined by two connector bolts with installed washer load cells. A crane was then used to gradually lift up the spring array until the post self-weight was offset (cancelled out). The bolted angles of the collar half were adjusted so that the connector bolts were not pre-stressed. For the “post pinned at fuse plate” configuration tests, a 5-kip pancake load cell with a screwed bolt was installed to monitor the reaction force at the pinned location. The screwed bolt was adjusted so that post lifting introduced an initial reaction of only 50 lbf (to ensure contact between the bolt head and reaction support). The jack load was then applied gradually until one of the collar connector bolts failed. The lifting force

applied on the post was kept constant for the “no post restraint” and the “post pinned at fuse plate” configurations and was continuously adjusted to prevent frictional resistance due to binding forces for the “zero moment at breakaway connection” configuration.

Before discussing the shear test results, for interpretation convenience and better understanding of loads acting on the breakaway post, an equation relating the loads is derived and presented. The equation accounts for the resistances and factors that governed the jack load that was required to break the connector bolts. A free body diagram of vertical forces acting on the main components of the system is shown in Figure 7-27.

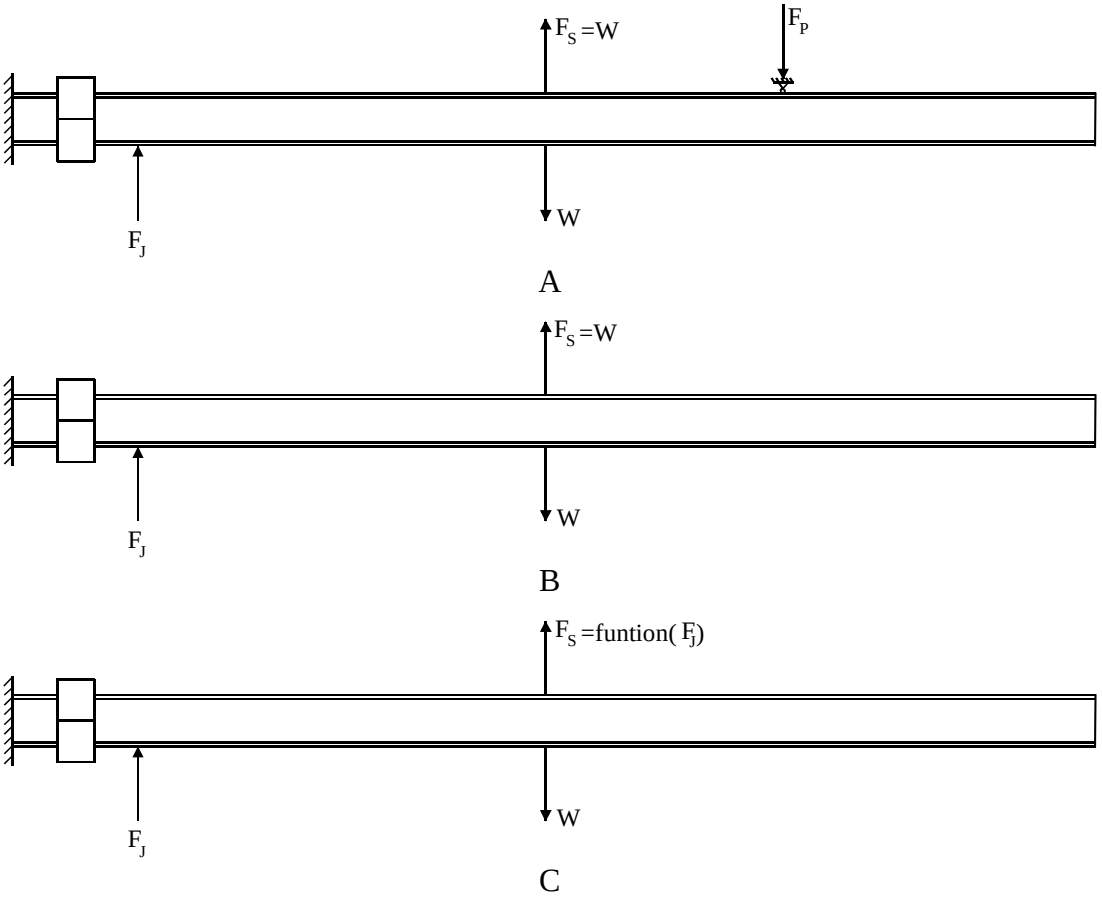

Figure 7-23. Schematic shear test setups: A) “post pinned at fuse plate” configuration; B) “no post restraint” configuration; C) “zero moment at breakaway connection” configuration

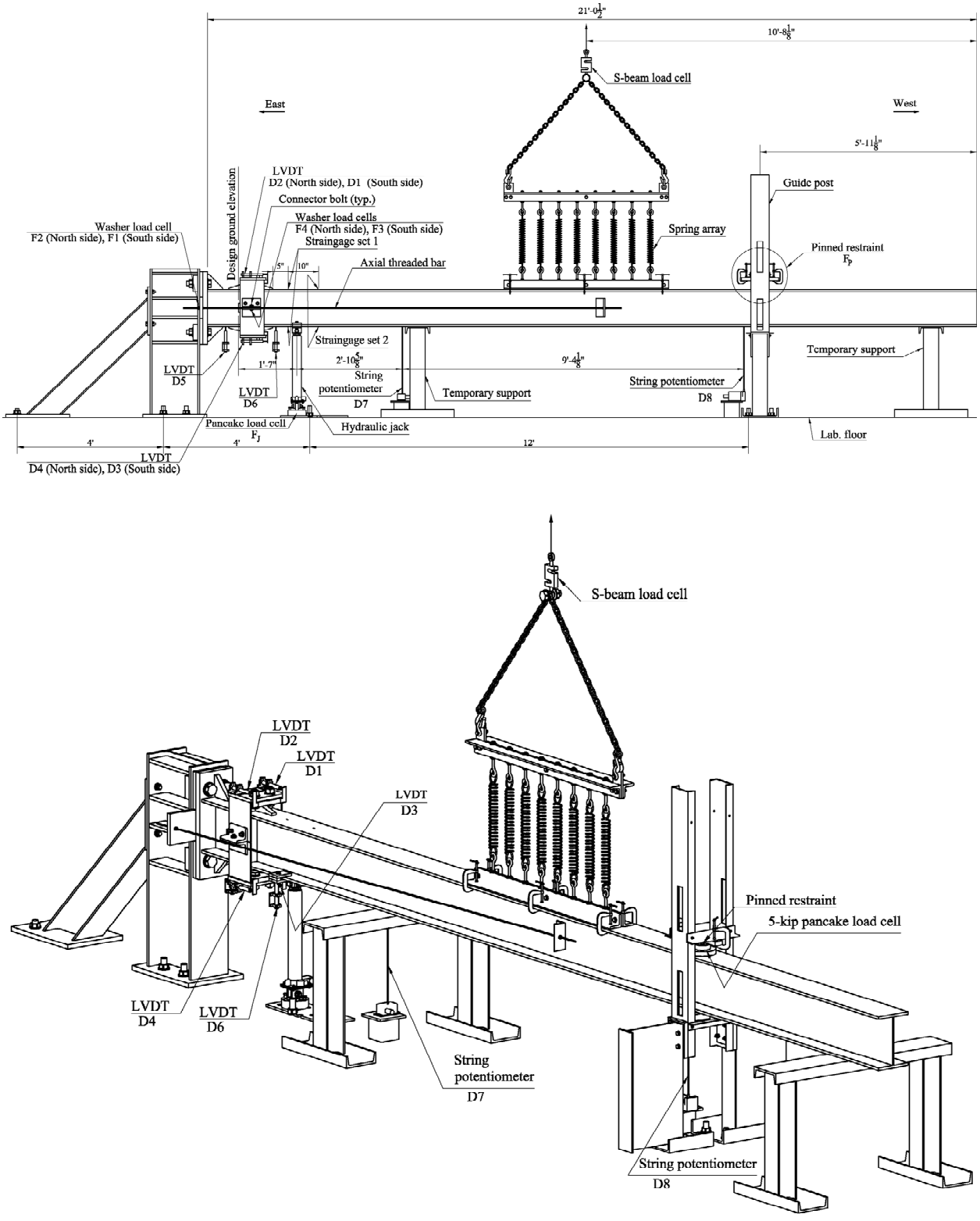

Figure 7-24. “Post pinned at fuse plate” shear test setup

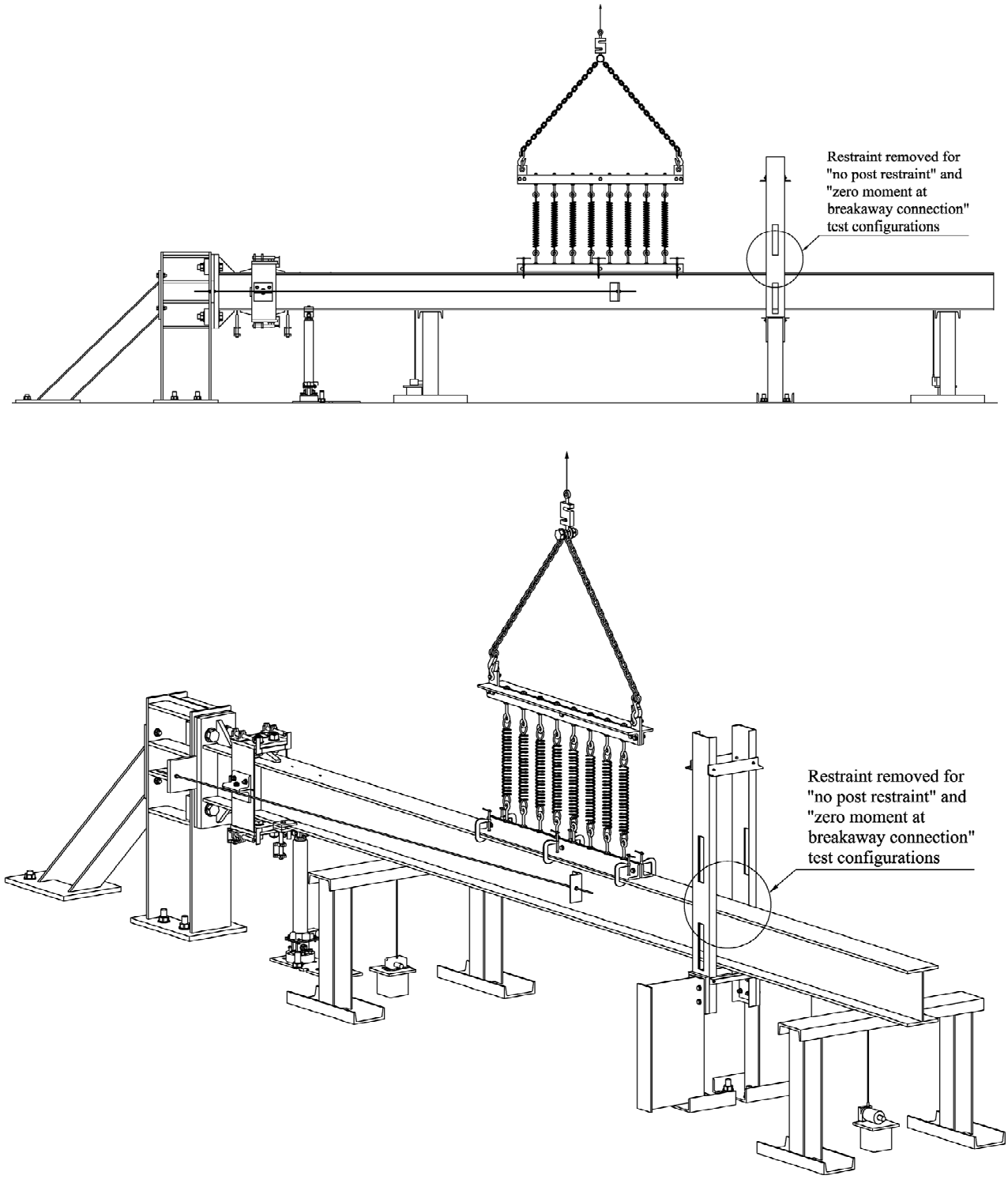

Figure 7-25. “No post restraint” and “zero moment at breakaway connection” shear test setup

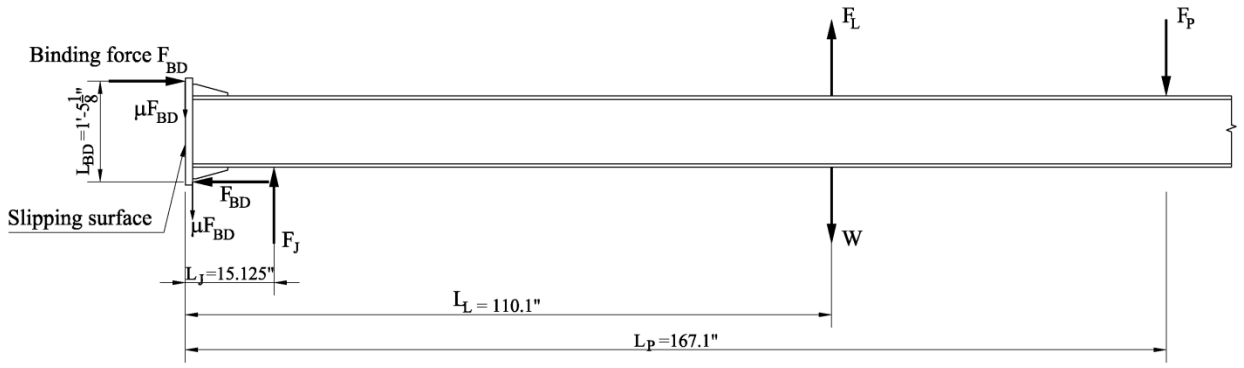

Figure 7-26. Binding forces on flange plates

When jack load was applied upward, the top of the flange plates tended to compress against each other while the bottom of the plates tended to separate. Post movement was restrained by the upper collar bearing force, frictional resistance from the post stub flange plate, and by the collar halves. This behavior can be represented by the following equation:

$$F_J = (W - F_S) + R_1 + R_2 + R_3 + R_4 \tag{7-3}$$

where F_J was the jack load, W was the post self-weight, F_S was the lifting force imposed by spring array, R_1 was the frictional resistance provided by the upper collar half, R_2 was the bearing force provided by the upper collar half, R_3 was the frictional resistance provided by the post stub flange plate, and R_4 was the frictional resistance provided by the lower collar half.

The relationships between forces acting on the upper and lower collar halves are described by the following equations:

$$R_1 + R_2 = F_B - P + R_5 + G_U \tag{7-4}$$

$$R_4 = -F_B + P + R_6 + R_7 + G_L \tag{7-5}$$

where F_B was the total of the two connector bolt forces (F_3 and F_4), R_5 and R_7 were the frictional resistances provided by the post stub flange plate, R_6 was the bearing force provided by the post stub flange plate, P was the total prying force (P_3 and P_4) between the collar angles when they were in contact, and G_U was the total frictional resistance of the guide plates G_1 and G_2.

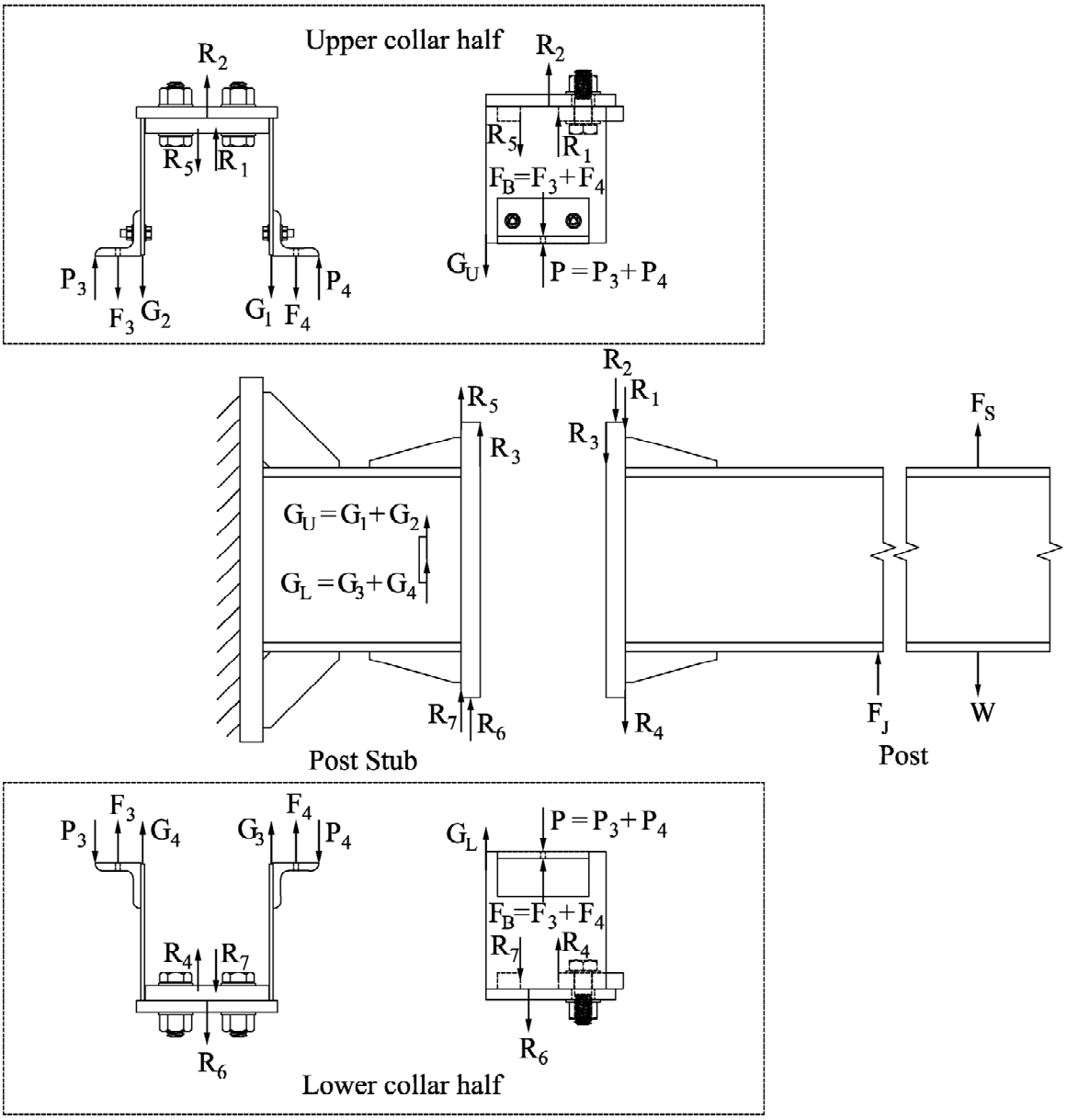

Figure 7-27. Free-body diagram of the post components with only lateral loads shown

Replacing the sum of frictional resistance R_1 and bearing force R_2 in equation 7-3 with the right hand side of equation 7-4 produces the following equation:

$$F_J = (W - F_S) + F_B - P + R \tag{7-6}$$

where $R = R_5 + R_3 + R_4 + G_U$ is referred to as the frictional connection resistance.

For the "no post restraint" and "post pinned at fuse plate" configurations, in which the lifting force was equal to the post self-weight, the equation above simplifies to:

$$F_J = F_B - P + R \tag{7-7}$$

7.5.2 Test Results

Results from the eighteen shear tests that were conducted (with three-post configurations and two friction conditions) are presented and discussed in this section. In each test, the breakaway connection was considered to have failed when either one of the two collar connector bolts broke. The jack load that was required to fail the connection was denoted the experimental shear strength. Test identification was designated in the following format:

Test configuration-Friction condition-Test number

where test configurations were denoted as PN for "post pinned at fuse plate", NR for "no post restraint", and ZM for "zero moment at breakaway connection"; friction conditions were denoted as BS for "bare steel" and TE for Teflon; test number for each type of test configuration and friction condition was denoted by a 2-digit number.

Figure 7-28 shows results of the total measured connector bolt force with respect to the applied jack load of the three shear tests with the "no post restraint" configuration and the "bare steel" friction condition. A line of equality, where total bolt force equals jack load, is also plotted for reference. This line represents the condition in which the connection is frictionless and components are rigid. It is observed that the experimental test traces have slopes that are less than (shallower than) the line of equality, indicating the presence of other sources of shear resistance separate from the connector bolts. The additional shear resistance developed from friction between various components of the connection. Up to a jack load of approximately 800 lbf (0.8 kip), the connector bolts carried virtually no load since the loading had not yet overcome the initial static frictional resistance generated by the axial load in the post and connection. Maximum jack loads required to fail the connection in the three tests varied from 17.8 kip to 19.3 kip, and all were much larger than the approximate total connector bolt strength of 6 kip. This behavior was attributed to frictional resistance caused by binding forces that were generated as a result of the applied jack load.

The total connector bolt force versus jack load results from the three shear tests with the "post pinned at fuse plate" configuration and the "bare steel" friction condition are plotted in Figure 7-29. Similar to the "no post restraint" configuration shown above, the connector bolts carried very little load until the applied jack load had overcome the initial frictional resistance. Figure 7-30 shows results of the binding force calculated from the measured jack load, the reaction at the pinned support, the lifting force, and post self-weight, using the equation:

$$F_{BD} = \frac{F_J L_J + (F_L - W) L_L - F_P L_P}{L_{BD}} \tag{7-8}$$

where F_{BD} and L_{BD} were the magnitude and moment arm of the binding force couple, F_J was the jack load, F_L was the lifting load, W was the post self-weight, F_P was the reaction at the pinned support, and L_J, L_L, and L_P were the distances from the connection slipping surface to

the jack load location, lifting load location (or post gravity location), and pinned support location, respectively (see Figure 7-26).

A negative computed binding force meant that the resultant moment at the slipping surface was opposite to the moment caused by the jack load (i.e., the moment at connection caused by the restraint was greater than that caused by applied jack load). Figure 7-30 also indicates that as binding forces grew larger, so did the jack loads that were required to fail the connection.

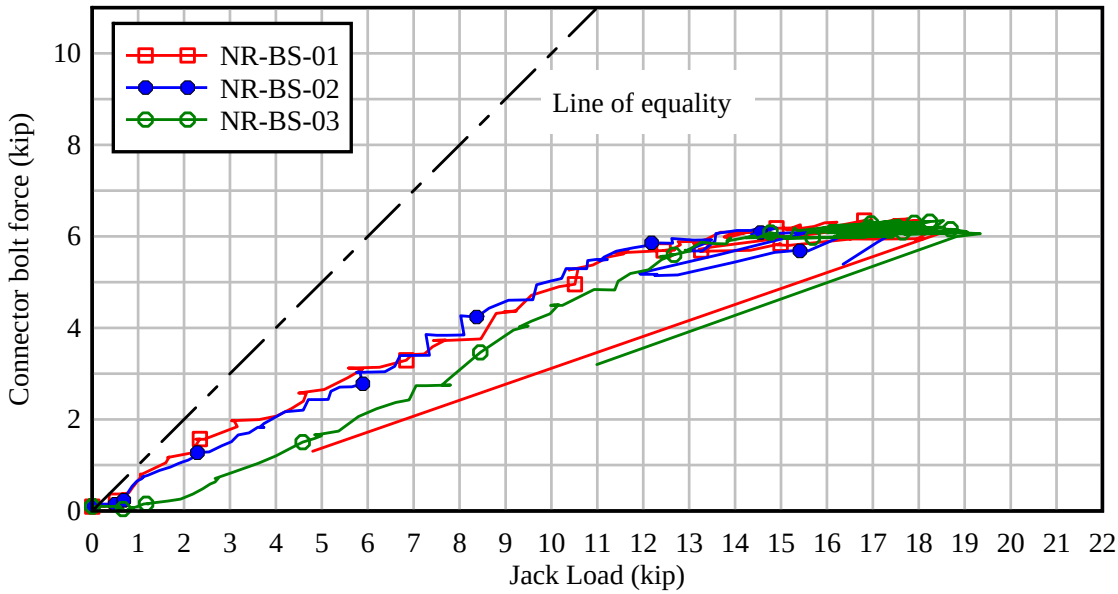

Figure 7-28. Total of connector bolt force vs. jack load under “no post restraint” configuration and bare steel friction condition

It should be noted that the post rotated counterclockwise about the connection in the “no post restraint” configuration but clockwise about the restraint in the “post pinned at fuse plate” configuration (Figure 7-31). In an actual two- or three-post sign structure, non-impact structural components will contribute a finite amount (not zero and not infinite) of restraint to the impacted post. Hence, the binding effect present in realistic sign structures will lie between the two bounding cases discussed here. Consequently, a lower SEISC can be expected than was measured in the “post pinned at fuse plate” case.

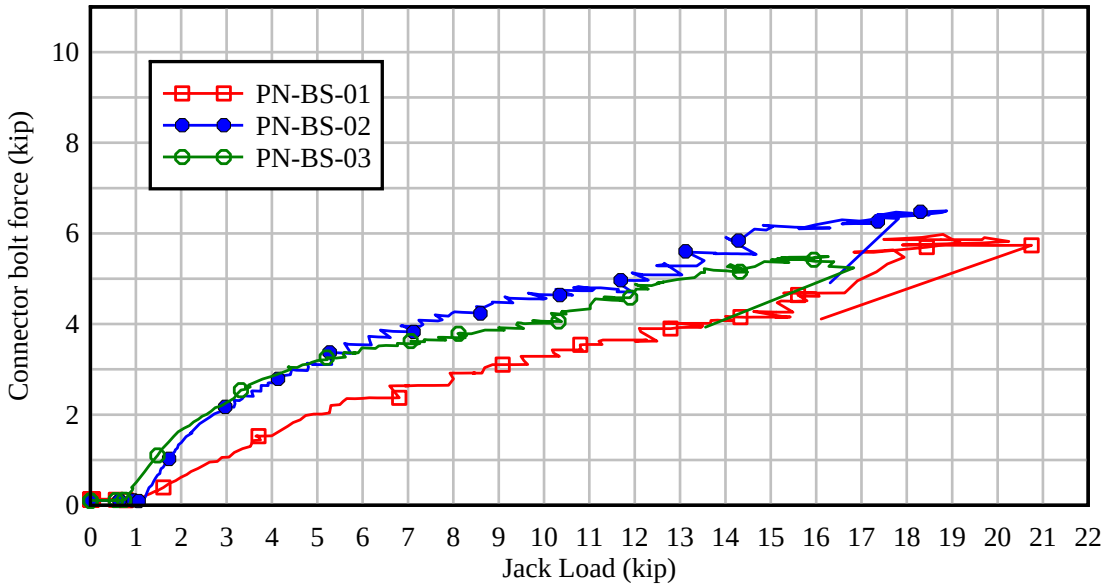

Figure 7-29. Total of connector bolt force vs. jack load under “post pinned at fuse plate” configuration and “bare steel” friction condition

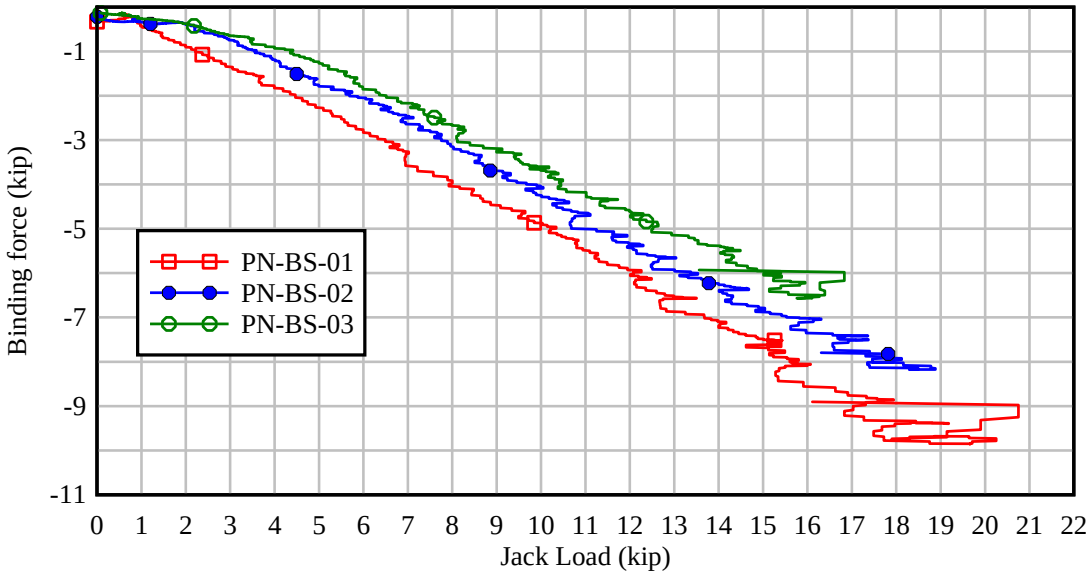

Figure 7-30. Binding force vs. jack load under “post pinned at fuse plate” configuration and “bare steel” friction condition

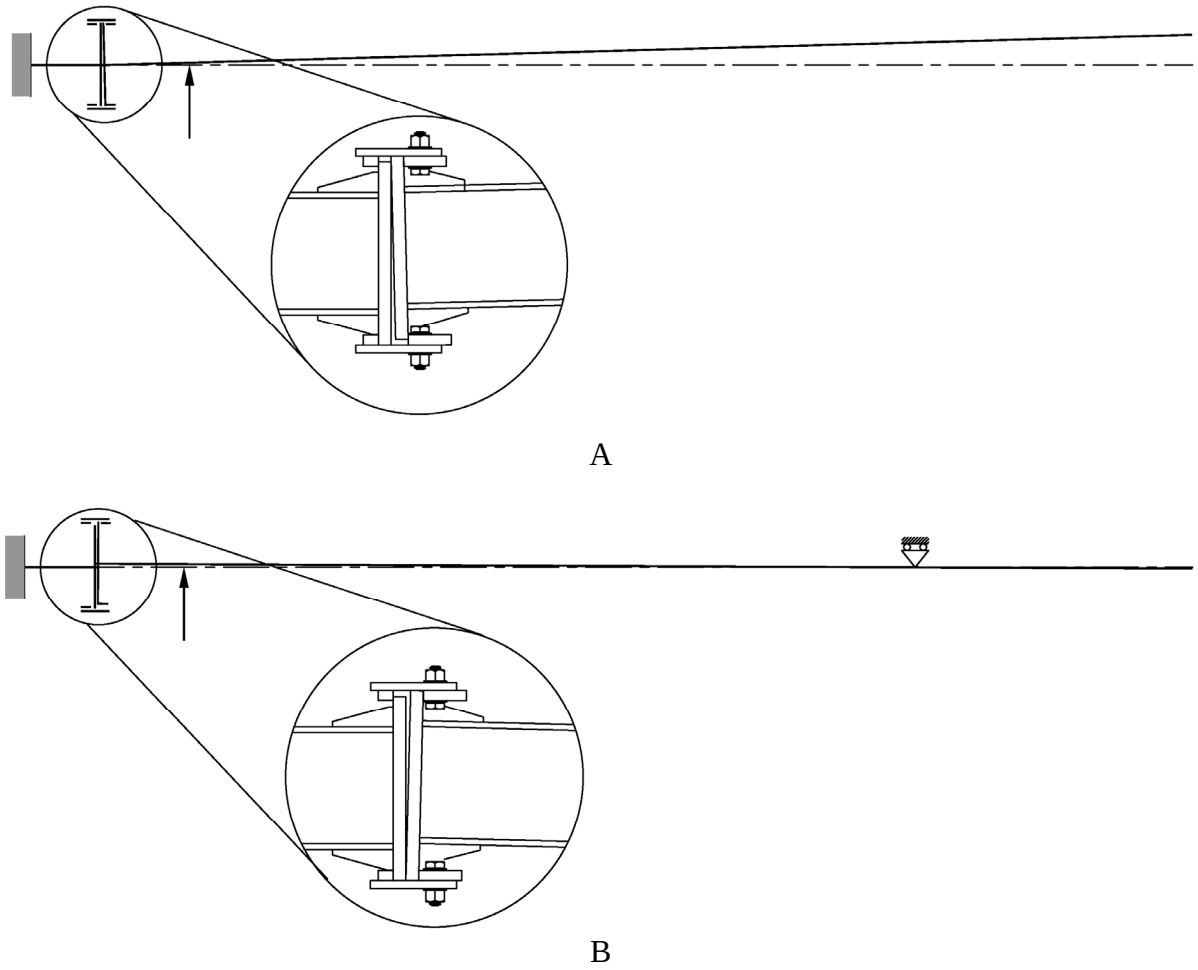

Figure 7-31. Post rotation (Side plates removed for clarity): A) Counterclockwise about connection in “no post restraint”; B) Clockwise about restraint in “post pinned at fuse plate”

A plot of total connector bolt force vs. jack load for the three shear tests with the “zero moment at breakaway connection” configuration and the “bare steel” friction condition are presented in Figure 7-32. Similar to the two test configurations above with the “bare steel” friction condition, the jack load also needed to overcome the initial frictional resistance of about 800 lbf (0.8 kip) before the connector bolts started carrying load. However, for this configuration, the slope of the traces are close to 1:1 indicating that jack load was approximately equal to connector bolt force total. Therefore, the load required to fail the connection was significantly reduced. The maximum jack loads from the tests were only 7.5 kip, 7.7 kip, and 7.8 kip. This was because the frictional resistance due to the binding force couple was eliminated. Moreover, at this “pure shear” loading condition, other sources of frictional resistance (between collar and flange plates; collar and guide plate) were also minimized since the flange plates were in flush contact.

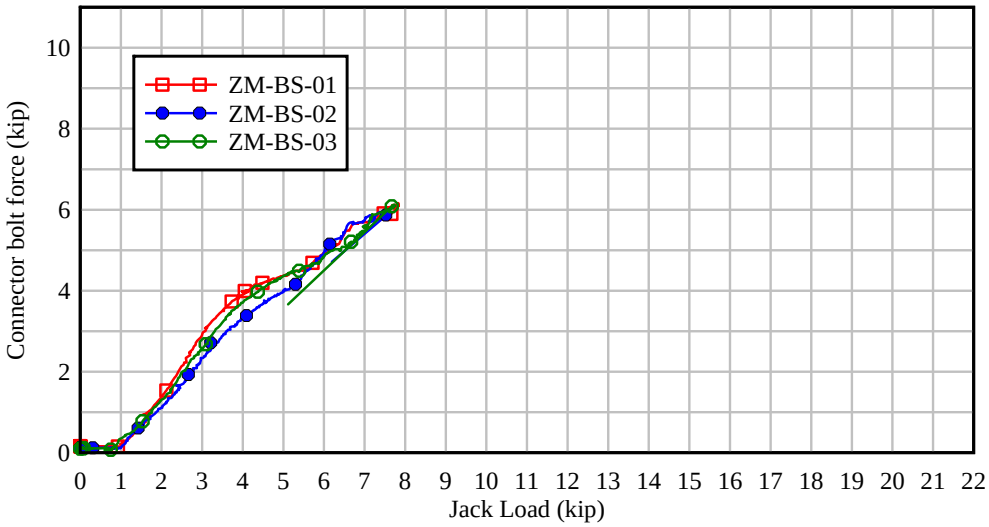

Figure 7-32. Total connector bolt force vs. jack load under the "zero moment at breakaway connection" configuration and "bare steel" friction condition

Measured total connector bolt force versus jack load from shear tests with the "no post restraint" configuration and the "Teflon" friction condition are presented in Figure 7-33. SEISCs obtained from these tests were close to the total of the connector bolt forces at failure as a result of the minimized frictional effects. By comparing the results with tests of the same configuration but with the "bare steel" friction condition, it is clear that improving the friction condition at the slipping surface, by using a Teflon sheet, reduced frictional resistance by more than 10 kip. Initial frictional resistance due to axial compression in the post and connection was also reduced, which is indicated by the fact that after overcoming the initial friction of approximately 350 lbf (0.35 kip) the connector bolts started carrying load.

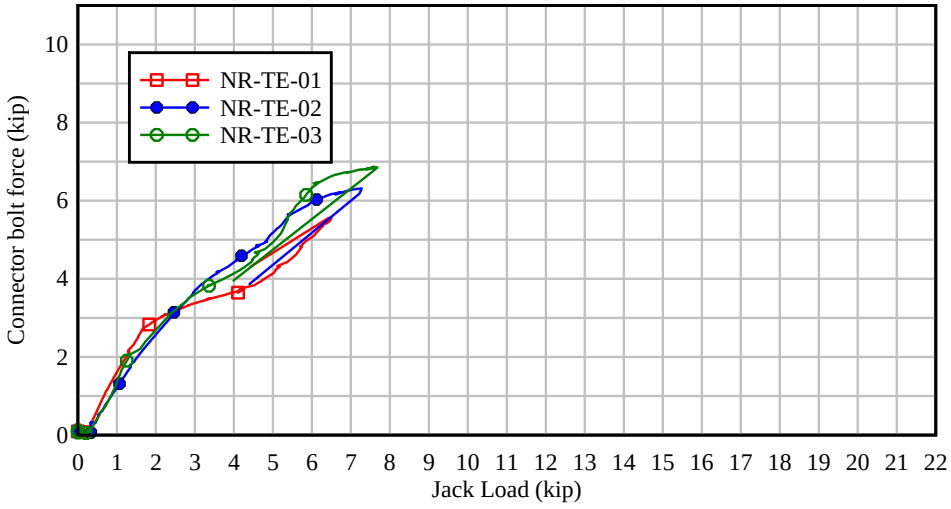

Figure 7-33. Total connector bolt force vs. jack load under the "no post restraint" configuration and the "Teflon" friction condition

Minimizing the frictional resistance at the slipping surface with Teflon also improved the desired frangibility of the connection in the "post pinned at fuse plate" configuration. In Figure 7-34, jack load and total of connector bolt forces are plotted against each other. A consistent decrease in SEISC, achieved by utilizing Teflon, was observed. For the same "post pinned at fuse plate" configuration, the connection SEISC was reduced from the range of 16.8 to 20.8 kip in the "bare steel" friction condition to the range of 7.5 to 8.7 kip in the Teflon friction condition. Initial friction results due to axial load were consistent and in agreement with results from the "no post restraint" configuration.

Connector bolt force and jack load relationship results from shear tests with the "zero moment at breakaway connection" configuration and the "Teflon" friction condition are shown in Figure 7-35. Characterized by two preferable conditions—no binding force couple, and minimized friction—these tests achieved a predictably low SEISC. Comparison of the SEISC values from these tests with corresponding values obtained under the same "Teflon" friction condition, but with different restraint/loading configurations, revealed only slight decreases in capacity. This indicates that the use of Teflon to reduce frictional forces also makes the post SEISC less dependent on the lateral stiffness of the non-impact structural components—a feature that will help ensure robust and predictable breakaway performance of the connection when integrated into an overall sign structure.

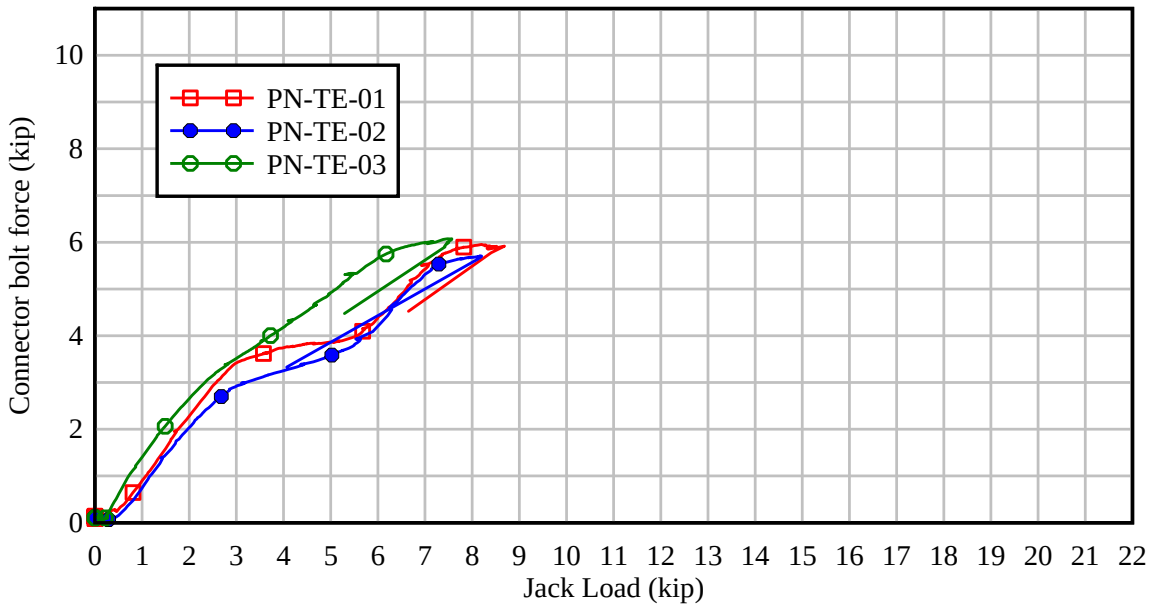

Figure 7-34. Total connector bolt force vs. jack load under the "post pinned at fuse plate" configuration and the "Teflon" friction condition

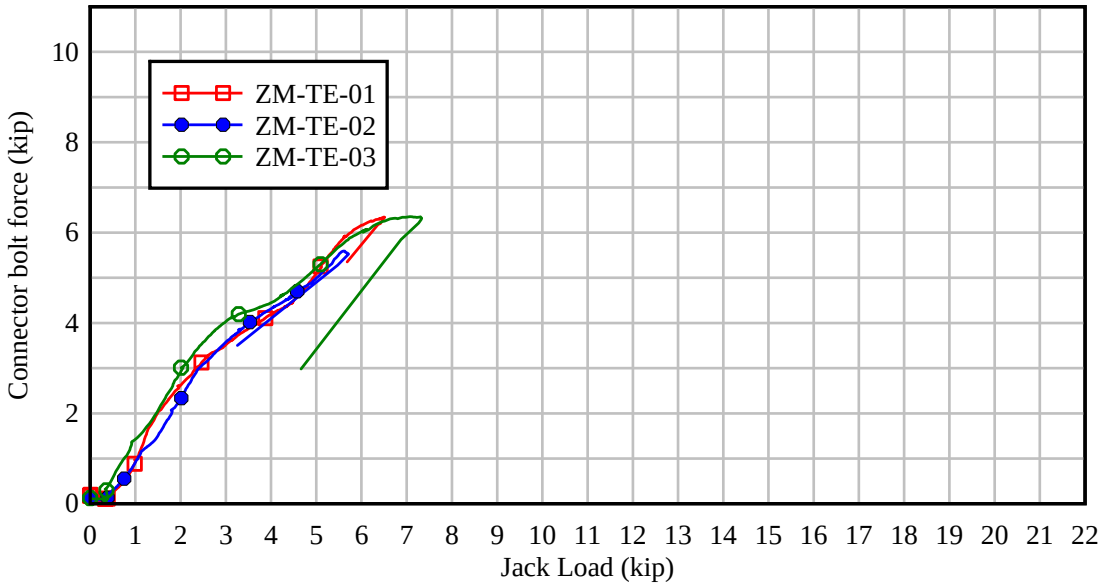

Figure 7-35. Total connector bolt force vs. jack load under the “zero moment at breakaway connection” configuration and the “Teflon” friction condition

Generally, the two collar connector bolts were not equally loaded during the shear tests. Test PN-TE-01 is selected to illustrate the connector bolt response. In Figure 7-36, the individually measured force in each connector bolt, along with total force, are plotted against the applied jack load. When jack force was applied, one connector bolt was loaded more rapidly than the other, due to tolerances in the fabrication of the connection collar. It is interesting to note that following initial yielding of the first bolt, the second bolt did not noticeably change its load carrying ratio with respect to the jack load. This means that the rate of total load application to the connector bolts became lower than the jack loading rate, as is indicated by the middle region of the total bolt force curve. This was attributed to a reduction of prying forces acting at the contact surfaces between the collar angles that were associated with the first bolt to yield.

When the jack load continued to increase beyond yielding of the first connector bolt, the collar angles gradually separated. It can be seen in Equation 7-7 that if the connection resistance (R) is negligible, as the prying force on the side of the first connector bolt is reduced, the jack load must overcome the loss of the prying force before it can load the connector bolts further. After the loss has been compensated for, the force in the second bolt would rise until both bolts were equally loaded. Failure would occur when the strain level in the bolt that yielded first reaches the limiting failure strain. Although the prying force (P) was not measured in the test program, its magnitude can be larger than the connection resistance in the Teflon sheet friction condition. This is evident in Figure 7-36 where in the primary loading stage (within the elastic range of the connector bolts) the rate of increase of total connector force was greater than the jack loading rate.

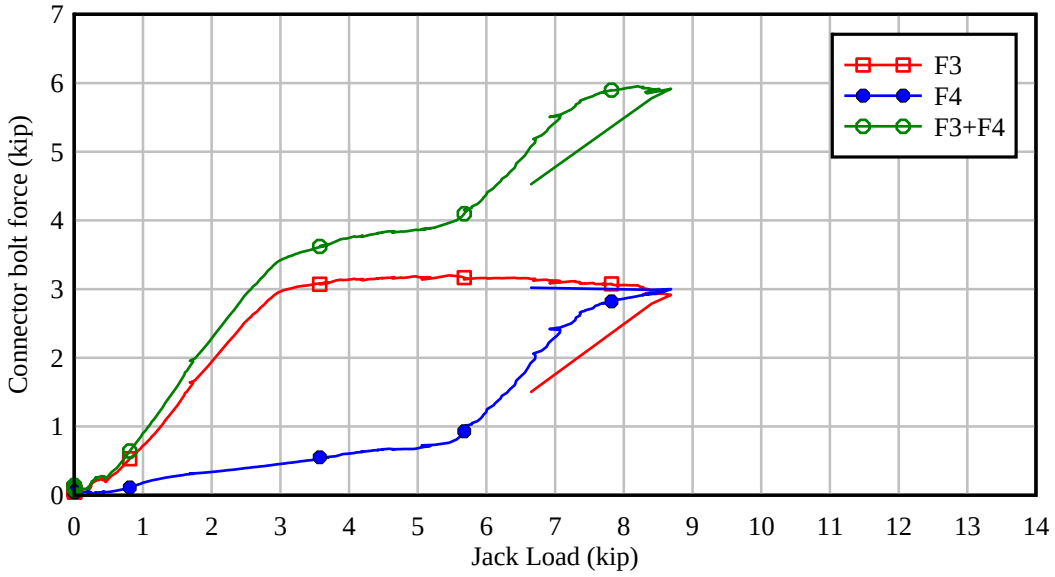

Figure 7-36. Connector bolt responses of the shear test with the "post pinned at fuse plate" configuration and the "Teflon" friction condition

The reduction in friction achieved by utilizing Teflon can be observed in the post slip response—relative displacement of the post with respect to the post stub—as a function of jack load. Post slip was computed from data recorded by LVDT D5 and D6 using the following equation:

$$PostSlip = D_6 - D_5 - \frac{D_5}{L_{D5\_sp}} L_{D5\_D6} \tag{7-9}$$

where D_5 and D_6 were the measured displacements of the post stub and the post (near the slipping surface) by LVDT D5 and D6, respectively, L_{D5_sp} was the distance from D5 to the support, and L_{D5_D6} was the distance between the LVDTs.

In Figure 7-37, 7-38, and 7-39, post slip versus jack load responses are plotted for three test types. Each figure shows results for the bare steel and the Teflon friction conditions. It is evident that with Teflon application, post slip values were greater for the same jack load level. The post slip vs. jack load curves generally had three distinguishable phases: non-slip, fast-slip, and bolt loading. The non-slip phase was characterized by a load level below the frictional resistance caused by axial load (in-service gravity representation). As applied loads exceeded initial resistances, the post slipped significantly (up to approximately 0.2 in.) with a correspondingly very low increase of jack load. This was primarily attributed to the slip of the bolted collar angles with respect to their collar side plates as a result of using slotted holes for the bolted connection of these components. Afterward, loading of the connector bolts increased. During this stage, the post continued to slip because the slip distance was still smaller than the available slotted length and due to the extension of the connector bolts. With the exception of the last phase (bolt loading) of the bare steel friction condition of the "no post restraint" and the "post pinned at fuse plate" configurations, the post did not slip during significant jack loading

(due to friction caused by the binding forces). It should be noted that in the bolt loading phase, both connector bolts and friction generally contributed to the shear resistance.

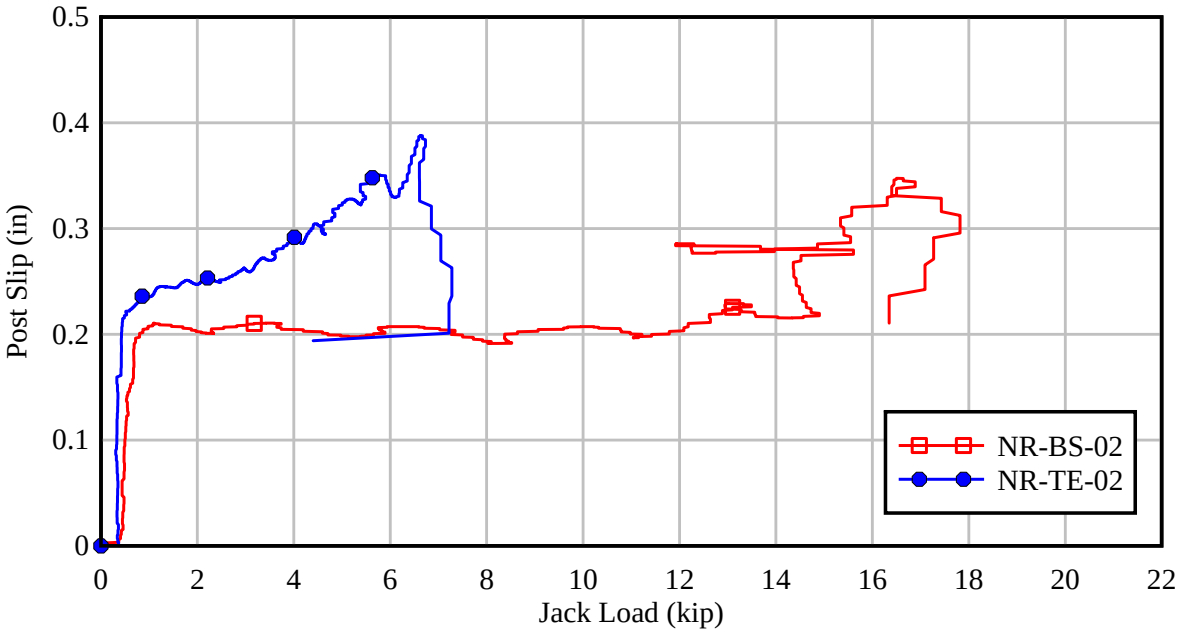

Figure 7-37. Post slip vs. jack load of the “no post restraint” configuration

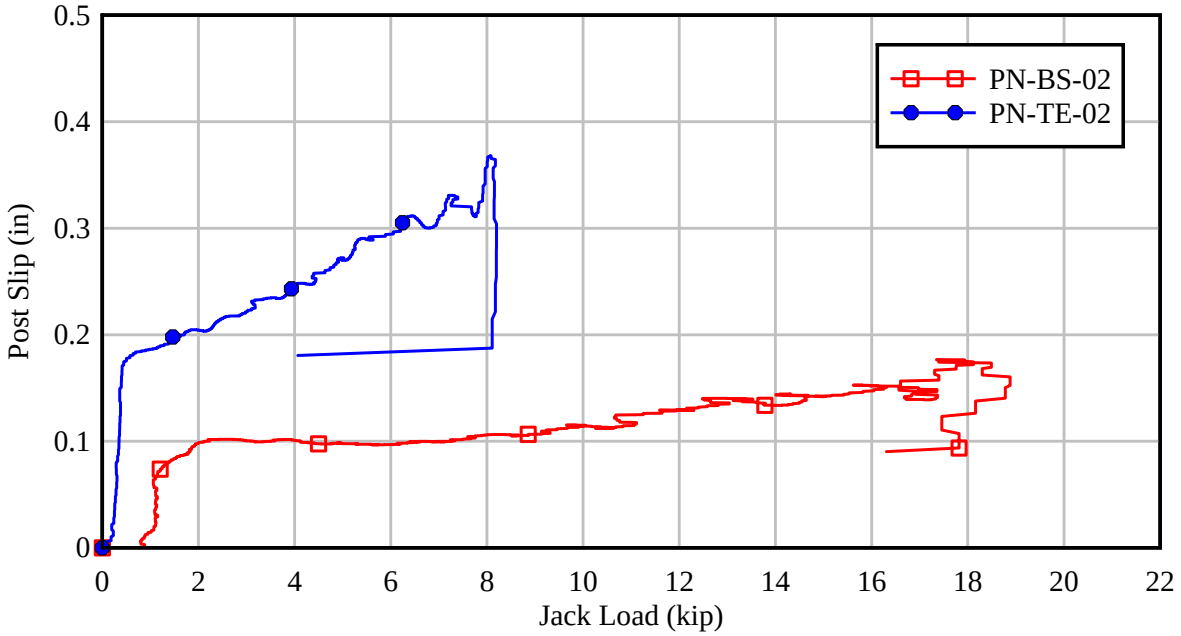

Figure 7-38. Post slip vs. jack load of the “post pinned at fuse plate” configuration

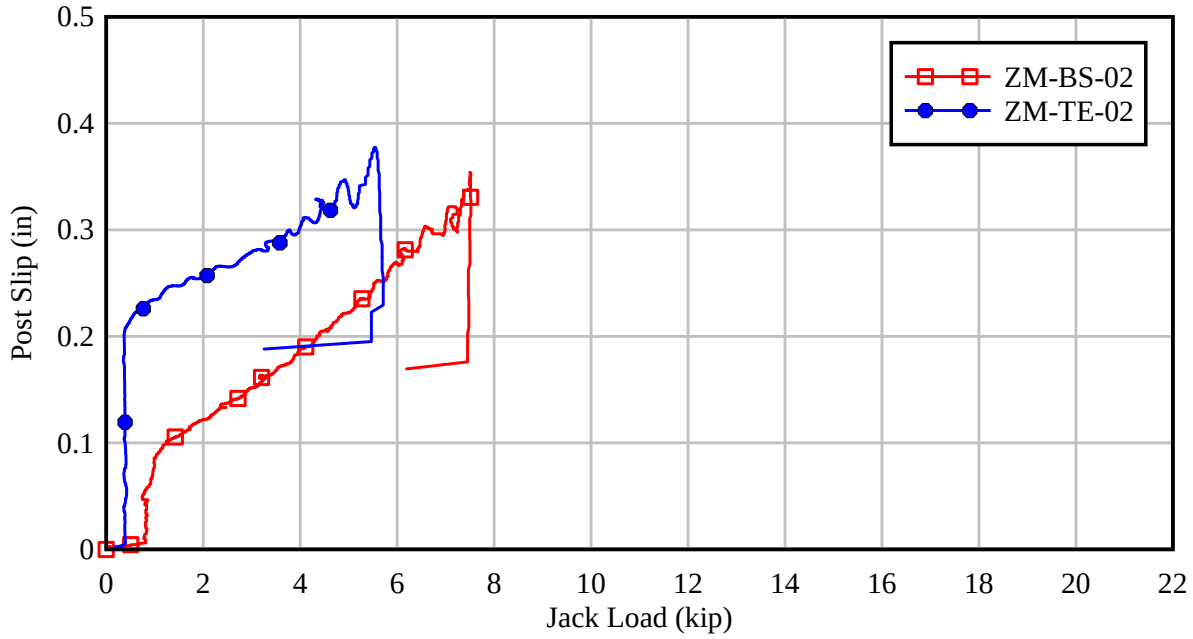

Figure 7-39. Post slip vs. jack load of the "zero moment at breakaway connection" configuration

Experimental results, determined by jack forces at connector bolt failure, are summarized in Figure 7-40. Average capacities for each test type are shown in Figure 7-41. For each friction condition, there was no marked difference of capacity (SEISC) between the "no post restraint" configurations and the "post pinned at fuse plate" configuration, even though resultant moments causing additional frictional resistance at the connection in these two configurations were opposite in sign. Since these configurations represent the limits of lateral stiffness of non-impact sign structural components, the maximum SEISC from shear tests of these configurations can serve as the upper limit of impact shear capacity of the breakaway connection integrated into a multi-post sign structure. Lower SEISCs obtained from the "zero moment at breakaway connection" configuration tests indicate that the experimental SEISC deviation from the design shear strength was primarily due to the frictional resistance caused by moment at the slip base. While it is not practical to achieve a "zero moment" condition for an in-service breakaway connection subjected to impact, the undesirable effect of the moment at the slip base has been adequately reduced by introducing Teflon at the slipping surface (as is demonstrated in the experimental results for tests with the "Teflon" friction condition, Figures 7-40B and 7-41).

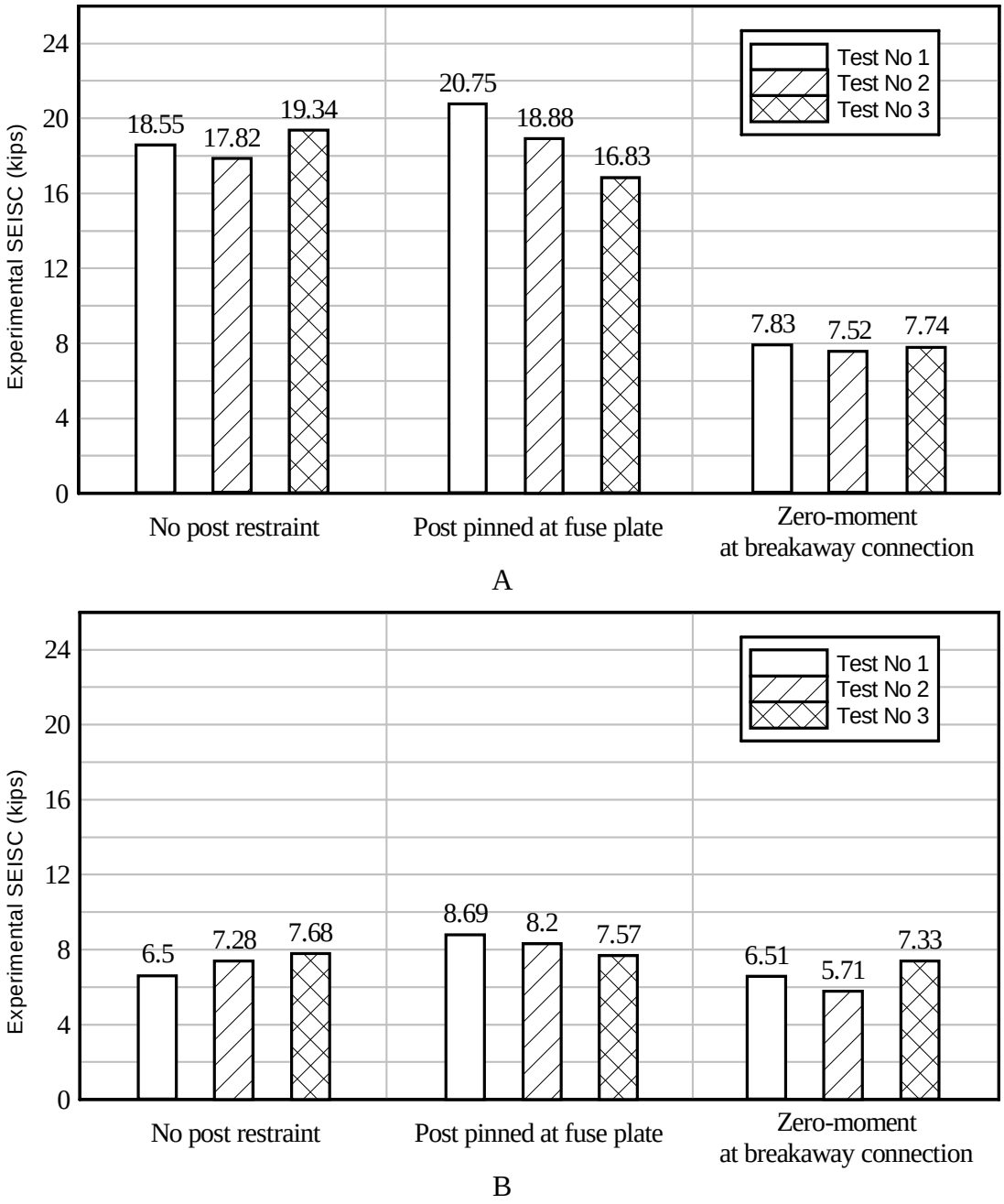

Figure 7-40. Experimental static equivalent impact shear capacity of breakaway connection: A) "Bare steel" friction condition; B) "Teflon" friction condition

Figure 7-41 shows that the shear-controlled moment collar connection with Teflon is capable of producing a shear capacity low enough to enable activation of the expected breakaway mechanism under impact loading. Specifically, the maximum experimental SEISC was 8.15 kip, which is lower than the impact loads—approximated as ranging from 12.5 kip to 72 kip—that were predicted by numerical simulation per NCHRP 350 (described in Section 6.8).

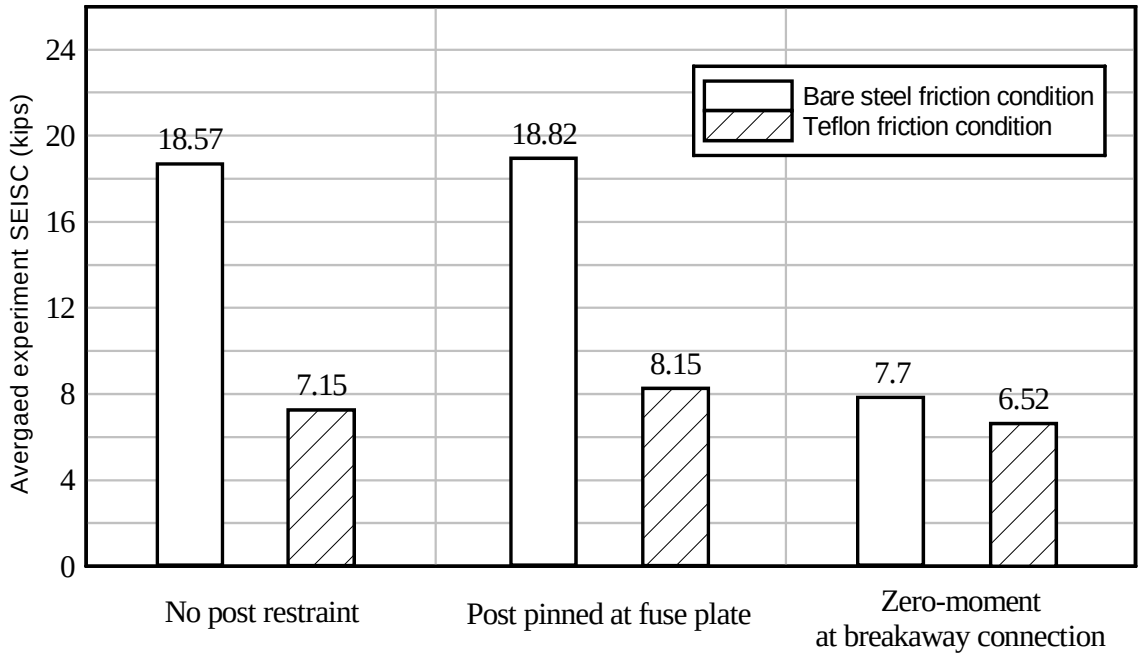

Figure 7-41. Average experimental static equivalent impact shear capacity of breakaway connection

The total strengths of the connector bolts, as measured during the shear tests, are shown in Figure 7-42. The average total connector bolt strength was 6.1 kip, which was about 8% higher than that determined from the direct connector bolt tests (section 7.2). The deviation was attributed to difference in bolt loading conditions in the shear tests and the connector bolt tests, especially near the ultimate bolt capacity stage when prying and inward bending of the collar side plates was considerable.

SEISC of the breakaway connection was governed by connector bolt strength and frictional resistance in the connection. Since significant frictional resistance is detrimental to the frangibility of the shear-controlled moment collar connection, and since connector bolts are necessary for structural adequacy against wind load, an experimental SEISC (of the overall connection) that is as close as the combined strength of connector bolts is desirable. Therefore, the difference, and ratio, between the experimental SEISC and the combined (total) strength of connector bolts are good indicators of effectiveness of the connection design.

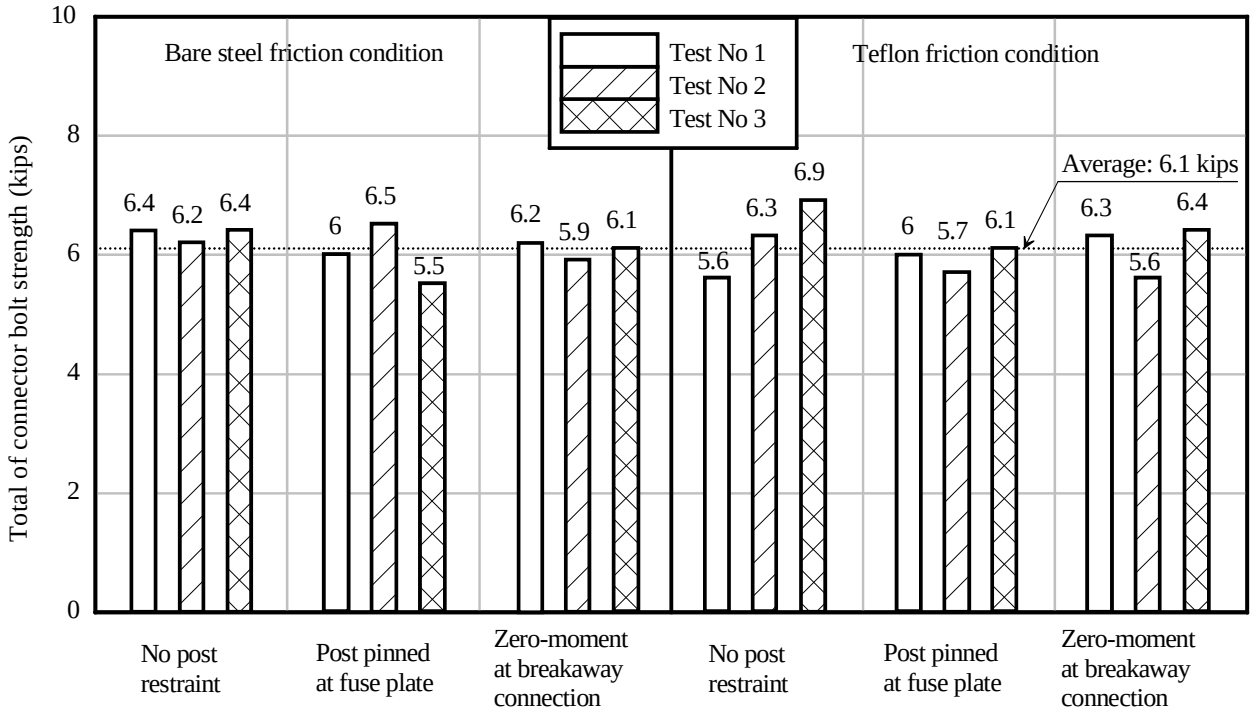

Figure 7-42. Total connector bolt strength

Average differences between experimental SEISC and the total strength of the connector bolts are shown in Figure 7-43. It is evident that differences were minimized as a result of using Teflon. For the selected connector bolts, the maximum difference was reduced from 12.83 kip (corresponding to bare steel friction) to only 2.24 kip. It should be noted that the differences that are plotted were computed as the connection resistance (R) minus the prying force (P), as defined in the equations 7-4, 7-5, and 7-6. In Figure 7-44, the average ratios of experimental SEISC and total strength of connector bolts are presented. The figure suggests that the SEISC of a breakaway post in a multi-post sign structure, with bare steel friction condition, could be as high as 3.15 times the total strength of connector bolts. However, when Teflon sheets are used in the connection, the SEISC is no more than 1.38 times the total strength of connector bolts.

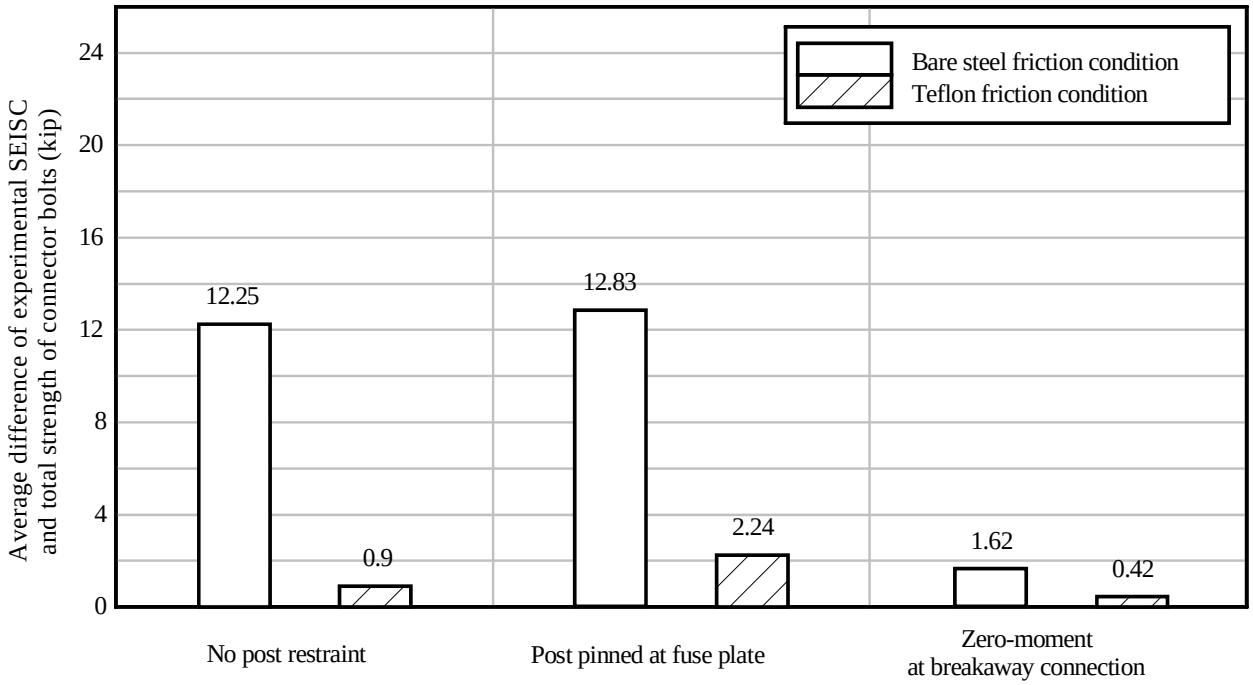

Figure 7-43. Average difference of experimental SEISC and total strength of connector bolts

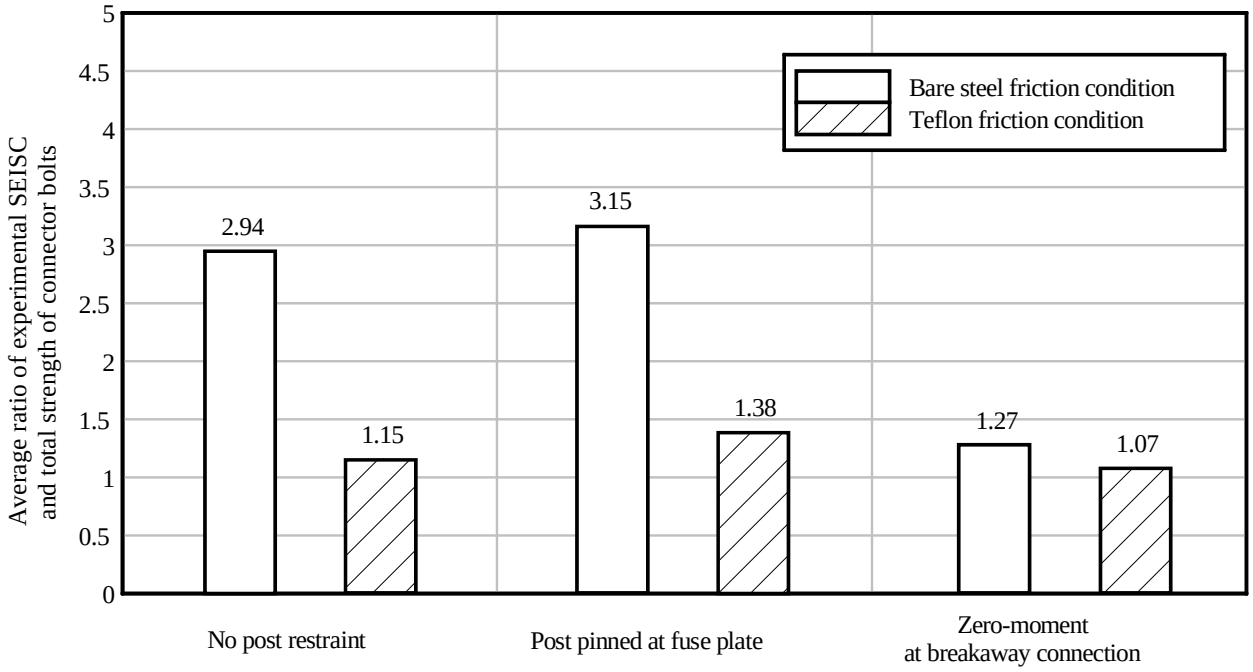

Figure 7-44. Average ratio of experimental SEISC and total strength of connector bolts

7.6 Static Moment Test Configurations and Results

7.6.1 Test Configurations

The purpose in conducting static moment tests was to determine ultimate flexural capacity of the breakaway connection as it related to wind load. In Figure 7-45, the moment test setup is presented.

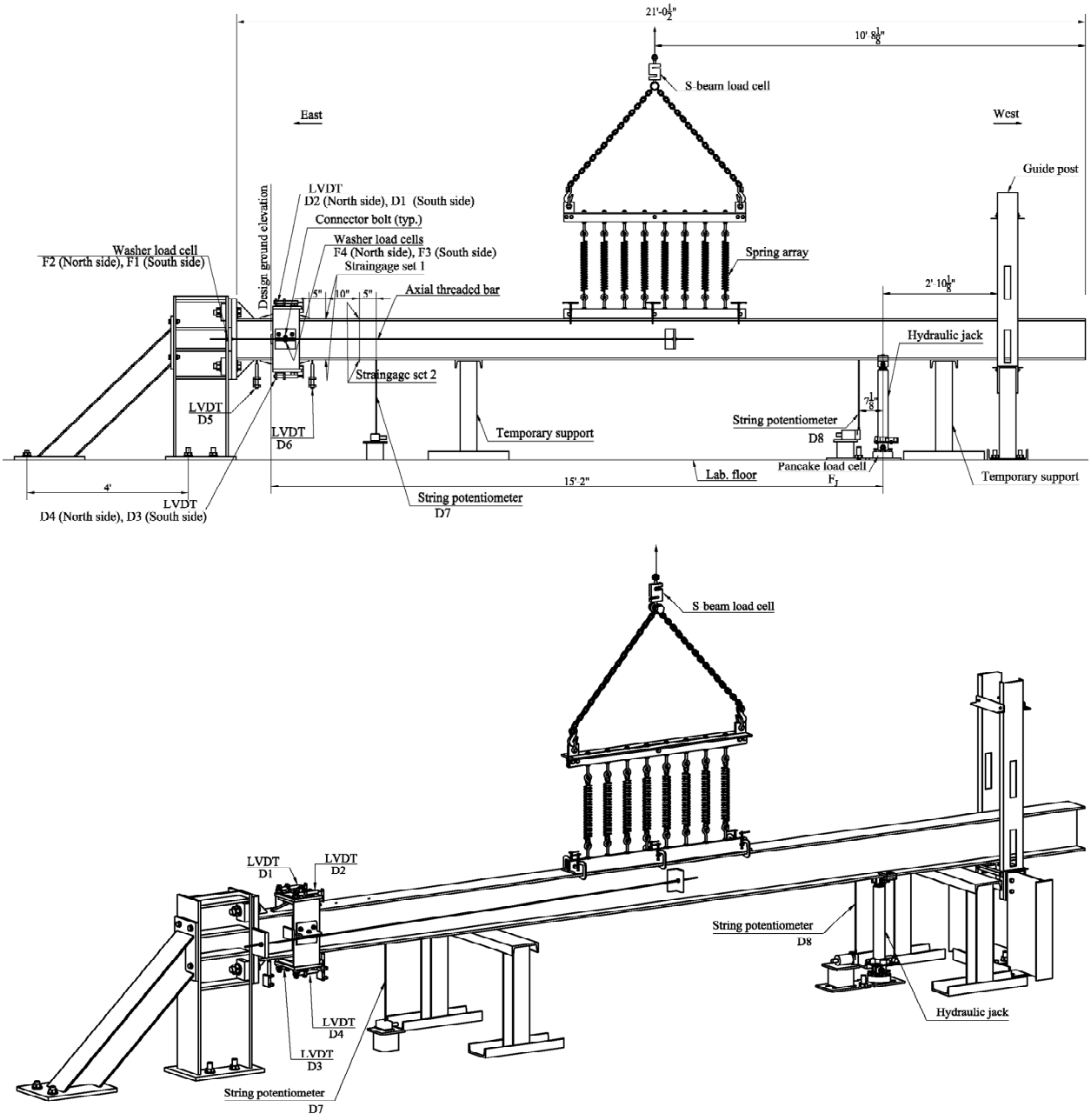

Figure 7-45. Moment test setup

Jack load was applied at 15 ft - 2 in. from the theoretical ground elevation. This location was selected based on the design wind loading condition and the spacing of strong floor anchor points. The distance was less than 5% different from the moment arm of the resultant wind load on the post (15 ft - 8.83 in.; sign panel tributary load and load directly applied to the post itself). Therefore, the test setup was reasonably matched to the design wind loading condition.

Four moment tests were conducted in the study. The same post and collar used in previous shear tests were employed in the first two moment tests (Test #1, Test #2). However, in the last two tests (Test #3, Test #4), the collar was modified by adding external stiffeners to the primary plates. Collar halves before and after modification are illustrated in Figure 7-46. The design change was made based on test results obtained from Test #1 and #2. Detailed collar behavior will be discussed later in the test results section. In addition to using a large Teflon sheet between the flange plate surfaces of the breakaway connection, finite element simulations of the connection under high-speed impact loading of a small vehicle (under NCHRP 350) revealed that it was also desirable to use Teflon sheets between the moment collar and the flange plates (see Figure 7-47) to further decrease (improve) occupant impact velocity. Consequently, this configuration of Teflon was employed in all static moment tests except for Test #4 (in which case only a single large Teflon sheet was used between the flange surfaces).

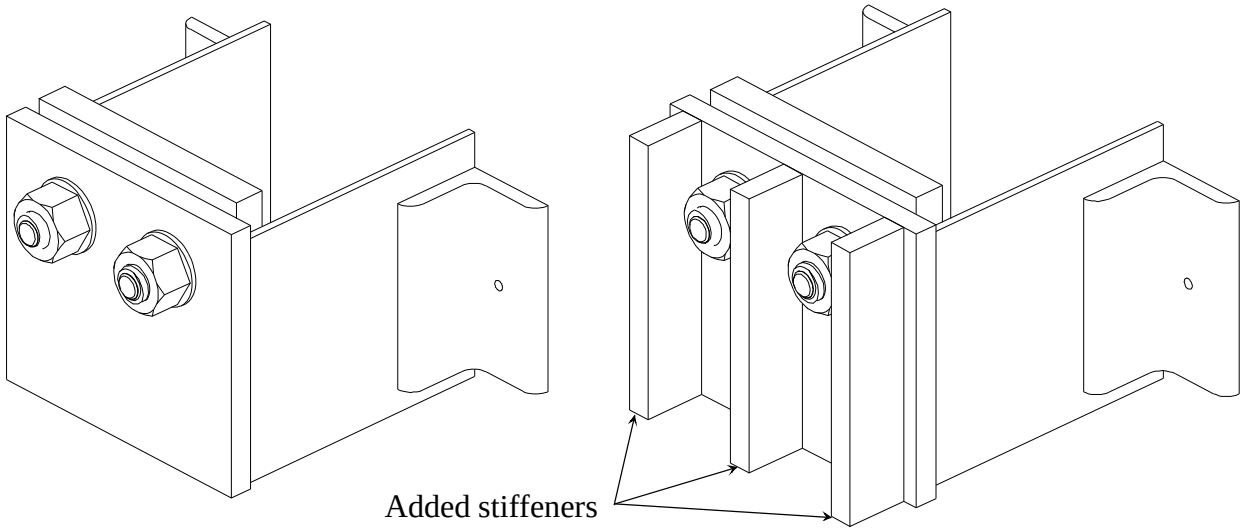

Collar half for Test #1 and #2 Collar half for Test #3 and #4

Figure 7-46. Collar half before and after design modification

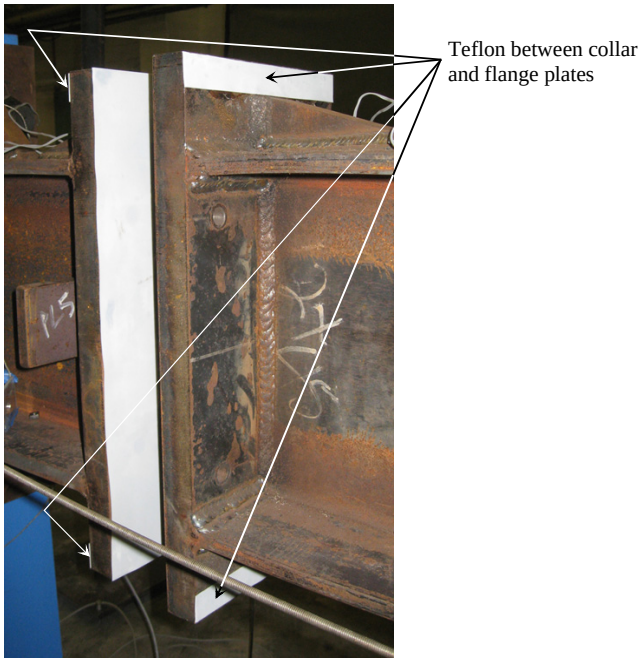

Figure 7-47. Multiple Teflon sheet application

The moment test procedure was similar to that of the shear test procedure in the "no post restraint" configuration. Prior to jack loading, a lifting force was applied to cancel out the post lateral self-weight and was maintained constant afterward. The axial threaded bars, however, were not pre-stressed but instead kept at virtually zero force. Not using axial prestress ensured a conservative determination of connection flexural capacity since frictional resistance was maintained at a level well below that which would be present (due to gravity and sign self-weight) in normal field-installed conditions. Moment tests were performed by loading the post end until connector bolt failure. Up to the maximum jack load, the applied load was increased at an approximate loading rate of 30 lbf/sec. Each test lasted less than 10 minutes and the maximum jack load was generally reached within the first 5 minutes of the loading duration.

7.6.2 Moment Capacity Determination

Under wind loading, the moment at ground level is the largest moment that the system carries. Therefore, the structural posts were designed based on the ground moment induced by the design wind load. With the introduction of the breakaway connection, it was important to ensure that the breakaway post system still had a moment capacity exceeding the wind induced moment at ground level. The moment capacity of the breakaway post system was determined independently from jack loading and from moments computed at each strain gauge set location. Performing multi-channel measurement of the moment capacity enhanced the reliability of the moment capacity results. In Figure 7-48, free body diagrams for moment capacity determination at the theoretical ground elevation are presented.

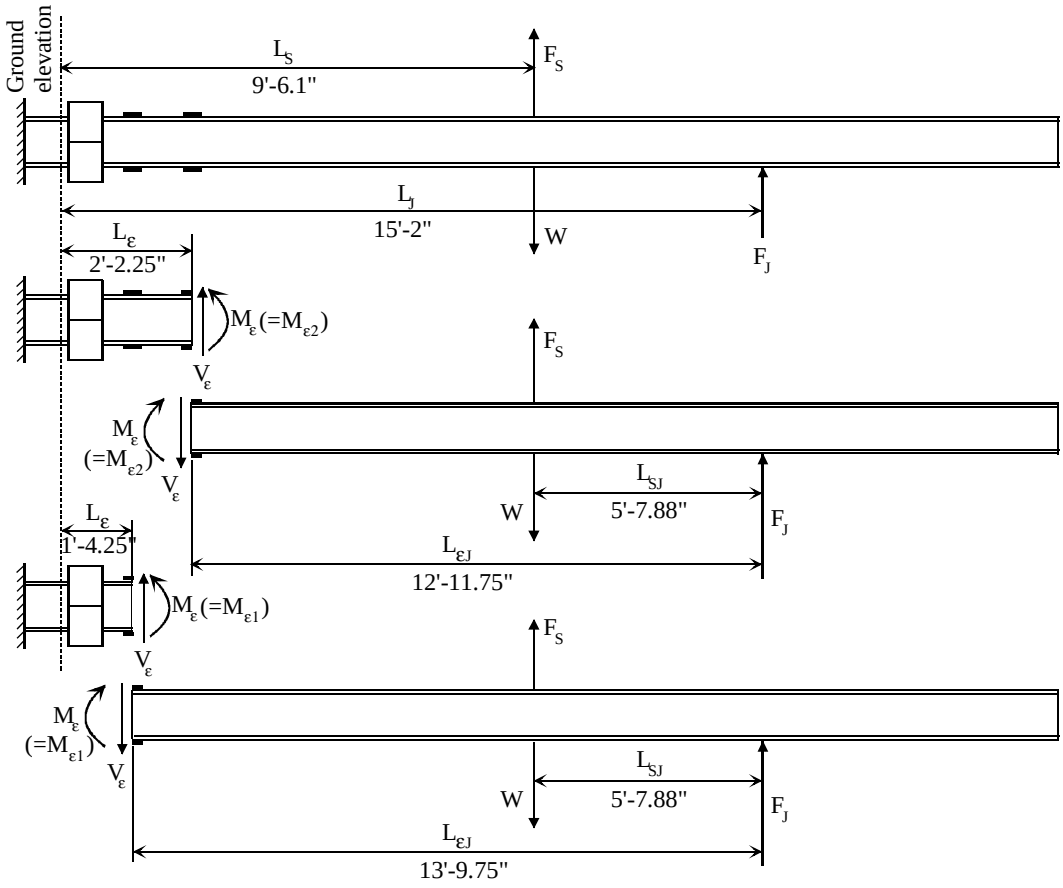

Figure 7-48. Post free-body diagrams for determination of moment at ground level

Although the lifting force was maintained reasonably constant throughout the loading process, it was still included together with the post self-weight in the moment capacity determination equation. From Figure 7-48, the moment at the ground level determined from jack load was computed as:

$$M_G = F_J L_J + (F_S - W) L_S \tag{7-10}$$

where F_J was the jack load, W was the post self-weight, F_S was the lifting force applied by the spring array, L_J was the distance from the jack load to the ground level, and L_S was the distance from the lifting load and post gravity to the ground level.

Moments at ground level (M_G), determined from the strain gauge sets, were calculated using the following equations:

$$M_\varepsilon = \frac{2\varepsilon E I_x}{d} \tag{7-11}$$

$$V_\varepsilon = \frac{M_\varepsilon + (F_S - W)L_{SJ}}{L_{\varepsilon J}} \tag{7-12}$$

$$M_G = M_\varepsilon + V_\varepsilon L_\varepsilon \tag{7-13}$$

where M_ε and ε were the moment and strain at the referenced strain gauge set, E was the Young's modulus of the post steel, I_x and d were the strong axis moment of inertia and height of the post section, V_ε was the shear force at the referenced strain gauge set, L_{SJ} was the distance from the lifting load or post gravity to the jack load, $L_{\varepsilon J}$ was the distance from the referenced strain gauge set to the jack load, and L_ε was the distance from the referenced strain gauge set to the ground level.

Determining moment at ground level from the measured jack load was a direct computation process, but it was also subject to variation due to slight changes in jack load direction as the post displaced and rotated. In contrast, moment determined from the strain gauges eliminates such possible issues. The latter method also minimized errors introduced as a result of possible shifting of the lifting load location as the post rotated.

7.6.3 Post Displacement Components

Since the stiffness of the breakaway post was characterized by the post displacement and jack load relationship, a string potentiometer (D8) was placed adjacent to the jack (offset 7.125 in. from the jack) to measure displacement. However, the displacement (D_8) reflected the combined displacement contributions from a variety of sources located between the support and applied load, such as the non-rigid support, deformation of the post, and the connection. Therefore, in order to better understand system behavior, in addition to direct measurement of post displacement (D_8), total displacement at D8 and its components (excluding crack and plastic deformation contribution discussed later) were also quantified in the vicinity of the connection and the load cell that recorded the applied load.

The first component was the displacement associated with post stub rotation. Since the bolted connection between the tested post and support fixture was not perfectly fixed, the post rotated about the upper tip of the base plate. In the Figure 7-49, a schematic of the rigid-body rotation of the post about the support is illustrated for determination of the displacement component at D8 due to post stub rotation. The displacement was calculated as:

$$D_{8\_sp} = D_5 + \frac{D_5}{L_{D5\_sp}} L_{D8\_sp} \tag{7-14}$$

where D_5 was the measured displacement by LVDT D5, L_{D5_sp} was the horizontal distance from D5 to rotation center, and L_{D8_sp} was the horizontal distance from D8 to the rotation center.

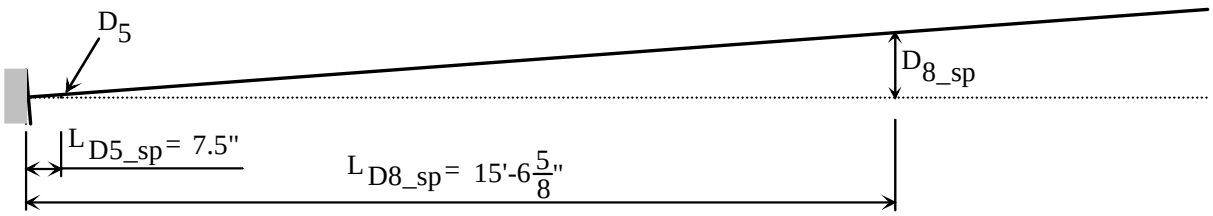

Figure 7-49. Post displacement due to flexible support

The second displacement component at D8 was associated with slip of the binding plate on the tension side of the connection. Since the binding plate was bolted to the primary plate through slotted holes (on the primary plate) that were designed to adapt fabrication tolerance, it was able to slip with respect to the primary plate. In Figure 7-50, a rigid-body diagram of the post rotation and slip of the binding plate are illustrated.

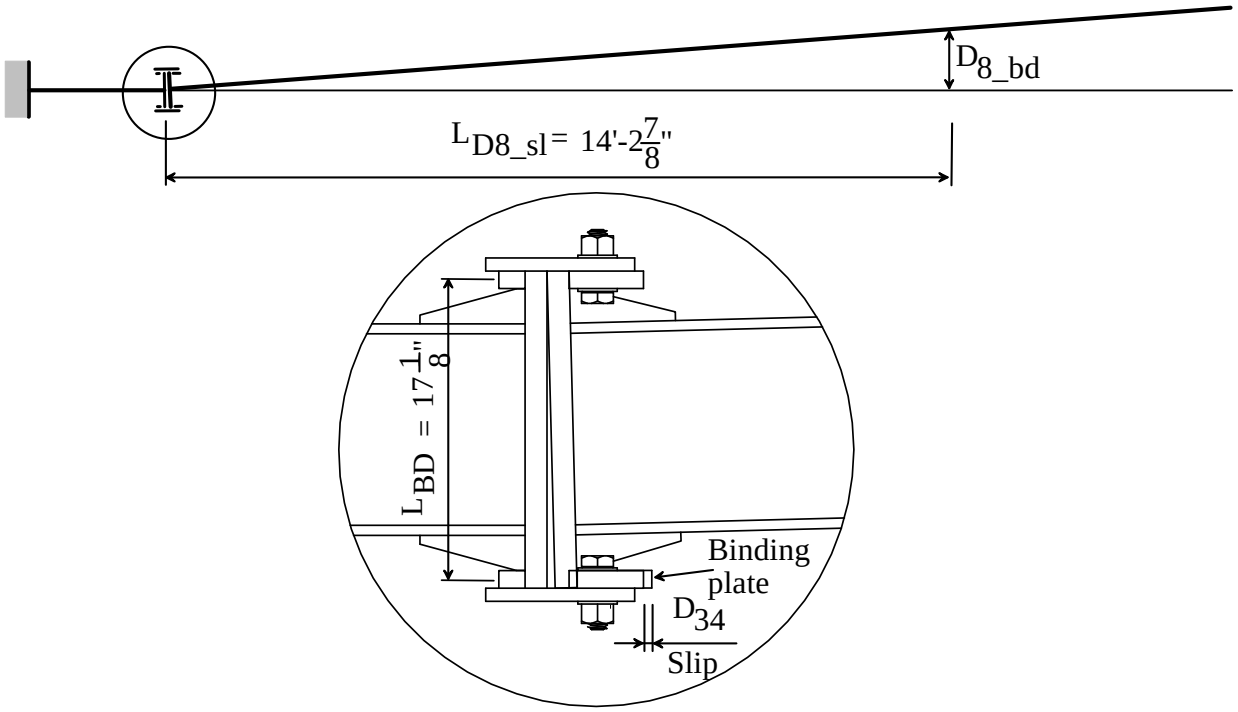

Figure 7-50. Post displacement due to slip of the binding plate (Collar side plates removed for visibility)

Post displacement at D8 due to the binding plate slip was computed by the following equation:

$$D_{8\_bd} = \frac{D_{34}}{L_{BD}} L_{D8\_sl} \tag{7-15}$$

where D_{34} was the average of the measured displacement of the binding plate by LVDT D3 and D4, L_{BD} was the moment arm of the binding force couple, and L_{D8_sl} was the distance from D8 to the slipping surface of the connection (contact surface of flange plates).

The third displacement component at D8 was the relative slip of the post with respect to the post stub (Figure 7-51). The displacement was calculated as:

$$D_{8\_sl} = D_6 - D_5 - \frac{D_5}{L_{D5\_sp}} L_{D5\_D6} - \frac{D_{34}}{L_{BD}} L_{D6\_sl} \tag{7-16}$$

where D_5 and D_6 were the measured displacements of the post stub and the post (near the slipping surface) as measured by LVDT D5 and D6 respectively, and L_{D6_sl} was the distance from D6 to the slipping surface.

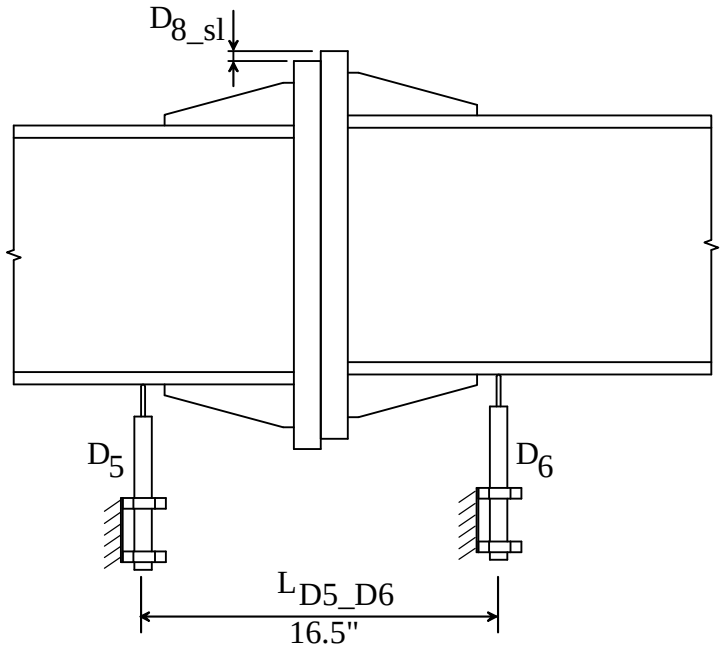

Figure 7-51. Post slip

The fourth displacement component was the elastic deflection of the post under applied load (Figure 7-52). The elastic deflection at D8 was computed as follows:

$$D_{8\_el} = \frac{F_J \left(L_{D8\_sp}\right)^2}{6EI_x} \left[3(L_{D8\_sp} + L_{D8\_j}) - L_{D8\_sp}\right] \tag{7-17}$$

where F_J was the jack load, L_{D8_sp} was the horizontal distance from D8 to the support, L_{D8_j} was the offset distance from the string potentiometer D8 to the jack, E was the Young's modulus of the post steel, and I_x was the strong axis moment of inertia of the post section. It was

assumed that I_x was constant for the entire deflected length of the system. Stiffeners at the connection and the base plates alter the section moment of inertia, but only over a very short length, therefore inclusion of these features would have little effect on the computed deflection.

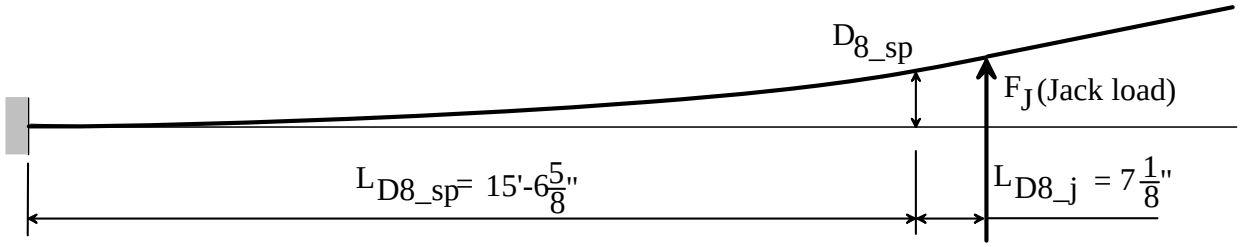

Figure 7-52. Post elastic deflection

Post displacement at D8 could then be calculated by summing all of the displacement components identified above as:

$$D_{8\_cal} = D_{8\_st} + D_{8\_bd} + D_{8\_sl} + D_{8\_el} \tag{7-18}$$

It should be noted that this calculated displacement was only valid when the post and collar components (except connector bolts) underwent small strain. Comparing the computed displacement to the directly measured displacement will be used later in this chapter to help in identifying when plastic deformation and cracking occurred during the moment tests.

7.6.4 Test Results

In Figure 7-53, time histories of the jack loads applied to the post are presented. Generally, jack loads were monotonically increased until maximum load levels were reached except during tests #2 and #3, in which jack loads were kept constant at certain levels for short periods of time (1 to 2 minutes). Low loading rates of approximately 30 lbf/sec were used to ensure that a static testing condition was maintained.

Flexural moments of the breakaway connection at the theoretical ground level were derived from three independent instruments: a load cell recording the jack load and two strain gauge sets located near the connection (Figure 7-45). Calculated moments are presented as time histories in Figure 7-54. It is evident from the plots that the moment results produced by the instruments agree very well for all moment tests conducted.

As discussed previously in the moment capacity determination section, in general, the flexural moments computed from strain gauge data had a higher level of accuracy than did moments computed from load cell data. However, the good agreement shown in Figure 7-54 indicates that errors due to displacement and rotation of the post were insignificant. Both strain gauge sets produced closely matched results over the entire loading process. Although strain gauge set 1 was located such that a complex stress state near connection stiffener tips had, if any, a negligible effect on the measured strain, the moment results from strain gauge set 2 were used for all later discussion since this set had a greater offset distance from the stiffeners.

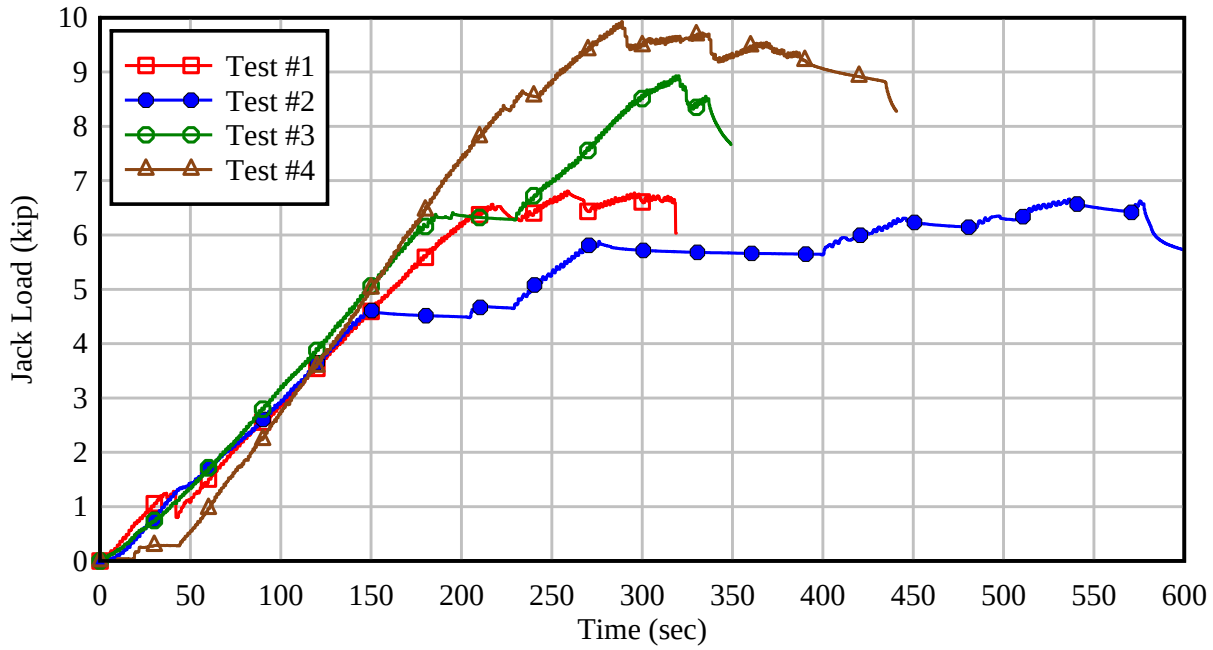

Figure 7-53. Time histories of jack loads applied to the post

The moment capacity of the breakaway post obtained from Test #1 was 105.6 kip-ft (Figure 7-54). This moment is slightly larger than the moment of 102.6 kip-ft (1231 kip-in, see Appendix A) at the ground level carried by a middle post (which is subject to the largest tributary wind load) caused by the design wind load acting on the sign structure (sign panel and posts). However, the AASHTO Highway Sign, Luminaire, and Traffic Signal Specifications require that the experimentally determined capacity be 1.5 times the nominally required capacity. The breakaway post was expected to reach a moment level of approximately (1.5)(102.6 kip-ft) = 153.9 kip-ft at which time yielding of the stiffening plates that connect the post to the flange plates, and connector bolt failure, were expected to occur. Instead, localized yielding of the collar primary plate on the tension side of the moment collar occurred. This local yielding (and nearby weld cracking) then led to connector bolt failure which subsequently allowed the two halves of the collar to separate (Figure 7-55).

In addition to visual detection, yielding of the primary plate manifested in the readings of the LVDTs monitoring the binding plate displacement. In Figure 7-56, displacement readings (D_1, D_2) of the upper binding plate at compression side and (D_3, D_4) of the upper binding plate at tension side are plotted against jack load. From the displacement curves of D_3 and D_4 in the plot, the effects of slip of the binding plate and bending of the primary plate were observed. Binding plate slip occurred at a low loading level (1 kip). As the jack load was increased, binding plate slip also increased. Meanwhile, an increase in the relative slip between the post and post stub accentuated eccentric loading of the binding force on the primary plate. Upon reaching the maximum slip, together with considerable bending moment in the primary plate, the displacement readings gradually decreased with jack load increase, as a result of binding plate rotation about the bending axis. After yielding of the primary plate, the jack load remained virtually constant whereas the binding plate continued to rotate until connector bolt failure. Displacement readings of the upper binding plate at the compression side, D_1 and D_2, were

negligible since that plate was on the compression side, therefore, no slip of the plate was expected.

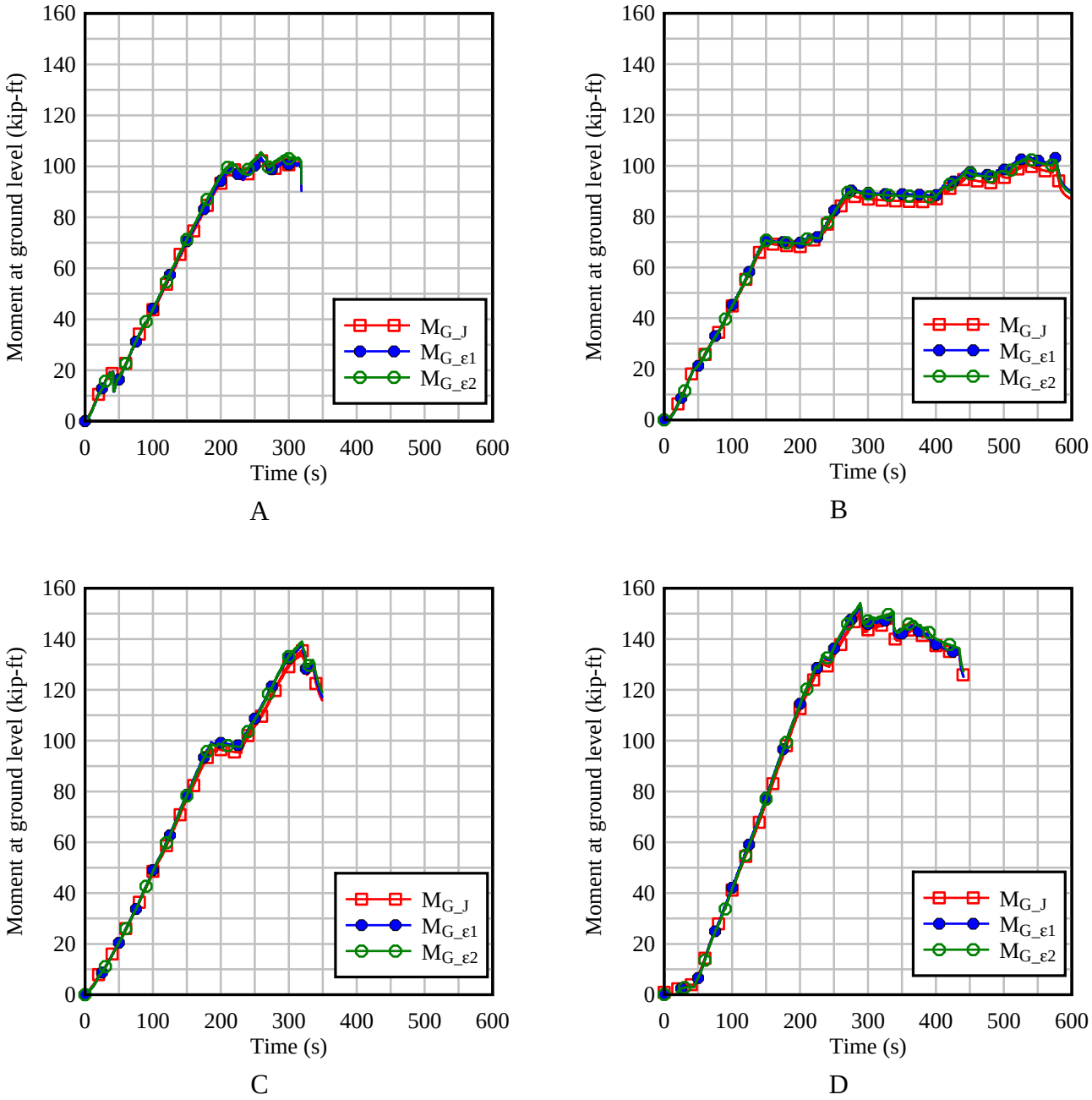

Figure 7-54. Time histories of flexural moments at ground level derived from the jack load, strain gauge set 1, and strain gauge set 2: A) Test #1; B) Test #2; C) Test #3; D) Test #4

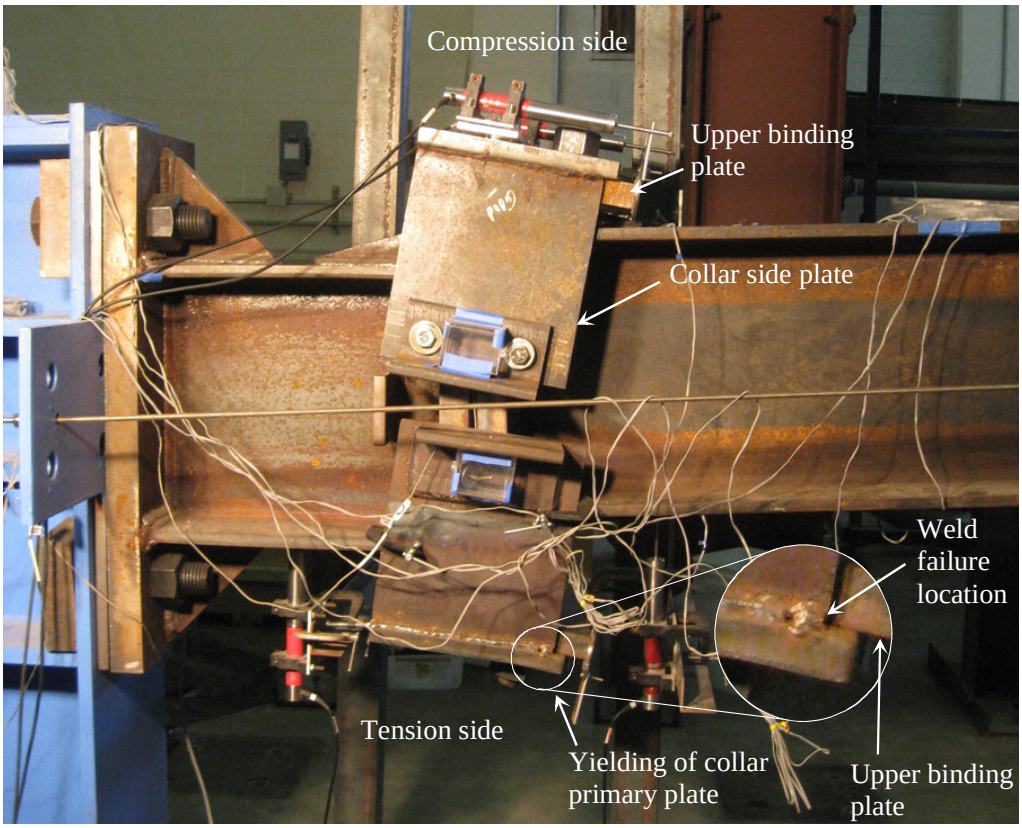

Figure 7-55. Connection failure in Test #1

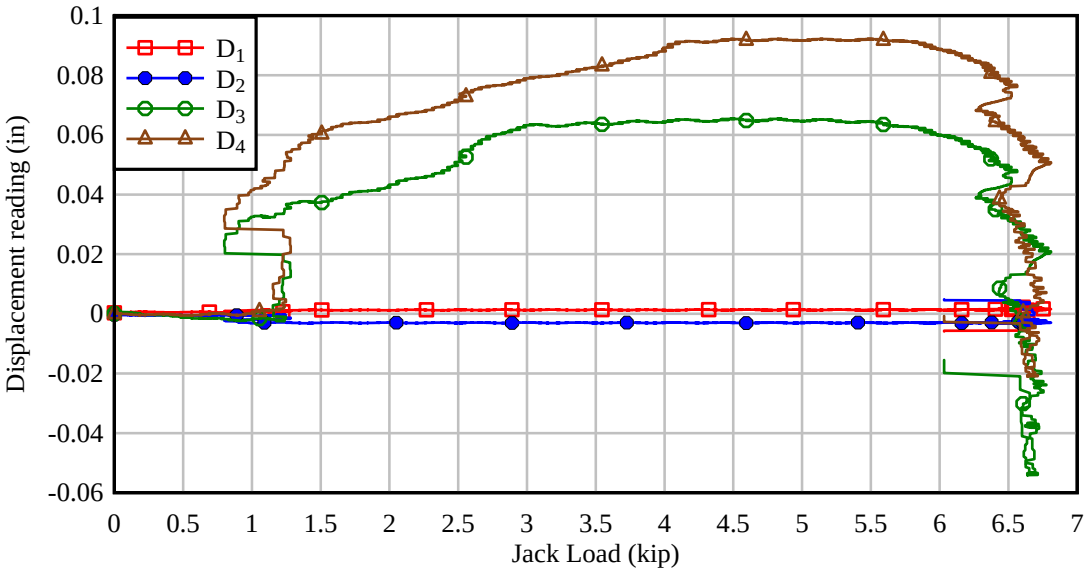

Figure 7-56. Displacement readings of LVDTs monitoring binding plate displacement (Test #1)

In Figure 7-57, the directly measured displacement D_8 (near the jack load) and the corresponding indirectly derived displacement components (see Section 7.6.3) are presented as time histories. It should be noted that the displacement component due to slip of binding plate (D_{8_bd}) was computed from LVDTs D3 and D4 up to their average maximum. When the average reading decreased, the average maximum was used because no additional slip of the binding plate relative to the primary plate occurred. It is evident that yielding of the primary plate significantly reduced the post stiffness, since, before eccentric bending of the primary plate occurred, the calculated displacement at the D8 location (D_{8_cal}) and directly measured displacement D_8 were in reasonable agreement. However, after bending and yielding occurred, the two curves increasingly deviated from each other as the effect of binding plate rotation was not included in the derived displacement (D_{8_cal}). Upon reaching the yield point, the post had been loaded to its maximum capacity. This is indicated in the constant portion of the elastic deflection curve D_{8_el} since the elastic deflection is proportional to the jack load. It was also observed that primary plate bending increased the slip rate of the post with respect to the post stub, therefore, the connector bolts were loaded to failure more rapidly. The displacement component $D_{8\_sp,}$ which was due to flexibility of the support and wsa therefore a characteristic of test setup—and not of the breakaway post itself—accounted for approximately 50% of the total measured displacement D_8.

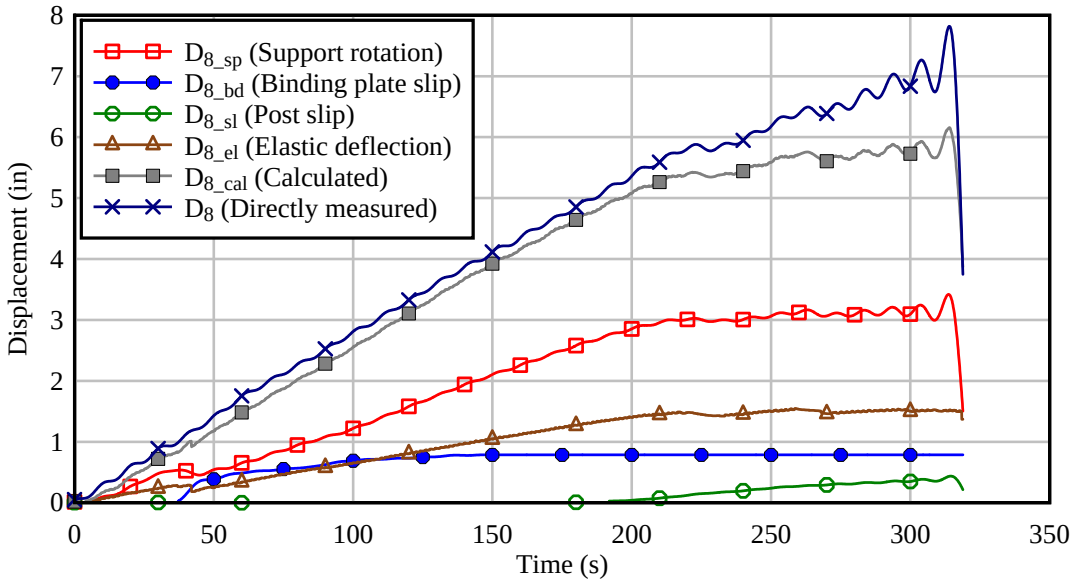

Figure 7-57. Time histories of post displacements (Test #1)

In Test #2, the collar was flipped over such that the undamaged half of the collar was positioned on the tension side of the connection. Moment capacity of the breakaway post in this test was 103.1 kip-ft (Figure 7-54), which was close to the previous test result. The yielding problem was thus repeatable since the behavior observed during Test #2 was very similar to Test #1. In Figure 7-58, displacement readings from LVDTs D3 and D4 also increased as the jack load ramped up (during the initial phase) due to slip of the binding plate. However, the readings later decreased as considerable bending moment on the primary plate developed due to increasing eccentric loading associated with post slip.

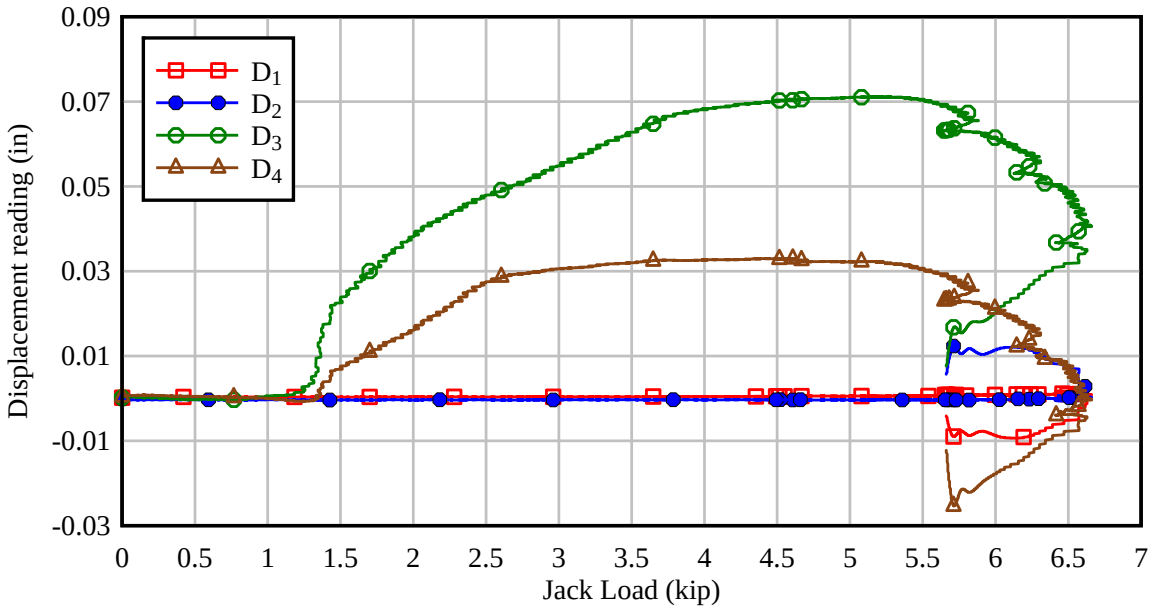

Figure 7-58. Displacement readings of LVDTs monitoring binding plate displacement (Test #2)

Directly measured displacement, computed displacement, corresponding displacement components, and scaled slip of the lower binding plate are shown in Figure 7-59. Within the slipping phase, during which there was insignificant bending deformation, the directly measured post displacement D_8 and the calculated displacement (D_{8_cal}) were in reasonable agreement. However, upon yielding, the post approached its maximum capacity whereas D_8 continued to increase, deviating from the calculated displacement (D_{8_cal}). During this loading stage, post slip was developing to a point sufficient for connector bolt failure.

Results from both tests indicated that the flexural moment in the collar primary plate (on the tension side of the connection) was more than expected as a result of post slippage and yielding. Consequently, the connector bolts were increasingly loaded until failure occurred. Although the collar halves yielded in both tests, the post, associated stiffeners, and flange plate all remained in the elastic range, therefore, only the collar halves needed to be modified to improve the overall moment capacity of the connection. Thus, an appropriate design modification was developed that consisted of adding external stiffeners to the collar primary plate (Figure 7-46). Two new collar halves based on this modified design were used in subsequent tests (Tests #3 and #4). The collar with additional stiffeners is shown in Figure 7-60.

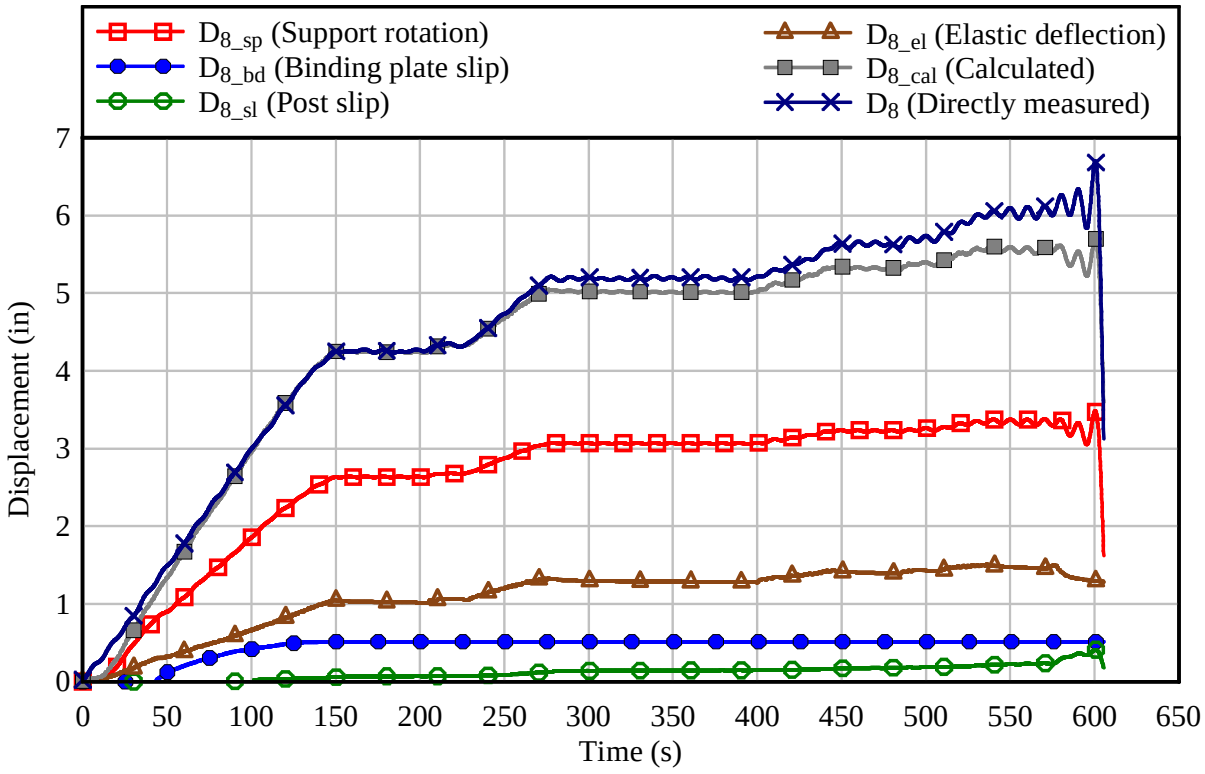

Figure 7-59. Time histories of post displacements (Test #2)

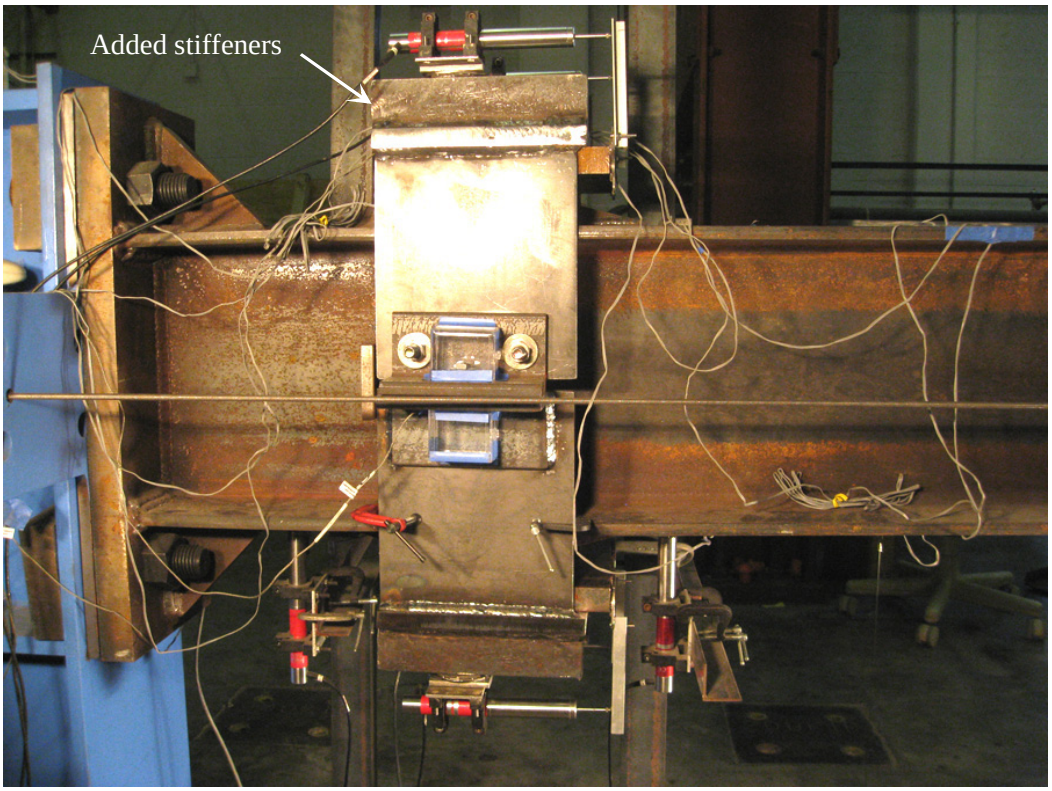

Figure 7-60. Installed collar with stiffeners (Test #3 and #4)

The maximum moment at the theoretical ground level (breakaway post moment capacity) obtained from Test #3 was 139.1 kip-ft (Figure 7-54) which is 1.36 times the moment of a single post that would be produced by the design wind load acting on the sign structure. The test results showed that stiffening the collar primary plates significantly improved the moment capacity of the connection. With the new collar design, the collar primary plates were able to resist the eccentric moment within the elastic range as the post flange plates slipped relative to each other. Increased loads on the connector bolts resulting from primary plate bending and local yielding, as was observed in earlier tests, were eliminated in the modified design. In Figure 7-61, displacements of the primary plates are plotted against jack load. The figure shows that the plate on the compression side did not slip (as anticipated). The plate on the tension side was not subjected to a high level of rotation due to primary plate bending as was seen in previous tests. In this test, the plate slip increased to a maximum value and only reduced slightly at the very last loading stage, at which the eccentric moment effect due to post slippage became noticeable. Consequently, connector bolt failure occurred at higher jack load levels.

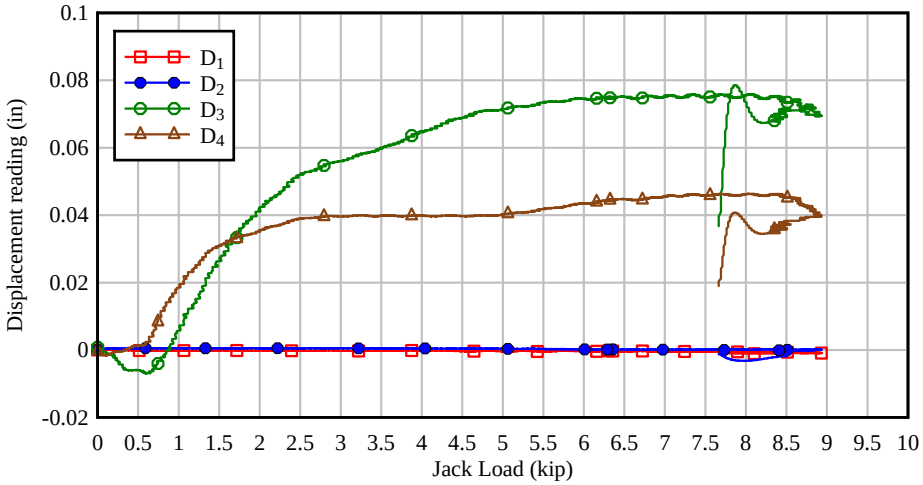

Figure 7-61. Displacement readings of LVDTs monitoring binding plate displacement (Test #3)

As designed, it was expected that at the ultimate moment capacity of the connection, the triangular flange stiffener plate would yield. Instead, the weld joining the stiffener plate and flange plate on the tension side of the connection cracked (Figure 7-62). As the crack grew, the flange plate was subjected to increasing bending moments due to moment arm development which led to larger deflection of the plate. Consequently, the connection stiffness was reduced, rotation of the collar halves increased, and the connector bolts were loaded quickly to failure. The effect of cracking on the post stiffness can be seen in Figure 7-63 in which post displacements measured directly and indirectly are plotted as time histories. After reaching the maximum post capacity (indicated by the peak of the elastic deflection D_{8_el}) the difference between the directly measured displacement (D_8) and the computed displacement (D_{8_cal}), which did not include contributions due crack or plastic deformation, became considerable. At this stage, since the post was loaded to its maximum capacity (no further increase in displacement due to elastic deformation), post rotation about the support, or binding plate slip, occurred.

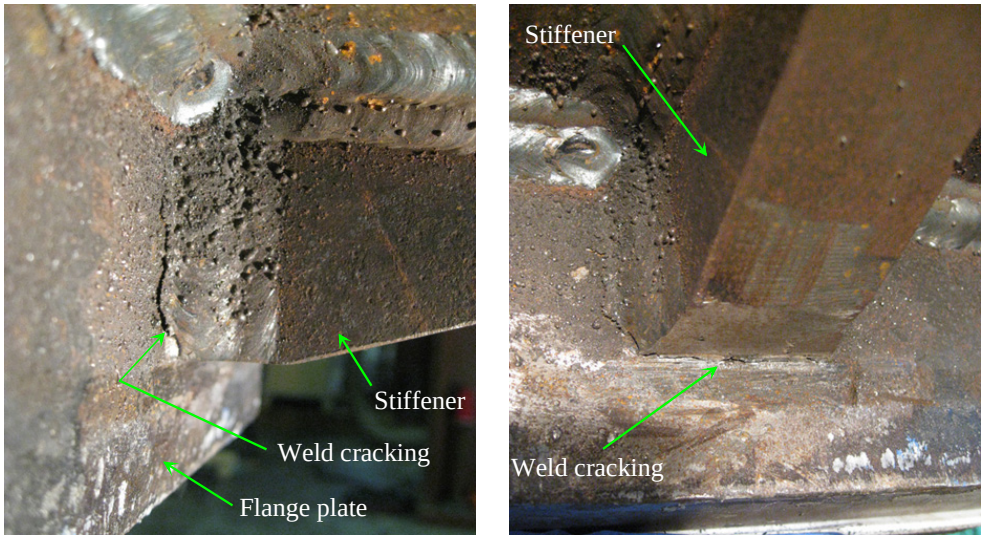

Figure 7-62. Close-ups of flange and stiffener on the post tension side after Test #3 (collar removed)

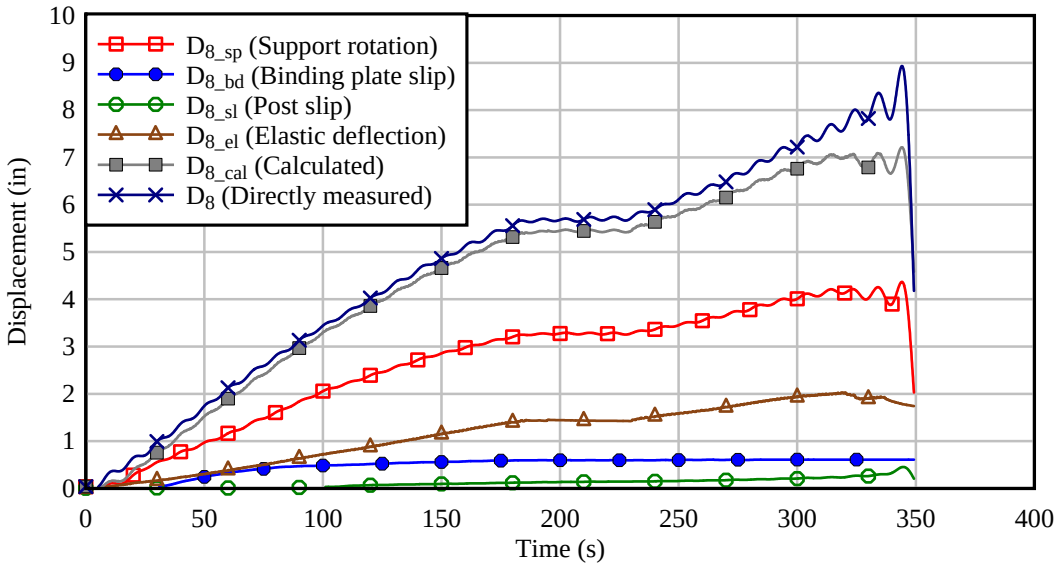

Figure 7-63. Time histories of post displacements (Test #3)

In Test #4, the post was flipped over such that the initially cracked weld was positioned on the compression side of the connection. Moment capacity of the breakaway post (moment at theoretical ground level) at connector bolt failure was 154.2 kip-ft which further indicated that the stiffening collar had increased the moment transfer capability of the connection significantly. Displacements of the binding plates plotted against jack load are shown in Figure 7-64. It can be seen that the lower binding plate slipped monotonically until the maximum jack load. Afterward, readings D_3 and D_4 decreased since eccentric moment had developed due to post slippage. However, bending of the primary plate was within the elastic range because no visible residual deformation was detected after testing.

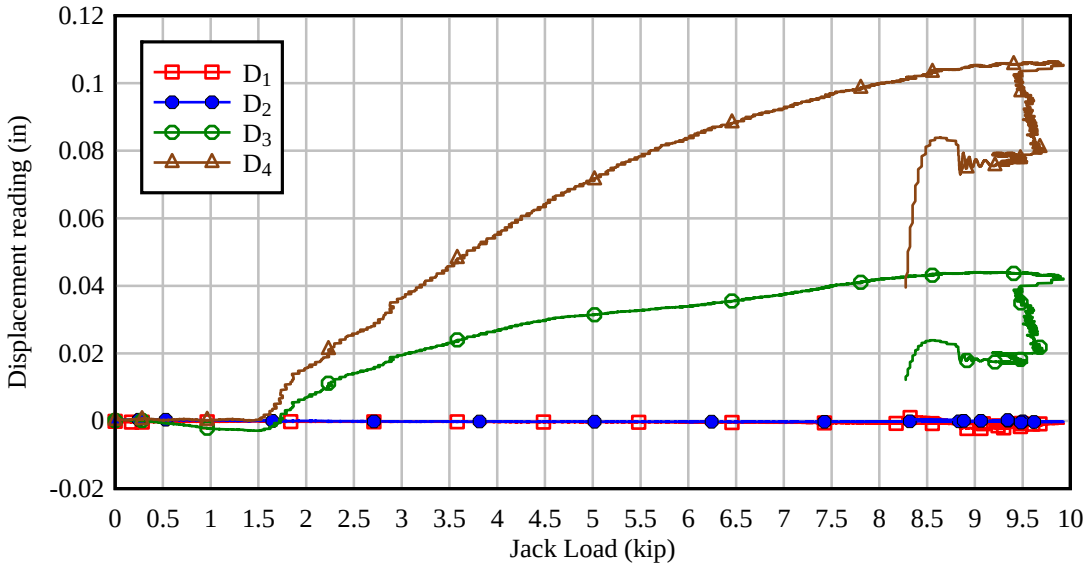

Figure 7-64. Displacement readings of LVDTs monitoring binding plate displacement (Test #4)

Although the post moment capacity was improved, the potential strength of the post was still not fully realized because weld cracking occurred again, in a manner similar to the previous test (#3). Cracking between the stiffener and flange plate after Test #4 is shown in Figure 7-66. The detrimental effect of cracking on the post capacity and stiffness can be observed in Figure 7-65, in which various post displacement measurements are plotted as functions of time. Once cracking occurred, the post was not able to carry any further load but the post displacement continued increasing, as is indicated by the growing separation between the D_8 and D_{8_cal} curves. During this stage, the post flange plate deformed considerably by yielding on the tension side due to increasing bending moment. As flexural deflection developed, the force that the bent plate imposed on the upper binding plate changed in direction which led to collar half rotation and consequently failed connector bolts. Plastic bending of the flange plate after Test #4 is shown in Figure 7-67.

Unexpected cracking of the full-penetration welds during Tests #3 and #4 suggest that the stiffener and flange plates were not adequately pre-heated during the welding process. Although weld cracking adversely limited the capacity of the connection, the moment capacity result from Test #4 (154.2 kip-ft) was 1.5 times the required design value of 102.6 kip-ft. This value exactly met the 1.5 factor specified by the AASHTO Highway Sign, Luminaire, and Traffic Signal Specifications for load tests on breakaway supports. It is expected that improved welding at this critical location in the connection would significantly improve the moment capacity and would yield experimentally measured capacities in excess of 1.5 times the design wind-load induced moment.

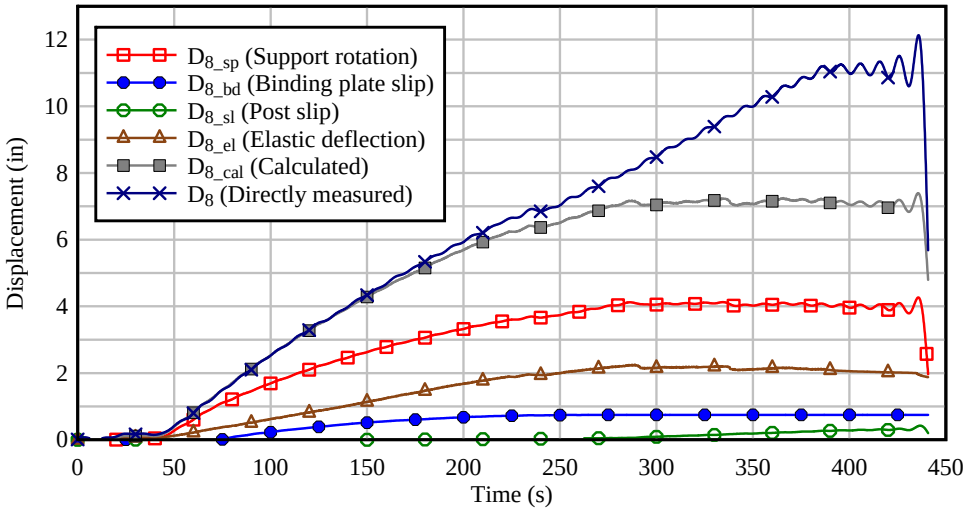

Figure 7-65. Time histories of post displacements (Test #4)

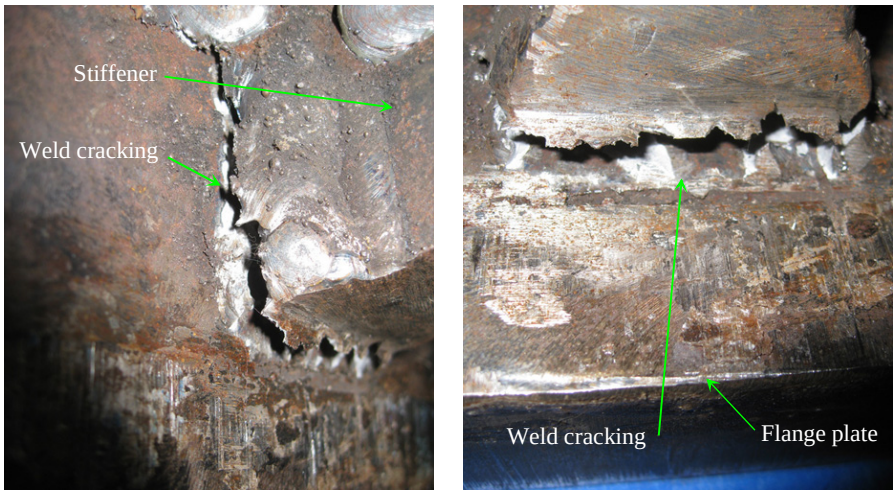

Figure 7-66. Close-ups of flange and stiffener on the post tension side after Test #4 (collar removed)

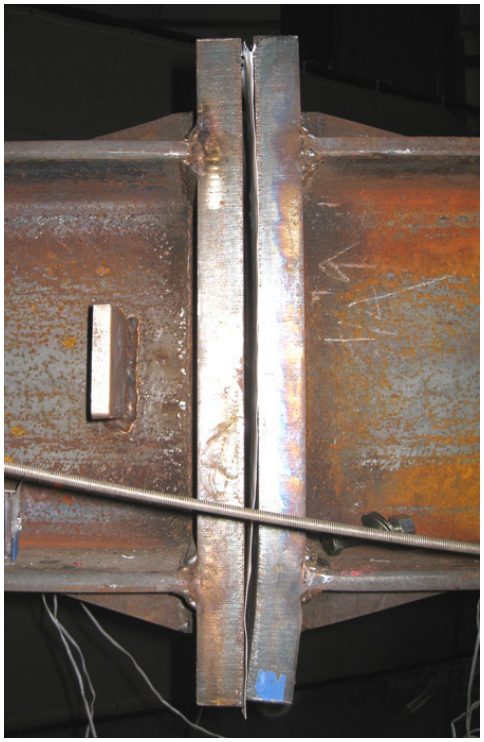

Figure 7-67. Bent flange plate after Test #4 (collar removed)

Since the connection is located near ground level (the slipping surface is 4 in. above ground level) and the lifting force was maintained equal to the post self-weight, the moment of the connection (computed at slipping surface) can be statically determined from the ground moment by the following equation:

$$M_C = \frac{M_G}{L_J} L_C \tag{7-19}$$

where M_C was the connection moment capacity, M_G was the moment capacity of the breakaway post at ground level, L_C was the distance from the jack location to the slipping surface (14 ft – 10 in.), and L_J was the distance from the jack load to the ground level (15 ft - 2 in.). A summary of connection moment capacities from the static moment tests is shown in Figure 7-68.

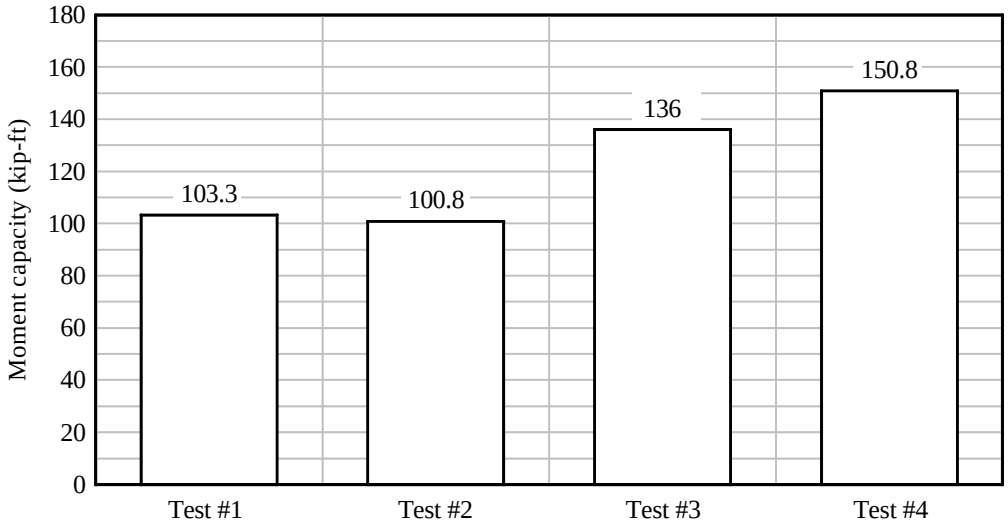

Figure 7-68. Connection moment capacities

The moment test results indicated that connector bolt failure was associated with eccentric moment on the collar half at the tension side as a result of post slippage. The loading level at which connector bolt failure occurred depended upon the bending stiffness of the collar and the slip level. Stiffening the collar clearly improved the moment capacity. However, the stiffened collar was still subjected to rotation due to the eccentric moment as the post slipped. Collar rotation consequently loaded the connector bolts in an undesirable manner. It should be noted that jack load is, in general, directly transferred to the connector bolts only when a frictionless condition exists. For the breakaway connection, most of the direct shear loading due to the jack load was resisted by friction between the flange plates. This was especially true for the moment test loading condition in which binding forces are much greater than the applied jack load since the distance between the jack and slipping surface is much longer than the moment arm of the binding force couples. Therefore, minimizing the eccentric moment on the collar by limiting post slippage is crucial in mobilizing post capacity to the fullest. In Figure 7-69 post slip computed by Equation 7-16 and jack loads from all the four tests are plotted. It can be seen that in all cases the post slipped until the bolted connection between the collar angles and side plates became snug. Such a large slip can be prevented by reducing the length of the slotted hole in each side plate.

To compare post stiffnesses across all conducted tests, the measured post displacement D_8 without the effect of the flexible support ($D_{8\_fixed\_sp}$) and the elastic deflection (D_{8_el}) are plotted against the applied jack load for each test in Figure 7-70. Since the displacement component due to the flexible support, which generally accounts for about 50% of the total post displacement as observed in individual plots of displacement time histories of each tests, was not necessarily representative of field support conditions, $D_{8\_fixed\_sp}$ was computed to better represent the “fixed” condition of the post stub embedded in a concrete foundation. The most important purpose, however, was to be able to determine the post stiffness decrease attributable to the introduction of the breakaway feature.

$D_{8\_fixed\_sp}$ was computed by subtracting the displacement component due to the flexible support (D_{8_sp}) from the total displacement (D_8). Incorporation of the breakaway connection decreased the post stiffness by approximately one-half as was indicated by the fact that the slope

of the post displacements ($D_{8\_fixed\_sp}$) was approximately double that of the elastic deflection. Near the end of each test, when primary plate yielding, weld cracking, and connector bolt yielding occurred, post displacements increased while jack loads decreased (Figure 7-70). Although the post became more flexible, the breakaway connection was experimentally proven to have adequate strength to ensure at least a load factor of 1.5 for the design wind load per the AASHTO load test requirement. Furthermore, reducing the lengths of the slotted holes used to bolt the angles to the collar side plates would increase post stiffness (since post displacement associated with slip would then be minimized).

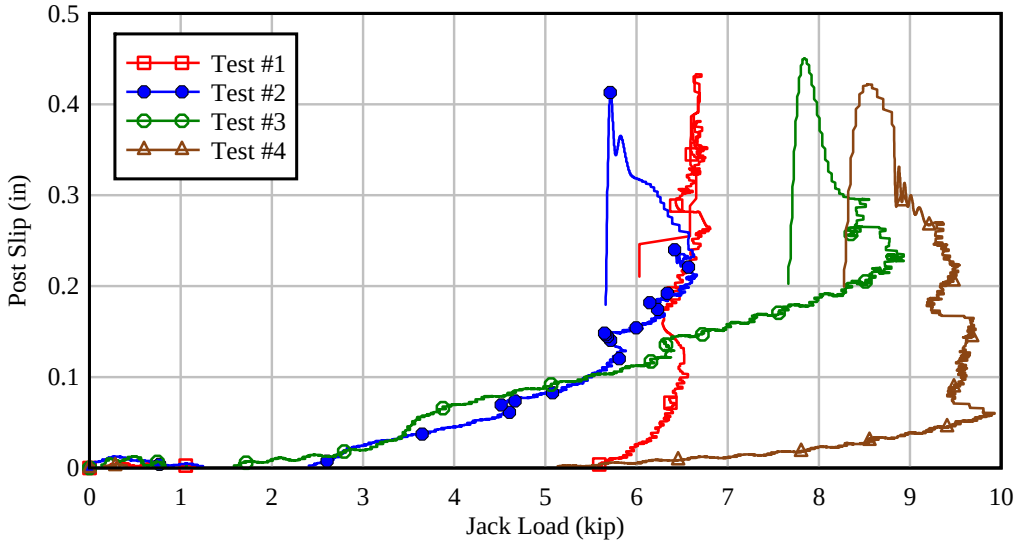

Figure 7-69. Post slip vs. jack load results

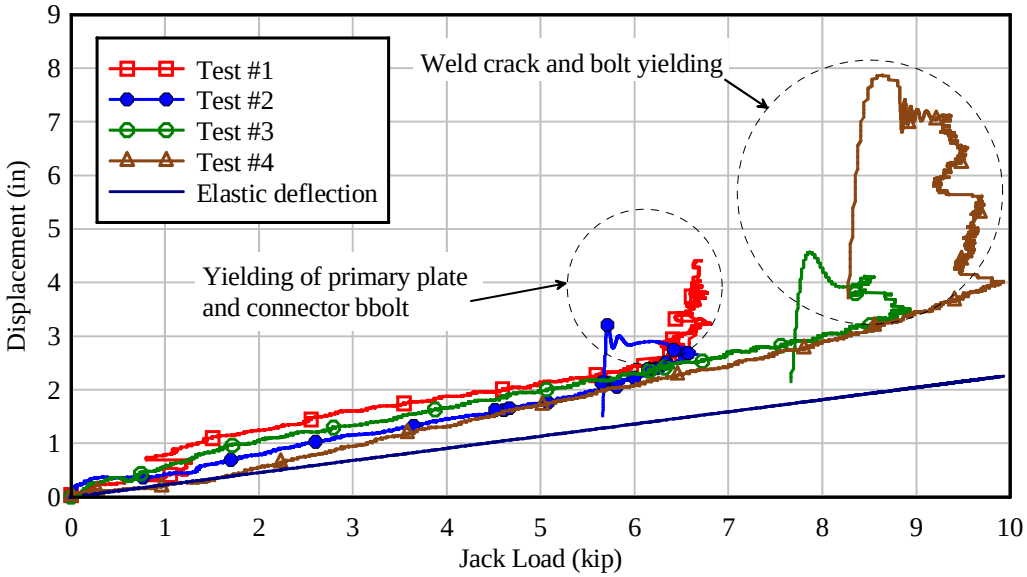

Figure 7-70. Post displacement (fixed support) and elastic deflection vs. applied jack load

CHAPTER 8
COMPARISON OF STATIC FINITE ELEMENT ANALYSIS AND EXPERIMENTAL RESULTS

8.1 Introduction

Development of the breakaway connection involved iteration between numerical analysis and experimental tests. In this chapter, the finite element model of the breakaway connection is calibrated and further refined based on static experimental testing results. Numerical simulations are performed in which design parameters, such as the friction coefficient, connector bolt type, and connection configurations used in each test type (shear test, moment test), are updated correspondingly. Insights from comparison of simulation and experimental results are presented and discussed.

8.2 Static Shear Test Comparison

The experimental static shear tests discussed in the previous chapter demonstrated the required frangibility of the breakaway connection under low level shear force. Upon completion of static testing, a high resolution finite element model, corresponding in configuration and loading to one of the shear test conditions, was developed to help calibrate the breakaway connection model. The same model was also used to quantify prying forces that developed at contact surfaces between the angles of two collar halves (forces which were not quantified during the experimental shear test program).

Figure 8-1 shows the refined finite element model of the connection that was used for shear test simulation. In the refined model, the collar angles were modeled with solid elements rather than with shell elements. Two contact pairs were defined for the angles to quantify prying forces. Welds between the angles and collar side plates were modeled by merging common nodes at the contact surface. Bolted connections on the opposite-side collar halves were modeled with spot weld constraints. The connector bolts themselves were represented by beam elements (Hughes-Liu beam element formulation) with the stress-strain relationship shown in Figure 8-2.

Since LS-DYNA permits material failure to be defined in terms of effective plastic strain, the bolt material was given a *plastic* failure strain of 0.005, which corresponds to a *total* strain of 0.007 (see Figure 8-2). Hence, when the beam elements reach this critical plastic strain, they provide no further resistance and are deleted from the computation. The material model (Figure 8-2) was derived from data obtained during tensile tests of the connector bolts (Chapter 7). In the earlier numerical development phase of the connection (Chapter 6), two spot weld constraints with a combined tensile strength of 6.5 kip, equivalent to the design wind load, were employed to model the connector bolts. The 6.5 kip value was slightly larger than the measured values obtained during connector bolt testing and static experimental testing. Use of a larger-than-actual 6.5 kip tensile bolt strength was conservative in the earlier evaluation of the connection frangibility. However, in order to calibrate the finite element model of the tested connection and facilitate comparison of experimental and simulated results, an update to the connector bolt material model, representing the actual behavior of connector bolts, was appropriate and necessary. Furthermore, the use of beam elements (rather than spot weld elements) to model the connector bolts in the updated model allowed the effects of connector bolt deformation to be taken into account.

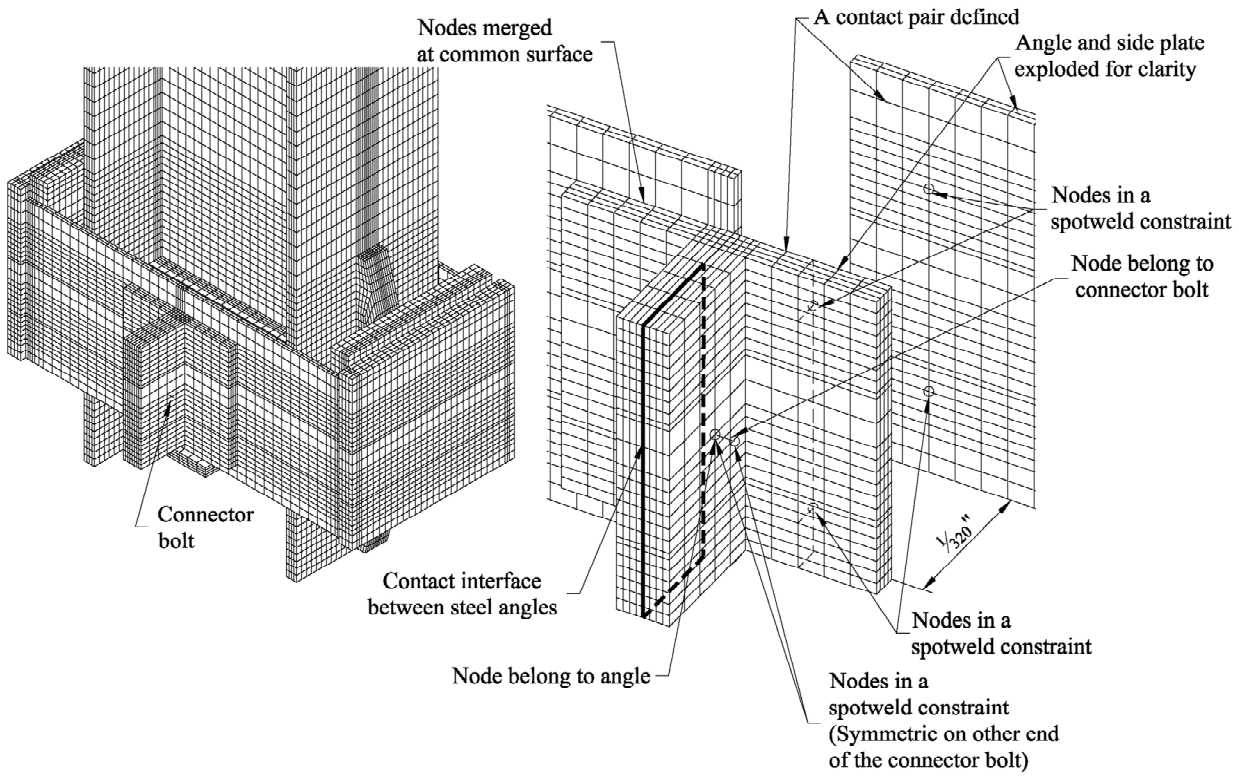

Figure 8-1. Refined finite element model of the connection for shear test simulation

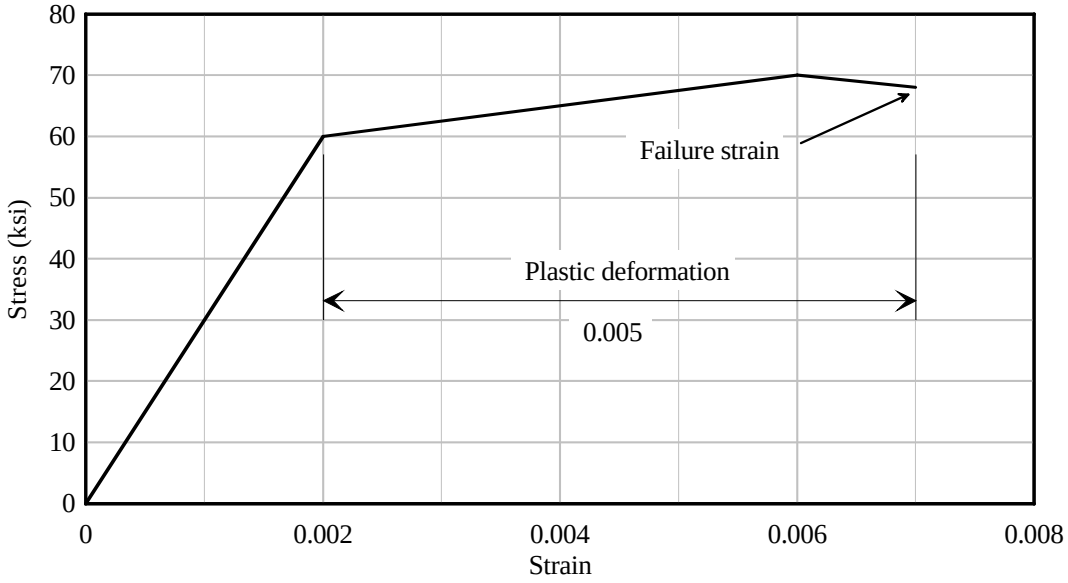

Figure 8-2. Stress-strain model of connector bolt steel

In Figure 8-3, a schematic diagram of the shear test simulation is presented. Shear test NR-TE-01 (the first (01) test of the no post restraint (NR) configuration, with a Teflon (TE) sheet inserted between the flange plates) was selected for simulation. The duration of the experimental shear test was approximately 100 sec. which would have required significant

computational cost if the entire process had been simulated. Instead, the time scale of the load history from the experimental shear test was compressed by one order of magnitude (i.e., the time duration was decreased by a factor of 10). It was anticipated that the decreased loading time (and therefore increased loading rate) would not significantly affect the "static" response of the system. The timescale-compressed load history from the shear test was applied to the post model at the same location as in the shear test setup (19 in. from the theoretical ground elevation).

Prior to conducting the numerical simulation, it was not known whether the ultimate shear capacity of the connection, as predicted by simulation, would be greater than or smaller than the capacity obtained from the experimental shear test. Therefore, once the end of the experimental jack load history (NR-TE-01) was reached, a constant loading rate of 7 kip/sec was specified in the simulation to continue loading the connector bolts until failure. It is also noted that prior to application of the shear loading, the post was subjected to a compressive axial load equal to the gravity load of the post and sign panel. The axial load was maintained at a constant value while the shear load was ramped up. Nodes below the theoretical ground level were fixed in all three translational degrees of freedom. A friction coefficient of 0.2 was specified for contact between the flange plates so as to simulate the presence of a Teflon sheet. All other potential contacts between various connection components were assigned a friction coefficient of 0.55 to represent the bare steel friction condition.

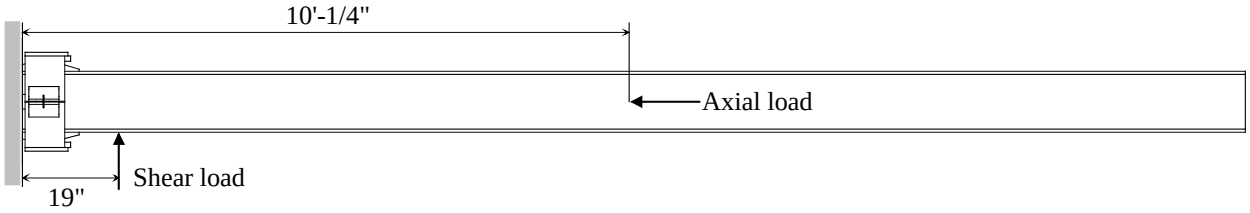

Figure 8-3. Schematic of breakaway post for shear test simulation

In Figure 8-4, simulation results for connector bolt forces and prying forces (between the collar angles) are plotted against the applied jack load. The results show that prying forces generally developed in a proportional manner with respect to the connector bolt forces. Prying forces were approximately 20% of the connector bolt forces. For convenience in result discussion, Equation 7.7 (Chapter 7) relating applied jack load, prying force, connector bolt force, and connection resistance, is reproduced and rearranged here as:

$$F_J + P = F_B + R \tag{8.1}$$

This equation shows that connector bolt forces develop when the applied jack load and prying force increase. Therefore, the prying force levels obtained from the simulation indicate an additional contribution to tensile loading of the connector bolts that result from the connection configuration. In Figure 8-5, a comparison is shown of simulation and experimental shear test results. In this figure, the sum of connector bolt forces is plotted against the applied jack load. Shear capacity of the connection, as predicted by simulation, was approximately 30% larger than that achieved from the experiment. A possible explanation for the difference is that in the finite element model of the connection, it was assumed that the binding plates would not slip relative to the primary plates. Consequently, the simulation model exhibited a greater influence of binding force which led to a higher shear capacity.

It can also be seen in Figure 8-5 that the connector bolts in the finite element model did not carry load until initial frictional resistance, due to axial gravity load, had been overcome. During the first half of the loading (below ~4.0 kip), there was a notable difference in total connector bolt force between the simulation and experiment. This is attributed to fabrication tolerances on the connection components which may have led to uneven loading of the two connector bolts (Chapter 7). In contrast, in the numerical model perfect symmetry of the geometry and properties were ensured, therefore the connector bolt force and prying force on one side of the connection respond similarly to their corresponding forces on the other side. After the second connector bolt was substantially loaded in the experiment, as indicated in the last region of the experimental curve (4 kip to 6.5 kip of jack load), the simulated and experimental total connector bolt forces are in very good agreement.

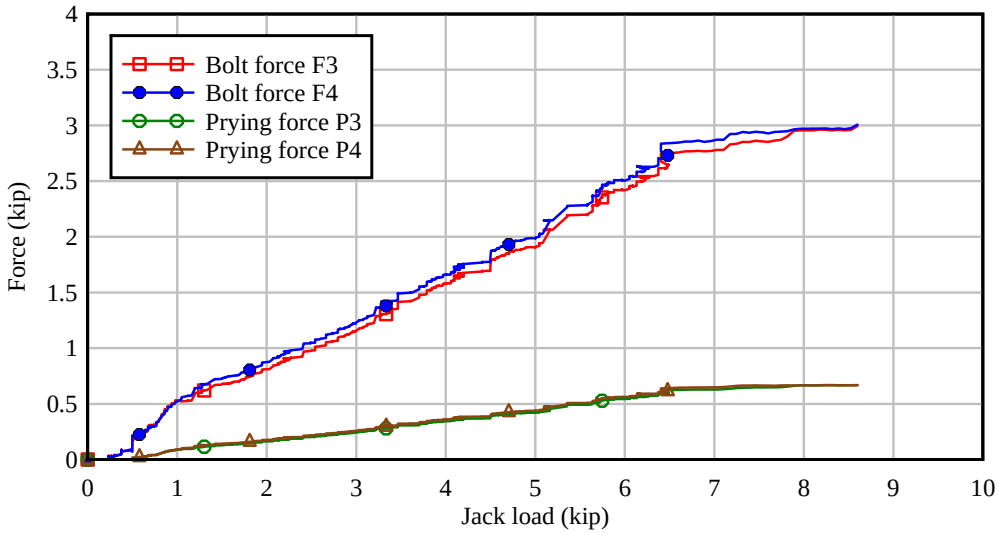

Figure 8-4. Bolt and prying forces vs. applied jack load results of shear test simulation

8.3 Static Moment Test Comparison

As discussed in Chapter 7, during the first two moment tests (Tests #1, #2), yielding of the collar primary plates occurred due to post slip, which itself was the result of slotted holes in the collar components. In the last two moment tests (Tests #3, #4), the collar design was modified by adding stiffeners to the primary plates to increase their bending capacity against eccentric flexural loading (caused by slippage). Based on the demonstrated effectiveness of these stiffeners, they were adopted as a permanent feature in the final breakaway connection design. Consequently, in this section, only numerical simulations of Tests #3 and #4, both of which included stiffeners on the primary plates, will be presented.

Before moment Tests #3 and #4 were conducted experimentally, the finite element connection model that was used in the shear test simulations was modified (including, among other additions, the introduction of primary plate stiffeners). The revised model was then used to conduct flexural (moment) test simulations to permit determination of ultimate capacity and to predict structural performance. In Figure 8-6, an exploded view of the refined finite element model, used for moment test simulation, is presented.

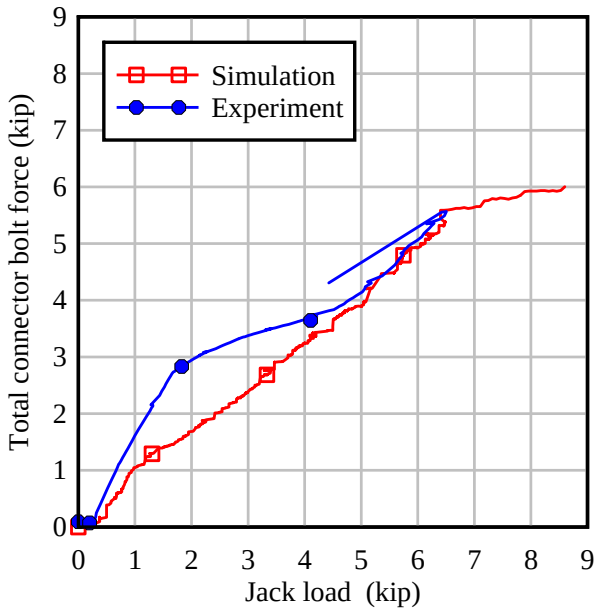

Figure 8-5. Comparison of results for shear test loading

Since experimental moment Tests #1 and #2 indicated that the binding plates slipped with respect to their associated primary plates at a low jack load level (~1.3 kip), modeling the plates (e.g. through nodal merging) with the assumption that no slip would occur could result in an overestimation of moment capacity of the connection. Therefore, in the refined model, the primary plates and binding plates were modeled as separate entities, with contact (permitting sliding) defined between them. The 1-1/8 in.-diameter bolts and nuts that keep the primary and binding plates in contact were modeled using a rigid material representation (since bolt deformations were expected to be negligible) to reduce the computational cost. It was also assumed that initial bolt tension, created by a 250 lbf-ft torque applied to a 1-1/8 in.-diameter bolt, would have a negligible effect on the connection behavior. This modeling assumption was further justified by the fact that slip between the binding plates and primary plates occurred (during moment Tests #1 and #2) at a low jack load level where the axial deformations of a 1-1/8 in.-diameter bolt would extremely small. The 1-1/8 in.-diameter bolts were modeled such that the shaft length between bolt head and nut was equal to the combined thickness of the primary plate and binding plate.

After test article assembly, but *prior* to conducting moment Tests #3 and #4, gaps between the bolt shafts and slotted holes in the primary plates were observed. These gaps existed partially as a result of the intentional use of slotted holes in the primary plates, and partially due to the fabricated slot lengths being somewhat longer than intended (i.e., fabrication tolerance). Consequently, prior to conducting Tests #3 and #4, steel shims (with thicknesses ranging from 1/8 in. to 1/4 in.) were inserted to fill the gaps. To mimic this condition in the finite element model, the holes in the primary plates were modeled as 1-3/16 in.-diameter *circular* (not slotted) holes.

Friction conditions between components in the connection were similar to those used in the shear test simulation except that the contact surfaces between the flange plates and binding plates were specified a friction coefficient of 0.2 (to represent the Teflon friction condition of

moment Test #3). A schematic diagram moment test that was numerically simulated is shown in Figure 8-7. After axial compressive load was fully applied, lateral load was ramped up at a rate of 6.5 kip/sec.

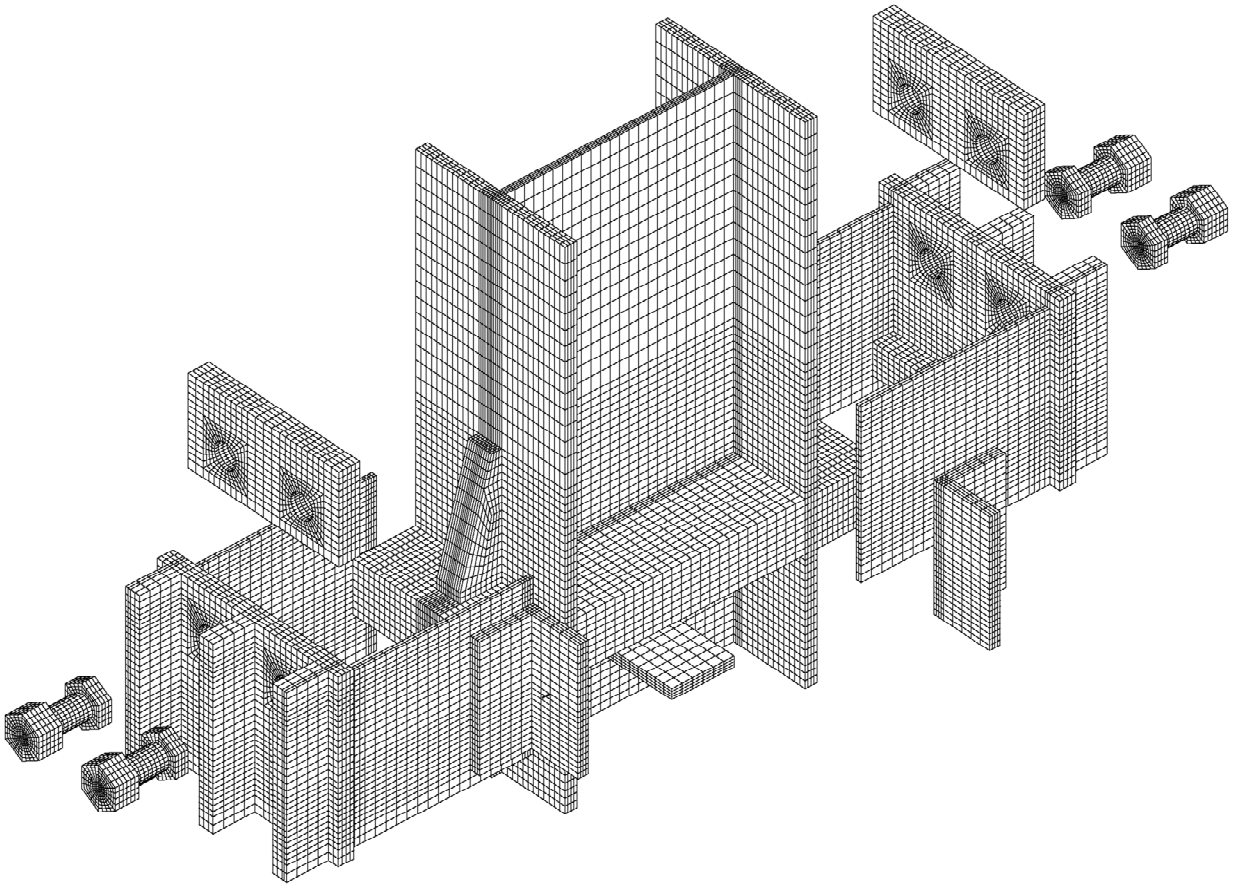

Figure 8-6. Finite element model of the modified connection used in moment Tests #3 and #4

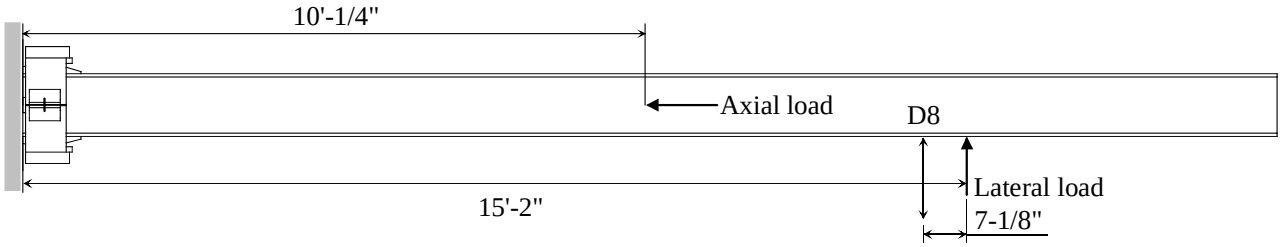

Figure 8-7. Schematic of breakaway post for moment test simulation

In Figure 8-8, a comparison of connector bolt response, from simulation and from two moment experiments, is presented. It is evident that a higher jack load was required to produce connector bolt loading in the simulation than in the experimental tests. There are two possible causes for the difference. The first one is attributed to the difference in the representation of the bolted connection between the side plates and steel angles. The slotted holes present in the side plates that were used during testing were not included in the finite element model of the

connection. The second possible cause is due to the fabrication tolerances of the connection components. Despite differences between simulation and experiment, it was found that connector bolt forces in the moment loading condition generally developed at a higher jack load level than in the shear loading tests, due primarily to the greater binding forces exerted by a larger bending moment at the base.

In Figure 8-9, the relationship between post deflection at the D8 location (potentiometer location adjacent to the jack, see Figure 8-7) and the applied jack load obtained from the simulation and experiments is shown. To enable a consistent comparison, the displacement component due to flexibility of the support structure used in the experimental tests (below theoretical ground level) has been subtracted from the experimental post deflections presented in Figure 8-9. Experimental data points after weld cracking occurred have also been removed from the plot. Good agreement between the simulation and experimental results is evident in the figure. The bending stiffness of the breakaway connection and post was appropriately represented in the finite element model. Note that the sinusoidal oscillation in the numerically simulated deflection trace is due to the fact that a dynamic analysis procedure was employed and the loading rate in the simulation was slightly faster than that needed to completely eliminate dynamic effects.

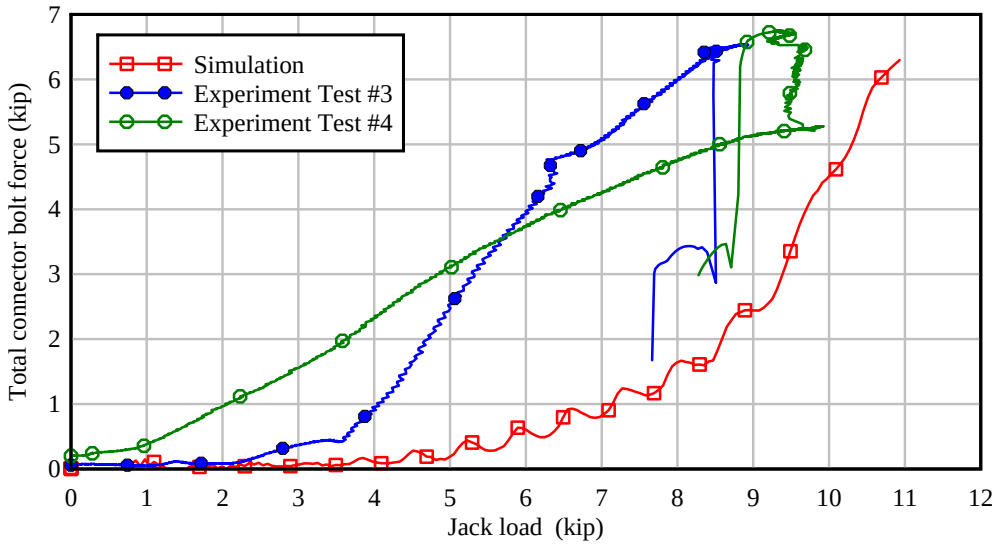

Figure 8-8. Connector bolt response to applied jack load

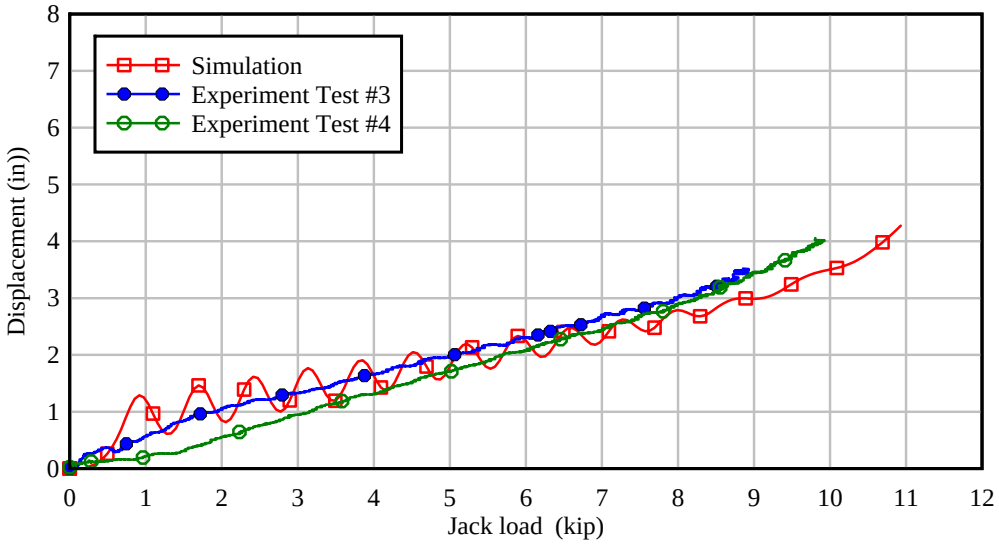

Figure 8-9. Comparison of post deflection characteristics

CHAPTER 9
DESIGN MODIFICATION OF SHEAR-CONTROLLED MOMENT COLLAR BREAKAWAY CONNECTION

9.1 Introduction

The shear-controlled moment collar connection presented in Chapter 6 was developed for a low-speed, 0-degree impact case. The post and connection were fabricated and experimentally tested for static equivalent impact shear capacity and structural resistance against the design wind load. Further refinement of the breakaway connection, presented in this chapter, was carried out to address oblique and high-speed impact conditions. The refinement process also took into account the beneficial effects of Teflon, as noted during the static experimental testing program, to reduce frictional effects in the connection.

9.2 Design Modification

9.2.1 Connection Design Refinement for Breakaway Performance under Oblique Impact

Dynamic simulation of the connection under the upper bound friction coefficient of 0.8 and a 20-degree impact angled revealed the presence of a lock-up mechanism. Under this impact scenario, the collar side plates prevented the flange plate from moving laterally (perpendicular to the side plate) which introduced frictional resistance in the longitudinal direction (parallel to the side plate). This condition made the connection susceptible to binding effects. To resolve the problem, the middle regions of side plates were removed (Figure 9-1) so that resistance forces acting on the flange plate were minimized and binding was prevented. In addition, 1/4 in.-thick square bars were added vertically to the primary plates to prevent lateral post slip should low-level lateral loads occur under service conditions.

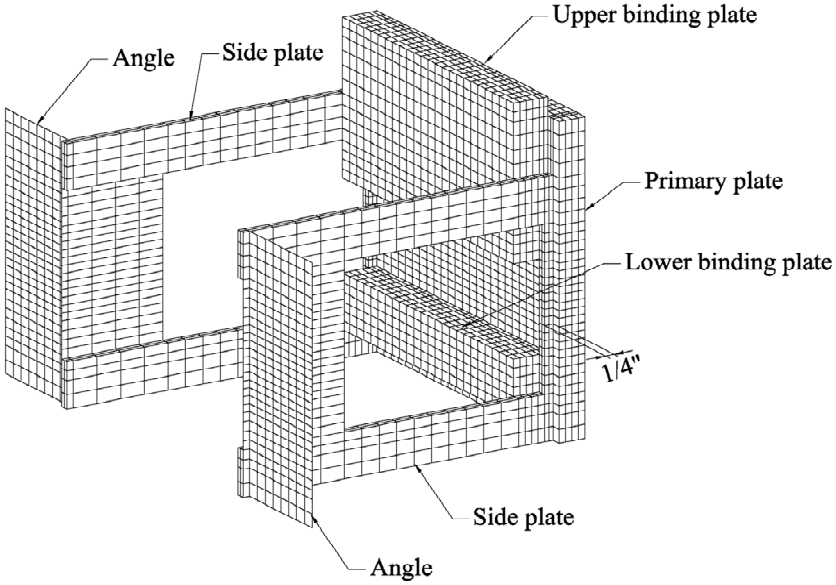

Figure 9-1. Finite element model of a modified collar half

In Figure 9-2, impact simulation results are presented for the system without and with the collar design modifications. With modifications, a lock-up mechanism caused a drastic decrease

of vehicle velocity which dropped below zero even before the occurrence of the theoretical occupant impact. Therefore the OIV was predicted to be higher than the initial vehicle velocity of 9.72 m/s. However, the collar design modifications improved the breakaway performance by reducing the OIV to 5 m/s. Maximum vehicle deceleration was also reduced from 18.9 g (without modification) to 11.6 g (with modification). Occupant ridedown accelerations (ORA) in both cases were not critical since after the occupant impact event, vehicle decelerations were well below the limit of 20 g.

Impact simulations of the sign structure with the breakaway connection indicated a satisfactory performance over a broad range of friction coefficients, up to 0.8, under low-speed impact. In addition to numerical simulations, experimental static shear tests demonstrated that a significant decrease in frictional connection resistance was produced when a Teflon sheet was inserted at the slipping surface (see Chapter 7). Therefore, to reduce frictional effects to the lowest level practically attainable, a Teflon sheet was incorporated into the connection design.

A series of low-speed impact simulations in which the slipping contact surface was given a friction coefficient of 0.2 were conducted to evaluate the dynamic performance of the breakaway sign structure. The remainder of the contact surfaces in the connection—of the galvanized steel to galvanized steel type—were assigned a friction coefficient of 0.55. The value of 0.55 was intentionally chosen to be conservatively high. Recall that the experimentally determined value obtained in this study was 0.45 (Table 5-1) and that values from the literature (Kulak et al. 1987) ranged from 0.08 to 0.36. Results obtained from simulations of two test vehicle types, the 820-kg pendulum impactor (small car surrogate) and 2,000-kg pickup truck, impacting the structure at 35 km/h and at impact angles of 0 and 20 degrees, are shown in Figures 9-3 and 9-4. The simulations indicated favorable dynamic performance of the connection—the connection failed as expected, and the post separated from the base under the low-speed impact condition. Both the OIV and ORA were below the permissible limits set by NCHRP 350. Furthermore, the lateral OIV evaluation criteria, per NCHRP 350, are not applicable to sign support structure impact. Thus, only longitudinal results that govern the dynamic performance are presented.

A comparison of results for pendulum impacts at 20-degrees, with and without Teflon, indicated that the use of Teflon improved the connection performance by reducing both the OIV and ORA. The 20-degree oblique impact was also shown to be more critical than the 0-degree impact. Maximum vehicle accelerations in the 0-degree and 20-degree cases differed very little, however, a difference in OIV values of up to 0.43 m/s was predicted. The OIV difference decreased with increasing mass of the test vehicles. While occupant impact occurred at 0.20 sec and 0.21 sec for simulated cases with the pendulum test vehicle, a longer time was predicted for the cases of the pickup truck because the truck experiences lower velocity change. Although simulations with the pickup truck were not extended to the time of hypothetical occupant impact, the OIV can be estimated using the velocity change of the vehicle (since the post was pushed away from the vehicle, and the vehicle reached a constant velocity condition). ORA values for the four cases were insignificant because vehicle accelerations had virtually ceased (constant velocity) after the occupant impact event.

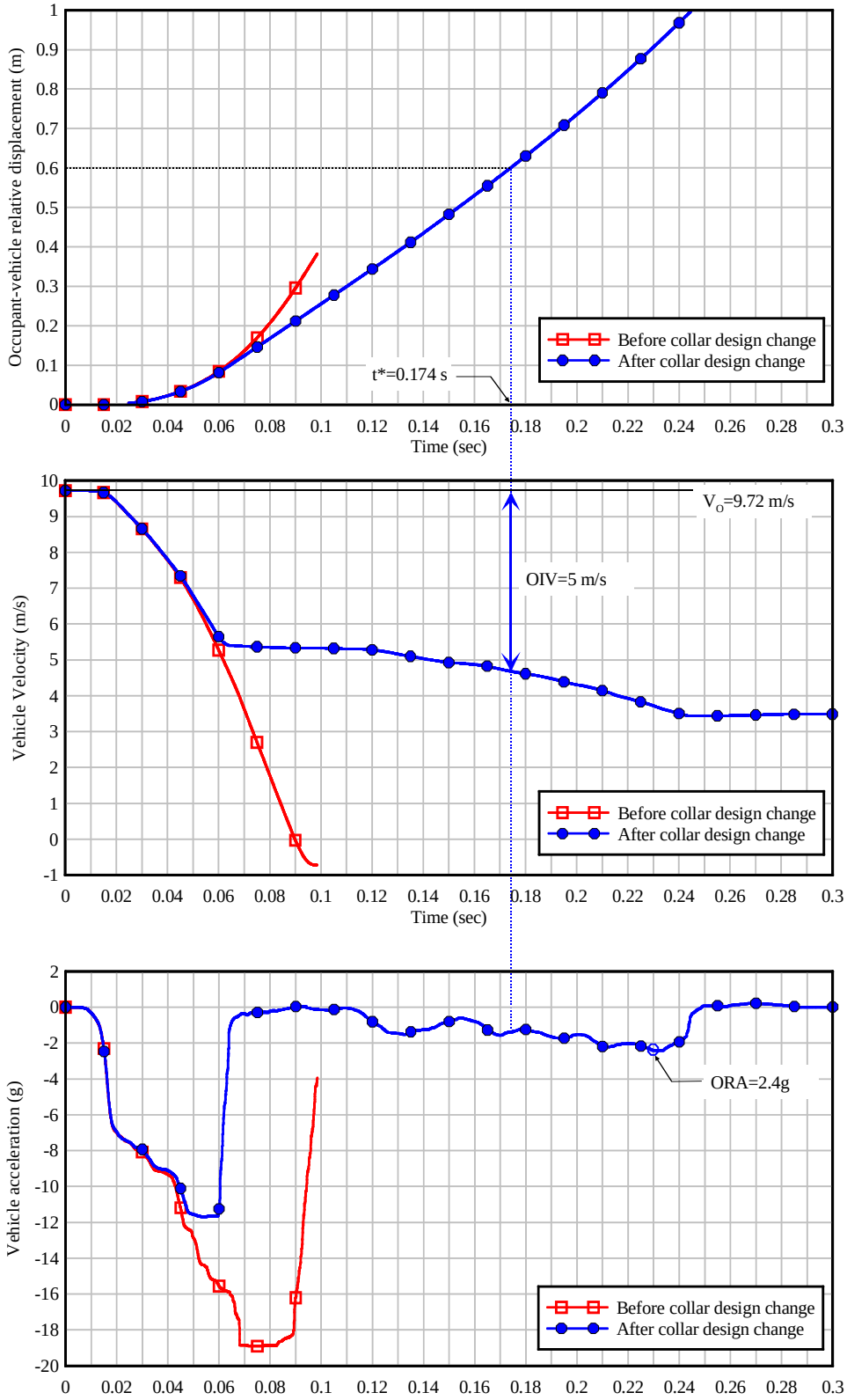

Figure 9-2. Simulation results for the connection before and after the collar design change in the 20-deg, 35 km/h impact condition with a coefficient of friction of 0.8

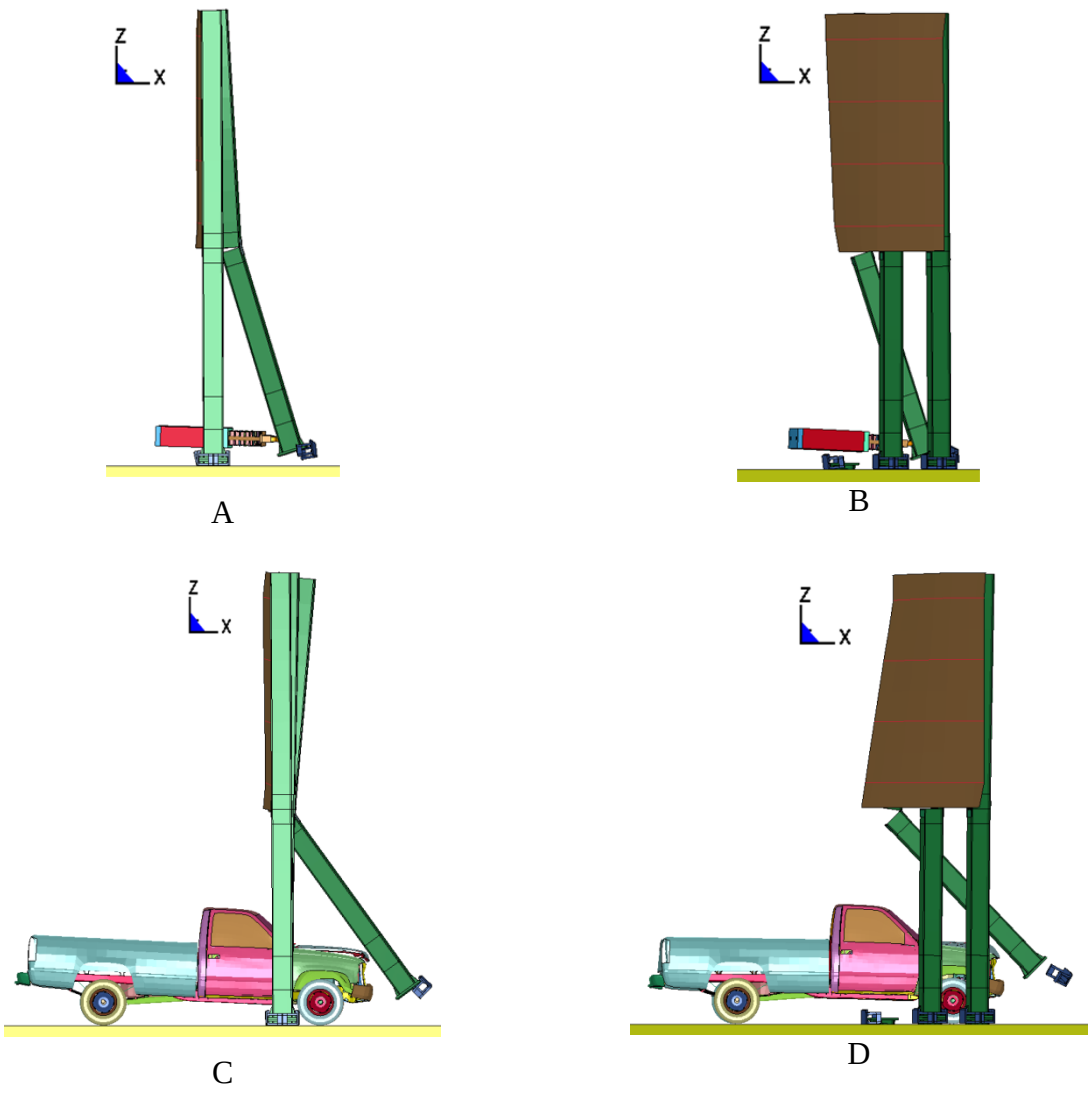

Figure 9-3. Failure of breakaway connection with Teflon sheet inserted at the slipping surface under the 35 km/h impact condition: A) Pendulum, 0-degree; B) Pendulum, 20-degree; C) Pickup truck, 0-degree; D) Pickup truck, 20-degree

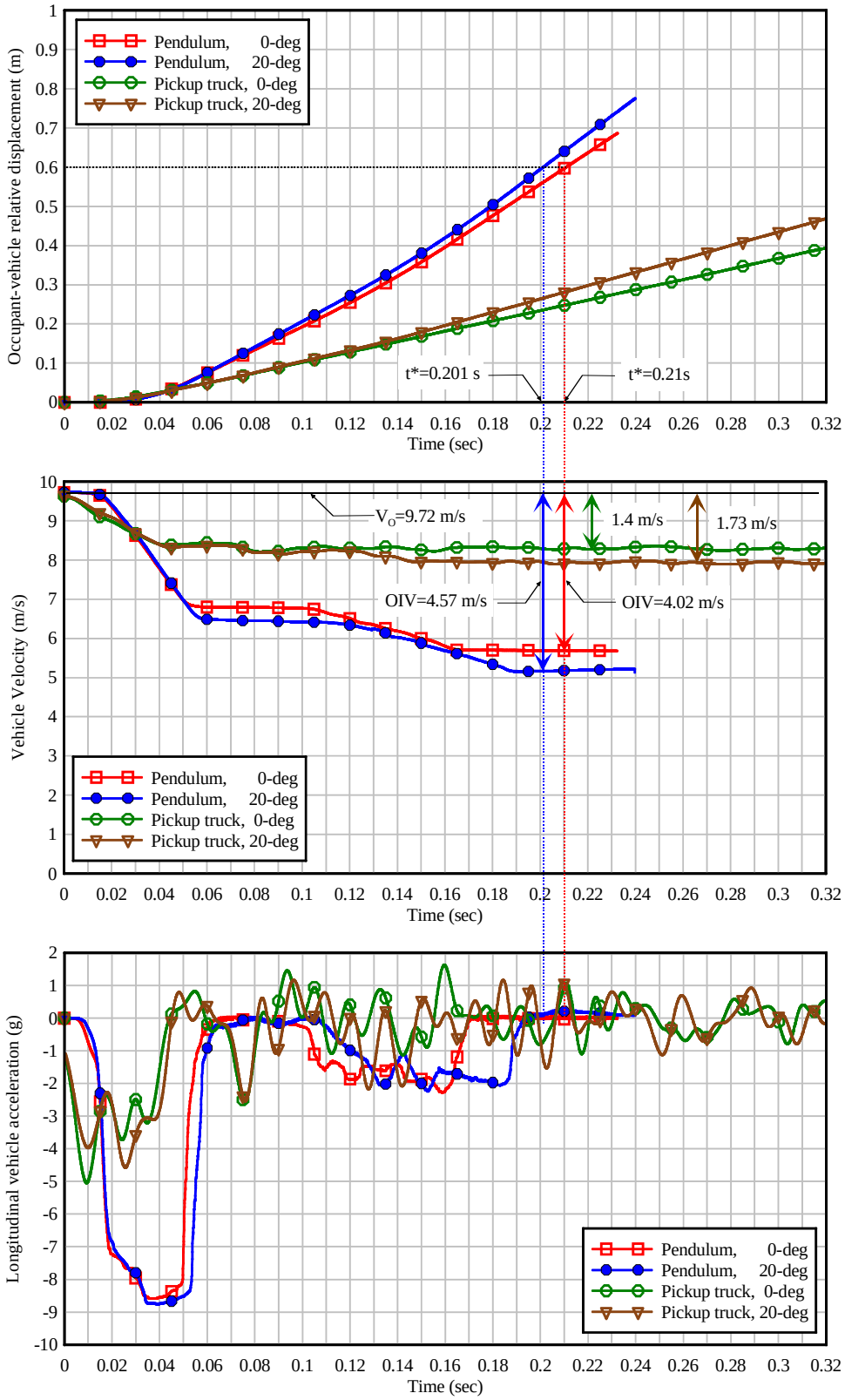

Figure 9-4. Simulation results for the connection with Teflon inserted at slipping surface under 35 km/h impact condition

9.2.2 Connection Design Refinement for Breakaway Performance under High-speed Impact

Typically, a key purpose for conducting a high-speed impact test is to evaluate vehicle and test article trajectory. However, numerical simulations indicated that, under high-speed impact, occupant impact risk was more likely to control the system design than was vehicle trajectory or post trajectory. Figures 9-5 and 9-6 show simulation results for the pendulum impacting, at a high-speed velocity of 100 km/h, the same breakaway structure that met the dynamic performance requirements under low-speed impact discussed above. Simulations predicted severe vehicle deceleration up to 28 g in both cases; however, after the travel time required for theoretical head impact had elapsed, vehicle accelerations diminished such that occupant ridedown acceleration (ORA) values were negligible.

It can be seen that although the pendulum impactor successfully broke the connection and was able to swing the post upward and pass underneath, the OIVs for both the 0-degree and 20-degree impact conditions exceeded the allowable limit of 5 m/s. This was due to the greater influence of binding force and inertial resistance on the support post under higher speed impacts. The binding forces were directly proportional to the impact force acting on the post. Figure 9-7 indicates that for a 20-degree impact on the breakaway connection with Teflon, the maximum impact force induced at 100 km/h (high-speed) was approximately five (5) times larger than at 35 km/h (low-speed). Therefore, despite the fact that the connection failed faster and the post separated completely from the pendulum in a shorter duration of time, a greater quantity of kinetic energy was dissipated at high-speed (than at low-speed) due to post acceleration, plastic deformation of the support structure, and a greater level of crushing in the pendulum nose. In Figure 9-8, simulated results from the low-speed and high-speed impacts are shown after separation of the pendulum and the post. The post was damaged under the high-speed impact, while it was virtually undamaged in the low-speed case.

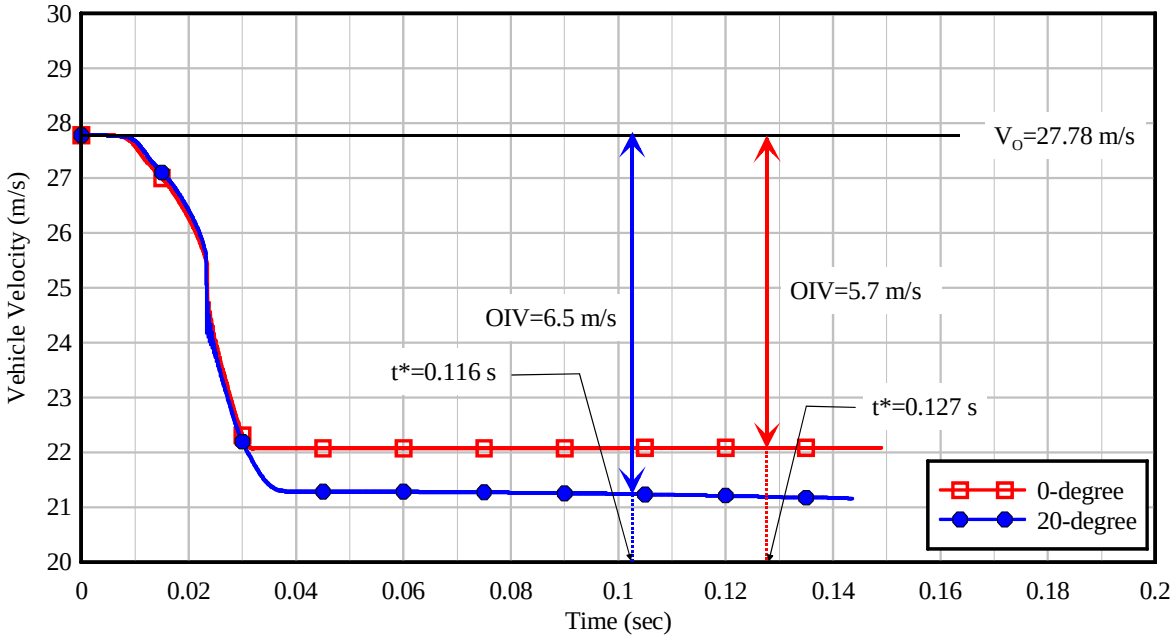

Figure 9-5. Simulated vehicle velocity time histories and OIV results for the connection with the Teflon sheet inserted at slipping surface under the 100 km/h impact condition

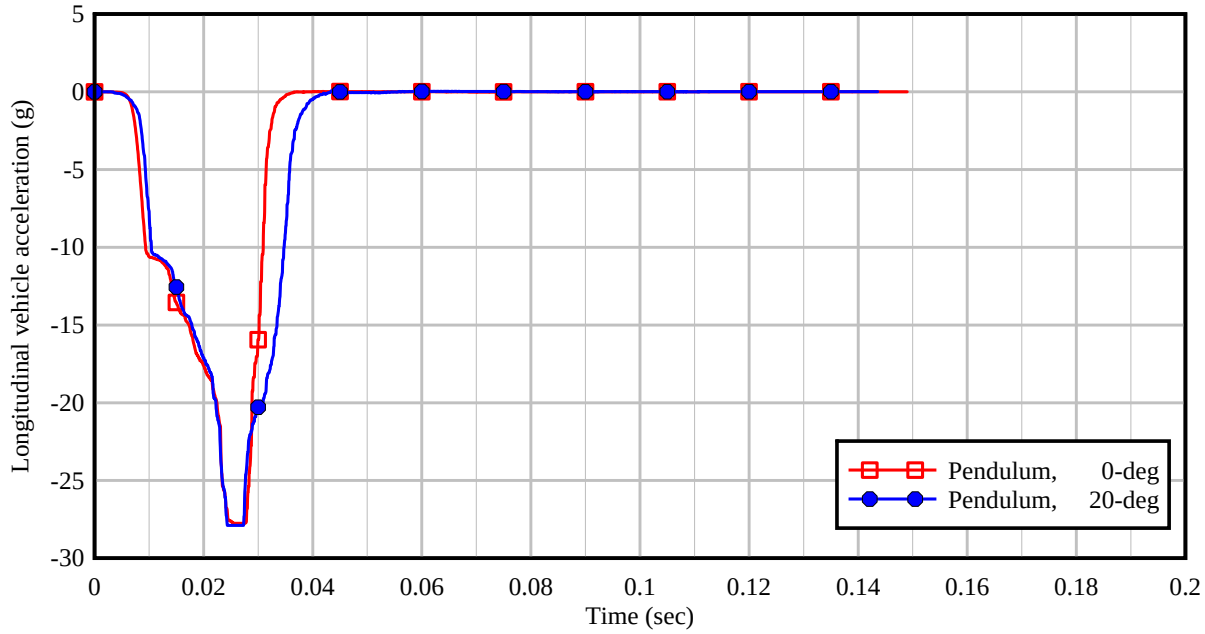

Figure 9-6. Simulated vehicle acceleration time histories for the connection with the Teflon sheet inserted at slipping surface under the 100 km/h impact condition

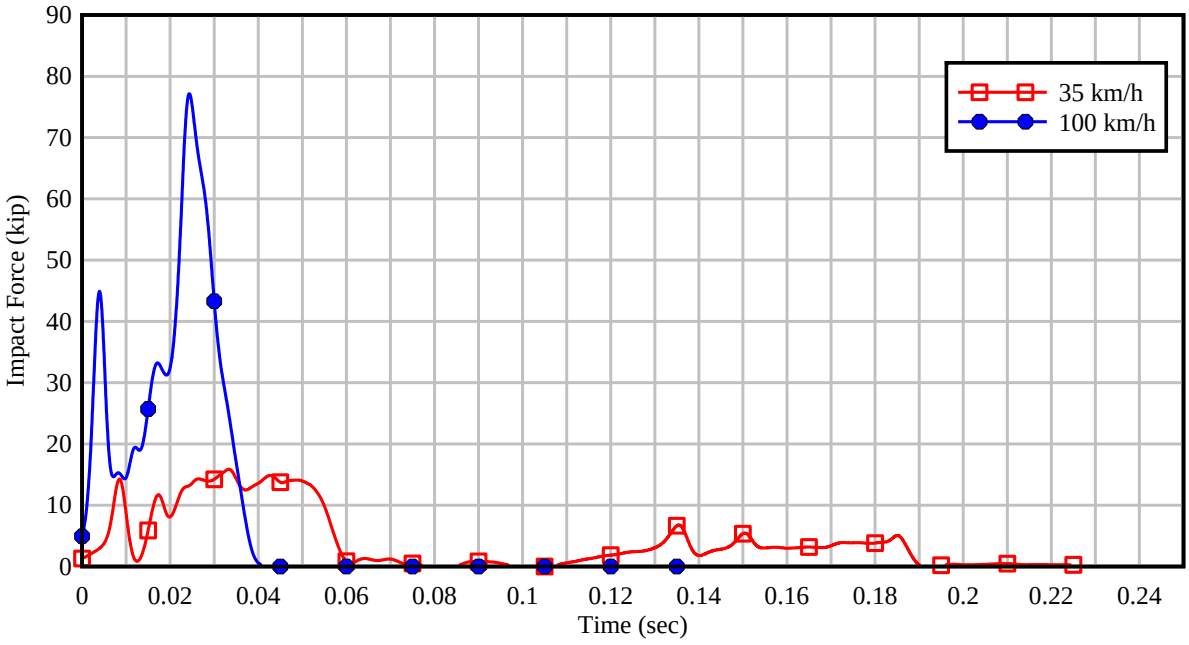

Figure 9-7. Comparison of impact force time histories for the connection with the Teflon sheet inserted at slipping surface under a 20-degree impact

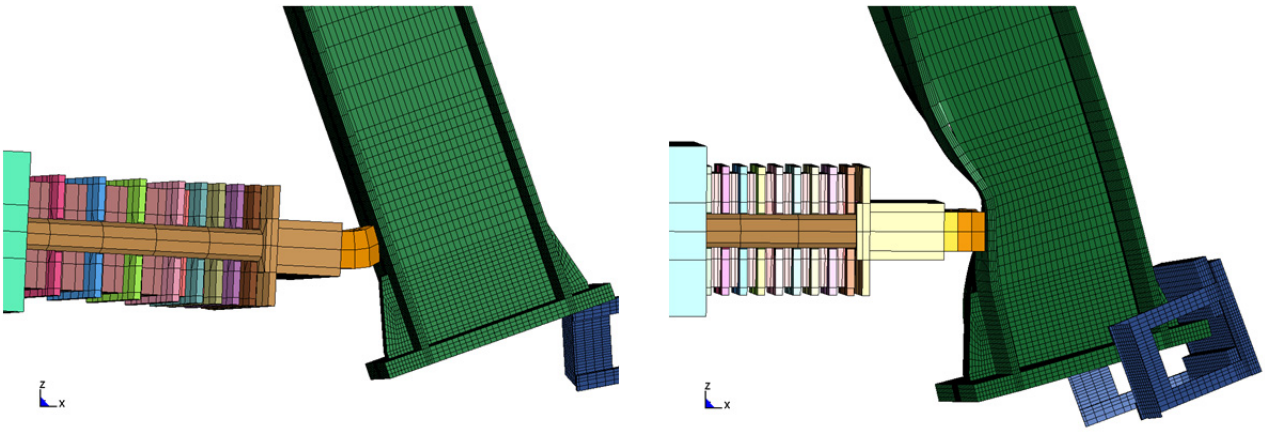

A B

Figure 9-8. Simulation results for the connection with Teflon sheet inserted at slipping surface under 20-degree impact: A) Impact speed of 35 km/h; B) Impact speed of 100 km/h

Comparisons of dynamic connection performance under different impact speeds indicated that although the breakaway connection functioned well under low speed (low kinetic energy) impacts, it needed further refinement to work effectively under high-speed impacts. To minimize the binding effect, which was more detrimental to system performance under high speed impacts, additional Teflon sheets were introduced to reduce friction at contact surfaces between the post flange plates and the collar binding plates (Figure 9-9). This change was implemented in LS-DYNA by specifying a frictional coefficient of 0.2 for these contact interfaces. For discussion purposes, the friction condition in which a single Teflon sheet was inserted at the flange plate slipping surface, is designated as the "1-Teflon-insert friction condition". The revised friction condition that used Teflon sheets both at the flange plate slipping surface and at the binding interfaces is designated as the "5-Teflon-insert friction condition". To quantify OIV improvement, a simulation was performed with the 5-Teflon-insert friction condition, and the pendulum impacting the post at a speed of 100 km/h and at an angle of 20 degrees.

Results from the simulation are shown in Figure 9-10. It is evident that the pendulum velocity change was improved considerably by introduction of the four additional Teflon sheets. The OIV was reduced by approximately 0.9 m/s and brought down to 5.59 m/s. It must be noted that a larger mass vehicle will generally result in a smaller velocity change. Therefore, even though the predicted OIV for the most critical case (5.59 m/s) exceeded the maximum allowable limit of 5 m/s per NCHRP 350, it is very probable that the connection performance would be adequate under the AASHTO MASH code. Recall that in the AASHTO MASH code (which supersedes NCHRP 350), the mass of the small car (820 kg in NCHRP 350) was increased to 1100 kg. The additional 280 kg of mass would very likely reduce the OIV from 5.59 m/s to a value below the permissible threshold of 5 m/s.

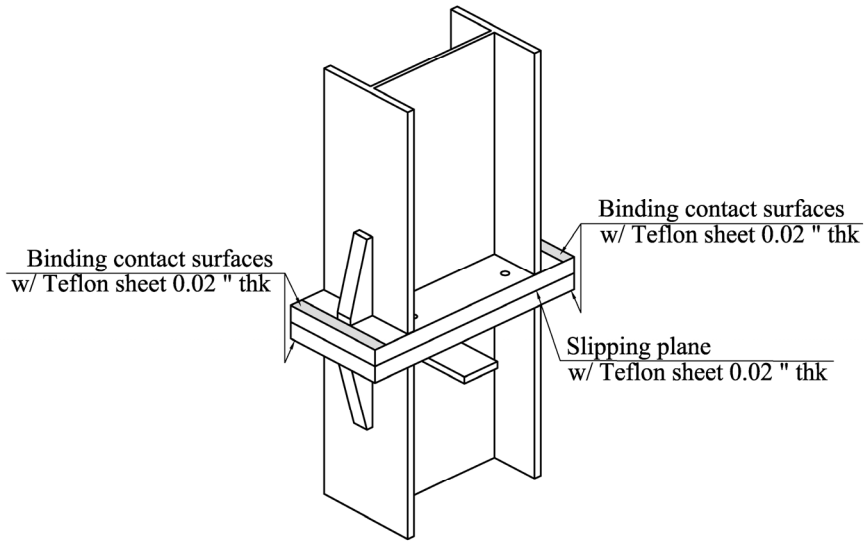

Figure 9-9. 5-Teflon-insert friction condition (collar is removed for clarity)

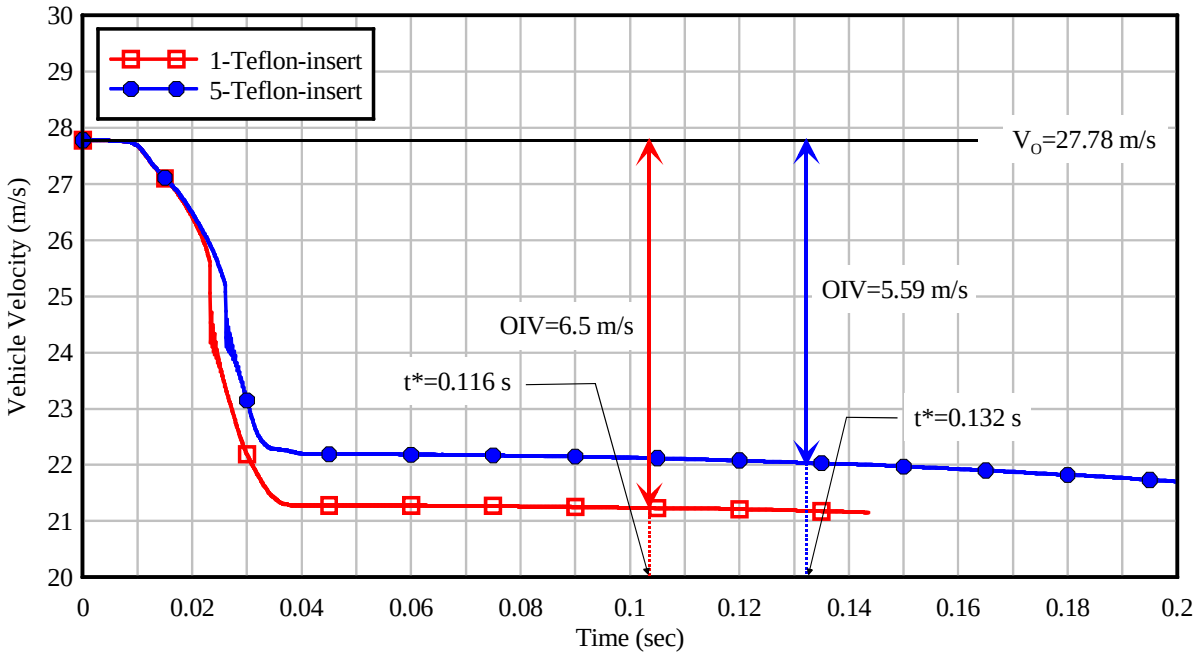

Figure 9-10. OIV and vehicle velocity time history comparison of different Teflon sheet applications

Nevertheless, further improvement in the dynamic performance of the connection, to meet the evaluation criteria per NCHRP 350 for high-speed impact scenarios and to enable an even wider margin to safety per MASH, was still preferable. Generally, under crash conditions, the ratio of masses of the impacting objects significantly affects the responses of the objects after impact. Hence, for a small car mass of 820 kg, the impact severity can be improved by reducing the mass of the structural supports (posts and breakaway connections). Materials with a higher ratio of strength and mass density, such as high strength steel and fiber-reinforced composites, would be appealing candidates for this application. However, it was determined that selecting an alternative post section to reduce the mass of the structural support—with minimal change to the current sign structure configuration—was desirable. Hence, a W12x40 wide flanged beam, which has a lower distributed mass per unit length than a W12x45 beam, was selected for the structural supports. Note that the W12x40 beam also meets the structural wind load requirements per AASHTO (see structural calculation in Appendix A). Furthermore, there is strong similarity between the height and width dimensions of W12x40 and W12x45 beams, so that only minimum modifications to the breakaway connection components were needed.

Simulation of an impact by an 820 kg vehicle, at 100 km/h and 20-degree impact angle, impacting the sign structure with W12x40 posts above the connection zone was performed to evaluate the OIV. As expected, by reducing the post weight by 5 lbf/ft (i.e., W12x40 vs. W12x45), an improved OIV of 5.2 m/s for the critical condition was obtained (Figure 9-11). Hence, the simulation results indicate that the OIV is close to the limit set by NCHRP 350, and is very likely to pass MASH (where the small car mass is 1100 kg). Although newly developed highway safety hardware must conform to MASH testing and evaluation criteria, a validated finite element model of an 1100 kg test vehicle is not yet available. As such, the 820 kg pendulum impactor model was used as the small car test vehicle in the numerical development of the breakaway connection.

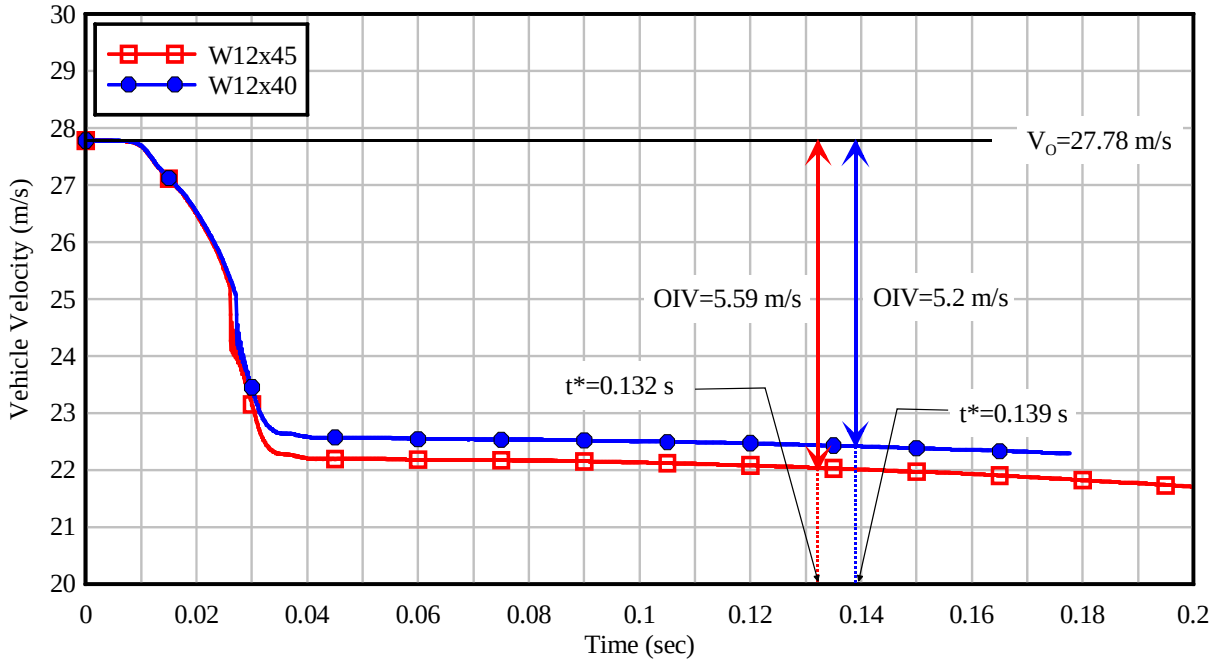

Figure 9-11. Comparison of OIV results for different post sizes

CHAPTER 10
IMPACT PENDULUM TESTING

10.1 Introduction

Using structural impact modeling and analysis techniques, a shear-controlled moment collar connection was developed and discussed in previous chapters. The breakaway connection was numerically evaluated to assess structural adequacy and dynamic performance criteria set forth by AASHTO and NCHRP 350. In addition to numerical evaluation, static experimental (laboratory) tests were performed to quantify the moment capacity and static equivalent impact shear capacity of the connection.

Although numerical impact simulation played a key role in the development of the connection, physical impact testing was still required to confirm adequate breakaway performance of the connection under impact loading conditions. Hence, the breakaway performance of the newly developed post connection was confirmed experimentally using pendulum impact testing. During the course of this study, the AASHTO (2009) MASH guidelines were adopted by AASHTO as an update to NCHRP 350. For this reason, the pendulum impact tests described in this chapter were conducted using the impact conditions (impactor mass, speed, and angle) specified in the MASH guidelines rather than the NCHRP 350 guidelines.

10.2 Breakaway Connection System Subjected to Pendulum Impact Testing

In Figure 10-1, an exploded view is presented of the final design of the shear-controlled moment collar connection that was subjected to impact pendulum testing. The final connection design was developed from numerical simulation and static experimental testing, as presented in Chapters 6, 7, 8 and 9.

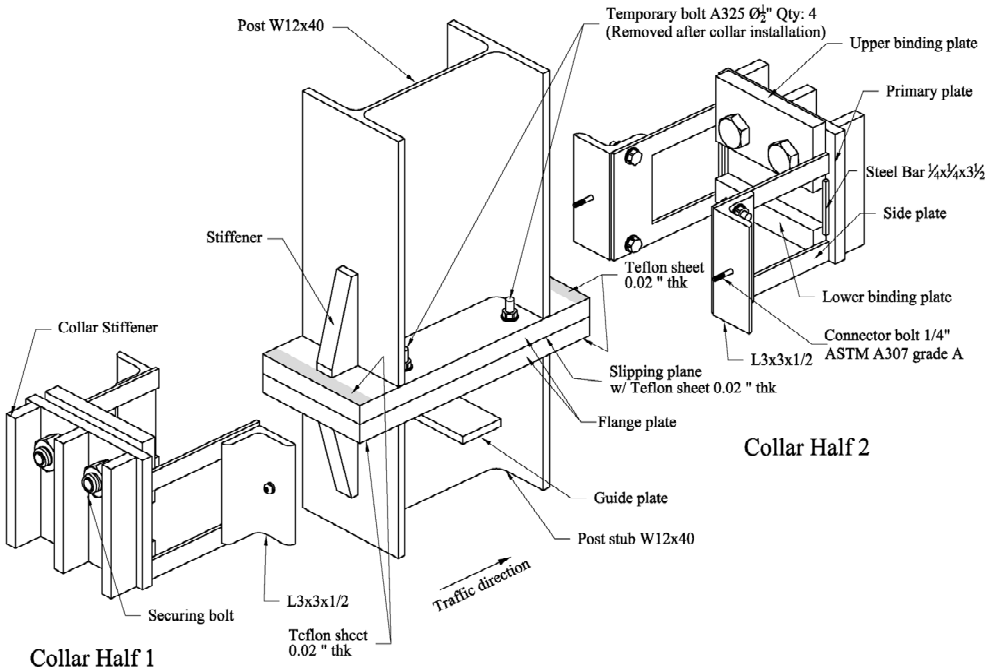

Figure 10-1. Breakaway connection subjected to impact pendulum testing

The breakaway connection that was subjected to impact testing featured three main parts: post, post stub, and collar halves. Teflon was used at all key sliding interfaces to minimize connection friction so that the impact shear capacity of the breakaway connection was governed by the connector bolt strength. Based upon results obtained from the static experimental test program described earlier, minor modifications were made to selected details of the connection to improve the connection strength. For example, the lengths of slotted holes in the collar side plates and in the primary binding plates were reduced. A detailed set of fabrication drawings for the final connection design can be found in Appendix E.

10.3 Test Configuration and Procedure

Pendulum impact testing of the breakaway connection was conducted on the structure shown in Figure 10-2. The test structure consisted of a channel attached to a single post of the size that would be used in a three-post sign support structure. The attached channel was employed to account for the added mass of sign panel components that were not present in the impact test article. The mass of the attached channel therefore equaled that of the sign panel and associated hardware that was located within the tributary width of the middle post of a three-post sign system.

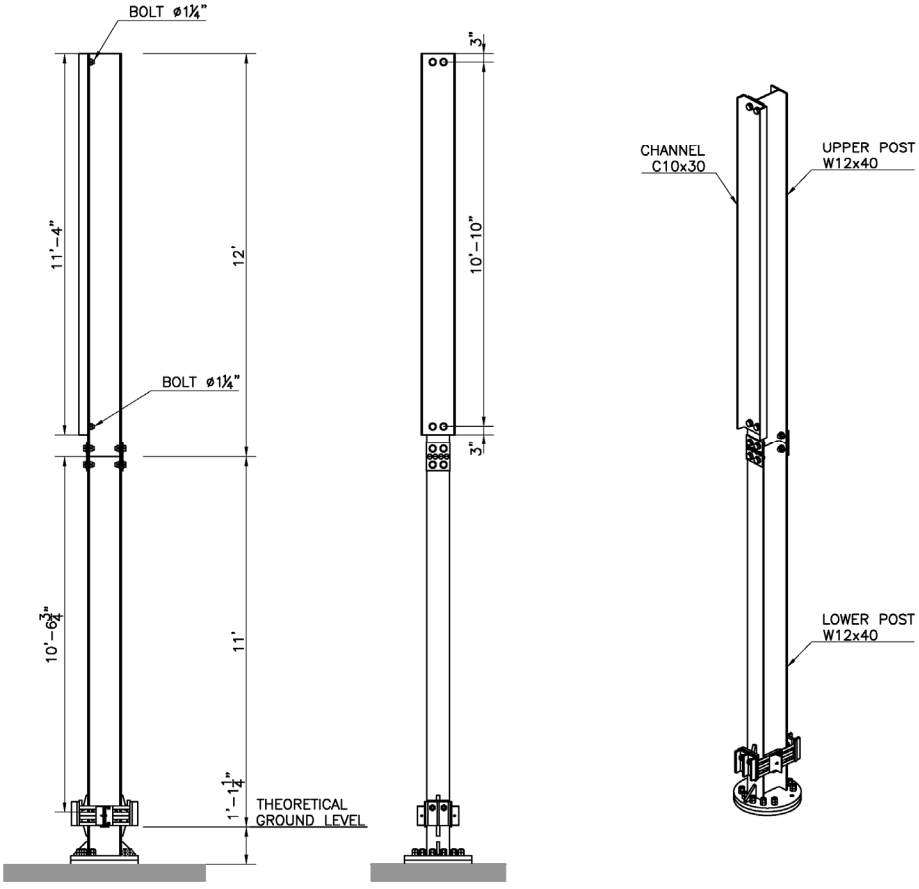

Figure 10-2. Breakaway post structure used in impact tests

The pendulum impactor used in this study was fabricated to match the 1100 kg MASH-specified mass. The mass of the small car test vehicle used in impact testing of roadside

hardware changed from 820 kg in NCHRP 350 to 1100 kg in MASH. In Figure 10-3, an isometric view of the 1100 kg pendulum impactor used in this study is presented. The pendulum impactor consisted of two main parts: a mass block and a rigid nose. In this system, the weight of the mass block can be adjusted by adding or removing steel side plates.

At the time this study was conducted, due to the fact that MASH is a relatively new standard, the frontal crush stiffness of a suitable 1100 kg car was not defined either in a publicly available finite element model (e.g., from NCAC) or in a documented surrogate test vehicle, such as a pendulum impactor or bogie. Lacking a clear definition of the crush stiffness of the 1100 kg vehicle, it was determined that initial testing of the breakaway connection would be performed instead using a rigid nose impactor, as shown in Figure 10-3. It is important to note that, in this study, the pendulum impactor was designed and fabricated such that the rigid nose can be detached, and a crushable impact nose re-attached. In the future, when frontal crush stiffness data become available for the 1100 kg vehicle, more refined pendulum impact tests should be performed on the breakaway connection using a crushable nose. (Detailed fabrication drawings for the pendulum impactor are given in Appendix F).

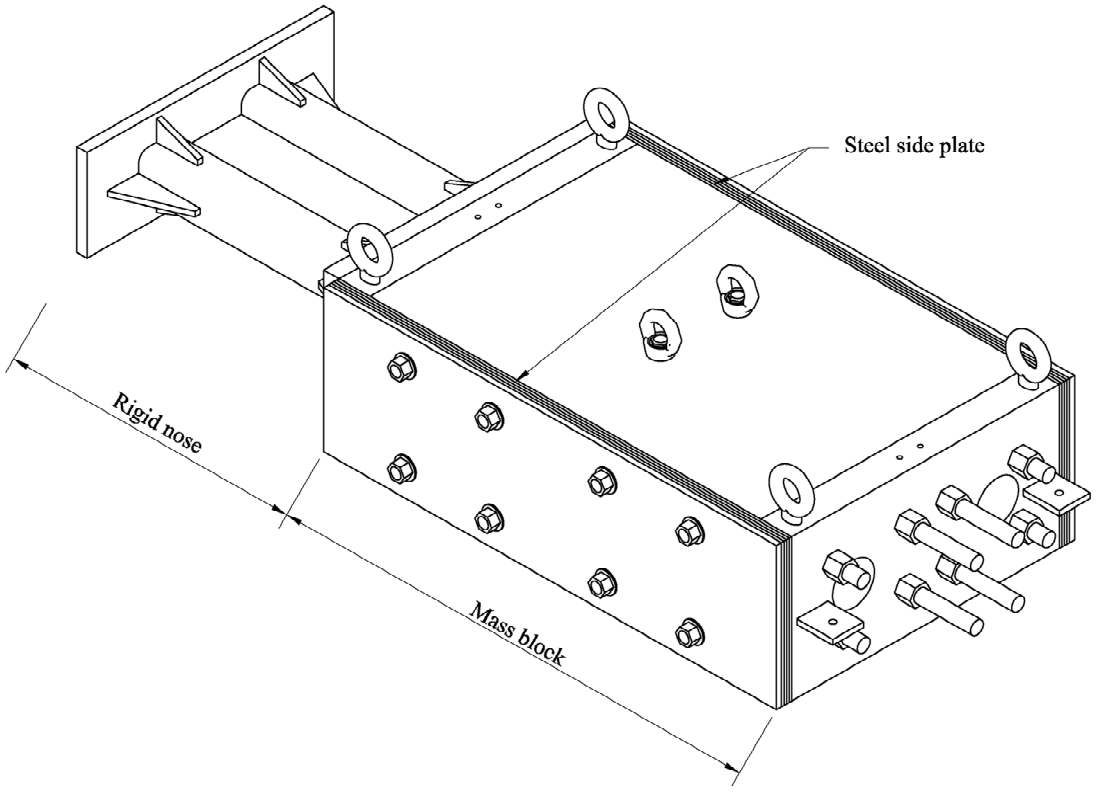

Figure 10-3. Pendulum impactor with rigid nose (1100 kg)

Four tests were conducted to evaluate the dynamic performance of the breakaway system. Two test repetitions each were conducted at impact angles of 25 degrees (referred to as T-25-1 and T-25-2) and 0 degrees (referred to as T-0-1 and T-0-2) as shown in Figure 10-4. In accordance with the requirements of MASH, the impact speed of the pendulum was targeted at 30 km/h (18.64 mph) for all tests. To achieve this impact velocity, the pendulum impactor was raised to a height of 12 ft (illustrated in Figure 10-5) above the impact point, as determined from the relationship:

$$h = \frac{v^2}{2g} \tag{10-1}$$

where v is the target impact speed (30 km/h), g is gravitational acceleration, and h is the drop height. After raising the impactor to the necessary height, it was released to strike the post. The mid-height of the impact zone on the post was located 19 in. above the theoretical ground level as shown in Figure 10-6.

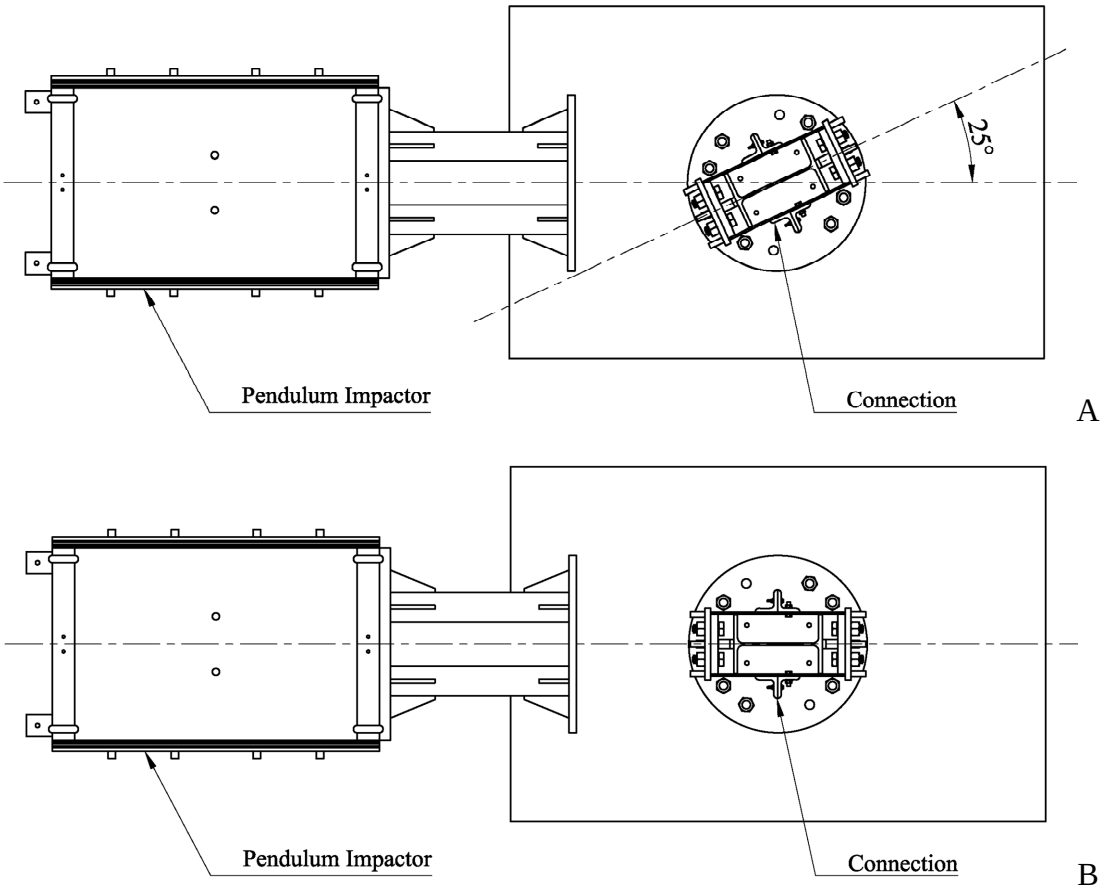

Figure 10-4. Pendulum impact test angles: A) 25-degree; B) 0-degree

10.4 Instrumentation Plan

During each pendulum impact test, an instrumentation and data acquisition (DAQ) system was used to measure the responses of both impactor and breakaway support prior to, during, and following impact. All instrumentation attached to the data acquisition system was sampled at a frequency of 10 kHz (10,000 samples/second/channel) to provide ample data collection during the impact event. The instrumentation network used during testing is presented in Figures 10-7 and 10-8, and consisted of:

- Infrared optical break beam sensors
- Pressure sensitive tape switches
- Accelerometers
- High-speed cameras
- Washer load cells
- Strain gauges

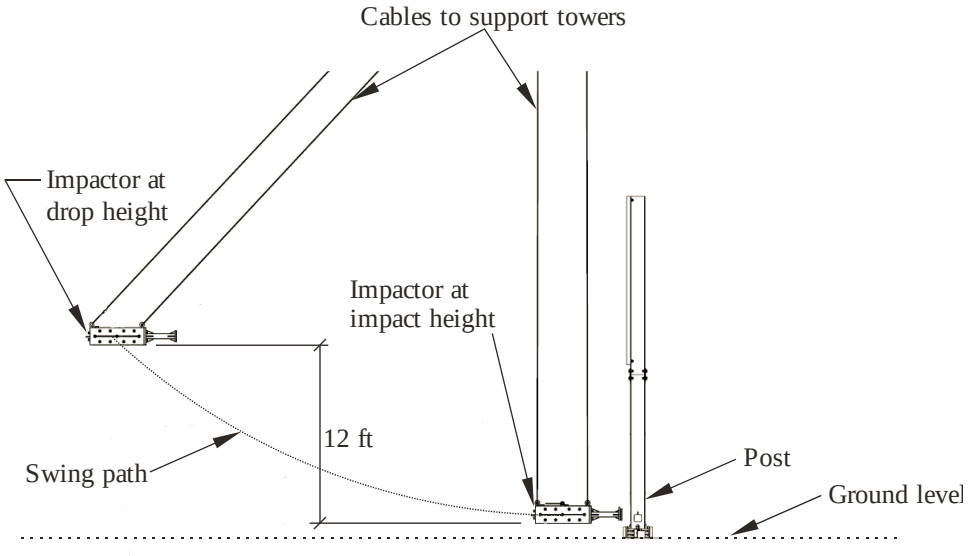

Figure 10-5. Pendulum impactor at drop height (cable support towers not shown for clarity)

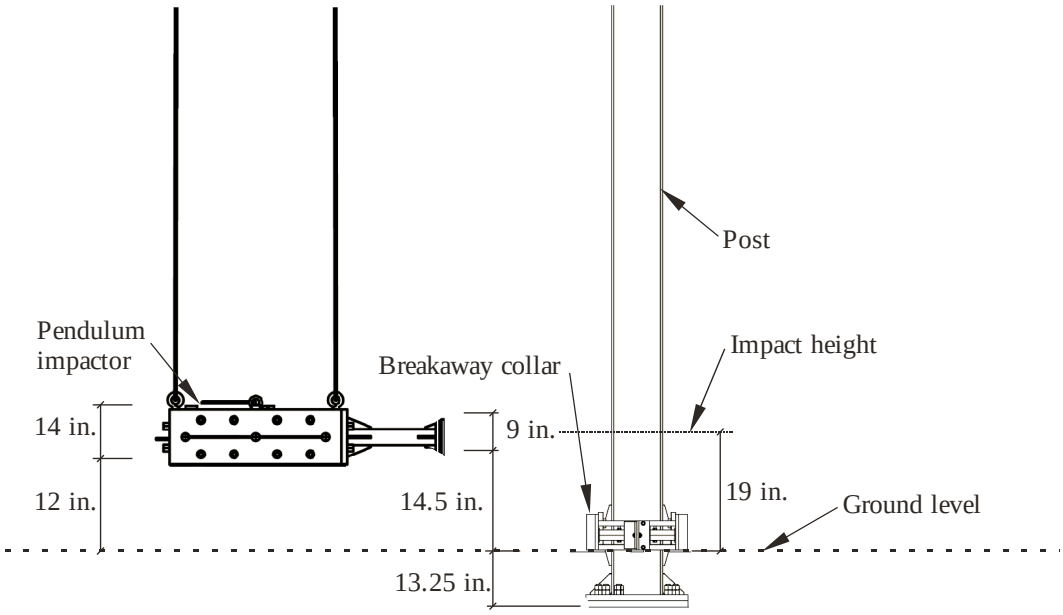

Figure 10-6. Pendulum impactor at point of impact

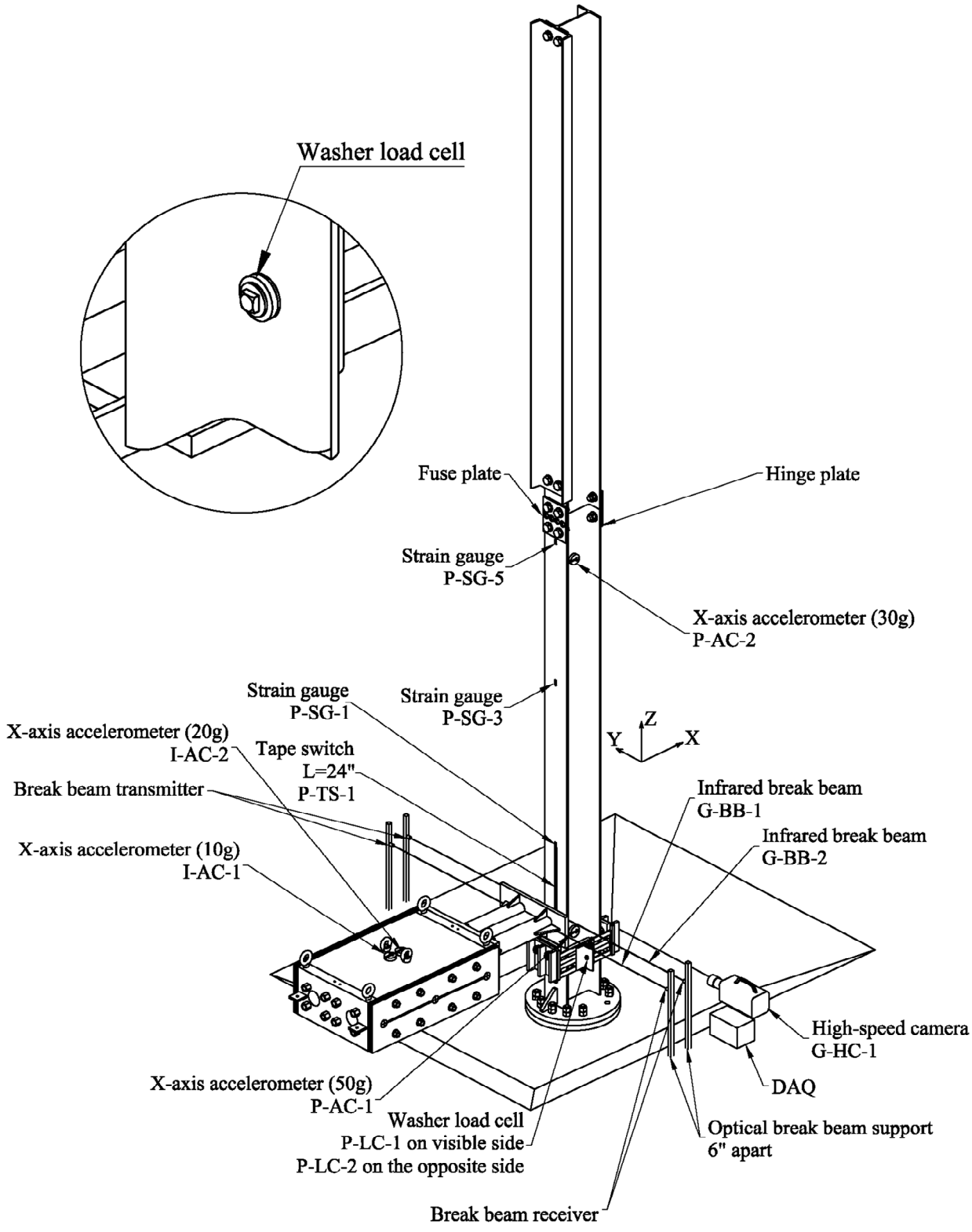

Figure 10-7. Isometric front view of instrumentation setup for impact pendulum test

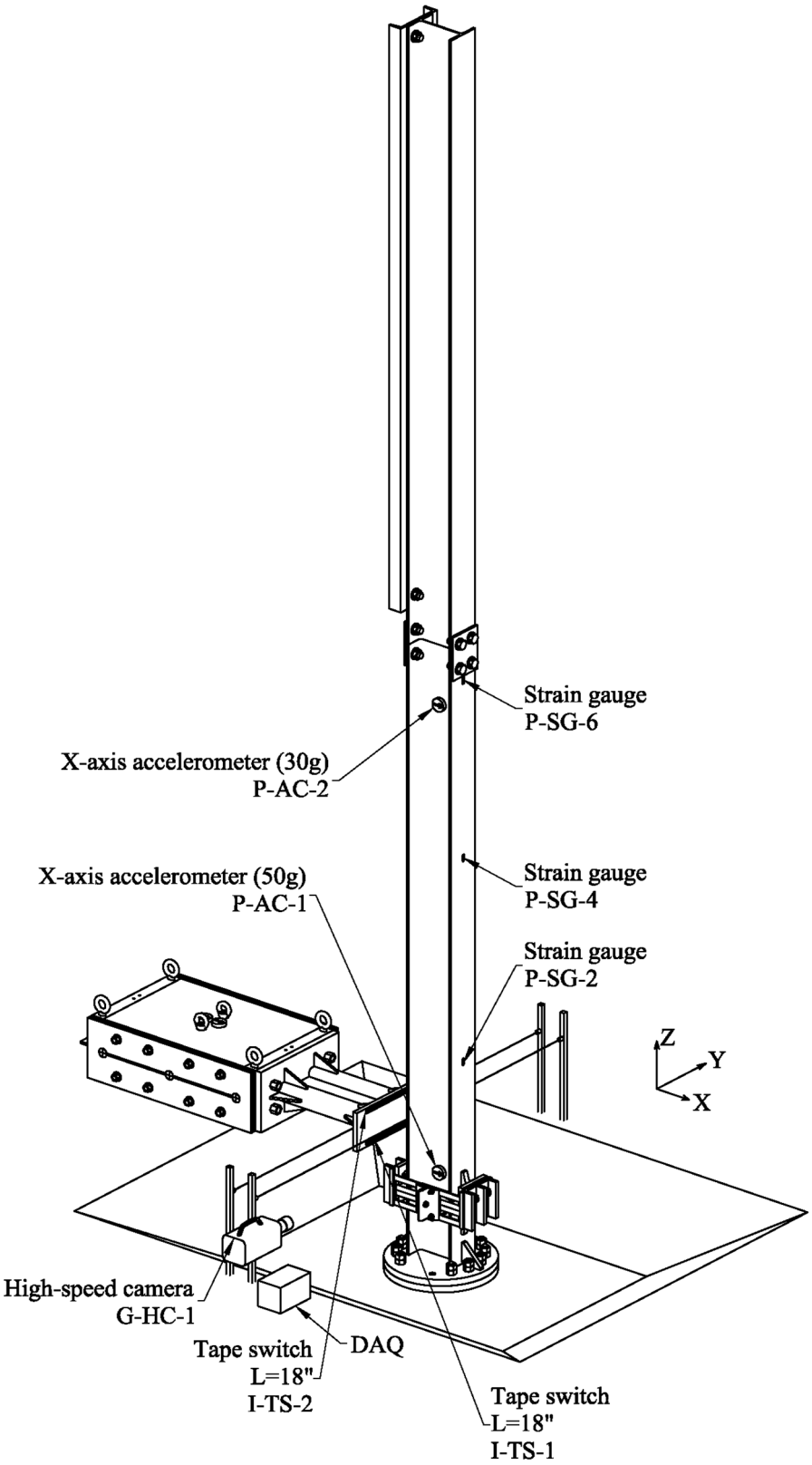

Figure 10-8. Isometric back view of instrumentation setup for impact pendulum test

10.4.1 Infrared Optical Break Beam Sensors

Optical break beams were used to quantify pendulum speed at the point of impact (Figure 10-9). Two pairs of infrared optical break beam sensors (four total) were used: one pair located near the impact point on the post and the other pair located 12 in. farther away (i.e., the separation distance between the sensor pairs was 12 in.). Each sensor pair consisted of a transmitter and receiver, mounted on an aluminum stand (see Figure 10-10), that were positioned at the mid-height of the rigid nose of the impactor at the bottom of the swing. When the impactor passed between the transmitter and the receiver, the infrared beam was interrupted and the data acquisition system captured the time at which the interruption occurred. From the distance between the sensors, and the time duration between the beam interruption events, the speed of the impactor just before contact with the test article was accurately determined. Specifications for each sensor are given in Table 10-1.

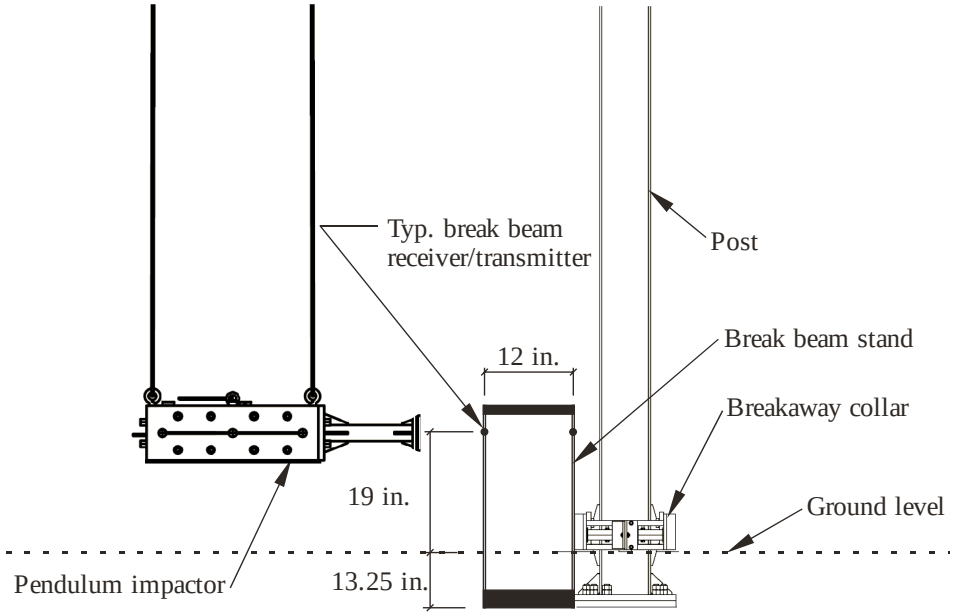

Figure 10-9. Location of break beams (elevation view)

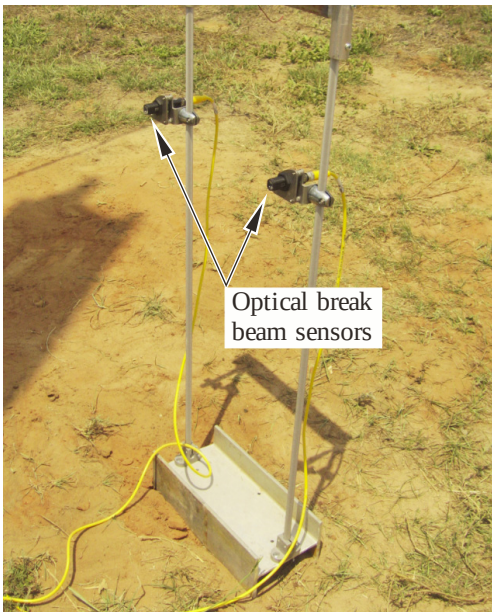

Figure 10-10. Optical break beams mounted on stand

Table 10-1. Specifications for optical break beams

Manufacturer	Balluff
Receiver model	BLS 18KF-NA-1PP-S4-C
Transmitter model	BLS 18KF-XX-1P-S4-L
Range (ft)	65 ft.

10.4.2 Pressure Sensitive Tape Switches

Tape switches are sensors that close an electrical circuit when compressed, and can therefore be used to detect contact without altering the dynamic response of the test article. In this study, two switches were attached to the impact face of the rigid nose (at the top and bottom of the impact face as shown in Figure 10-11), which were used to send a “zero time” marker signal to the data acquisition system immediately upon impact. By positioning two tape switches at different vertical elevations on the impact face, it was possible to determine if impact occurred flush to the face of the post (e.g. if pitching of the impactor occurred prior to impact). Furthermore, the “zero time” marker provided a reference point showing the instant in time at which impact occurred with the post. An additional tape switch, intended for redundancy, was also installed along the center of front flange (impact face) of the post in the head-on (0-degree) impact tests. Technical specifications for the tape switches are provided in Table 10-2.

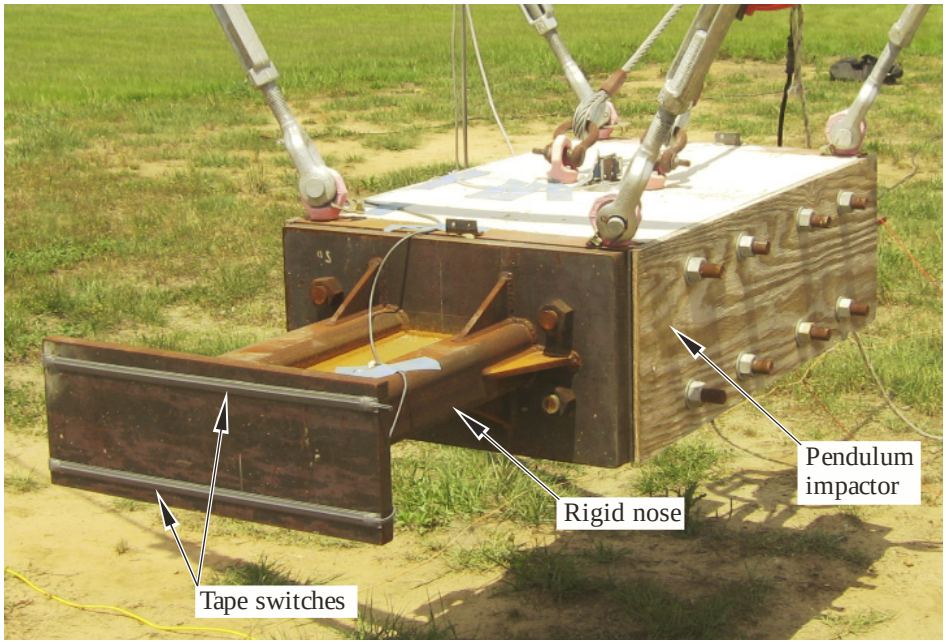

Figure 10-11. Tape switches mounted on rigid nose of impactor

Table 10-2. Specifications for tape switches

Manufacturer	Tapeswitch Corporation
Ribbon switch type	131-A
Actuation force	60 oz.
Switch lengths used	18 in. and 24 in.
Dimensions	3/4" in. wide, 3/16 in. thick
Minimum bend radius	1 in.

10.4.3 Accelerometers

To measure acceleration and to indirectly quantify impact force through the duration of the impact event, accelerometers were installed on the pendulum impactor and, in selected cases, on the post. Based on acceleration results obtained from numerical impact analyses of the connection, accelerometers with a measurement range of 0 – 50 g were employed for the impact experiments. A summary of accelerometer specifications is presented in Table 10-3. Each accelerometer was calibrated by Summit Instruments prior to usage to verify accuracy.

Typical impact tests utilized three accelerometers attached to a mounting bracket at the center of the top face of the impactor: two accelerometers in the direction of impact and a third in the vertical direction (Figures 10-12 and 10-13). Two accelerometers were also installed on the web of the post and were aligned with the direction of the impact. One accelerometer was positioned 6 in. above the top of the flange plate at the bottom of the post and the other was positioned 12 in. below the mid-height of the fuse plate (Figure 10-14). Note however, that for the tests conducted at a 25-degree impact angle, accelerometers were not installed on the post.

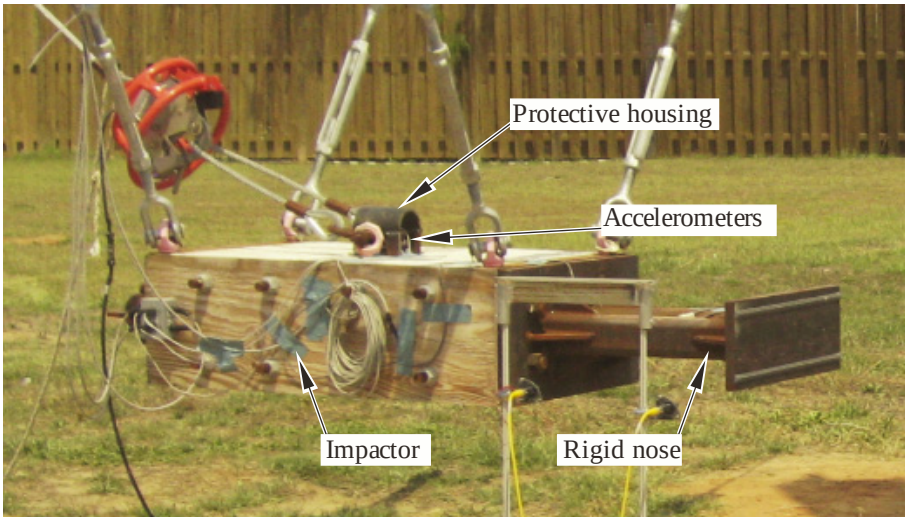

Figure 10-12. Location of accelerometers on impactor

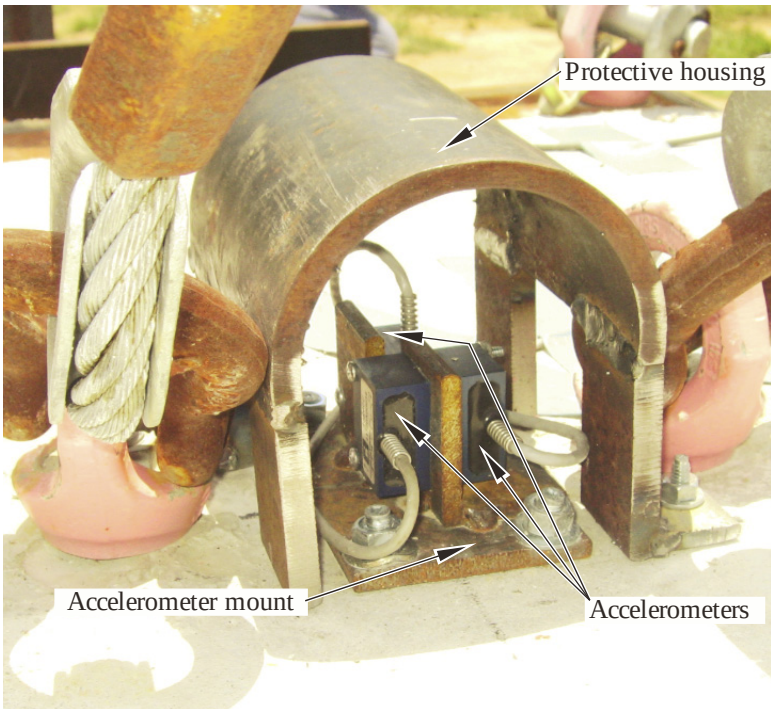

Figure 10-13. Accelerometers mounted on top of impactor

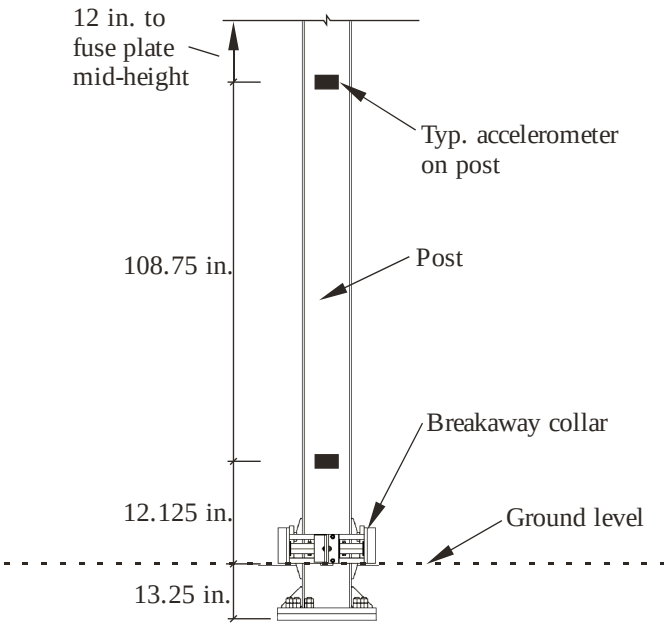

Figure 10-14. Location of accelerometers on post (elevation view)

Table 10-3. Specifications for accelerometers

Manufacturer	Model number	Range (g)	Bandwidth (Hz)
Summit Instruments	13200B	10	223
Summit Instruments	13200C	30	400
Summit Instruments	13200C	50	400

10.4.4 High-speed Cameras

During each impact test, two high-speed digital video cameras (shown in Figure 10-15) were directed toward the test article to enable qualitative evaluation of the breakaway connection behavior (for comparison to predictions from numerical simulation) as well as redundant quantitative determination of impactor speed at the point of contact. One camera was configured to produce a close-up side view of the impact zone and the breakaway connection, while the second was configured to produce a wide angle view of the overall behavior of the post during and after impact. Each camera recorded the impact events at a rate of 2000 frames/second, as noted in the specifications in Table 10-4.

Figure 10-15. High-speed digital video cameras

Table 10-4. Specifications for high-speed cameras

Manufacturer	Integrated Design Tools (IDT)
Distributor	Dynamic Imaging, LLC
Camera model	MotionXtra N-3
Image resolution	1280 x 1024
Frame rate	1000 fps (frames/sec)
Frame rate (plus mode)	2000 fps (frames/sec)
Memory	1.25GB
Maximum recording time	0.76 sec.

10.4.5 Washer Load Cells

During a vehicle impact event, impact forces are transmitted through the post and into the breakaway collar, the two halves of which are held together by two connector bolts. For the breakaway mechanism to work correctly, the bolts must fracture, separating the collar halves from each other and allowing the post to translate away from the impacting vehicle. To capture the force transmitted through these frangible connector bolts during the pendulum impact testing, a washer load cell was installed on each of the two connector bolts to measure bolt loads during impact. Since the connector bolt strength used in the breakaway connection was approximately 2.8 kip (as confirmed during static testing), washer load cells with a capacity of 5 kip were used during the pendulum tests. Each washer load cell was installed using spherical washer sets as shown in Figure 10-16 and 10-17. Washer load cell specifications are given in Table 10-5.

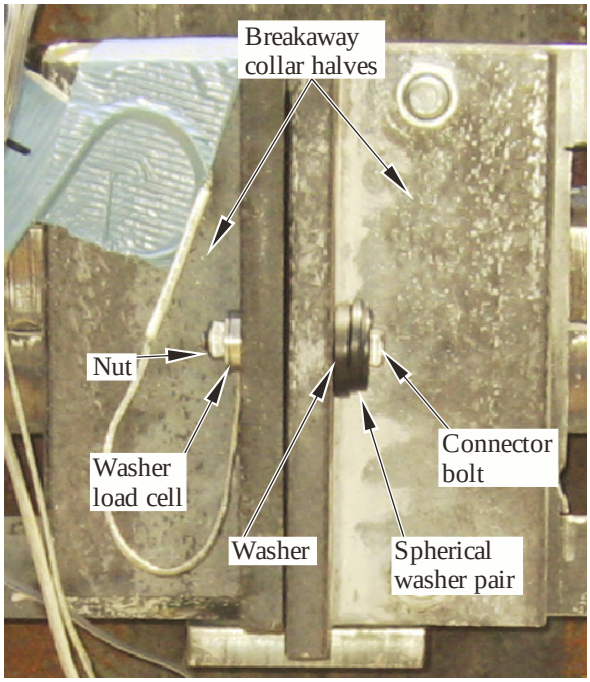

Figure 10-16. Washer load cell installation

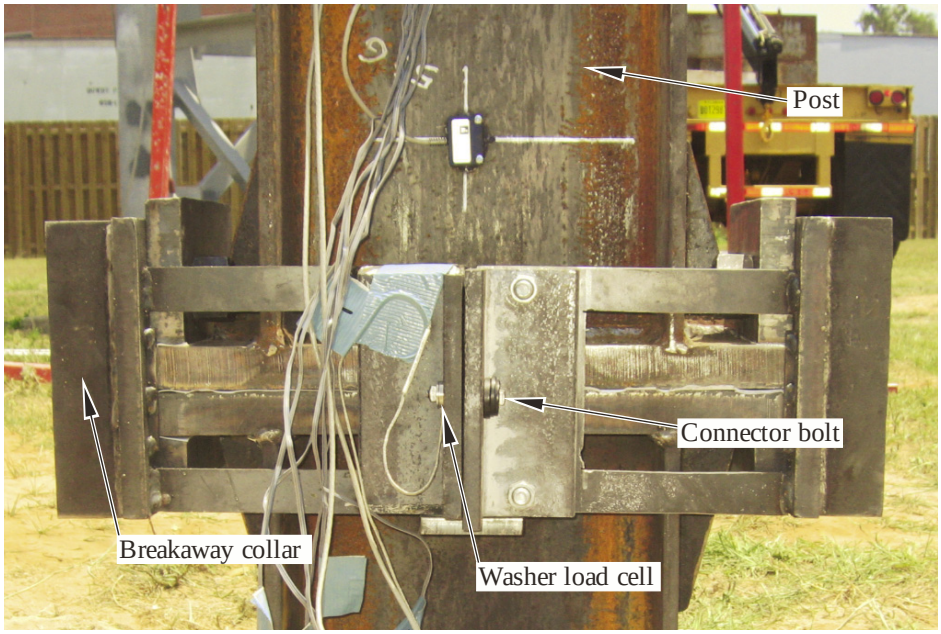

Figure 10-17. Washer load cells installed on breakaway collar

Table 10-5. Specifications for washer load cells

Manufacturer	Omega Engineering, Inc.
Model	LC901-3/8-10K
Capacity	10 kip
Bolt hole diameter	3/8 in.

10.4.6 Strain Gauges

Three sets of strain gauges were installed on the sign post, at various elevations (Figure 10-18), to facilitate determination of flexural moments in the post during impact. Each set consisted of two strain gauges installed on opposite outer sides of the post flanges. In addition, for the oblique test series (impact angle of 25-degrees), two additional strain gauges were installed on the side surfaces of the fuse plate as shown in Figure 10-19. The fuse plate strain gauges were installed to aid in determining whether the fuse plate yielded during or after impact.

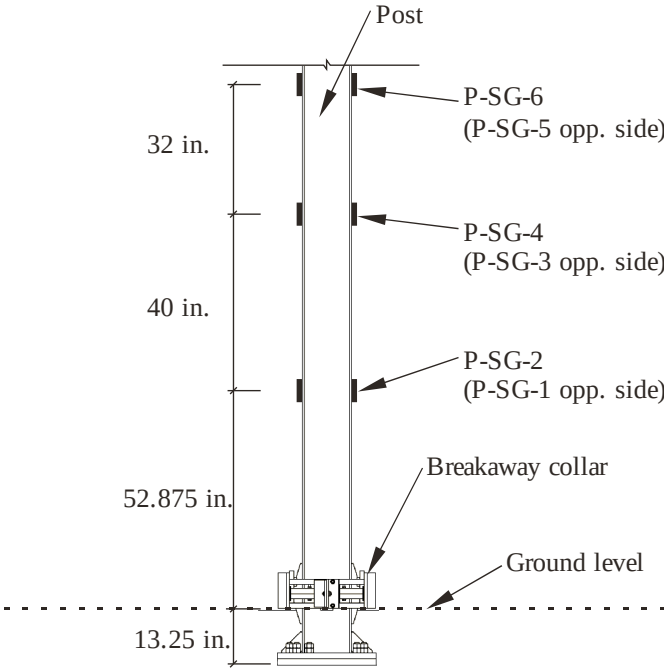

Figure 10-18. Strain gauge locations on post

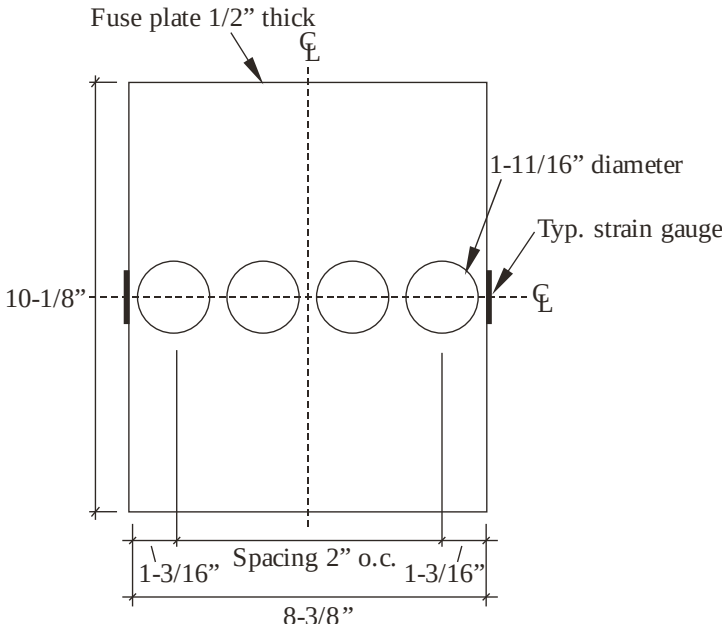

Figure 10-19. Strain gauge locations on fuse plate

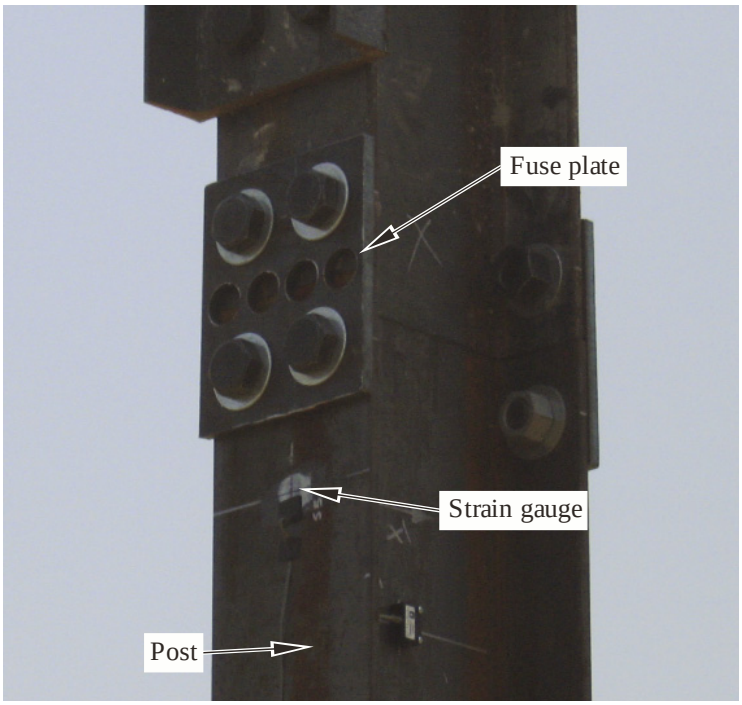

Figure 10-20. Strain gauge installed on post

10.5 Oblique Impact Experiments

Two oblique impact experiments were conducted on the breakaway connection system at an angle of impact of 25-degrees (recall Figure 10-4A). In the first test (T-25-1), all system components (connector bolts, collar, lower post segment, upper post segment, and upper channel) were newly purchased or newly fabricated (i.e., undamaged and previously untested). In the second test repetition (T-25-2), system components were either replaced with new parts (e.g., connector bolts), were undamaged from the previous test (e.g., upper post segment), or repaired/refabricated (e.g., new side plates were welded to the primary end plates in the collar halves). Hence, each test was conducted on a functionally undamaged system.

In both tests, the target impact velocity of 30 km/hr, as measured from the optical break beams, was achieved with less than 3% error: Test T-25-1: 29.50 km/hr (-1.6%); Test T-25-2: 29.34 km/hr (-2.2%). Figure 10-21 presents a series of snapshots taken from the wide-angle high-speed camera during the impact experiment T-25-2. (Note that for all data shown, including the snapshots from the high-speed camera, impact is defined to occur at t = 0 sec, which indicates contact as determined by the tape switches). Overall behavior of the system, as presented in the snapshots, was as expected: the breakaway collar separated cleanly from the post stub upon impact, thus eliminating possible spikes in impactor (surrogate vehicle) deceleration that would be associated with snagging of the collar on the post stub.

In contrast to simulation results presented in previous chapters, the fuse plate (located immediately below the installed channel on the impact side of the post) did not fail during the pendulum tests as would be typical for a full three-post sign structure (such as illustrated in Figure 2-2). This is due to the fact that only the tributary mass, and not the rotational stiffness, of a full three-post sign was accounted for during the impact experiments. Importantly, numerical simulations (discussed later in this section) of impacts on the same single-post configuration that was used in the experimental testing showed the same behavior: no fuse plate failure and no significant rotation of the upper post segment relative to the lower segment. Hence, for the single post configuration, predictions of overall system response and base connection breakaway behavior that were obtained from numerical impact simulation agreed with results obtained from physical testing of a corresponding test article and impact condition.

As noted in previous chapters, however, finite element models of three-post systems (which include both the mass of the sign panel and the stiffness of the panel and the adjacent posts), subjected to impacts by either a pendulum impactor or vehicle model, indicate fuse plate failure and rotation of the lower post segment away from the impactor. Given the agreement observed between simulation and test results for the single post configuration, it is expected that testing of a three-post sign structure would likely produce fuse plate failure and lower post segment rotation as predicted by simulation.

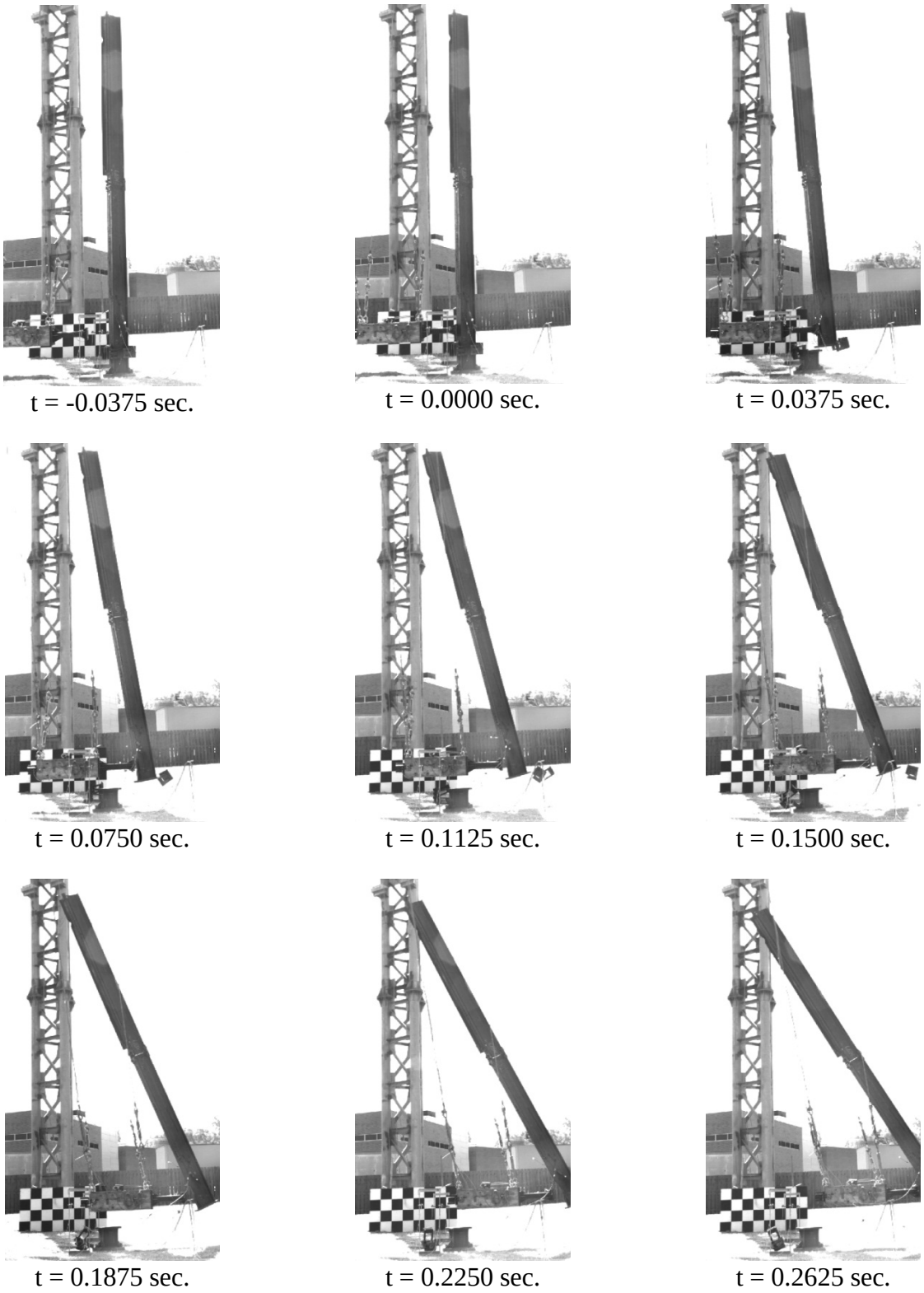

Figure 10-21. Oblique impact from high-speed camera (where t = 0 sec. indicates contact between post and pendulum) for experiment T-25-2

Accelerations of the pendulum impactor for test T-25-1 are shown in Figure 10-22. Three accelerometers are shown in this plot: I-AC-1 and I-AC-2 were oriented in the direction of impact; I-AC-3 was oriented in the vertical direction. Accelerations experienced by the surrogate vehicle peaked at 26 g, which occurred immediately after the connector bolts fractured. In comparison to the maximum ridedown deceleration permitted by MASH, the recorded acceleration level is relatively high. However with the introduction of a crushable nose on the pendulum impactor, which will emulate the frontal stiffness of a small passenger car, the acceleration levels will be reduced dramatically due to the lower stiffness of a crushable nose as compared to the rigid nose.

Loads from the washer load cells (which measured connector bolt loads) are plotted in Figure 10-23. Peak loads measured for the connector bolts were found to be 315 lbf and 452 lbf, respectively for P-LC-1 and P-LC-2. These loads are substantially less than the 2.8 kip bolt ultimate failure capacity observed during earlier static bolt testing (see Section 7.2). It is suspected that the lower than expected bolt forces measured during pendulum impact testing are the result of non-concentric loading of the washers. During the static testing phase of this study (Chapter 7), the accuracy of the washer load cells was found to be sensitive to the uniformity of load application. Reliable static load measurements were ultimately achieved in the static test program by using spherical washer sets that reduced (or eliminated) load eccentricities on the washer load cells. Similar spherical washer sets (Figure 10-16) were therefore also employed in the pendulum impact tests. However, it is hypothesized that sudden application of impact loading likely caused the spherical washer set to slip (displace) in a manner that produced eccentric loading on the washer load cells.

Stress results computed from strain gauge readings recorded during test T-25-1, with an assumed modulus of elasticity of 29,000 ksi (typical for mild steel), are shown in Figure 10-24. Note that the pairs of strain gauges are consecutively numbered (e.g., P-SG-1 and P-SG-2 are a pair, with P-SG-1 on the impact face of the post and P-SG-2 on the opposite side). Figure 10-24 shows an immediate spike of stress (i.e. strain) just after contact is made at t = 0.0008 seconds. Following this spike, strains rise slowly through time as the pendulum impactor applies force to the post, accelerating the post and causing rotation about its center of mass.

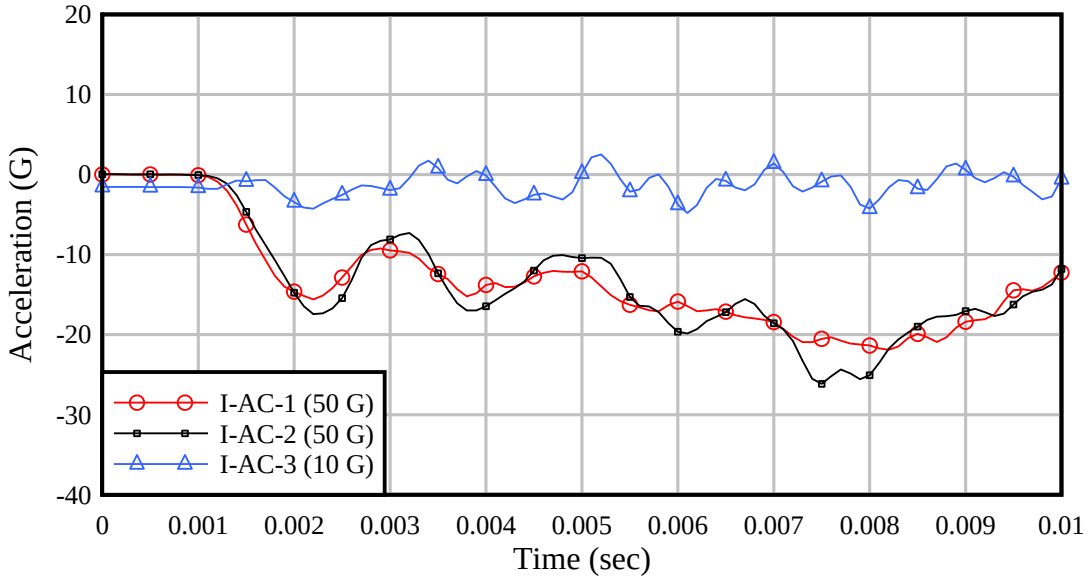

Figure 10-22. Acceleration data from impactor for test T-25-1

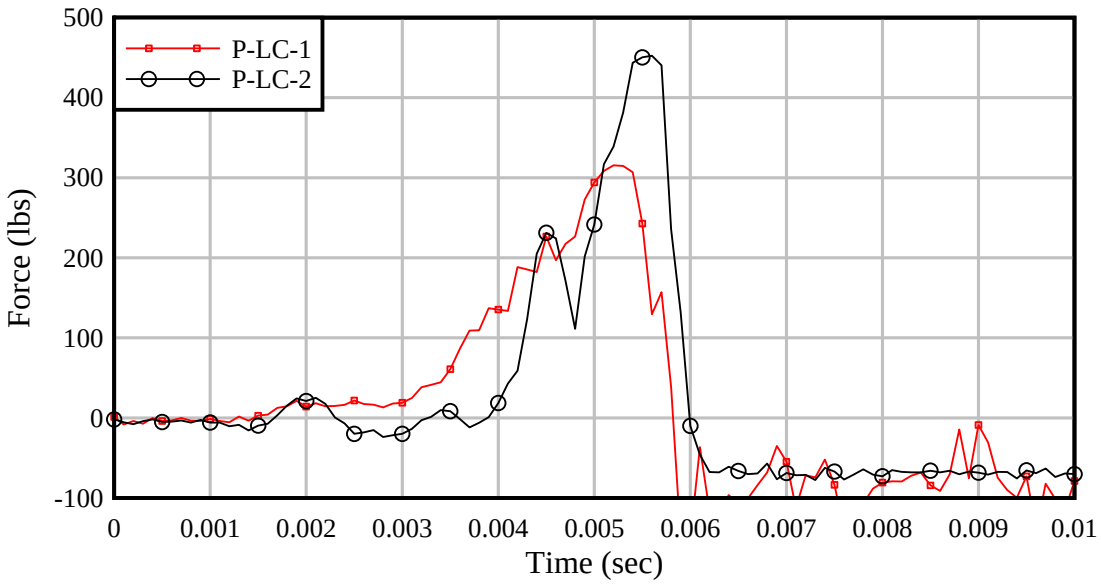

Figure 10-23. Washer load cell data for test T-25-1

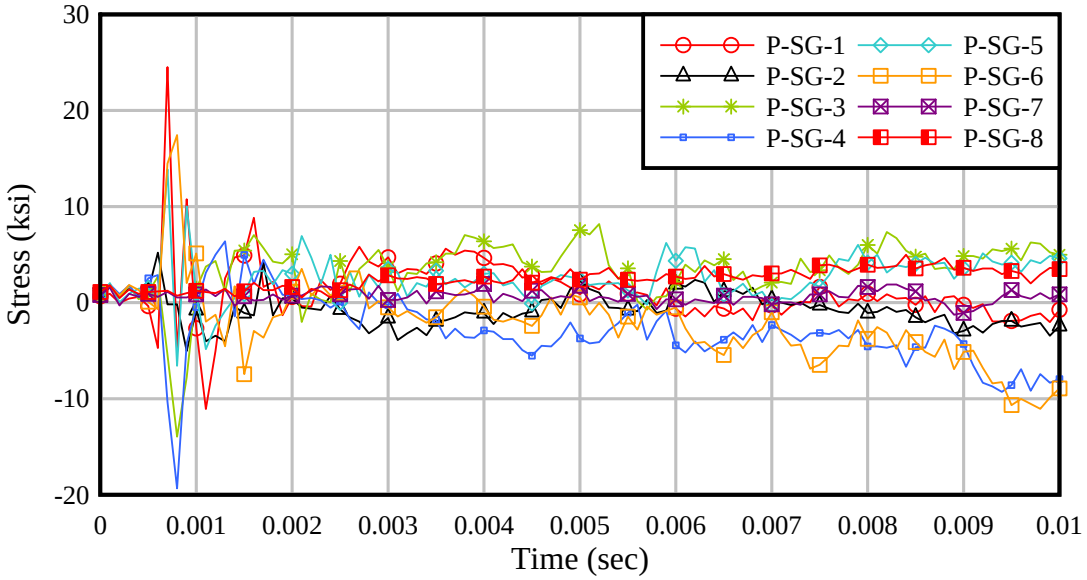

Figure 10-24. Strain gauge data converted to stress (assuming E = 29000 ksi) for test T-25-1

Accelerations of the pendulum impactor for test T-25-2, also conducted at an impact angle of 25-degrees, are shown in Figure 10-25. Data from three accelerometers are shown in this plot: I-AC-1 and I-AC-2 were oriented in the direction of impact; I-AC-3 was oriented in the vertical direction. Accelerations experienced by the surrogate vehicle peaked at 26 g, as was the case in the first test (T-25-1) at this impact angle. Hence, repeatability of the surrogate vehicle deceleration level from one test to the next was excellent. Furthermore, peak deceleration levels for tests T-25-1 and T-25-2 occurred at approximately the same point in time (0.0075 sec) after contact was made, again underscoring the repeatability of impact experiments.

Loads measured by the washer load cells during test T-25-2 are plotted in Figure 10-26. Peak loads measured were 316 lbf and 882 lbf for P-LC-1 and P-LC-2, respectively, which are again substantially less than the known ultimate bolt capacity of 2.8 kip. Stress results obtained from the strain gauge readings recorded during the test are shown in Figure 10-27, again, based on an assumed modulus of elasticity of 29,000 ksi. As in the previous test, there was a spike of strain occurring shortly after contact was made (approximately t = 0.0002 seconds). From this point forward, the strains rise slowly through time, as was observed with the previous test. Note that gauge P-SG-1 appears to have malfunctioned, as evidenced by the fact that a stress of 6 ksi was observed before impact even occurred. Hence, data corresponding to gauge P-SG-1 is considered invalid.

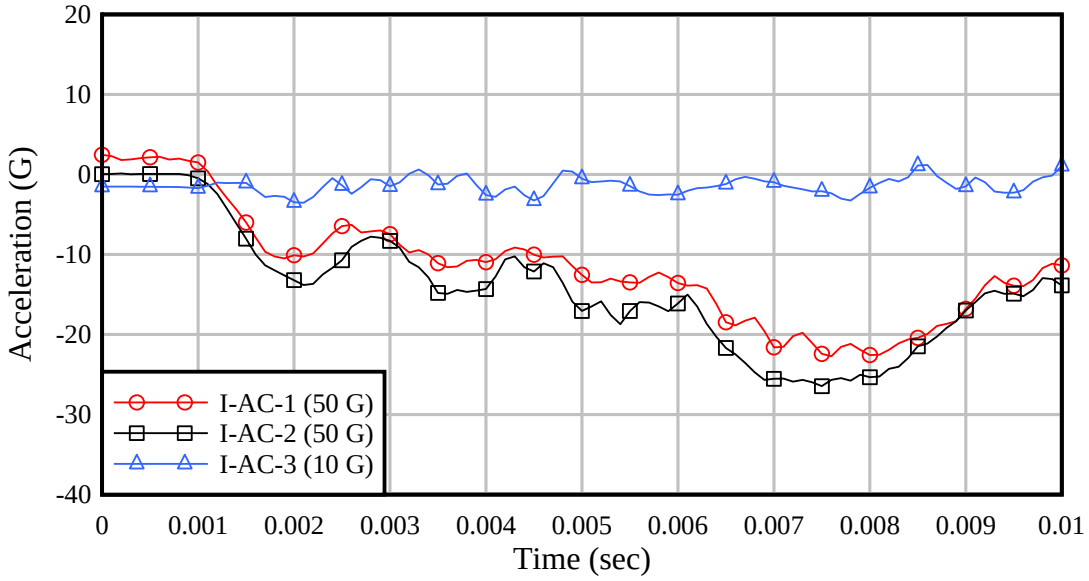

Figure 10-25. Acceleration data from impactor for T-25-2

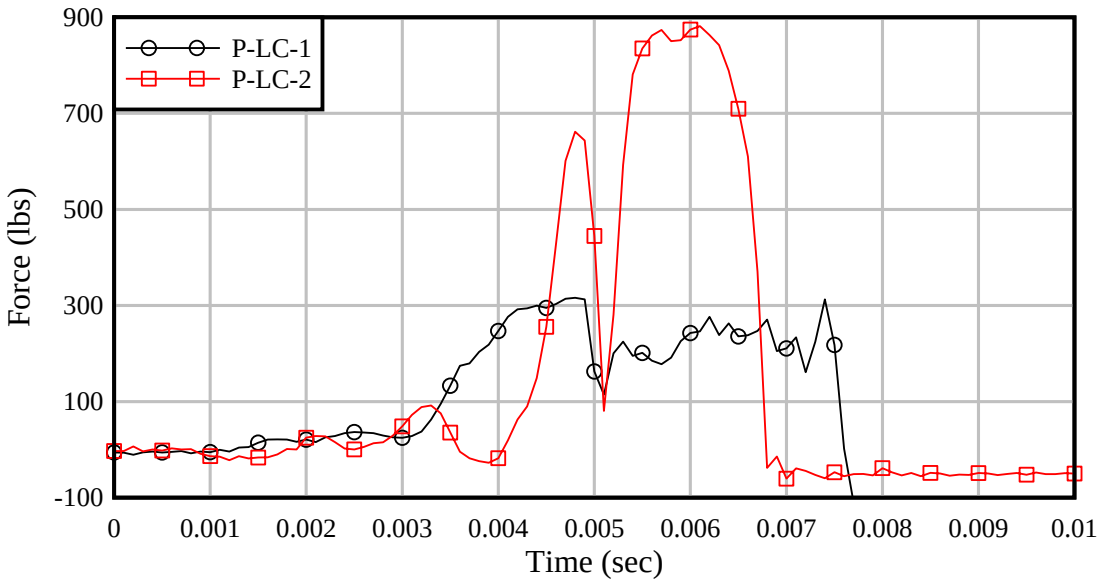

Figure 10-26. Washer load cell data for test T-25-2

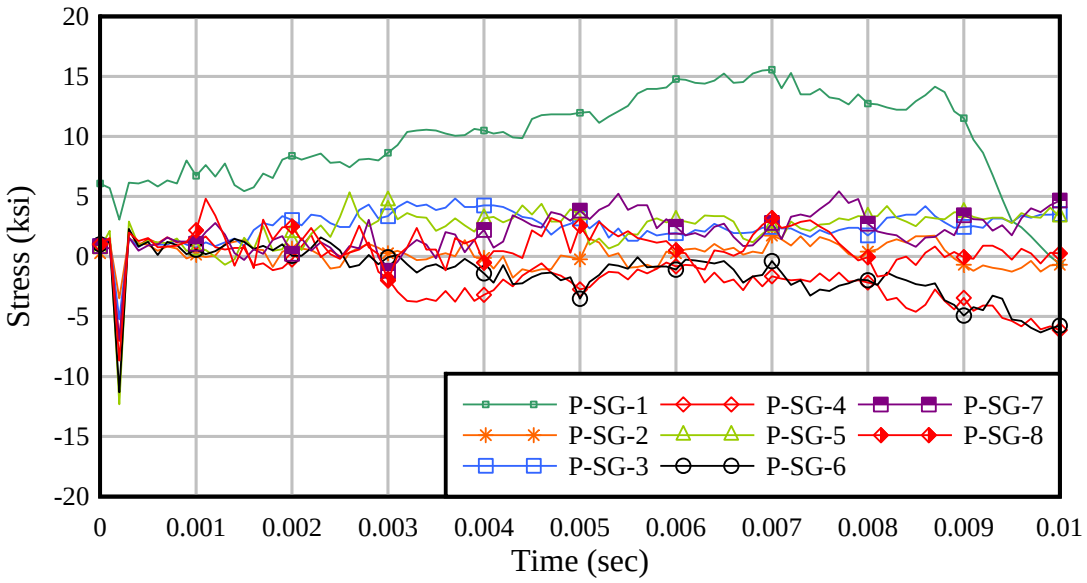

Figure 10-27 Strain gauge data converted to stress (assuming E = 29000 ksi) for test T-25-2

10.5.1 Comparison of Experimental Results and Rigid Nose Finite Element Impact Simulation

Dynamic finite element impact simulations described previously in this report have utilized either a crushable nose pendulum impactor model or a crushable vehicle model (either a small car or pickup truck) and either a two- or three-post complete sign structure model. The intent in conducting such simulations has been to assess anticipated breakaway connection response parameters, vehicle (or surrogate vehicle) response parameters, and occupant risk measures so that the adequacy—as defined by standards such as NCHRP 350 and MASH—of various candidate breakaway connection concepts could be evaluated. The iterative process of concept development and numerical assessment culminated in the previous chapter where a crushable nose small car surrogate (impact block) model and a crushable pickup truck model were used to assess the performance of the final breakaway connection system—integrated into a three-post sign structure model—that was ultimately subjected to pendulum impact testing. Simulation results obtained from the crushable impactor three-post sign structure simulations indicated that the new breakaway connection is likely to meet the AASHTO MASH requirements, when impact testing using a crushable nose impactor is conducted in the future.

Since such assessments of connection adequacy are based on the predictive capabilities of numerical impact simulations, it is important to evaluate the accuracy of the impact simulation techniques employed. Clearly, the most direct means of assessing simulation accuracy is to compare simulation results to data from experimental testing. To do so, however, requires that the numerical model and impact conditions being simulated match the conditions tested experimentally. Since the physical pendulum impact tests described in this chapter were conducted using a rigid nose impactor (rather than a crushable nose impactor) and a single sign post structure (rather than a three-post structure with an attached sign panel), a finite element model corresponding to the physical test condition was developed. Specifically, a finite element model of an 1100 kg impactor block with a rigid (steel) nose was developed (Figure 10-28) to match the configuration used in the pendulum impact tests. Similarly, a model of a single sign

post structural model (Figure 10-28) was developed to match the configuration presented in Figure 10-2 (i.e., the proposed breakaway connection at the base; a fuse and hinge plate connection at approximately mid-height; and an attached channel on the upper post segment to represent the tributary mass of a sign panel). After merging the rigid nose impactor model with the single sign post model, impact simulations were conducted at conditions corresponding to those used during physical testing (30 km/hr impact speed and 25-degree impact angle).

In Figure 10-29, a comparison is presented of overall dynamic system response as observed during physical testing and as predicted using numerical simulation. Evident from the figure is the fact that the behavior of the breakaway mechanism predicted numerically is in very good agreement with the experimental test results. Even though this is an oblique 25-degree impact condition, in both the experiment and the simulation, the breakaway collar cleanly separates from the post stub thereby removing the potential for deceleration spikes associated with snagging of the collar. Agreement is also observed between the simulation and experiment in that there is no failure of the fuse plate at the post mid-height (as would be expected for a full three-post sign structure).

Moreover, a comparison of acceleration time-histories (Figure 10-30) reveals similar deceleration levels between the experiments (26 g) and the numerical simulation (23 g). Although there is a slight phase shift between the experimental acceleration data and acceleration data obtained from the simulation, the overall characteristics of the time histories are in reasonable agreement. Favorable agreement between the rigid nose, single post simulation, and experimental test results, both in terms of overall behavioral mechanics as well as quantifiable parameters, such as impactor deceleration, suggest that the simulation results obtained and presented in previous chapters—for *crushable nose* impacts on sign structures utilizing *three posts and a sign panel*—should be reasonable predictors of what will occur when physical testing under these same conditions is eventually carried out in the future.

10.6 Head-On Impact Experiments

To complement the oblique 25-degree impact experiments, two additional impact experiments were conducted at an impact angle of 0-degrees (recall Figure 10-4B) as is required by both NCHRP 350 and MASH. Before each test, instrumentation was installed on both the post and impactor in the form of accelerometers, strain gauges, and load washers. In addition, optical break beams were once again positioned adjacent to the post to record impactor velocity just prior to impact. For both tests (T-0-1 and T-0-2), the target impact velocity of 30 km/hr, as measured by the optical break beams, was achieved with less than 2% error: Test T-0-1: 29.50 km/hr (-1.6%); Test T-0-2: 29.90 km/hr (-0.3%).

Figure 10-31 presents a series of snapshots taken from the wide angle high-speed camera during impact experiment T-0-1. Overall behavior of the post and breakaway collar was as expected, and was, in many ways, similar to the oblique impact tests. The breakaway collar separated cleanly from the post and post stub without snagging. Further, the fuse plate at post mid-height did not fail, in contrast to the behavior that would be expected for a three-post sign structure with an attached panel.

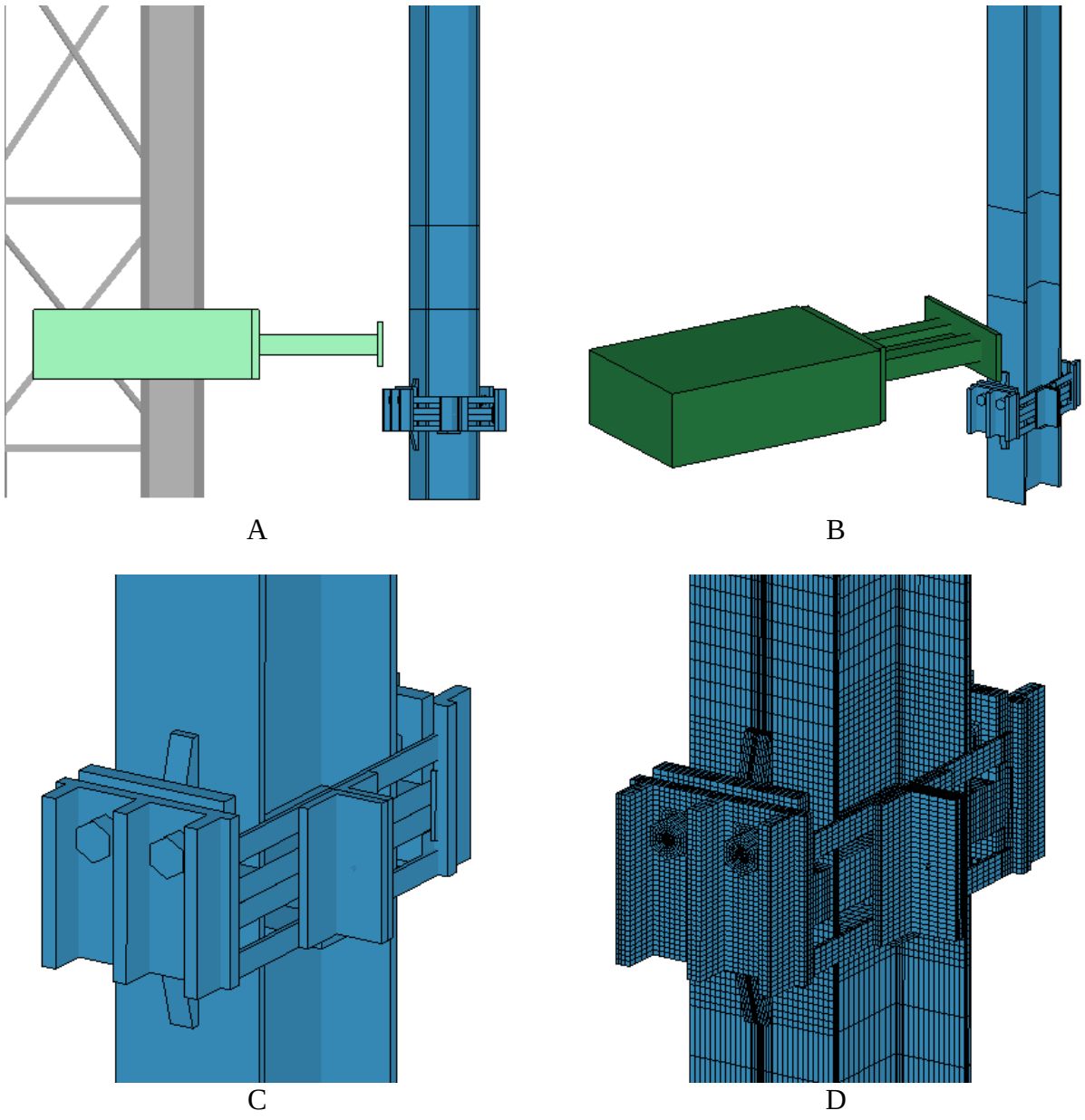

Figure 10-28. Finite element model developed to match physical test conditions: A) Overview of model near impact zone; B) Rigid nose impactor; C) Single sign post with breakaway base connection; D) Single sign post with breakaway base connection (with mesh visible)

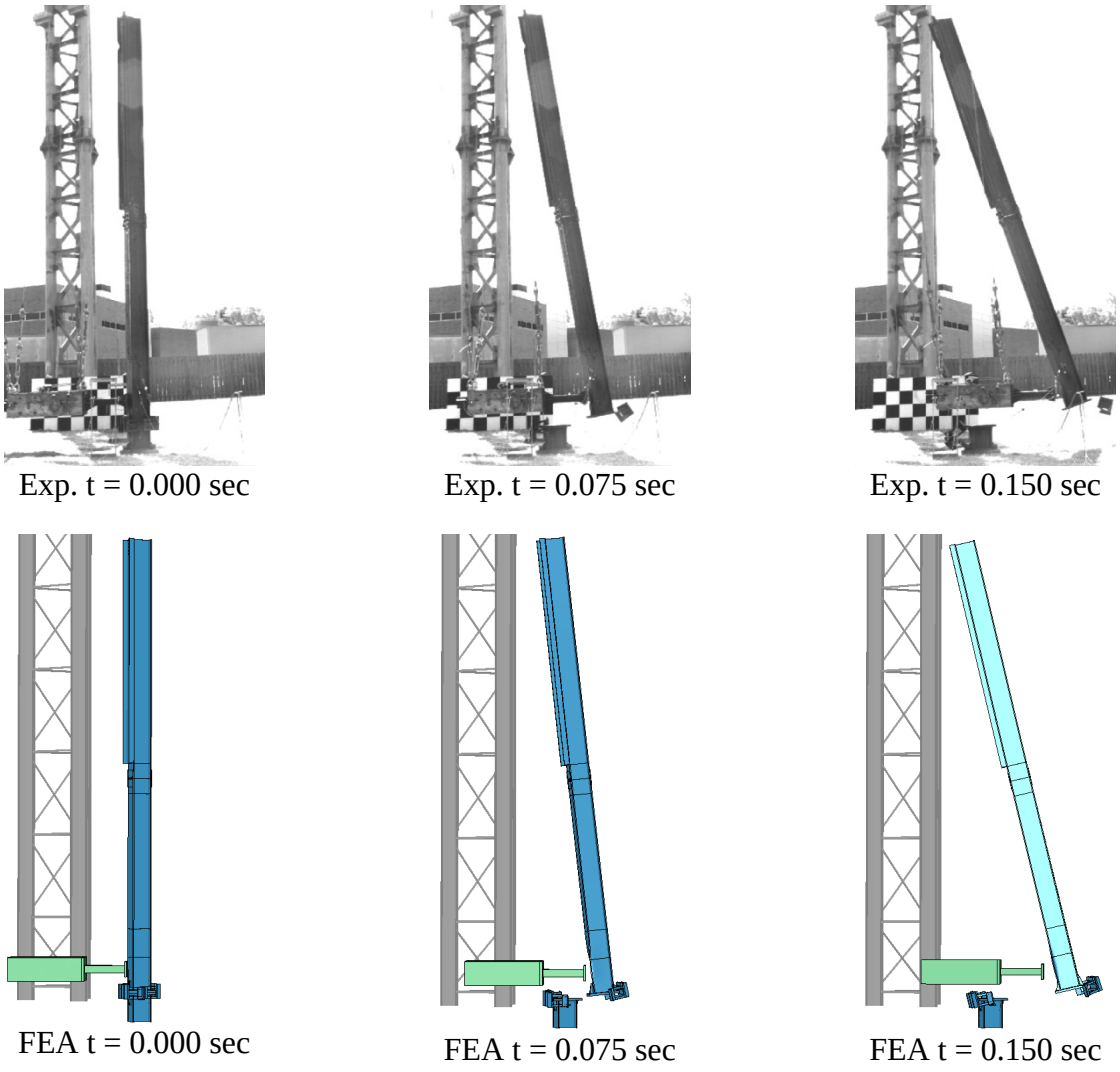

Figure 10-29. Comparison of breakaway connection dynamic behavior between experimental impacts and numerical simulation (25-degree impact angle)

Accelerations from both the post and pendulum impactor for test T-0-1 are shown in Figure 10-32. Acceleration traces for four accelerometers are shown in the plot: I-AC-1 and I-AC-2 were located on the impactor and oriented in the direction of impact; P-AC-1- and P-AC-2 were located on the post and oriented in the direction of impact. Plateaus in the acceleration data presented in the plot (between 0.001 and 0.003 sec) indicate that all four accelerometers over-ranged during the impact test. Acceleration levels generated during the head-on (0-degree) impact tests were much higher than those generated during the oblique (25-degree) impact tests. This difference was attributed to the differences in interaction between the rigid nose of the impactor and the lower steel post segment. In the oblique (25-degree) impact tests, the impactor nose made initial contact with the tip of the post flange and bent (flexed) the flange inward (toward the web) during impact. In contrast, during a head-on (0-degree) impact tests, the rigid

steel nose of the impactor contacted the full width of the flange, which was stiffened from behind by the post web. As a result, the post had a much higher impact (contact) stiffness in the head-on impact cases, and produced much higher acceleration levels. As a consequence of over-ranging of the accelerometers, peak impactor decelerations could not be determined from the measured data. However, finite element simulations (discussed below) indicate that the pendulum impactor underwent accelerations of approximately 93 g during the head-on impact test condition. Loads measured by the washer load cells are plotted in Figure 10-33. The peak loads measured by the load washers (P-LC-1 and P-LC-2) for the connector bolts were found to be 642 lbf and 763 lbf, respectively. Similar to the oblique impact tests, the loads measured by the washer load cells were significantly lower than the ultimate bolt capacity of 2.8 kip (as determined from static testing of the connector bolts). In addition, a clearly evident temporal lag of 0.005 seconds was observed in the data. Impact occurred at t = 0 sec. as determined by the tape switches; however, the washer load cells did not show a response until approximately 0.005 sec. This delay in response was determined to be related to the specific configuration of the data acquisition system used only during the T-0-1 test. In tests T-0-2, T-25-1, and T-25-2, a different configuration of the data acquisition system was used which prevented similar time delays from occurring.

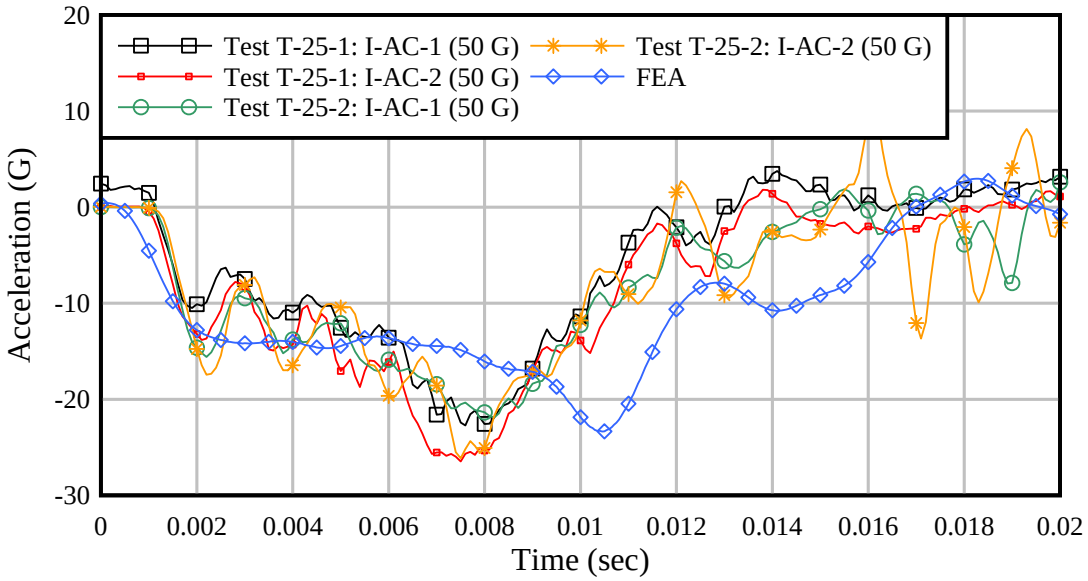

Figure 10-30. Comparison of surrogate vehicle accelerations from experimental impact tests and numerical simulation (25-degree impact angle)

t = -0.0375 sec.

t = 0.0000 sec.

t = 0.0375 sec.

t = 0.0750 sec.

t = 0.1125 sec.

t = 0.1500 sec.

t = 0.1875 sec.

t = 0.2250 sec.

t = 0.2625 sec.

Figure 10-31. Head-on impact from high-speed camera (where t = 0 sec. indicates contact between post and pendulum) for experiment T-0-1

Strain gauge results are shown in Figure 10-34, expressed as stresses computed by assuming a modulus of elasticity of 29,000 ksi. During test T-0-1, some instrumentation lead cables disconnected during impact and others snagged and were severed. For this reason, individual data traces in Figure 10-34 have been truncated when the data becomes meaningless due to cable disconnects. No immediate spikes in strain (or computed stress) are evident in the strain gauge data plots, as was typical in the oblique test data. Instead, pulses of strain (stress) suggest the propagation of a stress wave traveling through the post. The stress wave starts with P-SG-1/2 (t = 0.00525), moves through P-SG-3/4 (t = 0.00625) and then up to P-SG-5/6 (t = 0.0065).

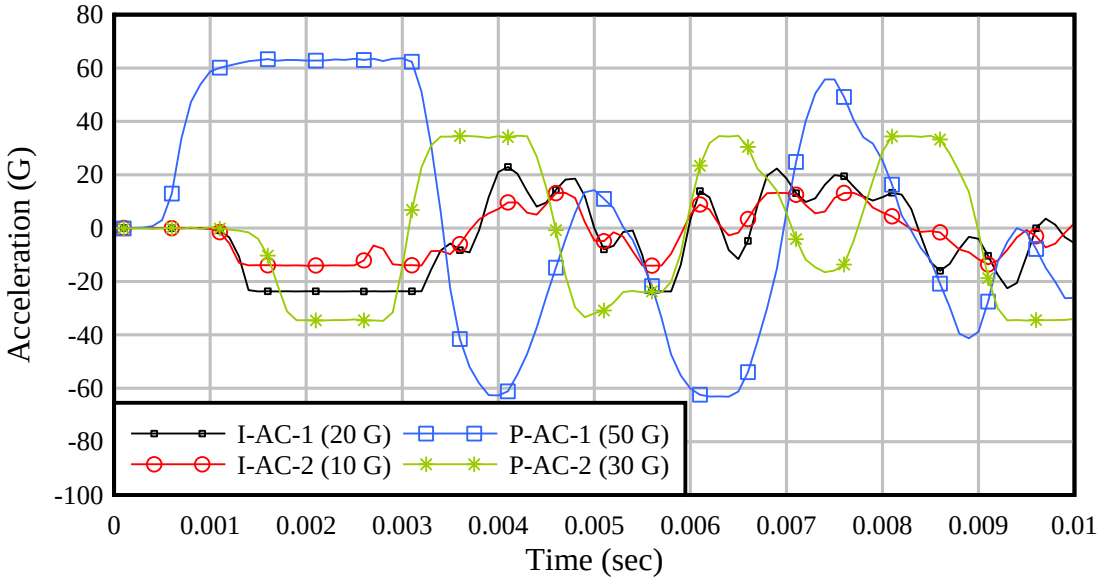

Figure 10-32. Acceleration data from impactor and post for test T-0-1

Accelerations of the post and pendulum impactor for head-on impact test T-0-2 are shown in Figure 10-35. Four accelerometers are shown in this plot: I-AC-1 and I-AC-2 were located on the pendulum impactor and aligned with the impact direction; I-AC-3 was located on the pendulum impactor and oriented in the vertical direction; P-AC-2 was positioned on the post, and aligned with the direction of impact. Note that for this test, a 50G accelerometer (I-AC-1) was installed on the impact block to attempt to capture the high level of acceleration occurring during impact. However, the accelerometers on the impactor still over-ranged so peak acceleration could not be quantified. Additionally, readings from accelerometer P-AC-2 prior to and following impact indicate a wiring or data acquisition problem, rendering the P-AC-2 data unusable.

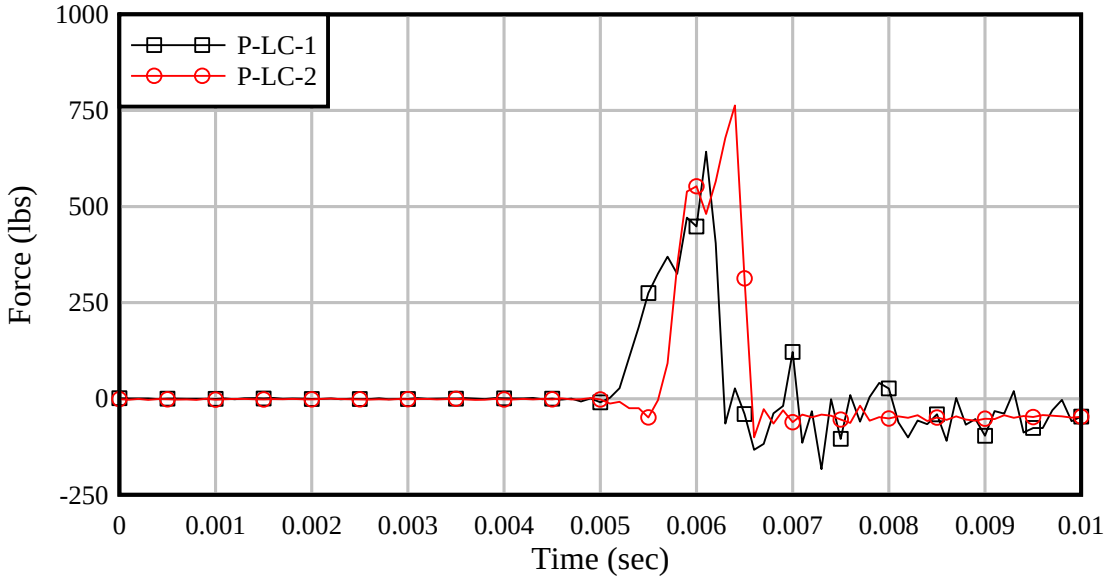

Figure 10-33. Washer load cell data for test T-0-1

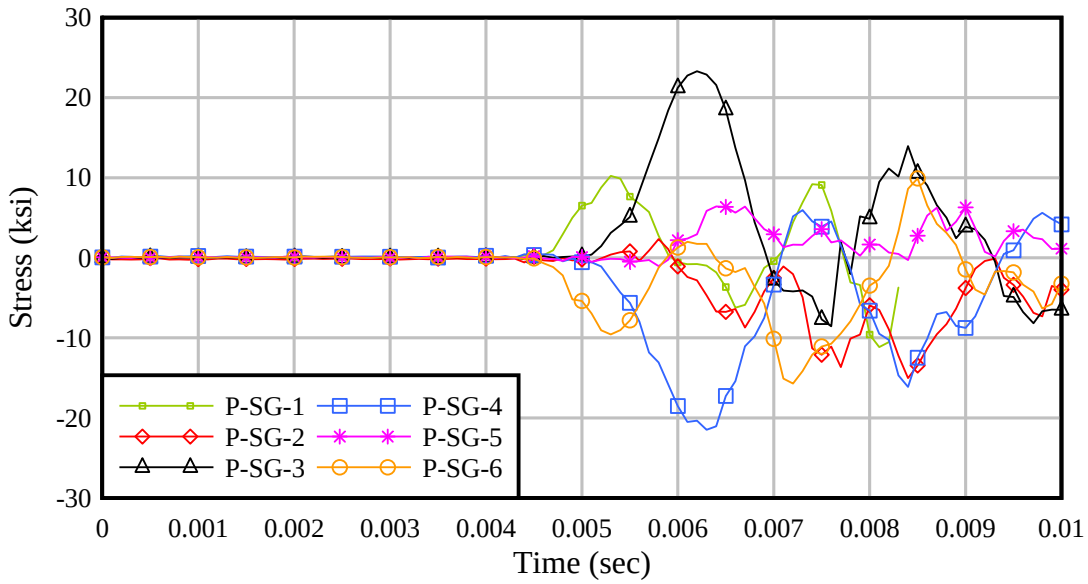

Figure 10-34. Strain gauge data converted to stress (assuming E = 29000 ksi) for test T-0-1

Loads measured by the washer load cells during test T-0-2 are shown in Figure 10-36. Peak loads from the washer load cells were 655 lbf and 90 lbf. These loads were again well below the static failure load of the connector bolts (2.8 kip). Furthermore, the low load level of P-LC-2 suggests that this washer load cell may have malfunctioned, either directly within the load cell, or indirectly due to the cabling or data acquisition system. Strain gauge data for test T-0-2 are shown (plotted as computed stresses) in Figure 10-37. Data traces in this plot are truncated when the data indicated disconnection or severing of the lead cables.

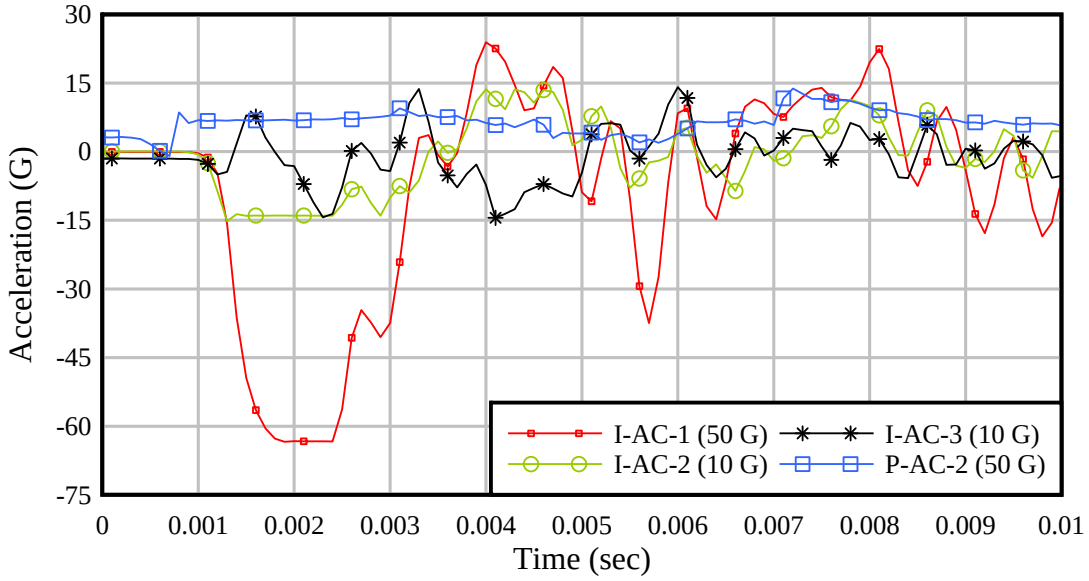

Figure 10-35. Acceleration data from impactor and post for test T-0-2

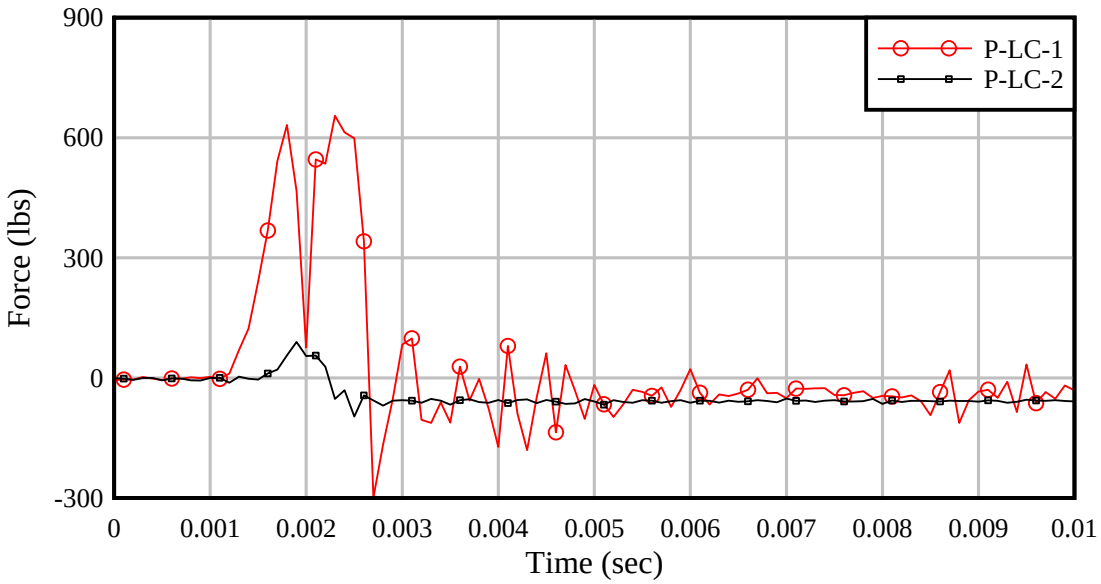

Figure 10-36. Washer load cell data for test T-0-2

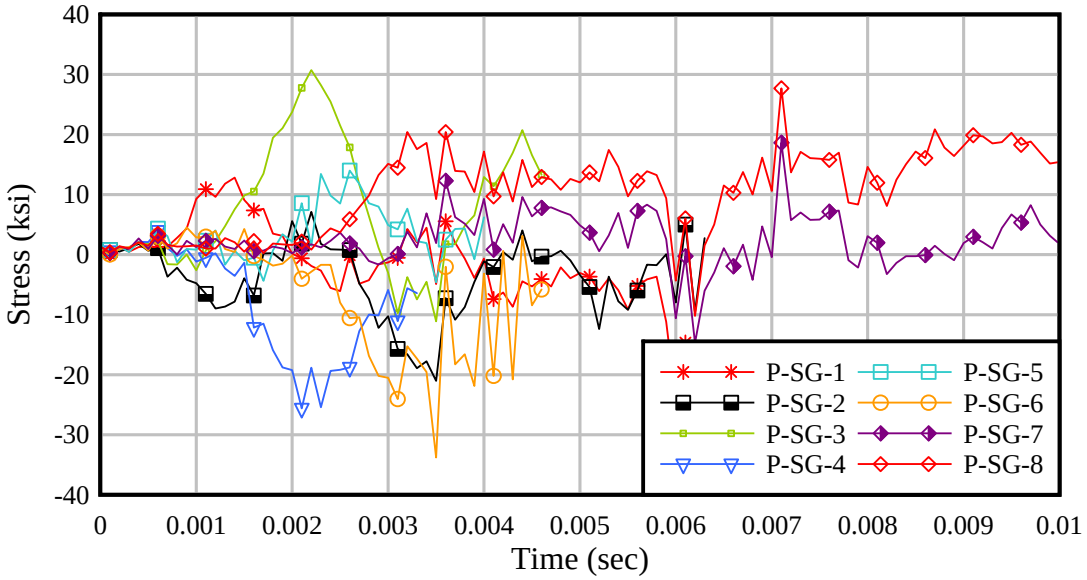

Figure 10-37. Strain gauge data converted to stress (assuming E = 29000 ksi) from test T-0-2 for head-on impacts

Using the previously described finite element models of an 1100 kg impactor block with a rigid (steel) nose and a single sign post, with a breakaway base connection (Figure 10-28) and fuse and hinge-plates at mid-height, finite element impact simulations were conducted at conditions corresponding to those used during the physical head-on impact tests (30 km/hr impact speed and 0-degree impact angle). In Figure 10-38, a comparison is presented of the overall dynamic system response as observed during physical testing and as predicted using numerical simulation. Evident from the figure is the fact that the behavior of the breakaway mechanism predicted numerically is in very good agreement with the experimental test results. In both the experiment and the simulation, the breakaway collar cleanly separates from the post stub thereby removing the potential for deceleration spikes associated with snagging of the collar. A comparison of accelerations obtained from finite element simulation and accelerations measured experimentally is presented in Figure 10-39. Due to the over-ranging (clipping) of the accelerometers that occurred during physical testing, peak accelerations predicted from the finite element simulation cannot be directly compared to corresponding experimental data. However, in regions where the experimental acceleration data were not clipped, there is general agreement between simulation data and test data. Furthermore, the duration of the initial acceleration pulse, spanning from approximately 0.001 sec. to 0.0035 sec. is evident in both the test data and simulation data indicating reasonable agreement.

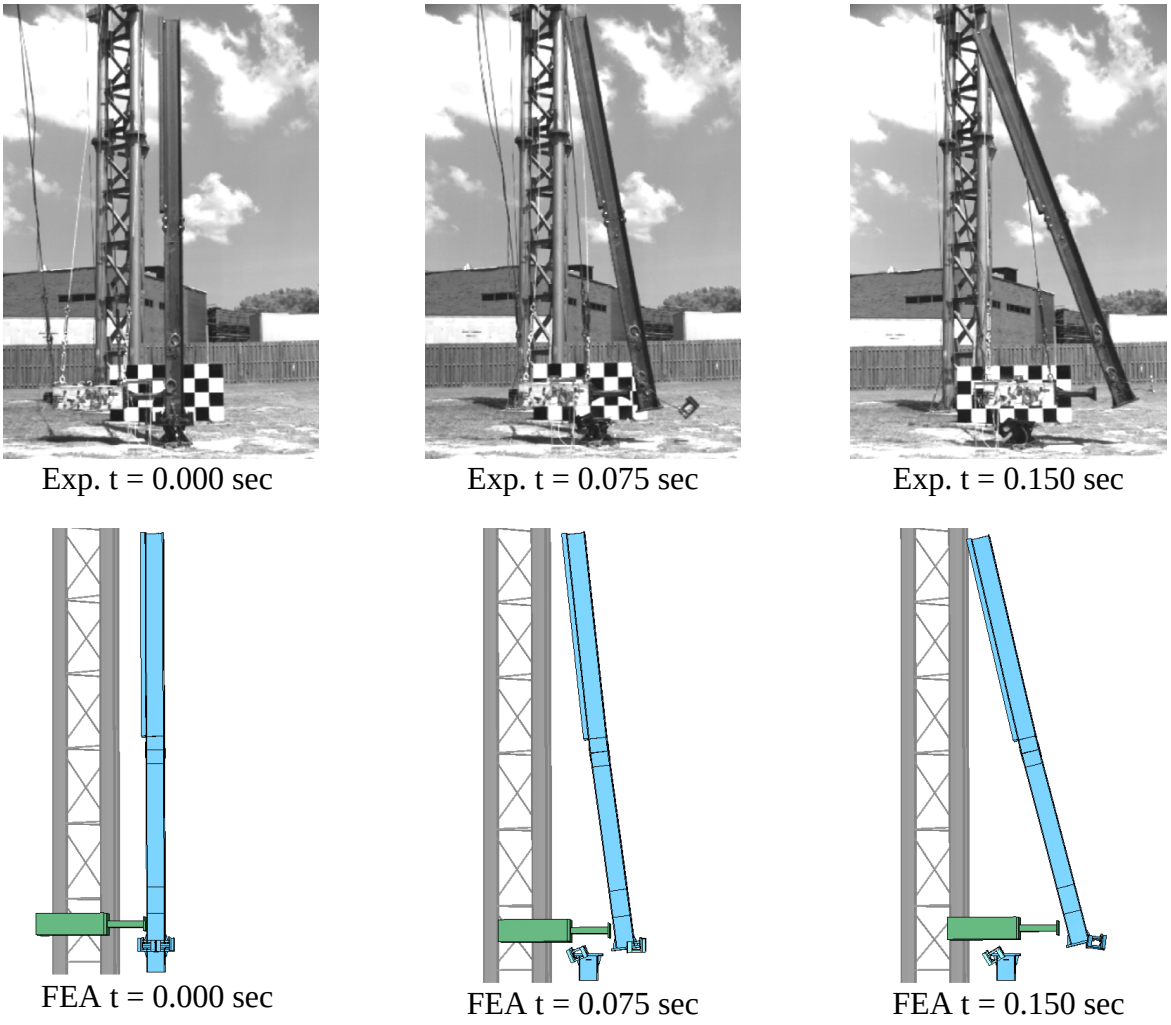

Figure 10-38. Comparison of breakaway connection dynamic behavior between experimental impacts and numerical simulations at 0-degrees

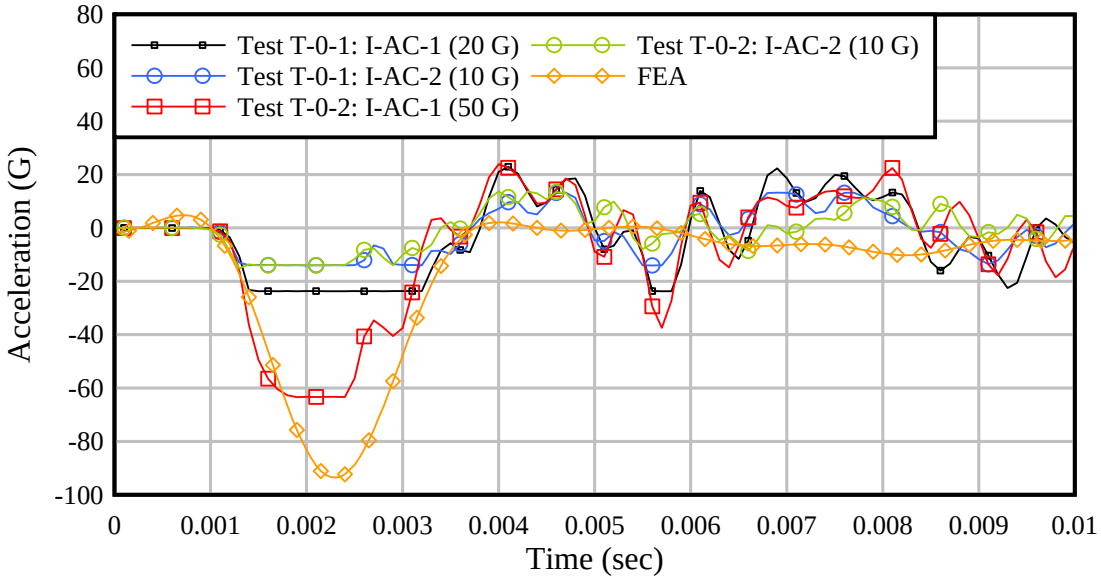

Figure 10-39. Comparison of surrogate vehicle accelerations between experimental impacts and numerical simulations at 0-degrees

CHAPTER 11
CONCLUSIONS AND RECOMMENDATIONS

11.1 Summary and Conclusions

The primary objective of this study was to develop an alternative breakaway solution for multi-post ground sign structures that presently, in the state of Florida, make use of the slip base connection. To address known problems with the slip base connection, a new breakaway concept, a shear-controlled moment collar, which maintains flexural moment capacity of the support system for wind load resistance while reducing shear capacity in a controlled manner, has been developed. By including a breakaway feature, the post shear capacity under vehicle impact loading (near ground level) is reduced, while preserving the flexural capacity that is needed to resist hurricane force wind loading. The breakaway connection concept is applicable to a variety of support structural systems (having lower wind induced moments at connection level than the developed connection). Another significant characteristic of the breakaway connection concept is that its breakaway performance does not require specific bolt torque. Consequently, it is relatively insensitive to installation and maintenance procedures. Development of the breakaway connection has involved combining traditional structural design procedures, extensive finite element analysis, and experimental static and dynamic impact testing.

The initial structural design procedure used in this study consisted of determining a target sign size and wind load level on the system and sizing the structural post according to relevant AASHTO and FDOT specifications by using conventional design and calculation tools. The breakaway connection developed in this study possesses adequate strength to resist hurricane wind loading, at a speed of up to 150 mph, acting on a three-post sign structure with a panel size of 12 ft x 20 ft (depth x width) and a clearance height of 11 ft. To compute the design static wind pressure (and ultimately the design wind load) using a 150 mph wind speed, a 50 year design life was selected for the breakaway connection design process. (Design ramifications of using a 50 year design life, and corresponding future recommendations, are offered in the following section.)

Finite element modeling and impact analysis techniques were extensively utilized in the process of developing the connection. Therefore, a wide variety of connection concepts and breakaway features were explored via simulation that would not have been possible to evaluate using only physical testing. A finite element model of the entire system, with a detailed high resolution model of the breakaway connection, was developed and analyzed under impact and static loading conditions. Several modifications were considered during connection design refinement to optimize performance while simultaneously attempting to minimize fabrication, installation, and maintenance sensitivity. For each candidate design, a corresponding finite element model of the connection was built and integrated into the support system for numerical analysis. Moment (flexural) capacity of the connection was assessed by finite element analysis to ensure structural adequacy and integrity under the static design wind loading condition. Extensive finite element impact simulations, of the breakaway connection being impacted by test vehicles under various impact scenarios, were conducted to evaluate the dynamic performance of the system. Specifically, impact simulations were conducted using both small car surrogate models (820 kg and 1100 kg pendulum impactors) and a full size pickup truck (2000 kg) vehicle model at impact angles of 0 degrees, 20 degrees, 25 degrees, and speeds of 30 km/h, 35 km/h, and 100 km/h.

Frictional effects within the connection components and occupant risk measures have been investigated and evaluated. It was observed that a binding effect associated with friction

between the collar binding plates and flange plates became more significant at higher impact speeds which increased occupant risk measures. To address this issue, low-friction Teflon sheets were introduced into the connection. Numerical simulations have shown that the newly developed connection with Teflon sheets is able to break away, as desired, under both low and high-speed impact conditions, as required by NCHRP Report 350.

Upon collision by a vehicle, impact force is primarily transferred to the connection in the shear loading mode, which fails low tensile strength connector bolts allowing the two collar halves to separate and the impacted post to rotate out of the path of the vehicle. Numerical simulation results of high-speed impacts have predicted that the breakaway connection will meet the dynamic performance requirements set forth in NCHRP Report 350, which specifies the use of an 820 kg impactor. However, in MASH, which now supersedes NCHRP Report 350 for evaluating new safety roadside hardware, the mass of the small car test vehicle has been increased from 820 kg to 1100 kg. As a result, testing the connection using an 1100 kg impactor is likely to reduce the occupant risk measures of small car impacts even further. Numerical impact simulations employing a 2000 kg pickup truck model and the breakaway connection (and post) indicated that the truck successfully passes underneath the sign structure without secondary contact. After collision, truck vehicles are predicted to move in a straight line or slightly toward the roadside, without intrusion into the adjacent traffic lane, which satisfies the post-impact vehicular trajectory requirement of NCHRP 350.

An experimental static test program was conducted that consisted of moment and shear tests to quantify the ultimate moment capacity of the connection for the design wind load and to evaluate frangibility of the connection under static equivalent impact load, respectively. Both moment and shear tests were conducted by statically applying lateral load to the specimens. In the shear tests, the lateral load was introduced at the impacted location on the post, which would be hit by a small test vehicle, while in the moment (flexural) tests, the load was applied at the location of the resultant wind force. Due to the non-destructive nature of the shear testing, in which only connector bolts needed to be replaced, shear tests with two friction conditions, bare steel and with the use of Teflon sheets, were conducted prior to flexural testing. Through the static shear tests, the low shear capacity of the proposed connection under lateral load near the connection was confirmed. The influence of frictional effects evaluated experimentally agreed with those demonstrated in finite element simulations. Experimental shear tests have shown that using a Teflon sheet at the slipping surface between the flange plates significantly reduced the shear load required to break the connector bolts.

Structural capacity of the breakaway post for the design wind load was validated by moment tests. Four moment tests were conducted in the refinement and validation process of the connection. Results from the first two tests led to design modifications involving the addition of external stiffeners to accommodate a higher eccentric moment on the collar primary plates. As a result, a much improved moment capacity was achieved in the last two moment tests. Although unexpected weld cracks, likely attributable to insufficient preheating, occurred at the interface of the flange plate and the associated stiffener on the tension side of the connection, moment capacities obtained in the last two tests were 1.36 and 1.50 times the design wind load. Therefore, a higher moment capacity of the system against wind load, exceeding the AASHTO load test requirement, can be achieved once the weld cracking issue is eliminated.

A dynamic pendulum impact test program was carried out to validate the breakaway behavior of the proposed connection system. Experimental instrumentation included accelerometers, strain gauges, washer load cells, and high-speed cameras. The final connection

design was tested under a low-speed impact condition (30 km/hr) conforming to the newly adopted AASHTO (2009) MASH. A rigid nose impactor having a mass of 1100 kg (the mass of a small vehicle per MASH) was developed for the impact tests. The impact testing was performed using the new FDOT pendulum impact test facility that was designed and constructed as part of this research study.

Four pendulum impact tests were conducted using a rigid nose impactor; two tests each at angles of 0 degrees and 25 degrees. In addition to the experimental tests, two high-fidelity finite element impact simulations (corresponding to the physical test conditions) were conducted, one for each impact angle, to assess the accuracy of finite element simulation in the prediction of breakaway system response under impact loading.

For both oblique (impact angle of 25 degrees) and head-on (impact angle of 0 degrees) pendulum impact tests, high-speed video of the impacts showed that the overall behavior of the breakaway collar upon impact was as expected based on simulation. Oblique impact tests produced repeatable (consistent) peak accelerations of 26 g between the two experiments conducted. Numerical simulations agreed well with the experiments, predicting a peak acceleration of 23 g for the oblique impacts. Peak experimental impactor accelerations from the head-on impact tests were unavailable for use in comparing to finite element simulation results, but good agreement in duration of the first acceleration pulse was observed between simulation and test.

11.2 Recommendations

This study focused on the development of an improved breakaway connection for multi-post ground signs. Based on the findings and observations made throughout the development process (numerical analysis, experimental testing), the following recommendations are made:

- The static wind loads that were used, in part, to design the breakaway connection developed in this study were based on a 150 mph wind speed, and a 50 year design life. The decision to select a 50 year design life (which lead to an importance factor of 1.0) rather than the more traditional 10 year design life (which is typical for signs and which leads to an importance factor of only 0.54) was based on the goal of ensuring that key roadside signs remain intact after a hurricane to aid emergency-responders during the post-hurricane recovery period. However, changing the design life for a sign (and the supporting base connections) from 10 years to 50 years increases the design static wind load by 85%. While the breakaway base connection developed in this study possesses adequate flexural capacity to resist wind loads associated with a 50 year design life, the steel post size and steel connection component sizes are significantly larger and heavier the those currently found in use by the FDOT for existing signs structures (which presumably have been designed based not on a 50 year design life, but on a 10 year design life). Significant savings in both material costs and fabrication costs could be achieved if the design life for the breakaway connection developed in this study could be reduced to 10 years, as is standard practice for sign structures. In addition, reductions in the sizes—and therefore weights and masses—of both the sign post and the breakaway connection components would further improve occupant risk measures associated with small car impact scenarios (lighter sign components would produce less severe occupant decelerations). Hence, benefits both in terms of improved safety and economic savings would be derived from adapting the design concept developed in this study to a design life of 10 years instead of 50 years. It is also important to note that, as a consequence of the 2004 and 2005 hurricane seasons, the FDOT now requires that exit numbers be painted directly on the

paved shoulders of major roadways, so as to assist emergency responders in exit identification. Hence, it is recommended that the breakaway connection system developed in this study be adapted and modified based on the use of a 10 year design life for wind load calculation. Combining the breakaway design innovations developed in this study with a reduction in design life would produce a base connection that offers improved safety and robustness (insensitivity to installation procedures) while also being economically comparable to existing, and less-robust, connection systems.

- For purposes of designing the new breakaway connection that was developed in this study, the required wind load capacity of the connection was based on maximum practical sign size and sign height. Such parameter selections produced a conservative design capable of resisting severe wind loads on very large signs. However, such parameter selections also resulted in a relatively large structural post size, and relatively heavy breakaway connection components. For signs that are substantially smaller than the maximum size assumed in the design process, the associated wind loads and flexural demands are considerably reduced. For such signs, it is recommended that a small number of "scaled-down" versions of the new breakaway connection (and corresponding scaled-down post sizes) be developed. Reduced post size and connection weight will reduce occupant risk in the event of small car impacts, and will also produce cost savings by reducing material and fabrication costs.

- It is recommended that additional impact tests—to validate system performance—be performed using a crushable-nose impact block. Impact tests conducted in this study on the full-size breakaway connection were performed using a rigid nose impact block with a mass that corresponds to a small car (1100 kg). In order to validate connection performance under small car impact conditions, additional tests should be conducted using a crushable-nose impact block. Use of a crushable nose is particularly important in terms of assessing risk measures, such as occupant ridedown deceleration.

- Since the shear-controlled moment collar connection concept is not limited to the use of steel, other types of materials that possess adequate strength but which have a lower mass density than steel are also desirable. Therefore, it is recommended that future research should investigate the use of alternative materials (e.g. fiber reinforced polymers) in the breakaway support system to further improve occupant risk measures, especially for high-speed impacts.

- Since a single breakaway post was statically tested for moment capacity in this study, load redistribution between posts, especially near ultimate capacity, was not captured. Therefore, the wind resistance strength of the breakaway system may have been underestimated since each breakaway post was designed to carry the tributary load of the middle post, which is larger than that on outer posts. Although it appears to be a conservative design for uniform wind pressure over the entire sign panel, actual wind pressures can vary in the horizontal direction and may cause a torsional load on the sign support system. Therefore, it is recommended that a full sign structure, utilizing three breakaway posts with a sign panel, be experimentally tested under uniform wind pressure, and under horizontally varied wind pressure.

REFERENCES

AASHTO (American Association of State Highway and Transportation Officials) (1996), *Roadside Design Guide*, American Association of State Highway and Transportation Officials, Washington, D.C.

AASHTO (American Association of State Highway and Transportation Officials) (2001), *Standard Specification for Structural Supports for Highway Signs, Luminaires and Traffic Signals*, Washington, D.C.

AASHTO (American Association of State Highway and Transportation Officials) (2009), *Manual for Assessing Safety Hardware (MASH) 2009*, American Association of State Highway and Transportation Officials, Washington, D.C.

ADINA (2005*), Theory and Modeling Guide, Volume I: ADINA Solids & Structures*, ADINA R&D, Inc.

ASCE (American Society of Civil Engineers) (2005). "Minimum design loads for buildings and other structures." *SEI/ASCE 7-05*, Reston, Va.

Andrle, S.J., Knapp, K.K., McDonald, T., and Smith, D.E. (2001), *Iowa Traffic Control Devices and Pavement Markings: A Manual for Cities and Countries.* Center for Transportation Research and Education (CTRE), Iowa State University, Iowa DOT Project TR-44.

Bickford, J.H. (2008), *An Introduction to the Design and Analysis of Bolted Joints, non-gasketed joints*, 4th ed., Boca Raton : CRC Press.

Bligh, R.P., Alberson, D.C., Menges, W.L., Haug, R.R. (2002), *"Evaluation of dual support, triangular slip-base sign installations"*, Report No. FHWA/TX-03/1792-8.

Brown C.M. (1998), "*Safety Performance Testing of a Modified Oregon Multidirectional Slip-base Sign Support: Foil Test Numbers 98F002 and 98F004"*, Report No. FHWA-RD-98-111.

Dutta P.K. (1998), *Investigations of plastic composite materials for highway safety structures,* CRREL Report 98-7, US Army Corps of Engineers.

Florida Department of Transportation (FDOT) (2007), "*FDOT Multi-Post 2001 Sign Program, v1.1"*, Structures Design Office, Tallahassee, FL.

FDOT (Florida Department of Transportation) (2006), Drawing Index 11200, "2006 *FDOT Design Standards*", Structures Design Office, Florida Department of Transportation, Tallahassee, FL.

FDOT (Florida Department of Transportation) (2008), Drawing Index 11200, "2008 *Interim Design Standards*", Structures Design Office, Florida Department of Transportation, Tallahassee, FL.

FDOT (Florida Department of Transportation) (2009), FDOT Modifications to Standard Specification for Structural Supports for Highway Signs, Luminaires and Traffic Signals (LTS-4), FDOT Structures Manual, Vol. 9.

Federal Highway Administration (FHWA) Acceptance Letter (1992), LS-26, *Direct Burial Breakaway Fiberglass Luminaire Supports.*

Kremer K., Liszkiewicz A., and Adkins J. (2004), *"Development of steel foam materials and structures"*, TRP0013 Final Report.

Kulak, G.L., Fisher, J.W., and Struik, J.H.A. (1987). *"Guide to Design Criteria for Bolted and Riveted Joints"* 2nd Edition, John Wiley & Sons, New York.

LSTC (Livermore Software Technology Corporation) (2006). *LS-DYNA Keyword User's Manual*. Livermore Software Technology Corporation, CA.

Nassar, S.A., Matin, P.H., and Barber, G.C. (2005), "Thread Friction Torque in Bolted Joints", *ASME Journal of Pressure Vessel Technology*, Vol. 127, pp. 387-393.

Pinelli, J.P. and Subramanian (1999), *"Study of Break-away Sign Base Connections, II"*, FDOT Report WPI No. 0510837.

Pinelli, J.P., Subramanian, C.S., Tabora, J. (2002), "Experimental Study of Breakaway Highway Sign Connections", *J. Transp. Engrg.*, Volume 128, Issue 1, pp. 17-20.

Reid, J.D. (1996), "Dual-Support Breakaway Sign with Modified Fuse Plate and Multidirection Slip Base," *Transportation Research Record 1528*, pp. 61-68, Transportation Research Board (TRB), National Research Council, Washington, D.C.

Reid, J.D. and Paulsen, G.W. (1998), "Design and Simulation of Large Breakaway Signs," *ASCE Journal of Transportation Engineering*, Vol. 124, No. 1, pp. 59-64.

Ross, H.E. Jr., Sicking, D.L., Zimmer, R.A., and Michie, J.D. (1993), *NCHRP Report 350: Recommended Procedures for the Safety Performance Evaluation of Highway Features,* Transportation Research Board (TRB), National Research Council, Washington, D.C.

APPENDIX A
STRUCTURAL DESIGN CALCULATION OF SHEAR-CONTROLLED MOMENT COLLAR BREAKAWAY CONNECTION

This appendix includes the determination of the design wind load on the structure, design calculation of structural posts, hinge connection.

References: *AASHTO Standard Specifications for Structural Supports for Highway Signs, Luminaires and traffic Signals, 2001; FDOT MultiPost2001v1.1*

Unis $kip := 1000 \cdot lbf$ $ksi := 1000 \cdot psi$ $psf := \frac{lbf}{ft^2}$

LOAD CALCULATIONS:

Panel Dimensions and Wind Speed:

$Panel_{Width} := 20 \cdot ft$ $Panel_{Depth} := 12 \cdot ft$ $Clear_{Height} := 11 \cdot ft$ $V_{Speed} := 150 \cdot mph$

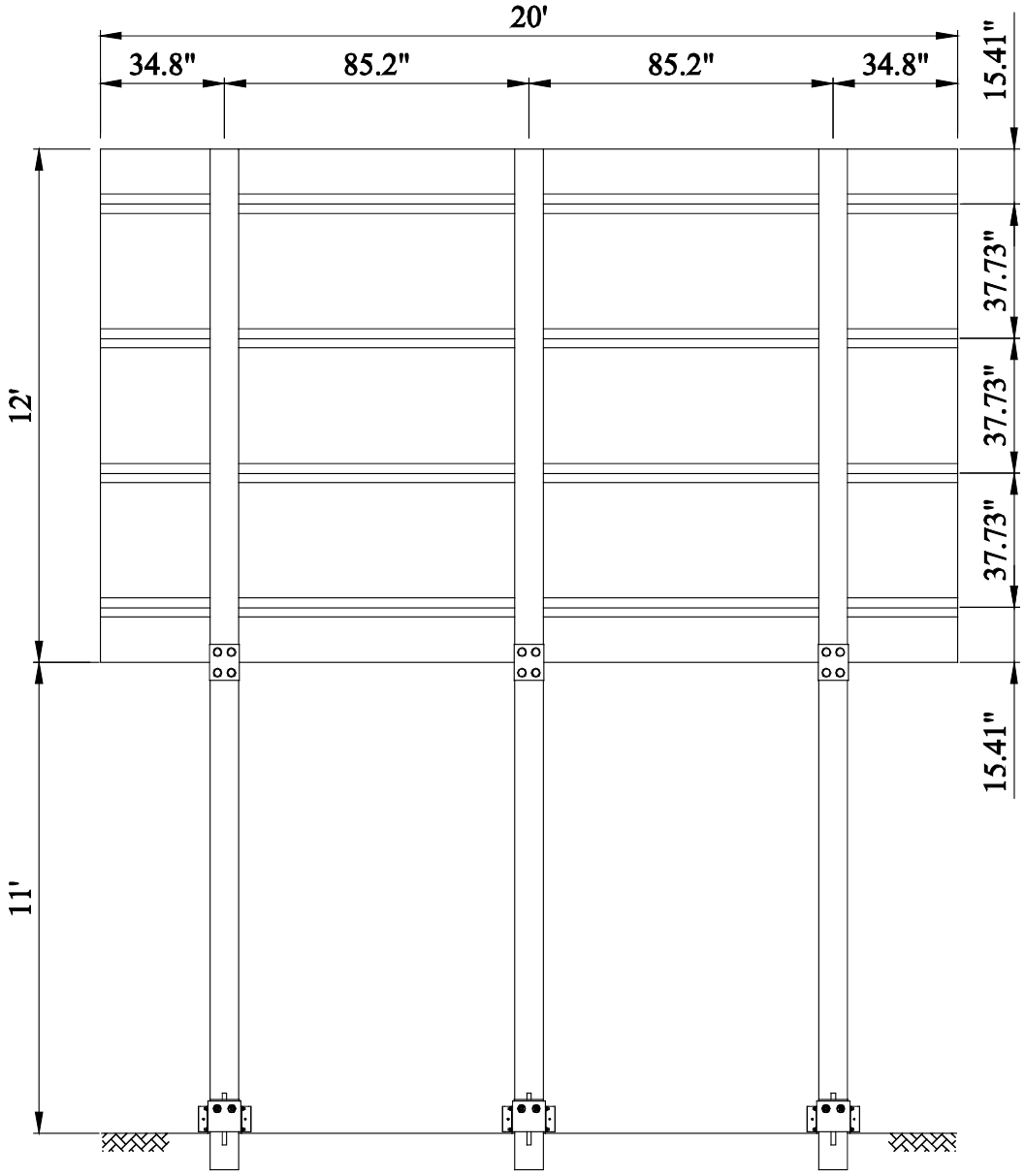

Wind Pressure and Loads

$Main_{Height} := Clear_{Height} + \frac{Panel_{Depth}}{2}$ $Main_{Height} = 17\,ft$

$I_r := 1$ $I_{r.Hurricane} := 1$ *(AASHTO Table 3-2 & Table 3-3)*

$C_v := 1$ $C_{v.Hurricane} := 1$

$1 < \left(\frac{Panel_{Width}}{Panel_{Depth}} = 1.667 \right) \leq 2$ ----> $C_d := 1.19$ *(AASHTO Table 3-6)*

$\alpha := 9.5$ *constant value exposure "C"* $\alpha = 9.5$ *(AASHTO 3.8.4)*

$z_g := 900 \cdot ft$ *constant value exposure "C"* $z_g = 900\,ft$

$G := 1.14$ *gust effect factor* $G = 1.14$

$K_z(Height) := if\left[2.01 \cdot \left(\frac{Height}{z_g} \right)^{\frac{2}{\alpha}} > 0.87, 2.01 \cdot \left(\frac{Height}{z_g} \right)^{\frac{2}{\alpha}}, 0.87 \right]$ $K_z\left(Main_{Height}\right) = 0.872$

Force on Panel

$P := 0.00256 \cdot G \cdot \left(\frac{V_{Speed}}{mph} \right)^2 \cdot psf$ $P = 65.664\,psf$ *(AASHTO Eq.3-1)*

$P_{Panel} := P \cdot K_z\left(Main_{Height}\right) \cdot C_d \cdot I_{r.Hurricane}$ $P_{Panel} = 68.103\,psf$

$P_{Panel.100mph} := 0.00256 \cdot G \cdot 100^2 \cdot psf \cdot K_z\left(Main_{Height}\right) \cdot C_d \cdot I_r$ $P_{Panel.100mph} = 30.268\,psf$

$P_{Panel} := if\left(P_{Panel} \geq P_{Panel.100mph}, P_{Panel}, P_{Panel.100mph}\right)$ $P_{Panel} = 68.103\,psf$

$WL_{Panel} := P_{Panel} \cdot Panel_{Width} \cdot Panel_{Depth}$ $WL_{Panel} = 16.34\,kip$

Weights of Panel and Supplemental Plaques

Panel Weight $Weight_{Panel} := 4 \cdot \frac{lbf}{ft^2} \cdot Panel_{Width} \cdot Panel_{Depth}$ $Weight_{Panel} = 0.96\,kip$

Since middle post is more critical, post design will be based on loads on the middle post

Windload and Weight from the Upper Structure to the Middle Post

$Shear\_up_{mp} := WL_{Panel} \cdot \frac{85.2in}{20ft}$ $Shear\_up_{mp} = 5.802\,kip$

$M\_up_{mp} := Main_{Height} \cdot Shear\_up_{mp}$ $M\_up_{mp} = 1183.69\,kip \cdot in$

$Axial\_up_{mp} := Weight_{Panel} \cdot \frac{85.2in}{20ft}$ $Axial\_up_{mp} = 0.341\,kip$

Unbraced Length

$L_{mp\_unbraced} := Clear_{Height} + 12.24in$ $L_{mp\_unbraced} = 12.02\,ft$

POST DESIGNS - W12x45

Steel Beam *Post Material and Section Properties of W12x45*

$F_{SteelBeam.y} := 36 \cdot ksi$ $E_{Steel} := 29000 \cdot ksi$

$Wpl := 45$ Weight per Length (lbf/ft)

$b := 8.05$ Flange Width (in)

$tf := 0.575$ Flange Thickness (in)

$h := 12.1$ Section height (in)

$tw := 0.335$ Web Thickness (in)

$A := 19$ Area (in^2)

$S := 57.7$ Section modulus (in^3)

$I := 348$ Moment of inertia (in^4)

$$r_t := \sqrt{\frac{tf \cdot b^3 + \frac{1}{6} \cdot (h - 2 \cdot tf) \cdot tw^3}{12 \cdot \left[tf \cdot b + \frac{1}{6} \cdot (h - 2 \cdot tf) \cdot tw \right]}} \qquad r_t = 2.184 \quad (in)$$

Windload directly apply on post

$C_{d.Steel} := 1.70$

$$P_{mp} := P \cdot K_z \left(\frac{Main_{Height}}{2} - \frac{Panel_{Depth}}{4} \right) \cdot C_{d.Steel} \cdot I_{r.Hurricane}$$

$P_{mp} = 97.117\,psf$

$$P_{mp.100mph} := 0.00256 \cdot G \cdot 100^2 \cdot psf \cdot K_z \left(\frac{Main_{Height}}{2} - \frac{Panel_{Depth}}{4} \right) \cdot C_{d.Steel} \cdot I_r$$

$P_{mp.100mph} = 43.163\,psf$

$P_{mp} := if\left(P_{mp} \geq P_{mp.100mph}, P_{mp}, P_{mp.100mph}\right)$ $P_{mp} = 97.117\,psf$

$$WL_{mp} := P_{mp} \cdot b \cdot in \cdot \left(Main_{Height} - \frac{Panel_{Depth}}{2} \right) \qquad WL_{mp} = 0.717\,kip$$

Forces of Middle Post due to Selfweight and Windload Applied Directly on Middle Post

$Shear\_p_{mp} := WL_{mp}$ $\quad Shear\_p_{mp} = 0.717\,kip$

$M\_p_{mp} := WL_{mp} \cdot \left[\left(Main_{Height} - \frac{Panel_{Depth}}{2} \right) \div 2 \right]$ $\quad M\_p_{mp} = 47.298\,kip \cdot in$

$Axial\_p_{mp} := Wpl \cdot \frac{lbf}{ft} \cdot \left(Main_{Height} + \frac{Panel_{Depth}}{2} \right)$ $\quad Axial\_p_{mp} = 1.035\,kip$

Total Middle Post Forces and Stresses

$Axial_{mp} := Axial\_up_{mp} + Axial\_p_{mp}$ $\quad Axial_{mp} = 1.38\,kip$ *(Axial load at ground level)*

$M_{mp} := M\_up_{mp} + M\_p_{mp}$ $\quad M_{mp} = 1230.98\,kip \cdot in$ *(Moment load at ground level)*

$f_{StlBm.mp.Bending} := \frac{M_{mp}}{S \cdot in^3}$ $\quad f_{StlBm.mp.Bending} = 21.334\,ksi$

$Shear_{mp} := Shear\_up_{mp} + Shear\_p_{mp}$ $\quad Shear_{mp} = 6.519\,kip$ *(Shear load at ground level)*

$L_{eq} := \frac{M_{mp}}{Shear_{mp}}$ $\quad L_{eq} = 188.83\,in$ *(Location of resultant wind load acting on the middle post from the ground level)*

$f_{StlBm.mp.Shear} := \frac{Shear_{mp}}{h \cdot tw \cdot in^2}$ $\quad f_{StlBm.mp.Shear} = 1.608\,ksi$

$f_{StlBm.mp.Axial} := \frac{Axial\_up_{mp} + Axial\_p_{mp}}{A \cdot in^2}$ $\quad f_{StlBm.mp.Axial} = 0.07241\,ksi$

Allowable Stresses *(AASHTO 5.7.1)*

$$fF_{bSteelBeam}(L_{Unbraced}) := \left| \begin{array}{l} T \leftarrow \frac{0.4138 \cdot E_{Steel} \cdot b \cdot tf \cdot in}{L_{Unbraced} \cdot h} \\ \lambda \leftarrow \frac{L_{Unbraced}}{r_t \cdot in} \\ F_b \leftarrow \left(\frac{2}{3} - \frac{F_{SteelBeam.y} \cdot \lambda^2}{52.759 \cdot E_{Steel}} \right) \cdot F_{SteelBeam.y} \quad \text{if} \quad \sqrt{\frac{3.517 \cdot E_{Steel}}{F_{SteelBeam.y}}} \le \lambda \le \sqrt{\frac{17.586 \cdot E_{Steel}}{F_{SteelBeam.y}}} \\ F_b \leftarrow \frac{5.862 \cdot E_{Steel}}{\lambda^2} \quad \text{if} \quad \lambda \ge \sqrt{\frac{17.586 \cdot E_{Steel}}{F_{SteelBeam.y}}} \\ F_b \leftarrow T \quad \text{otherwise} \\ F_b \leftarrow T \quad \text{if} \quad F_b < T \\ F_b \leftarrow 0.6 \cdot F_{SteelBeam.y} \quad \text{if} \quad F_b > 0.6 \cdot F_{SteelBeam.y} \\ 1.33 \cdot F_b \end{array} \right.$$

$F_{StlBm.mp.b} := fF_{b\,SteelBeam}(I_{mp\_unbraced})$ $F_{StlBm.mp.b} = 28.728\,ksi$

$F_{StlBm.v} := 0.33 \cdot F_{SteelBeam.y} \cdot 1.33$ $F_{StlBm.v} = 15.8\,ksi$ *(AASHTO 5.11.3)*

$$C_{a.mp.StlBm} := 1 - \left[\frac{Axial\_up_{mp} + 0.38 \cdot Axial\_p_{mp}}{\frac{2.46 \cdot E_{Steel} \cdot I \cdot in^4}{\left(Main_{Height} + \frac{Panel_{Depth}}{2} \right)^2}} \right]$$

$C_{a.mp.StlBm} := if(C_{a.mp.StlBm} \le 1, C_{a.mp.StlBm}, 1.0)$ $C_{a.mp.StlBm} = 0.998$

(AASHTO 5.12.1)

$$CSR_{StlBm.mp} := \frac{f_{StlBm.mp.Axial}}{1.33 \cdot 0.6 \cdot F_{SteelBeam.y}} + \frac{f_{StlBm.mp.Bending}}{C_{a.mp.StlBm} \cdot F_{StlBm.mp.b}} + \left(\frac{f_{StlBm.mp.Shear}}{F_{StlBm.v}} \right)^2$$

$CSR_{StlBm.mp} = 0.757$ < 1 ---> OK

(W12x45 satisfies structural requirements of AASHTO 2001 for use in the selected 3-post sign)

POST DESIGNS - W12x 40

Steel Beam *Post Material and Section Properties of W12x40*

$F_{SteelBeam.y} := 36 \cdot ksi$ $E_{Steel} := 29000 \cdot ksi$

$Wpl := 40$ Weight per Length (lbf/ft)

$b := 8.005$ Flange Width (in)

$tf := 0.515$ Flange Thickness (in)

$h := 11.94$ Section height (in)

$tw := 0.295$ Web Thickness (in)

$A := 11.8$ Area (in^2)

$S := 51.9$ Section modulus (in^3)

$I := 310$ Moment of inertia (in^4)

$$r_t := \sqrt{\frac{tf \cdot b^3 + \frac{1}{6} \cdot (h - 2 \cdot tf) \cdot tw^3}{12 \cdot \left[tf \cdot b + \frac{1}{6} \cdot (h - 2 \cdot tf) \cdot tw \right]}}$$ $r_t = 2.174$ (in)

Windload directly apply on post

$C_{d.Steel} := 1.70$

$P_{mp} := P \cdot K_z\left(\frac{Main_{Height}}{2} - \frac{Panel_{Depth}}{4}\right) \cdot C_{d.Steel} \cdot I_{r.Hurricane}$

$P_{mp} = 97.117\,psf$

$P_{mp.100mph} := 0.00256 \cdot G \cdot 100^2 \cdot psf \cdot K_z\left(\frac{Main_{Height}}{2} - \frac{Panel_{Depth}}{4}\right) \cdot C_{d.Steel} \cdot I_r$

$P_{mp.100mph} = 43.163\,psf$

$P_{mp} := if\left(P_{mp} \geq P_{mp.100mph}, P_{mp}, P_{mp.100mph}\right)$ $P_{mp} = 97.117\,psf$

$WL_{mp} := P_{mp} \cdot b \cdot in \cdot \left(Main_{Height} - \frac{Panel_{Depth}}{2}\right)$ $WL_{mp} = 0.713\,kip$

Forces of Middle Post due to Selfweight and Windload Applied Directly on Middle Post

$Shear\_p_{mp} := WL_{mp}$ $Shear\_p_{mp} = 0.713\,kip$

$M\_p_{mp} := WL_{mp} \cdot \left[\left(Main_{Height} - \frac{Panel_{Depth}}{2}\right) \div 2\right]$ $M\_p_{mp} = 47.034\,kip \cdot in$

$Axial\_p_{mp} := Wpl \cdot \frac{lbf}{ft} \cdot \left(Main_{Height} + \frac{Panel_{Depth}}{2}\right)$ $Axial\_p_{mp} = 0.92\,kip$

Total Middle Post Forces and Stresses

$M_{mp} := M\_up_{mp} + M\_p_{mp}$ $M_{mp} = 1230.72\,kip \cdot in$

$f_{StlBm.mp.Bending} := \frac{M_{mp}}{S \cdot in^3}$ $f_{StlBm.mp.Bending} = 23.713\,ksi$

$Shear_{mp} := Shear\_up_{mp} + Shear\_p_{mp}$ $Shear_{mp} = 6.515\,kip$

$f_{StlBm.mp.Shear} := \frac{Shear_{mp}}{h \cdot tw \cdot in^2}$ $f_{StlBm.mp.Shear} = 1.85\,ksi$

$f_{StlBm.mp.Axial} := \frac{Axial\_up_{mp} + Axial\_p_{mp}}{A \cdot in^2}$ $f_{StlBm.mp.Axial} = 0.10685\,ksi$

Allowable Stresses

(AASHTO 5.7.1)

$$fF_{bSteelBeam}(L_{Unbraced}) := \left| \begin{array}{l} T \leftarrow \dfrac{0.4138 \cdot E_{Steel} \cdot b \cdot tf \cdot in}{L_{Unbraced} \cdot h} \\ \lambda \leftarrow \dfrac{L_{Unbraced}}{r_t \cdot in} \\ F_b \leftarrow \left(\dfrac{2}{3} - \dfrac{F_{SteelBeam.y} \cdot \lambda^2}{52.759 \cdot E_{Steel}} \right) \cdot F_{SteelBeam.y} \quad \text{if} \quad \sqrt{\dfrac{3.517 \cdot E_{Steel}}{F_{SteelBeam.y}}} \le \lambda \le \sqrt{\dfrac{17.586 \cdot E_{Steel}}{F_{SteelBeam.y}}} \\ F_b \leftarrow \dfrac{5.862 \cdot E_{Steel}}{\lambda^2} \quad \text{if} \quad \lambda \ge \sqrt{\dfrac{17.586 \cdot E_{Steel}}{F_{SteelBeam.y}}} \\ F_b \leftarrow T \quad \text{otherwise} \\ F_b \leftarrow T \quad \text{if} \quad F_b < T \\ F_b \leftarrow 0.6 \cdot F_{SteelBeam.y} \quad \text{if} \quad F_b > 0.6 \cdot F_{SteelBeam.y} \\ 1.33 \cdot F_b \end{array} \right.$$

$F_{StlBm.mp.b} := fF_{bSteelBeam}(L_{mp\_unbraced})$ $\quad F_{StlBm.mp.b} = 28.728\,ksi$

$F_{StlBm.v} := 0.33 \cdot F_{SteelBeam.y} \cdot 1.33$ $\quad F_{StlBm.v} = 15.8\,ksi$ *(AASHTO 5.11.3)*

$$C_{a.mp.StlBm} := 1 - \left[\frac{Axial\_up_{mp} + 0.38 \cdot Axial\_p_{mp}}{\dfrac{2.46 \cdot E_{Steel} \cdot I \cdot in^4}{\left(Main_{Height} + \dfrac{Panel_{Depth}}{2} \right)^2}} \right]$$

$C_{a.mp.StlBm} := if(C_{a.mp.StlBm} \le 1, C_{a.mp.StlBm}, 1.0)$ $\quad C_{a.mp.StlBm} = 0.998$

(AASHTO 5.12.1)

$$CSR_{StlBm.mp} := \frac{f_{StlBm.mp.Axial}}{1.33 \cdot 0.6 \cdot F_{SteelBeam.y}} + \frac{f_{StlBm.mp.Bending}}{C_{a.mp.StlBm} \cdot F_{StlBm.mp.b}} + \left(\frac{f_{StlBm.mp.Shear}}{F_{StlBm.v}} \right)^2$$

$CSR_{StlBm.mp} = 0.845$ $\quad < 1 \quad$ ---> OK

(W12x40 is satisfy structural requirement by AASHTO 2001 for use in the selected 3-post sign)

HINGE DESIGNS

Steel Plates *Plate Material and Section Properties of fuse plate and hinge plate*

$f_y := 36ksi$ *Steel yield strength*

$E_{st} := 29000ksi$ *Steel Young's modulus*

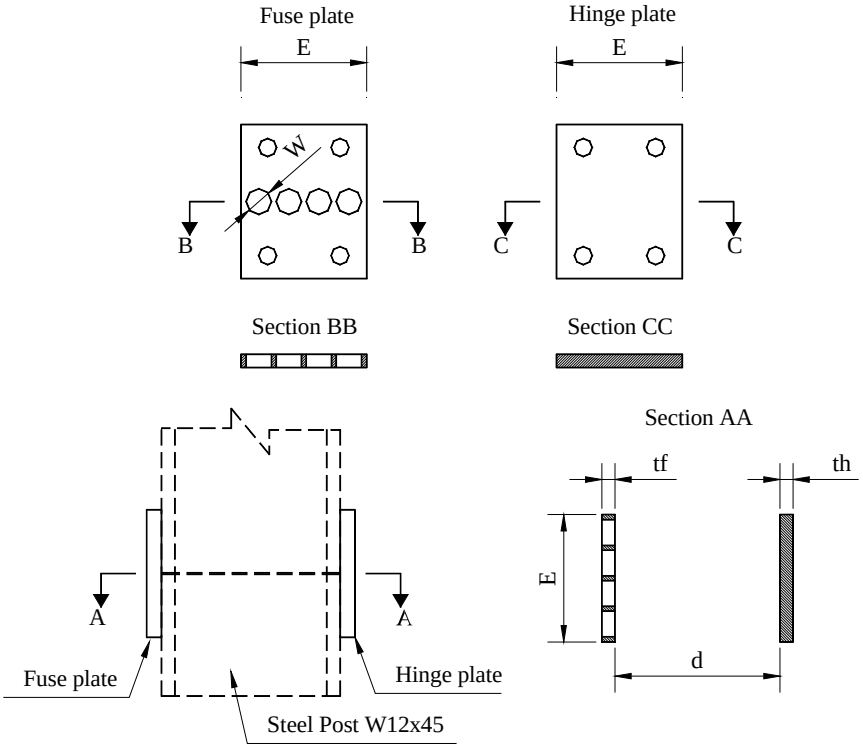

$E := (8 + 3 \div 8)in$ *Width of hinge and fuse plates*

$tf := 0.5in$ *Fuse plate thickness*

$th := 0.5in$ *Hinge plate thickness*

$d := 12.1 \cdot in$ *W12x45 section height*

$W := (1 + 11 \div 16)in$ *Hole diameter*

$Af := (E - 4W) \cdot tf$ *Section area of fuse plate at mid-height*

$Af = 0.813\,in^2$

$Ah := E \cdot th$ *Section area of hinge plate at mid-height*

$Ah = 4.188\,in^2$

$Moment := \left(WL_{Panel} \div 3\right) \cdot \left(Panel_{Depth} \div 2\right)$ *Moment applied on hinge*

$Moment = 392.273\,kip \cdot in$

$$x_c := \frac{Ah \cdot \left(d + \frac{th}{2} + \frac{tf}{2} \right)}{Ah + Af} \qquad x_c = 10.553\,in$$

Conservatively assume perfectly plastic steel:

$$M_{plastic} := f_y \cdot \left[Af \cdot x_c + Ah \cdot \left(d + \frac{tf}{2} + \frac{tf}{2} - x_c \right) \right]$$

$M_{plastic} = 617.321\,kip \cdot in$ > Moment $= 392.273\,kip \cdot in$ (OK)

Wind load on the sign system calculated according to ASCE7-5:

References: *ASCE. (2005). "Minimum design loads for buildings and other structures." SEI/ASCE 7-05, Reston, Va; FDOT MultiPost2001v1.1*

Unis $kip := 1000 \cdot lbf$ $ksi := 1000 \cdot psi$ $psf := \frac{lbf}{ft^2}$

LOAD CALCULATIONS:

Panel Dimensions and Wind Speed:

$Panel_{Width} := 20 \cdot ft$ $Panel_{Depth} := 12 \cdot ft$ $Clear_{Height} := 11 \cdot ft$ $V_{Speed} := 150 \cdot mph$

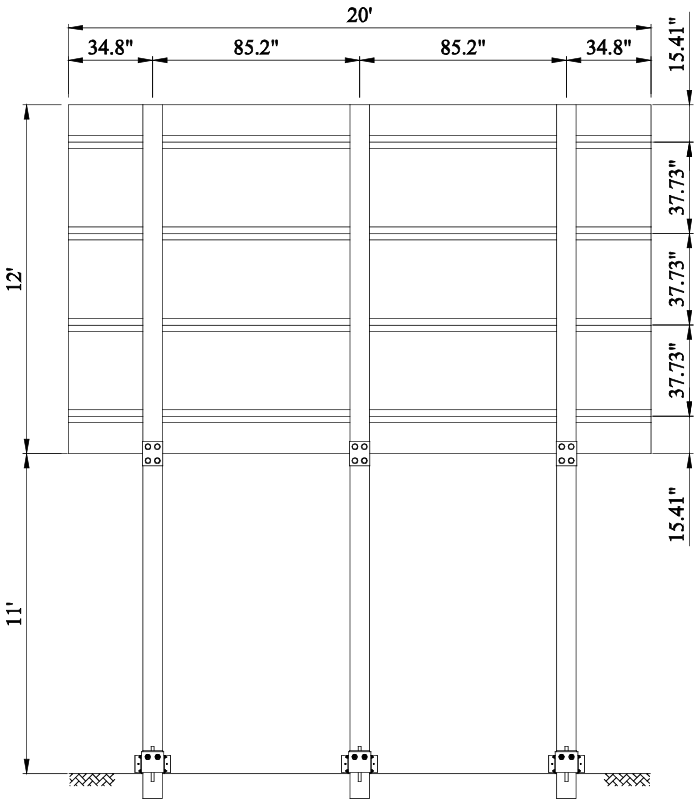
20'
34.8"
85.2"
85.2"
34.8"
15.41"
37.73"
37.73"
37.73"
12'
15.41"
11'

Flat and open terrain, Exposure C

$V_{Speed} := 150$ *Basic wind speed (mph)*

$Main_{Height} := Clear_{Height} + \frac{Panel_{Depth}}{2}$ $Main_{Height} = 17\,ft$

Structural characteristics:

$Weight_{Panel} := 4 \cdot \frac{lbf}{ft^2} \cdot Panel_{Width} \cdot Panel_{Depth}$ $Weight_{Panel} = 0.96\,kip$ *Panel Weight*

$Weight_{Post} := \left(40 \frac{lbf}{ft}\right) \cdot \left(Clear_{Height} + Panel_{Depth}\right) \cdot 3$ $Weight_{Post} = 2.76\,kip$ *Post Weight W12x40*

Estimate fundamental frequency based on cantilever model:

$Mass := \frac{Weight_{Panel} + Weight_{Post} \div 2}{g}$ $Mass = 1.061 \times 10^3\,kg$

$I := 307 \cdot in^4$ *Post moment of inertia*

$E := 29000ksi$

$k_0 := \frac{3 \cdot E \cdot I}{Main_{Height}^3} \cdot 3$ $k_0 = 9.438 \frac{kip}{in}$

$\omega_0 := \sqrt{\frac{k_0}{Mass}}$ $\omega_0 = 39.462 \frac{1}{s}$ $T_0 := \frac{2 \cdot \pi}{\omega_0}$

$f_0 := \frac{1}{T_0}$ $f_0 = 6.281\,Hz$

$k_1 := k_0 \div 2$ *Assume stiffness of the sign structure with breakaway feature introduced reduces 2 times*

$\omega_1 := \sqrt{\frac{k_1}{Mass}}$ $\omega_1 = 27.904 \frac{1}{s}$ $T_1 := \frac{2 \cdot \pi}{\omega_1}$

$f_1 := \frac{1}{T_1}$ $f_1 = 4.441\,Hz$

Since static experimental tests (Figure 7-69) shown that post stiffness reduce less than 2 times, actual frequency (f_a) of the breakaway support structure is within (f_1, f_0).

f_a > 1 Hz *-> Rigid structure*

Sign panel wind pressure

$q_z = 0.00256 \cdot K_z \cdot K_{zt} \cdot K_d \cdot V^2 \cdot I$ *velocity pressure*

$\alpha := 9.5$ *constant value exposure "C"* $\alpha = 9.5$

$z_g := 900 \cdot ft$ *constant value exposure "C"* $z_g = 900\,ft$ *Table 6-2*

$K_z := 0.85 + \frac{0.9 - 0.85}{20ft - 15ft} \cdot (Main_{Height} - 15ft)$ *Velocity pressure exposure coefficient* *Table 6-3*

$K_z = 0.87$

$K_{zt} := 1$ *Topographic factor(1.0 for flat terrain)*

$K_d := 0.85$ *Wind directionality factor (0.85 for solid sign , Table 6-4, ASCE 7-05)*

$I := 1$ *Important factor (Category I)*

Velocity pressure at center of sign panel:

$q_{z\_Panel} := 0.00256 \cdot K_z \cdot K_{zt} \cdot K_d \cdot V_{Speed}^2 \cdot I \cdot psf$

$q_{z\_Panel} = 42.595\,psf$

$G := 0.85$ *Gust effect factor for rigid structure*

Force coefficient factor C_f determination: *Figure 6-20 ASCE 7-05*

$R_{sh} := \frac{Panel_{Depth}}{Panel_{Depth} + Clear_{Height}}$ $R_{sh} = 0.522$ *Ratio s/h*

$R_{Bs} := \frac{Panel_{Width}}{Panel_{Depth}}$ $R_{Bs} = 1.667$ *Ratio B/s*

For B/s=1:

$C_{f\_1} := 1.75 - \frac{1.75 - 1.65}{0.7 - 0.5} \cdot (R_{sh} - 0.5)$ $C_{f\_1} = 1.739$

For B/s=2:

$C_{f\_2} := 1.7 - \frac{1.7 - 1.6}{0.7 - 0.5} \cdot (R_{sh} - 0.5)$ $C_{f\_2} = 1.689$

$C_f := C_{f\_1} - \frac{C_{f\_1} - C_{f\_2}}{2 - 1} \cdot (R_{Bs} - 1)$ $C_f = 1.706$

Force on panel:

$WL_{Panel} := q_{z\_Panel} \cdot G \cdot C_f \cdot (Panel_{Width} \cdot Panel_{Depth})$

$WL_{Panel} = 14.82\,kip$ *Close to force on panel calculated based on AASHTO 2001 and interims where WL_{Panel}=16.34 kip*

Windload from the Upper Structure to the Middle Post

$Shear\_up_{mp} := WL_{Panel} \cdot \frac{85.2in}{20ft}$ $Shear\_up_{mp} = 5.262\,kip$

$M\_up_{mp} := Main_{Height} \cdot Shear\_up_{mp}$ $M\_up_{mp} = 1073.44\,kip \cdot in$

Wind pressure directly applied on post

$K_d := 0.85$ *Wind directionality factor (0.85 for solid sign , Table 6-4, ASCE 7-05)*

Force coefficient factor C_f determination:

$WD_{post} := 8.01in$ *Post width*

$\frac{Panel_{Depth} + Clear_{Height}}{WD_{post}} = 34.457$ *Ratio h/D*

$C_f := 2$ *Figure 6-21 ASCE 7-05*

$K_z := 0.85$ *Velocity pressure exposure coefficient* *Table 6-3*

Velocity pressure on post:

$q_{z\_Post} := 0.00256 \cdot K_z \cdot K_{zt} \cdot K_d \cdot V_{Speed}^2 \cdot I \cdot psf$ $q_{z\_Post} = 41.616\,psf$

Force on post:

$WL_{mp} := q_{z\_Post} \cdot G \cdot C_f \cdot WD_{post} \cdot \left(Main_{Height} - \frac{Panel_{Depth}}{2} \right)$

$WL_{mp} = 0.519\,kip$ *Compared to force on post calculated based on AASHTO 2001 and interims where WL_{mp}=0.713 kip*

$Shear\_p_{mp} := WL_{mp}$ $Shear\_p_{mp} = 0.519\,kip$

$M\_p_{mp} := WL_{mp} \cdot \left[\left(Main_{Height} - \frac{Panel_{Depth}}{2} \right) \div 2 \right]$ $M\_p_{mp} = 34.284\,kip \cdot in$

Total Middle Post Forces due to Wind

$M_{mp} := M\_up_{mp} + M\_p_{mp}$ $M_{mp} = 1107.72\,kip \cdot in$

$Shear_{mp} := Shear\_up_{mp} + Shear\_p_{mp}$ $Shear_{mp} = 5.781\,kip$

APPENDIX B
PENDULUM SUPPORT STRUCTURE DRAWINGS

Structural design details of the pendulum support structure are presented in this appendix.

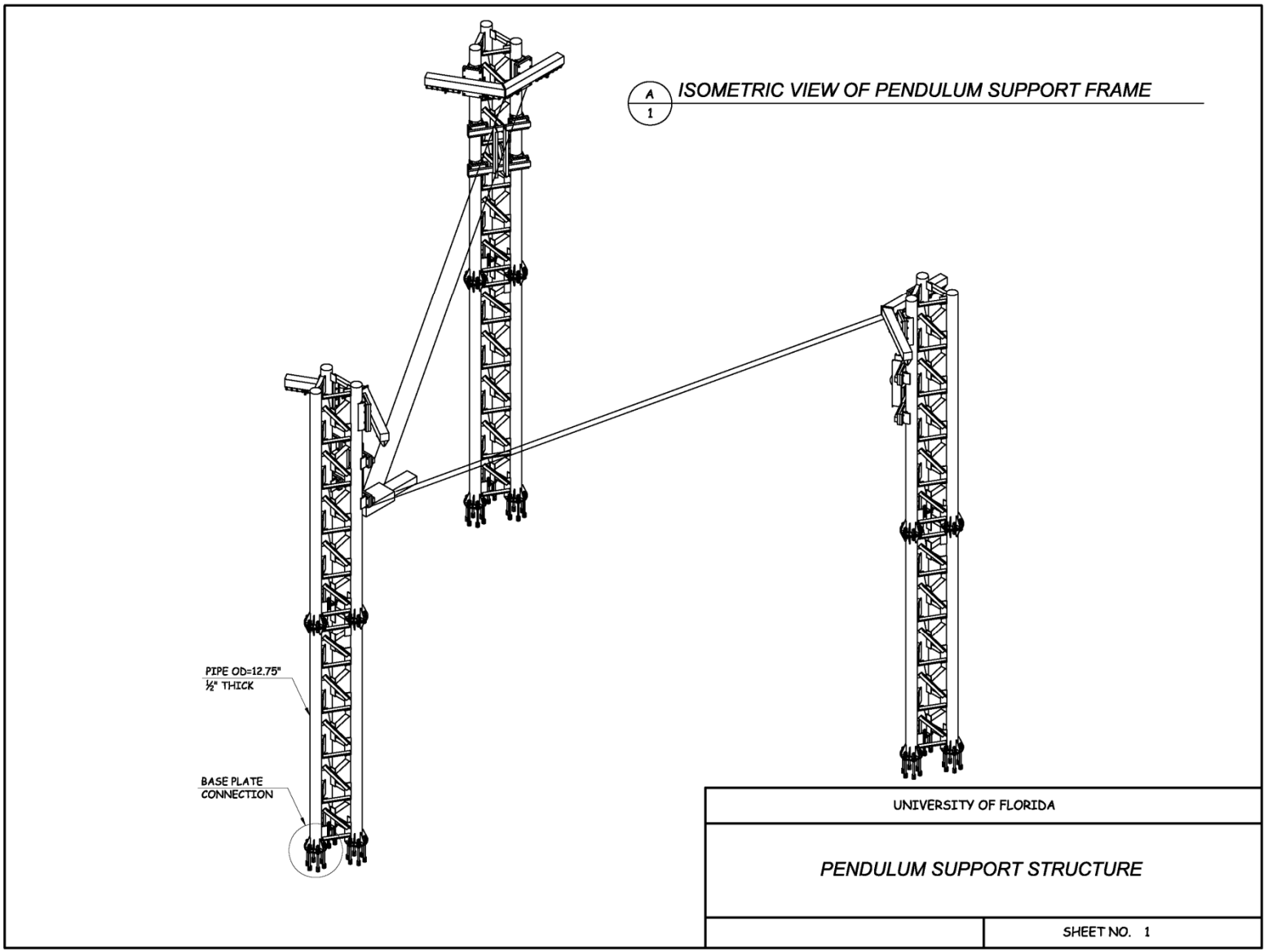
A
1
ISOMETRIC VIEW OF PENDULUM SUPPORT FRAME
PIPE OD=12.75"
½" THICK
BASE PLATE
CONNECTION
UNIVERSITY OF FLORIDA
PENDULUM SUPPORT STRUCTURE
SHEET NO. 1

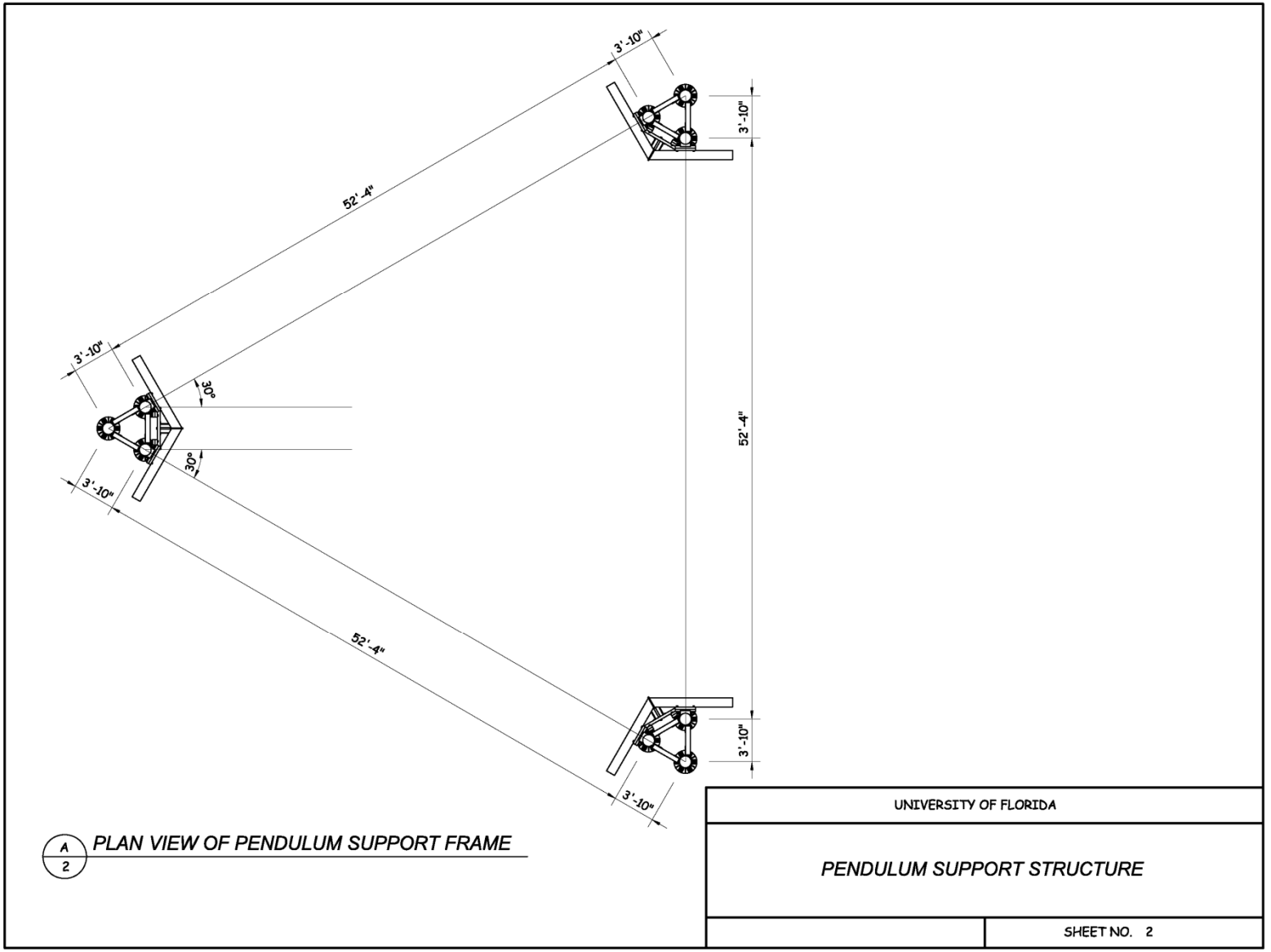
3'-10"
52'-4"
3'-10"
30°
30°
3'-10"
52'-4"
52'-4"
3'-10"
3'-10"
A
2
PLAN VIEW OF PENDULUM SUPPORT FRAME
UNIVERSITY OF FLORIDA
PENDULUM SUPPORT STRUCTURE
SHEET NO. 2

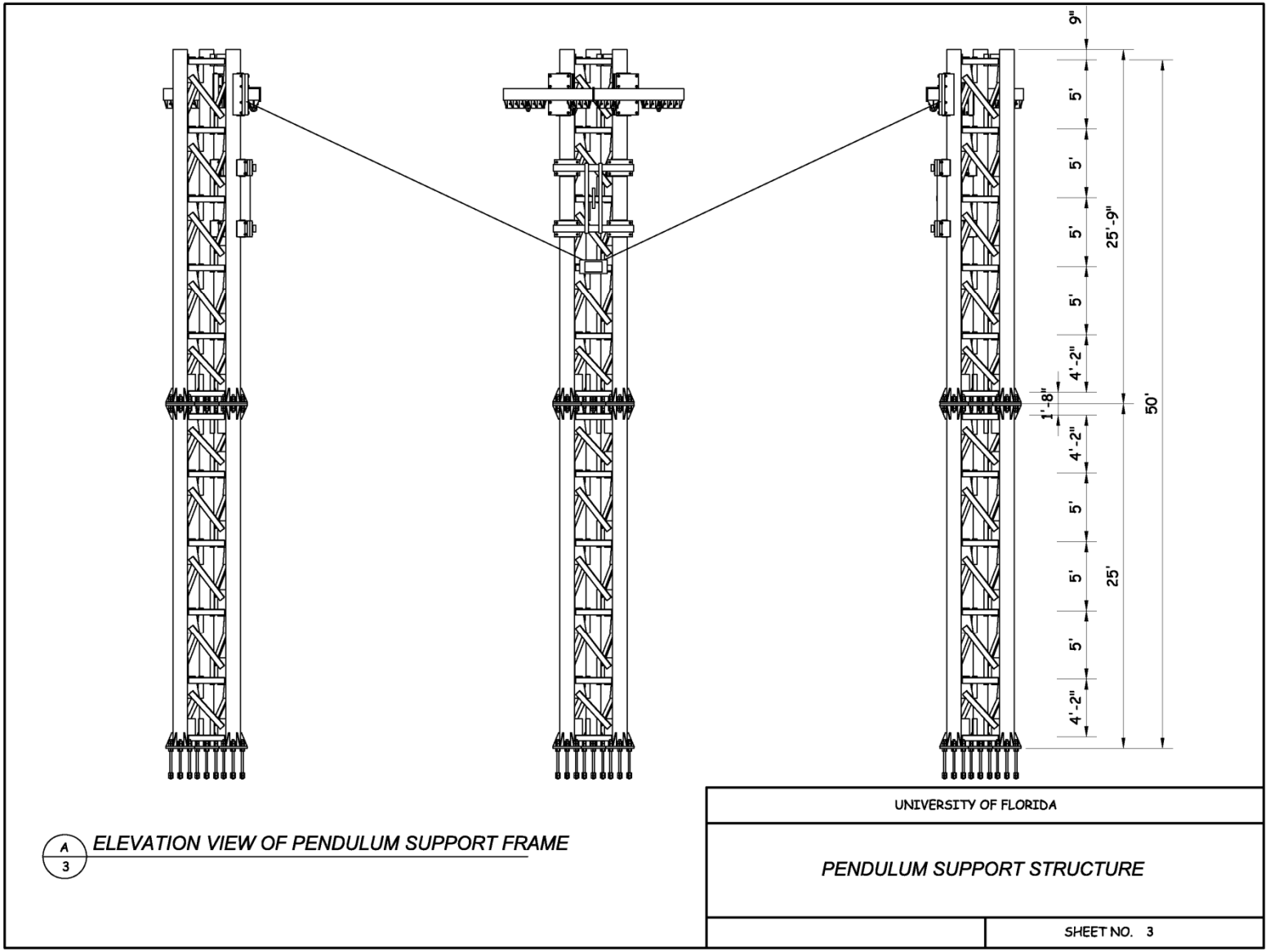

A/3 ELEVATION VIEW OF PENDULUM SUPPORT FRAME

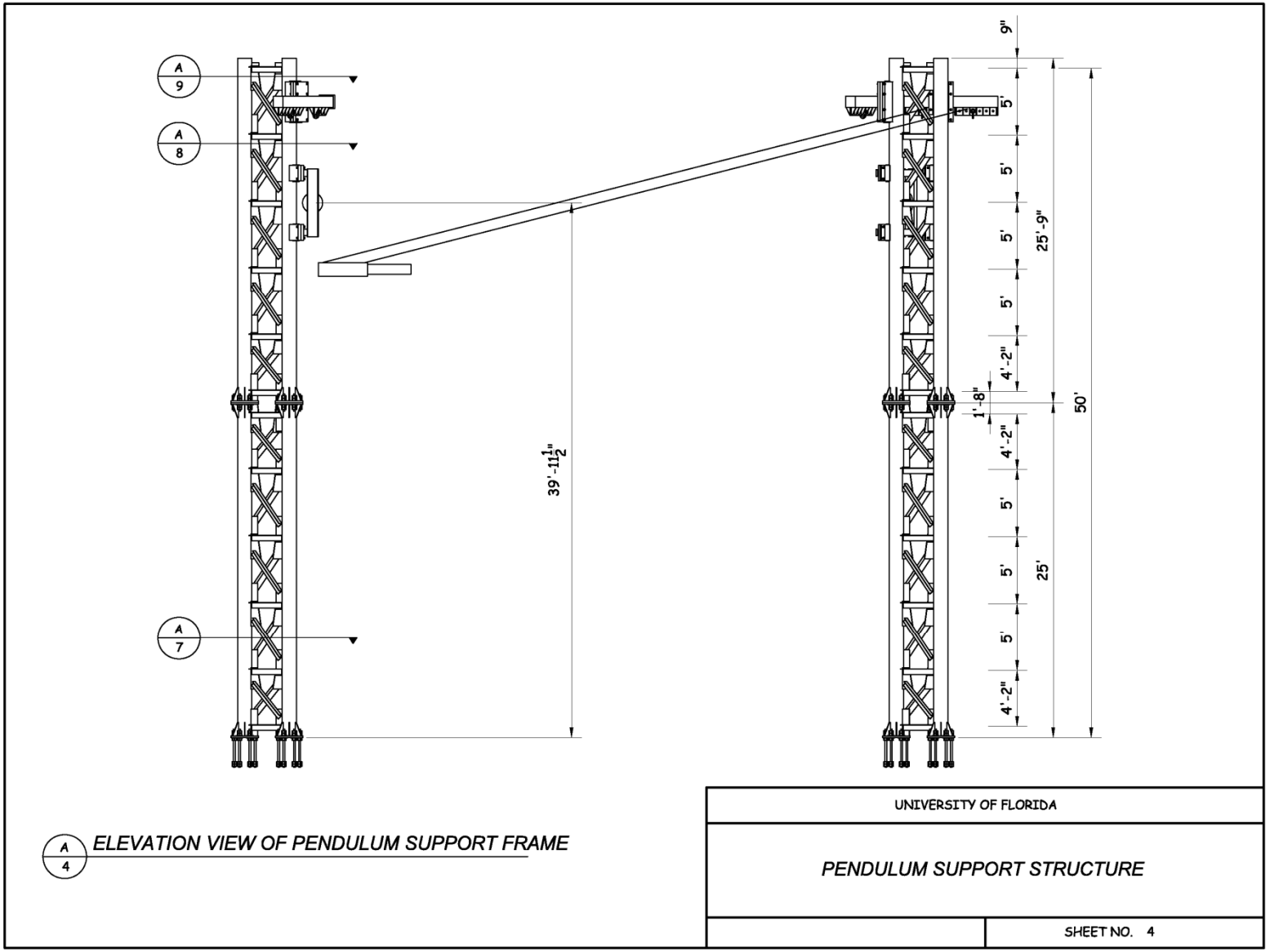
A 9
A 8
A 7
39'-11 1/2"
9"
5'
5'
5'
5'
5'
25'-9"
4'-2"
1'-8"
50'
4'-2"
5'
5'
25'
5'
4'-2"
A 4
ELEVATION VIEW OF PENDULUM SUPPORT FRAME
UNIVERSITY OF FLORIDA
PENDULUM SUPPORT STRUCTURE
SHEET NO. 4

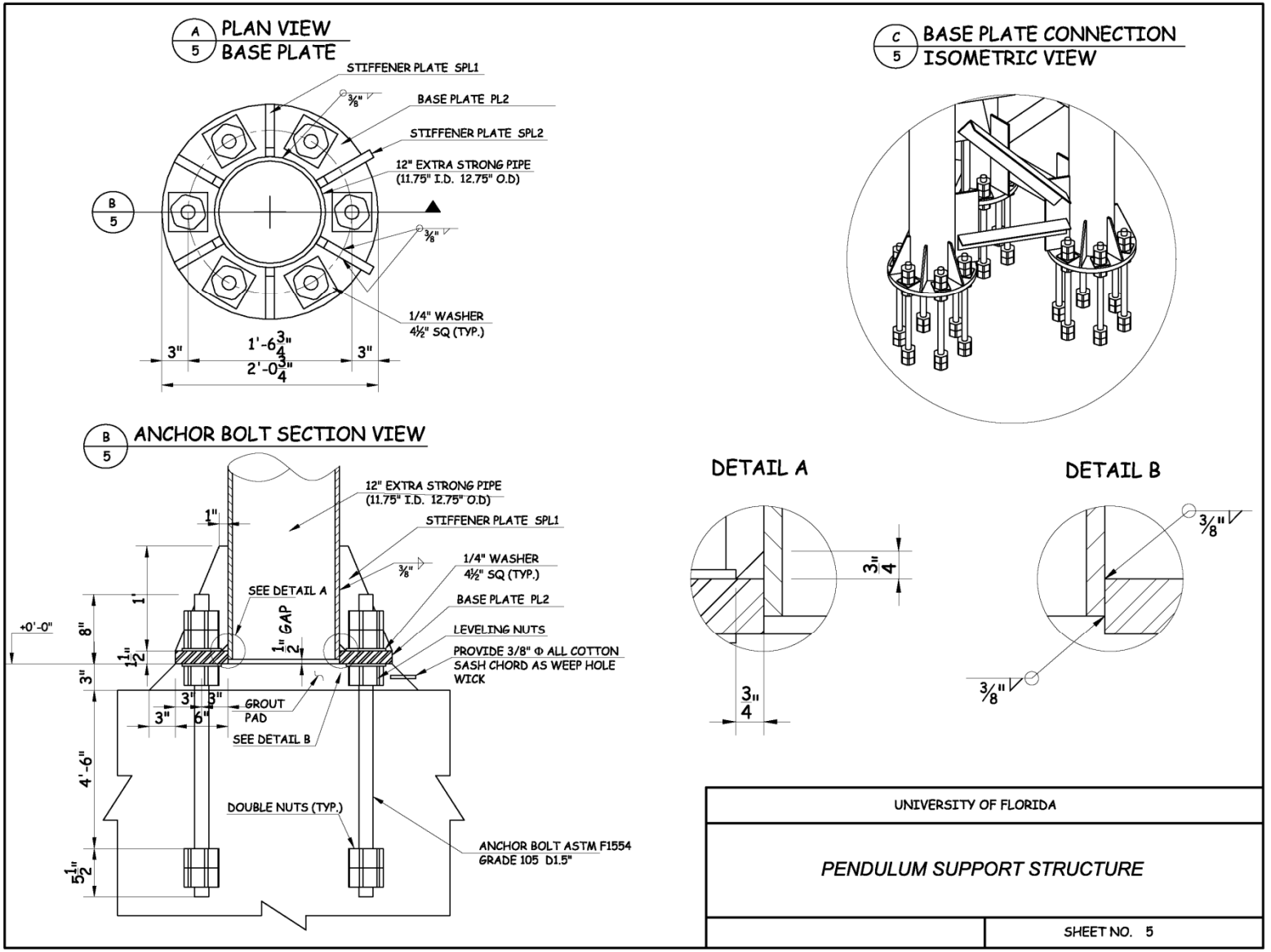
A 5 PLAN VIEW BASE PLATE
STIFFENER PLATE SPL1
BASE PLATE PL2
STIFFENER PLATE SPL2
12" EXTRA STRONG PIPE (11.75" I.D. 12.75" O.D)
B 5
1/4" WASHER 4½" SQ (TYP.)
3"
1'-6 3/4"
2'-0 3/4"
3"
C 5 BASE PLATE CONNECTION ISOMETRIC VIEW
B 5 ANCHOR BOLT SECTION VIEW
12" EXTRA STRONG PIPE (11.75" I.D. 12.75" O.D)
STIFFENER PLATE SPL1
1/4" WASHER 4½" SQ (TYP.)
SEE DETAIL A
BASE PLATE PL2
LEVELING NUTS
PROVIDE 3/8" Φ ALL COTTON SASH CHORD AS WEEP HOLE WICK
1" GAP
+0'-0"
GROUT PAD
SEE DETAIL B
DOUBLE NUTS (TYP.)
ANCHOR BOLT ASTM F1554 GRADE 105 D1.5"
DETAIL A
DETAIL B
UNIVERSITY OF FLORIDA
PENDULUM SUPPORT STRUCTURE
SHEET NO. 5

A 6 PLAN VIEW
COLUMN JOINT

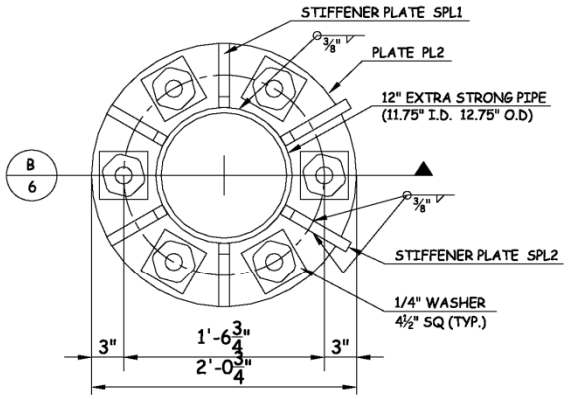

B 6 COLUMN JOINT SECTION VIEW

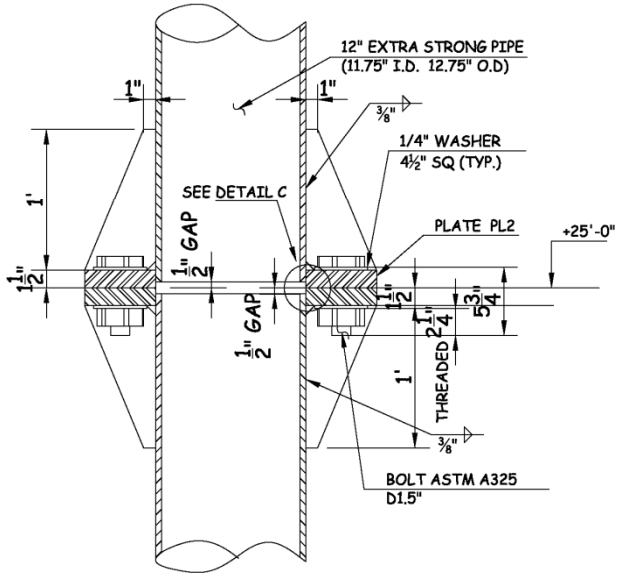

C 6 ISOMETRIC VIEW
COLUMN JOINT

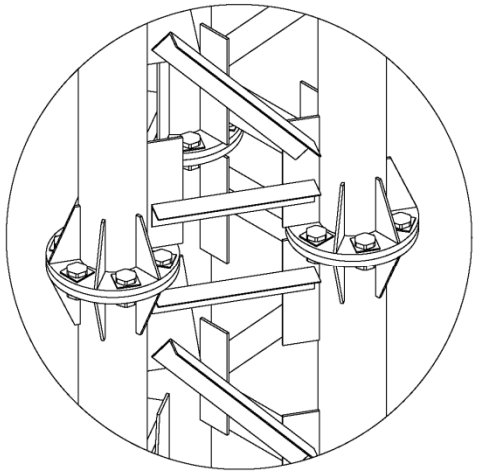

DETAIL C

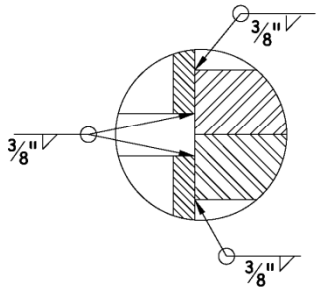

UNIVERSITY OF FLORIDA	
PENDULUM SUPPORT STRUCTURE	
	SHEET NO. 6

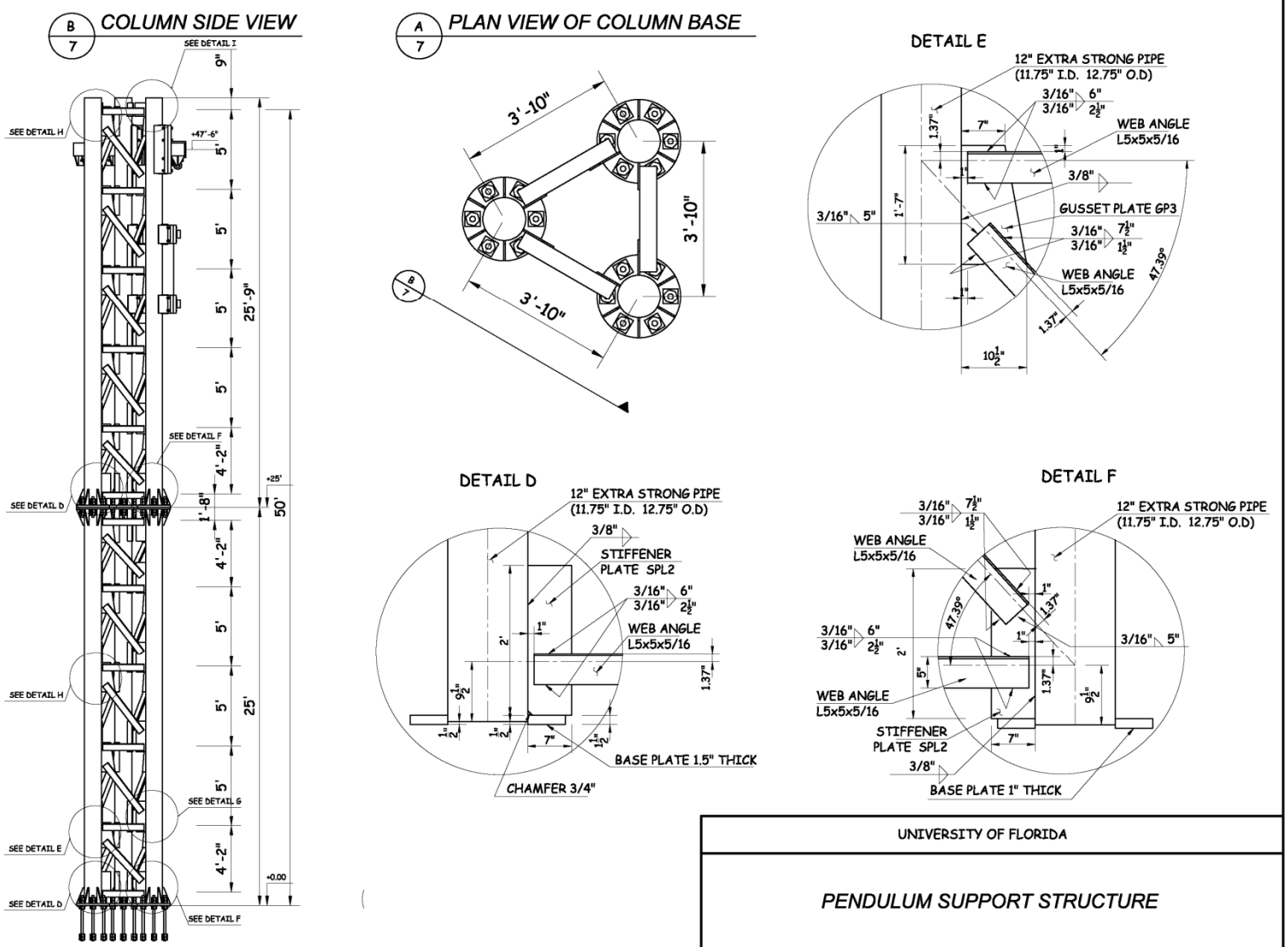
B
7
COLUMN SIDE VIEW
SEE DETAIL I
9"
SEE DETAIL H
+47'-6"
5'
5'
5'
5'
25'-9"
SEE DETAIL F
4'-2"
+25'
SEE DETAIL D
1'-8"
50'
4'-2"
5'
5'
SEE DETAIL H
25'
5'
SEE DETAIL G
SEE DETAIL E
4'-2"
+0.00
SEE DETAIL D
SEE DETAIL F
A
7
PLAN VIEW OF COLUMN BASE
3'-10"
3'-10"
3'-10"
7/8
DETAIL E
12" EXTRA STRONG PIPE
(11.75" I.D. 12.75" O.D)
3/16"
3/16"
6"
2½"
WEB ANGLE
L5x5x5/16
1.37"
7"
1"
3/8"
1'-7"
3/16"
5"
GUSSET PLATE GP3
3/16"
3/16"
7½"
1½"
WEB ANGLE
L5x5x5/16
47.39°
1.37"
10½"
DETAIL D
12" EXTRA STRONG PIPE
(11.75" I.D. 12.75" O.D)
3/8"
STIFFENER
PLATE SPL2
3/16"
3/16"
6"
2½"
WEB ANGLE
L5x5x5/16
1"
2'
1.37"
9½"
1"
2
1"
2
7"
1½"
BASE PLATE 1.5" THICK
CHAMFER 3/4"
DETAIL F
3/16"
3/16"
7½"
1½"
12" EXTRA STRONG PIPE
(11.75" I.D. 12.75" O.D)
WEB ANGLE
L5x5x5/16
1"
1.37"
47.39°
3/16"
3/16"
6"
2½"
2'
1"
3/16"
5"
5"
1.37"
WEB ANGLE
L5x5x5/16
9½"
STIFFENER
PLATE SPL2
7"
3/8"
BASE PLATE 1" THICK
UNIVERSITY OF FLORIDA
PENDULUM SUPPORT STRUCTURE
SHEET NO. 7

DETAIL G

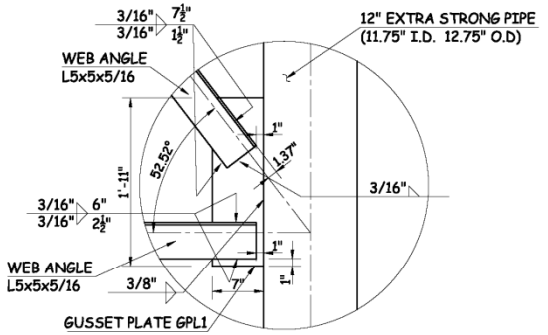

DETAIL H

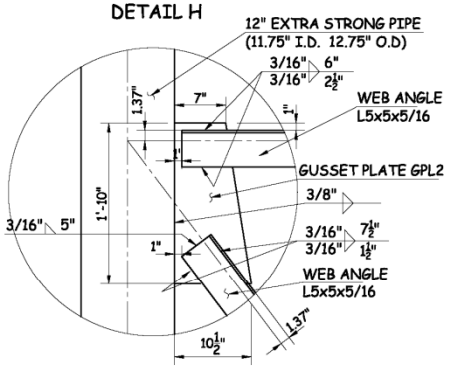

DETAIL I

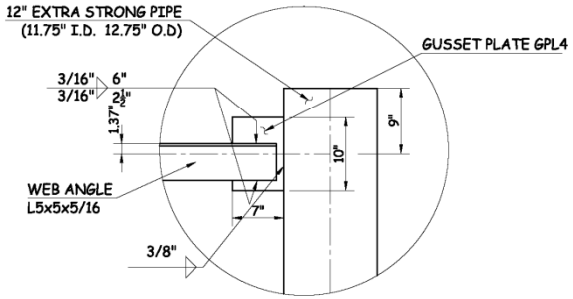

UNIVERSITY OF FLORIDA	
PENDULUM SUPPORT STRUCTURE	
	SHEET NO. 8

A 9 ISOMETRIC VIEW OF PULLEY HANGER

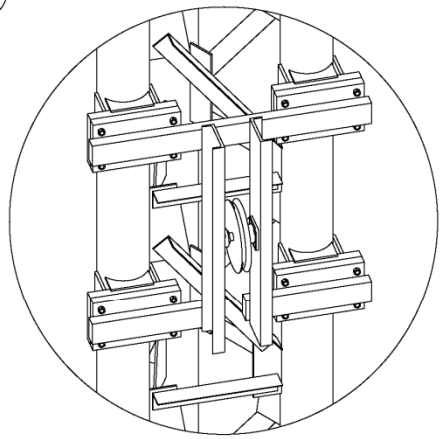

B 9 SIDE VIEW OF PULLEY HANGER

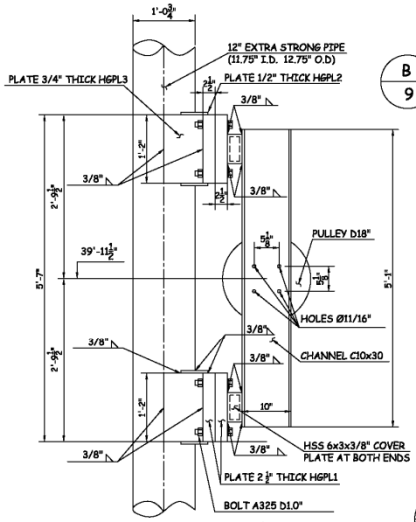

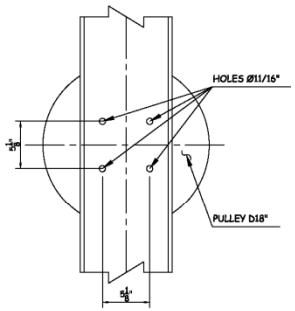

C 9 FRONT VIEW OF PULLEY HANGER

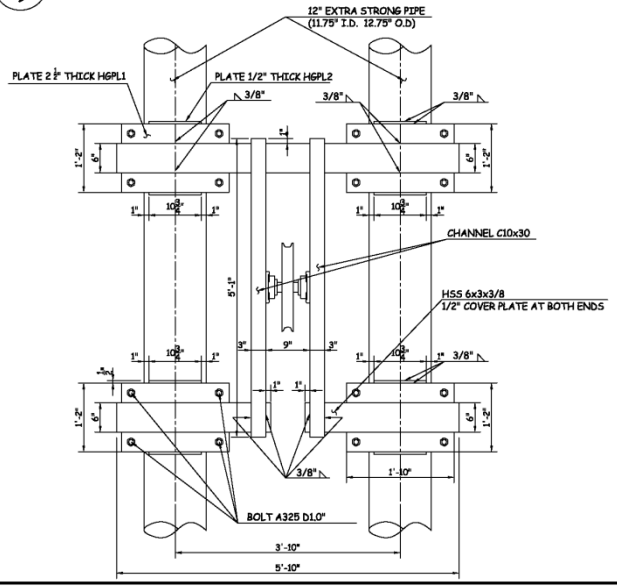

D 9 PLAN VIEW OF PULLEY HANGER

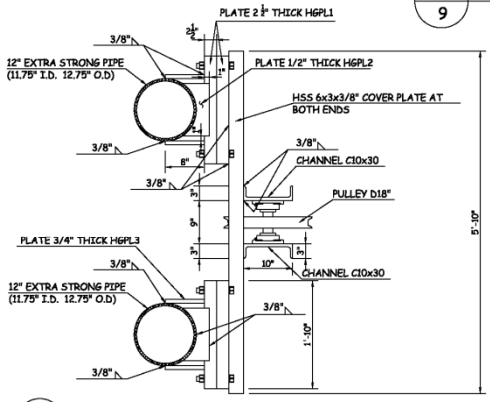

B 9

UNIVERSITY OF FLORIDA

PENDULUM SUPPORT STRUCTURE

SHEET NO. 9

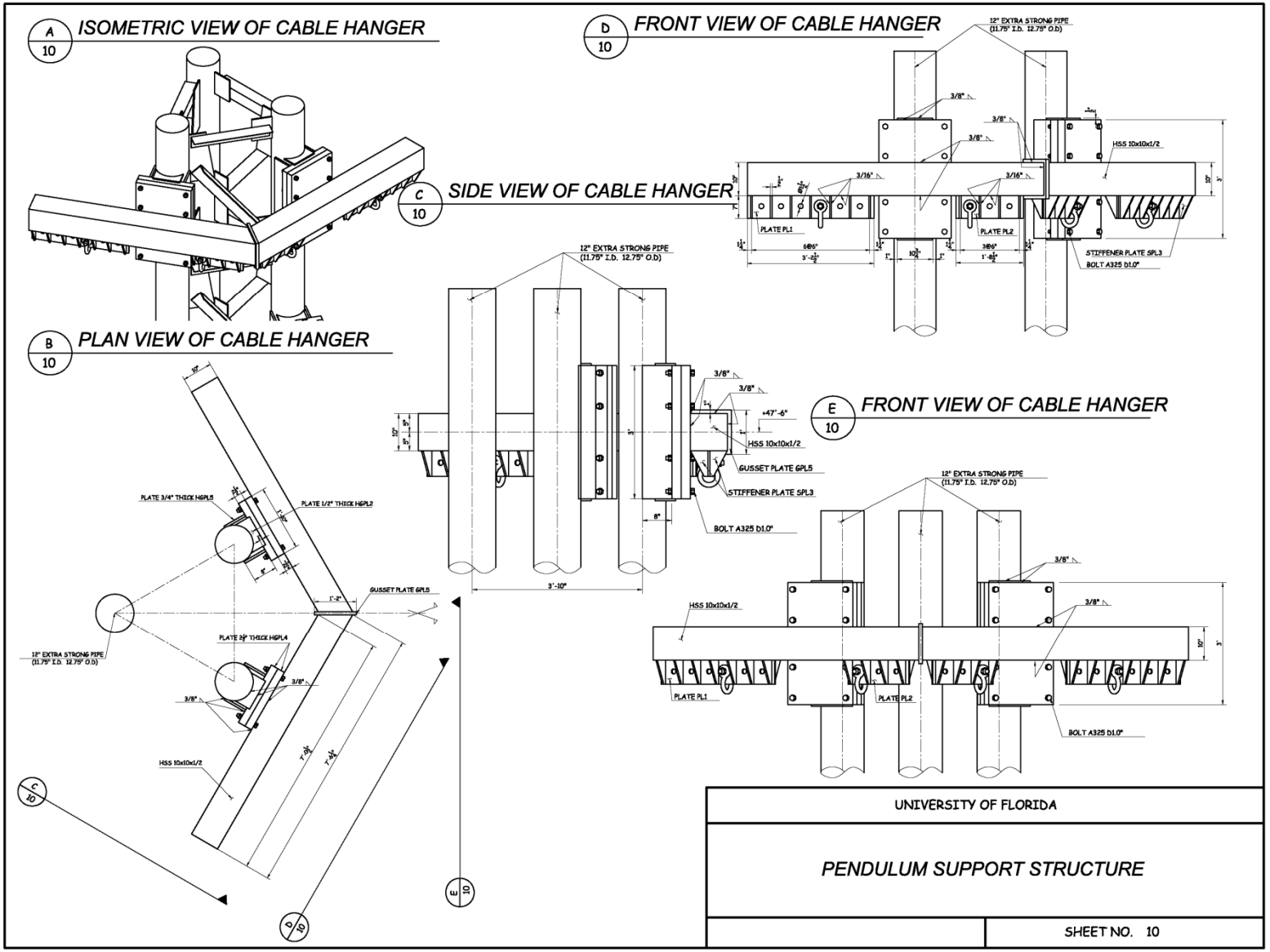
A 10
ISOMETRIC VIEW OF CABLE HANGER
B 10
PLAN VIEW OF CABLE HANGER
C 10
SIDE VIEW OF CABLE HANGER
D 10
FRONT VIEW OF CABLE HANGER
E 10
FRONT VIEW OF CABLE HANGER
12" EXTRA STRONG PIPE (11.75" I.D. 12.75" O.D)
HSS 10x10x1/2
PLATE PL1
PLATE PL2
STIFFENER PLATE SPL3
BOLT A325 D1.0"
GUSSET PLATE GPL5
PLATE 3/4" THICK HGPL5
PLATE 1/2" THICK HGPL2
PLATE 3/8" THICK HGPL4
3/8"
3/16"
3'-10"
UNIVERSITY OF FLORIDA
PENDULUM SUPPORT STRUCTURE
SHEET NO. 10

SCHEDULE FOR PLATES

PLATE	SIZE	THICKNESS
PL1	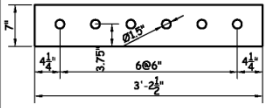	½"
PL2	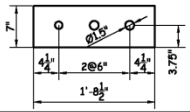	½"
PL3	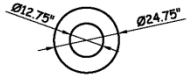	1.5"
GPL1		½"
GPL2	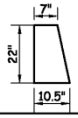	½"
GPL3	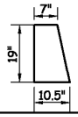	½"
GPL4		½"
GPL5		½"

PLATE	SIZE	THICKNESS
SPL1	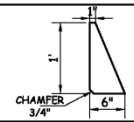	½"
SPL2	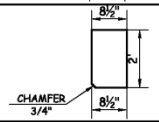	½"
SPL3		½"
HGPL1	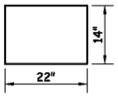	2½"
HGPL2	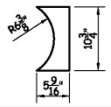	½"
HGPL3		¾"
HGPL4		2½"
HGPL5		¾"

UNIVERSITY OF FLORIDA

PENDULUM SUPPORT STRUCTURE

SHEET NO. 11

APPENDIX C
CABLE FORCE DETERMINATION

This appendix presents the calculation of cable forces for the simplified dynamic analysis of the pendulum support structure.

$\Xi \equiv 1$ ORIGIN$\equiv \Xi$ $kip \equiv 1000lbf$

$mass := 1.6(4090kg)$ $mass = 6544kg$

Determine cable force of a pendulum hung by one cable as a function of angle:

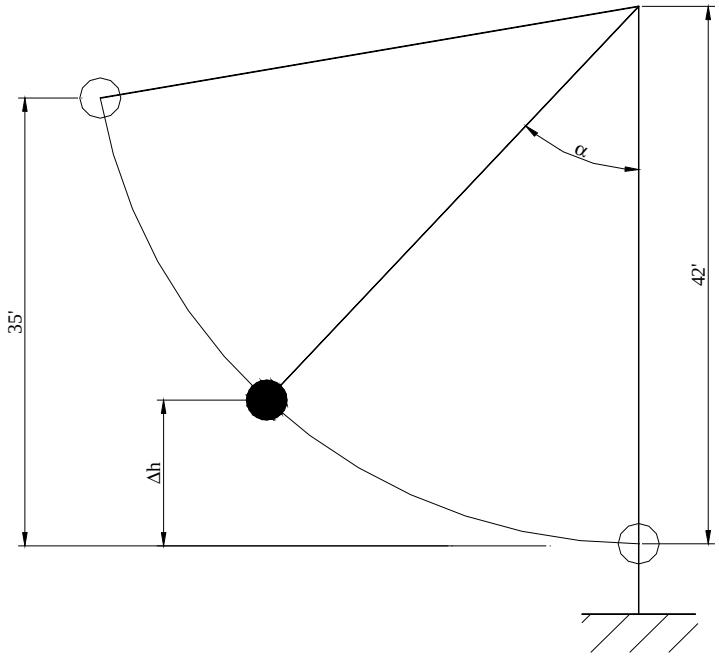

Maximum angle at 35ft drop height: $\alpha_{max} := \operatorname{acos}\left(\frac{42ft - 35ft}{42ft}\right)$ $\alpha_{max} = 80.41deg$

$L_{cb} := 42ft$ Cable length

$E := mass \cdot g \cdot (35ft)$ $E = 6.06 \times 10^{3}\, kip \cdot in$ Total Energy

$\Delta h(\alpha) := L_{cb} \cdot (1 - \cos(\alpha))$

$K(\alpha) := E - mass \cdot g \cdot \Delta h(\alpha)$ Kinetic energy

$v(\alpha) := \sqrt{2 \cdot K(\alpha) \div mass}$ Tangent Velocity

$F_{cf}(\alpha) := mass \cdot v(\alpha)^2 \div L_{cb}$ Centrifugal force in the cable

$F_{gr}(\alpha) := mass \cdot g \cdot \cos(\alpha)$ Gravity force in the cable

$F_{cb}(\alpha) := F_{cf}(\alpha) + F_{gr}(\alpha)$ Total force in the cable

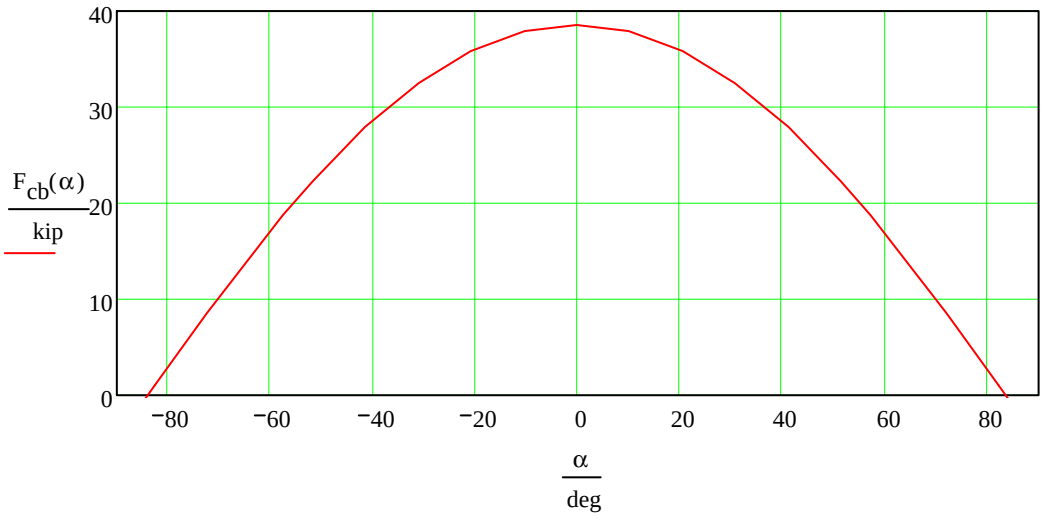

Determine cable force of the pylon structure:

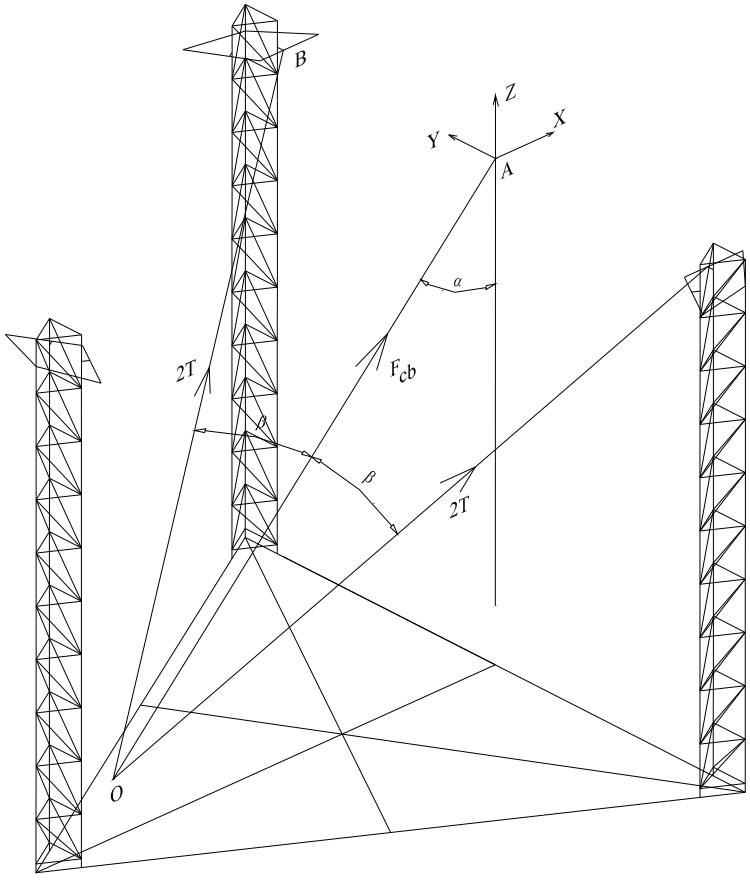

Choose the coordinate origin at the point A.

Coordinate of point A: $x_A := 0in$ $y_A := 0in$ $z_A := 0in$

Coordinate of point B: $x_B := 0in$ $y_B := 305.5in$ $z_B := 0in$

Coordinate of point O:

$x_O(\alpha) := L_{cb} \cdot \sin(\alpha)$ $y_O := 0in$ $z_O(\alpha) := -L_{cb} \cdot \cos(\alpha)$

Vector OA: $OA(\alpha) := \begin{pmatrix} x_A - x_O(\alpha) \\ y_A - y_O \\ z_A - z_O(\alpha) \end{pmatrix}$ Vector OB: $OB(\alpha) := \begin{pmatrix} x_B - x_O(\alpha) \\ y_B - y_O \\ z_B - z_O(\alpha) \end{pmatrix}$

Determine cosβ between vectors OA and OB:

$$\cos\beta(\alpha) := \frac{OA(\alpha) \cdot OB(\alpha)}{|OA(\alpha)| \cdot |OB(\alpha)|}$$

Force in a cable (4 cables are used to hang the pendulum):

$$T(\alpha) := \frac{F_{cb}(\alpha)}{4} \cdot \cos\beta(\alpha)$$

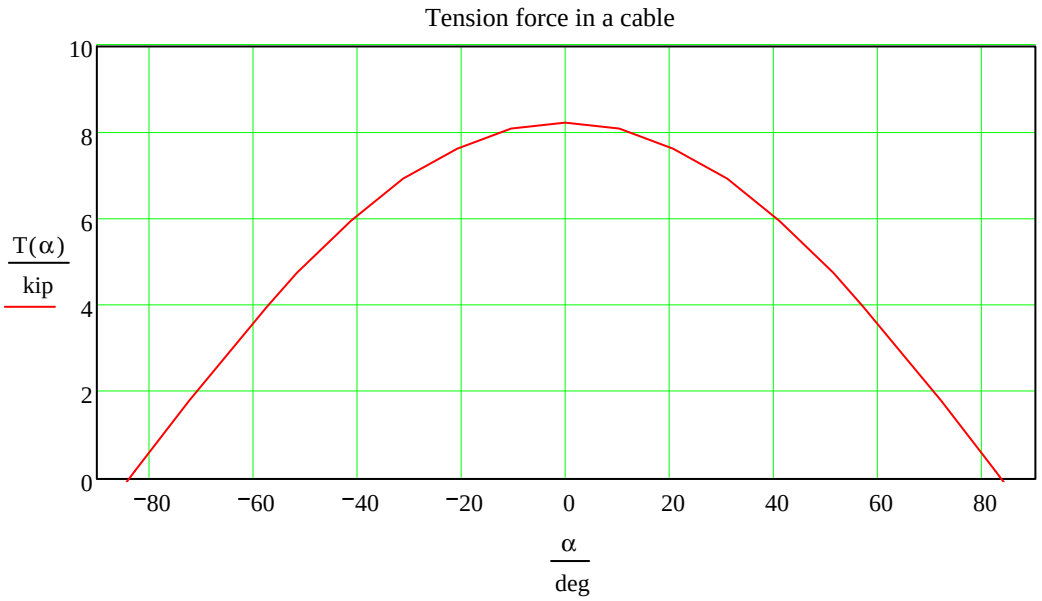

Resolve the force in each cable into 3 components:

Vector AX, AY, AZ:

$$AX := \begin{pmatrix} 1 \\ 0 \\ 0 \end{pmatrix} \text{in} \qquad AY := \begin{pmatrix} 0 \\ 1 \\ 0 \end{pmatrix} \text{in} \qquad AZ := \begin{pmatrix} 0 \\ 0 \\ 1 \end{pmatrix} \text{in}$$

$$\cos\_OB\_AX(\alpha) := \frac{OB(\alpha) \cdot AX}{|OB(\alpha)| \cdot |AX|}$$

$$\cos\_OB\_AY(\alpha) := \frac{OB(\alpha) \cdot AY}{|OB(\alpha)| \cdot |AY|}$$

$$\cos\_OB\_AZ(\alpha) := \frac{OB(\alpha) \cdot AZ}{|OB(\alpha)| \cdot |AZ|}$$

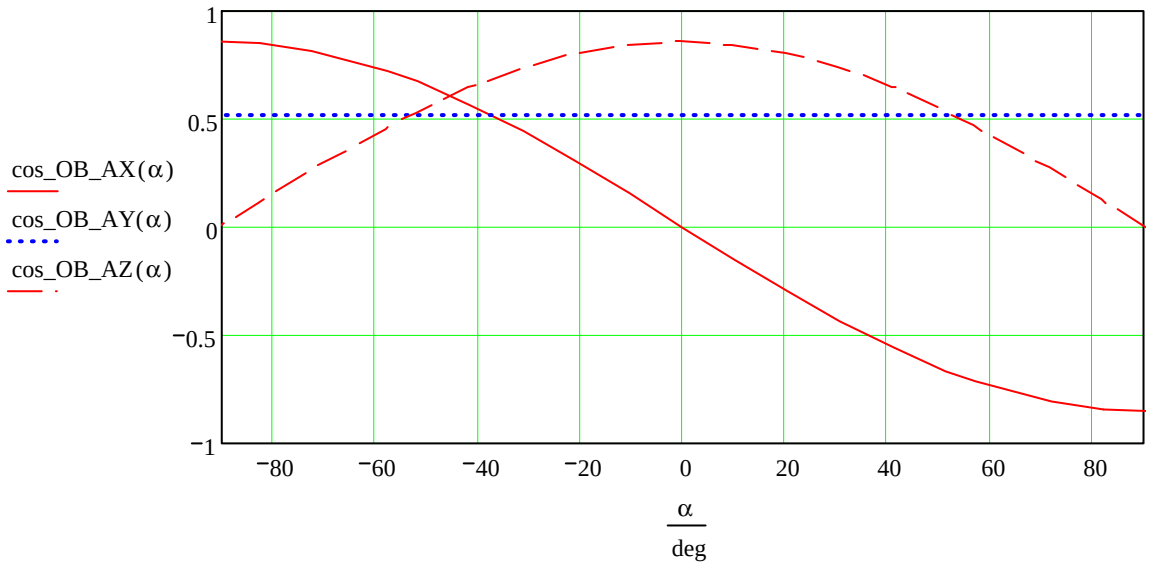

$TX(\alpha) := -T(\alpha)\cdot \cos\_OB\_AX(\alpha)$

$TY(\alpha) := -T(\alpha)\cdot \cos\_OB\_AY(\alpha)$

$TZ(\alpha) := -T(\alpha)\cdot \cos\_OB\_AZ(\alpha)$

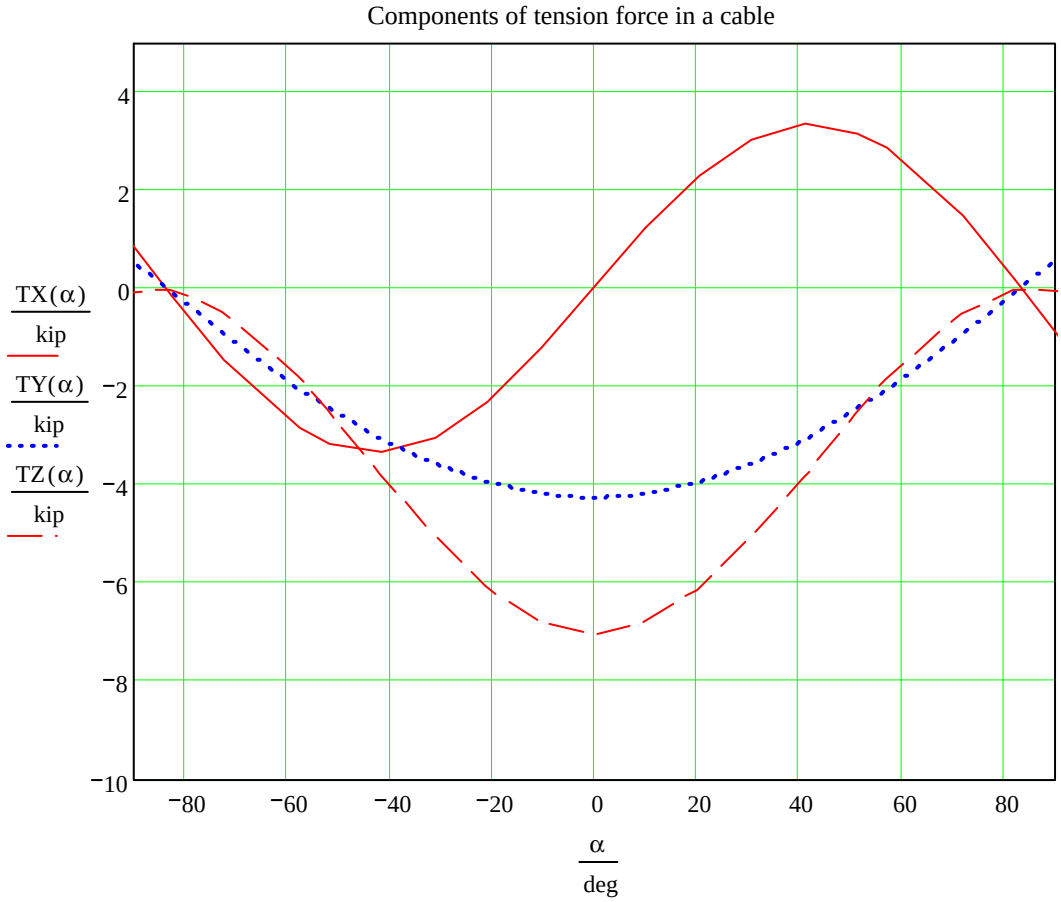

Determine maximum force components of the cable:

$n := 1001$ $\quad st := -90\frac{\pi}{180}$ $\quad end := 90\frac{\pi}{180}$ $\quad inc := (end - st) \div (n - 1)$

$i := 1..n$ $\quad inc = 0.18deg$ $\quad \boldsymbol{\alpha}_i := st + (i - 1)\cdot inc$

$\mathbf{TX}_i := \left|T(\boldsymbol{\alpha}_i)\cdot \cos\_OB\_AX(\boldsymbol{\alpha}_i)\right|$ $\quad maxTX := \max(\mathbf{TX})$ $\quad maxTX = 3.35kip$

$\mathbf{TY}_i := \left|-T(\boldsymbol{\alpha}_i)\cdot \cos\_OB\_AY(\boldsymbol{\alpha}_i)\right|$ $\quad maxTY := \max(\mathbf{TY})$ $\quad maxTY = 4.26kip$

$\mathbf{TZ}_i := \left|-T(\boldsymbol{\alpha}_i)\cdot \cos\_OB\_AZ(\boldsymbol{\alpha}_i)\right|$ $\quad maxTZ := \max(\mathbf{TZ})$ $\quad maxTZ = 7.03kip$

APPENDIX D
SHOP DRAWINGS OF SHEAR-CONTROLLED MOMENT COLLAR BREAKAWAY CONNECTION FABRICATED FOR STATIC TESTS

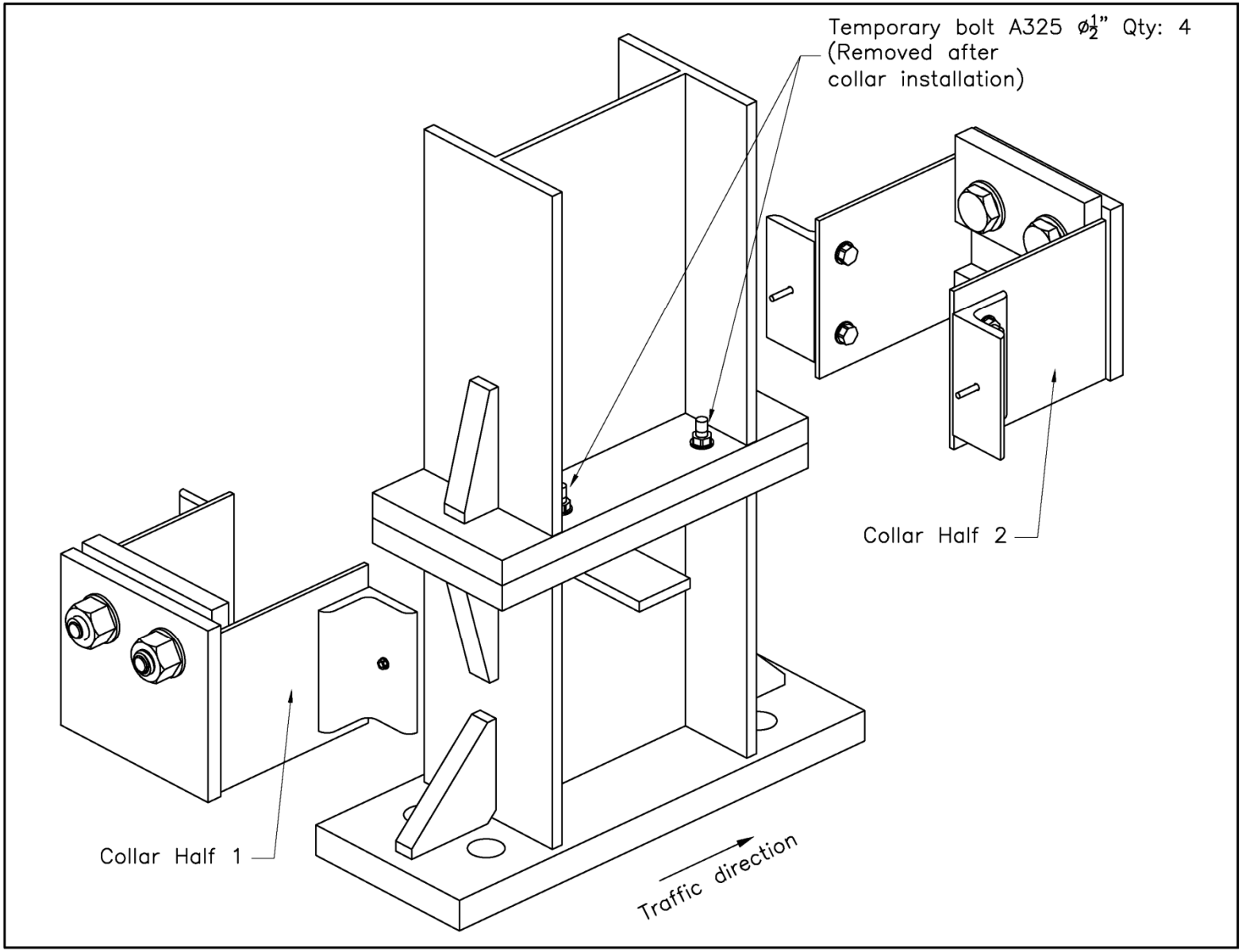
Temporary bolt A325 ø1/2" Qty: 4
(Removed after
collar installation)
Collar Half 2
Collar Half 1
Traffic direction

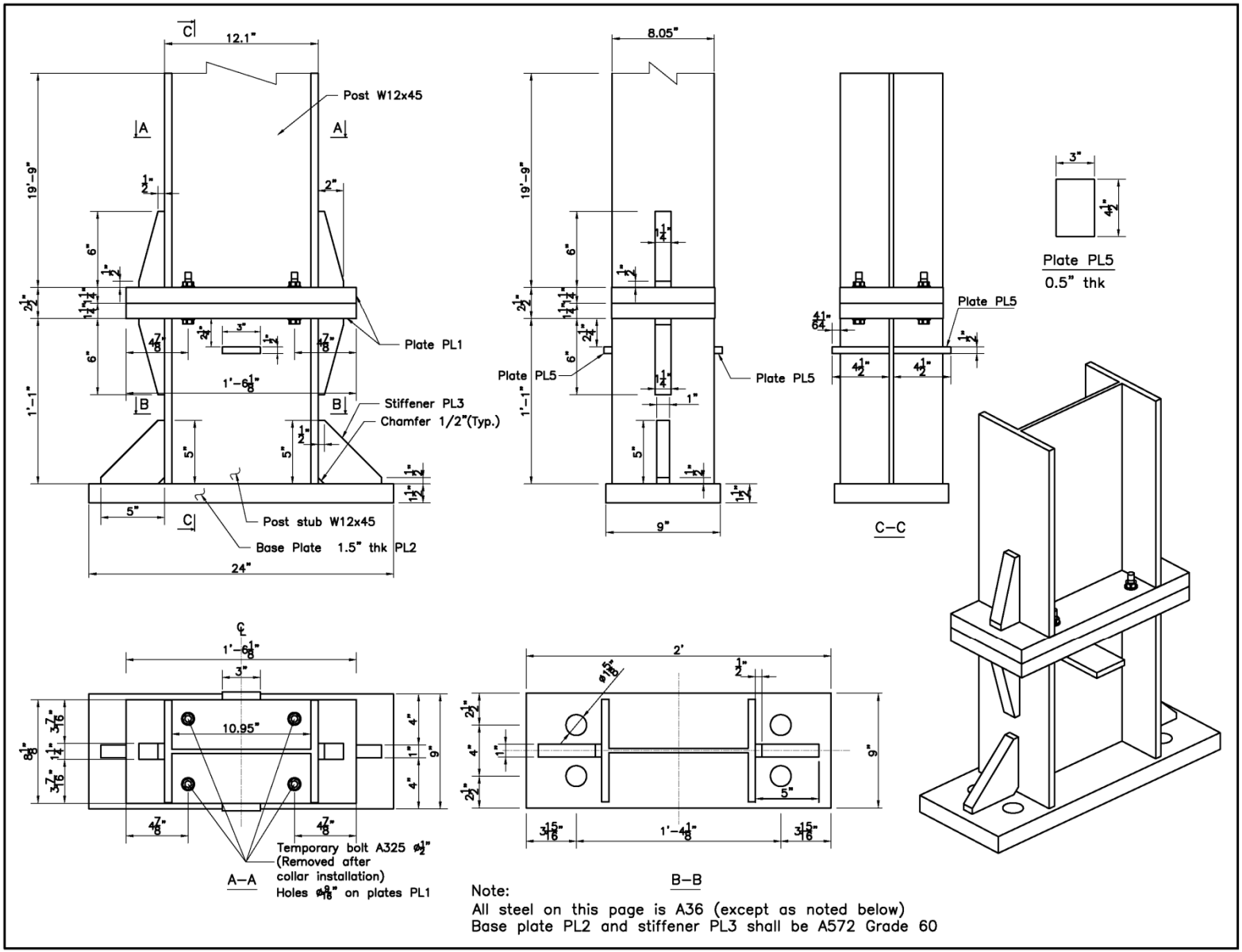
12.1"
Post W12x45
19'-9"
Plate PL1
Stiffener PL3
Chamfer 1/2"(Typ.)
1'-6 1/8"
Post stub W12x45
Base Plate 1.5" thk PL2
24"
8.05"
Plate PL5
9"
C–C
Plate PL5
0.5" thk
10.95"
Temporary bolt A325 ø1"
(Removed after
collar installation)
Holes ø 9/16" on plates PL1
A–A
2'
1'-4 1/8"
B–B
Note:
All steel on this page is A36 (except as noted below)
Base plate PL2 and stiffener PL3 shall be A572 Grade 60

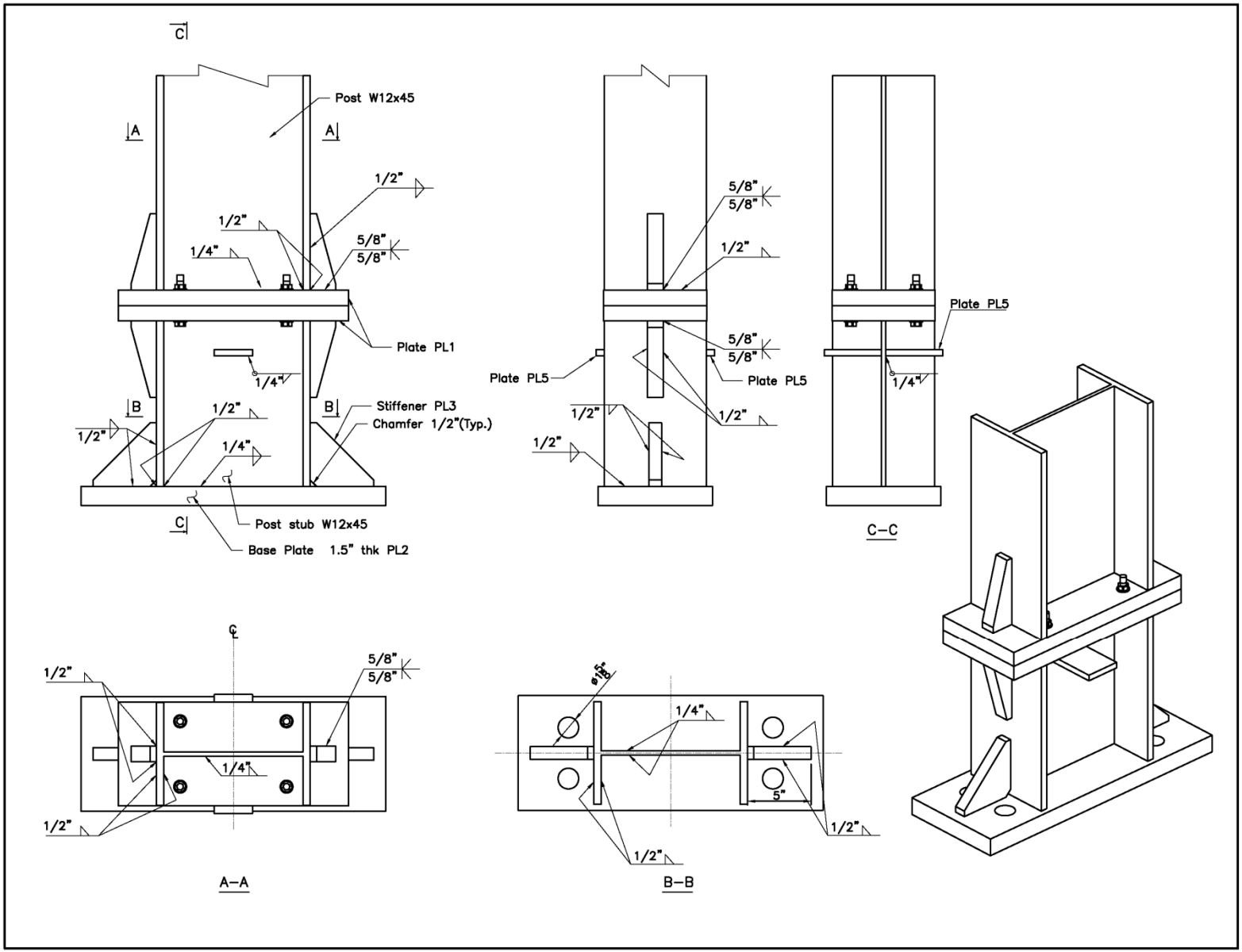
C
Post W12x45
A
A
1/2"
1/2"
1/4"
5/8"
5/8"
Plate PL1
1/4"
B
B
1/2"
1/2"
1/4"
Stiffener PL3
Chamfer 1/2"(Typ.)
C
Post stub W12x45
Base Plate 1.5" thk PL2
5/8"
5/8"
1/2"
5/8"
5/8"
Plate PL5
Plate PL5
1/2"
1/2"
Plate PL5
1/4"
C–C
C
1/2"
5/8"
5/8"
1/4"
1/2"
A–A
1/4"
5"
1/2"
1/2"
B–B

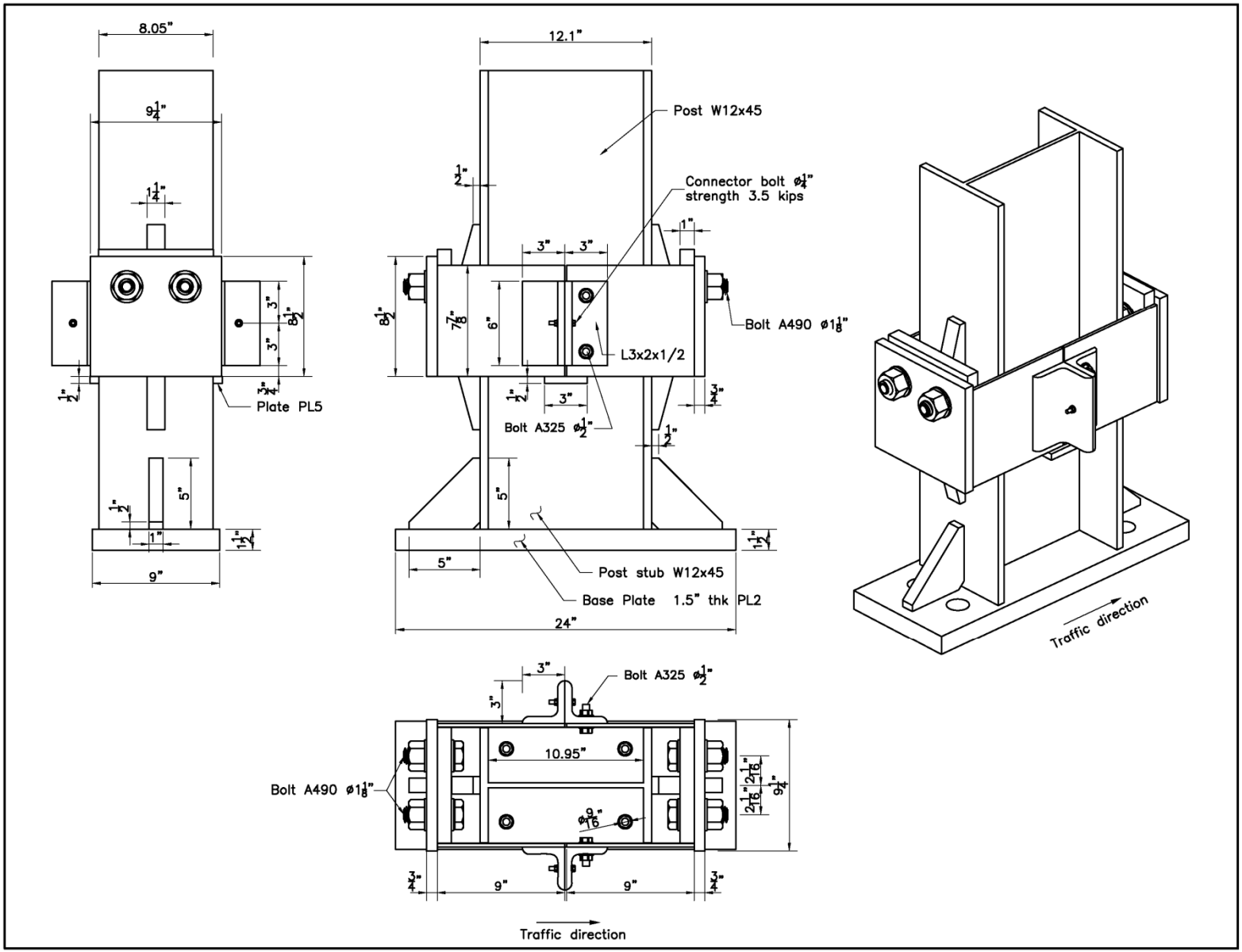
8.05"
12.1"
Post W12x45
Connector bolt ø¼" strength 3.5 kips
Bolt A490 ø1⅛"
L3x2x1/2
Bolt A325 ø½"
Plate PL5
Post stub W12x45
Base Plate 1.5" thk PL2
24"
9"
10.95"
Traffic direction

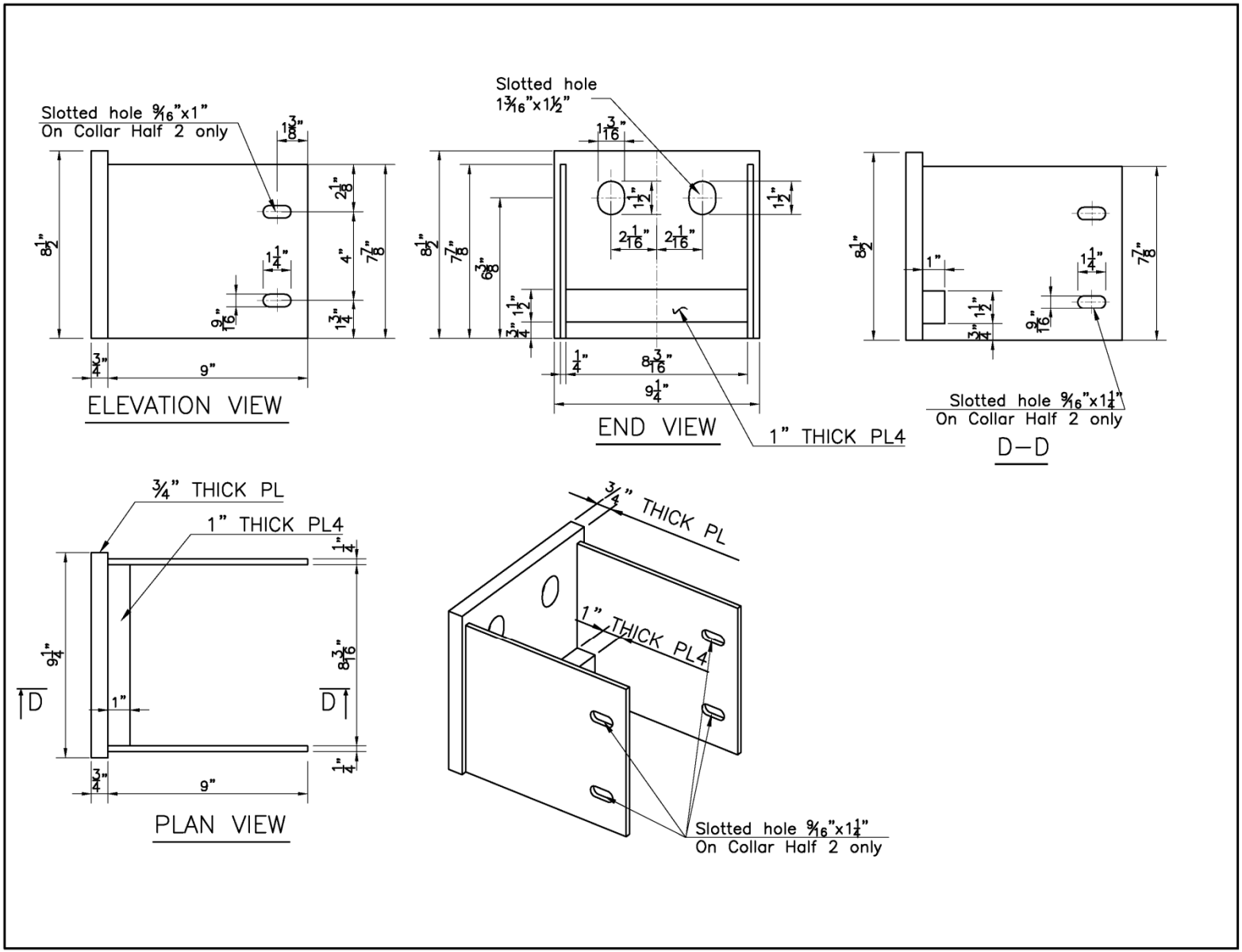
Slotted hole 9/16"x1"
On Collar Half 2 only
ELEVATION VIEW
Slotted hole
1 3/16"x1 1/2"
END VIEW
1" THICK PL4
Slotted hole 9/16"x1 1/4"
On Collar Half 2 only
D–D
3/4" THICK PL
1" THICK PL4
PLAN VIEW
3/4" THICK PL
1" THICK PL4
Slotted hole 9/16"x1 1/4"
On Collar Half 2 only

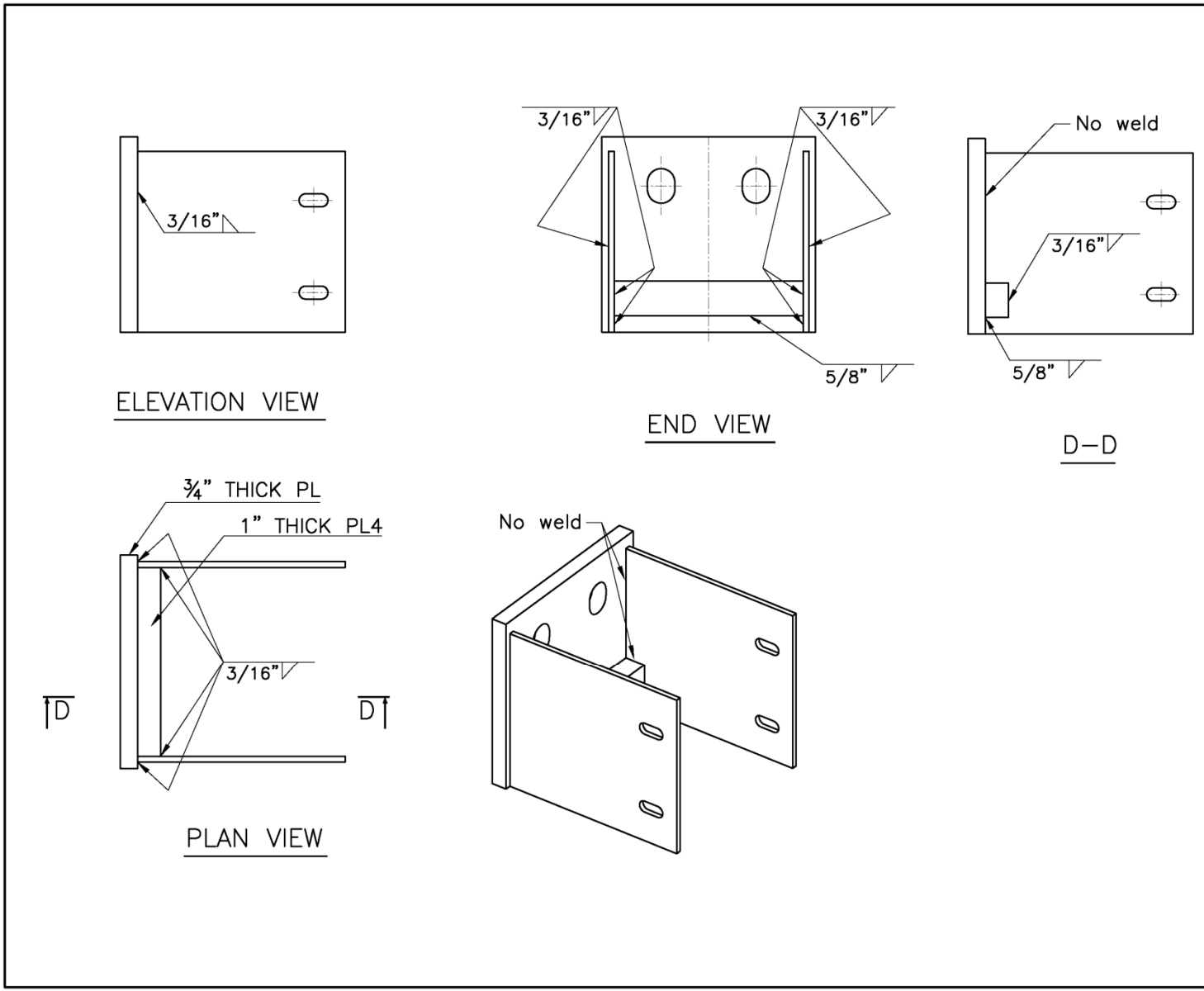
3/16"
ELEVATION VIEW
3/16"
3/16"
5/8"
END VIEW
No weld
3/16"
5/8"
D–D
¾" THICK PL
1" THICK PL4
3/16"
D
D
PLAN VIEW
No weld

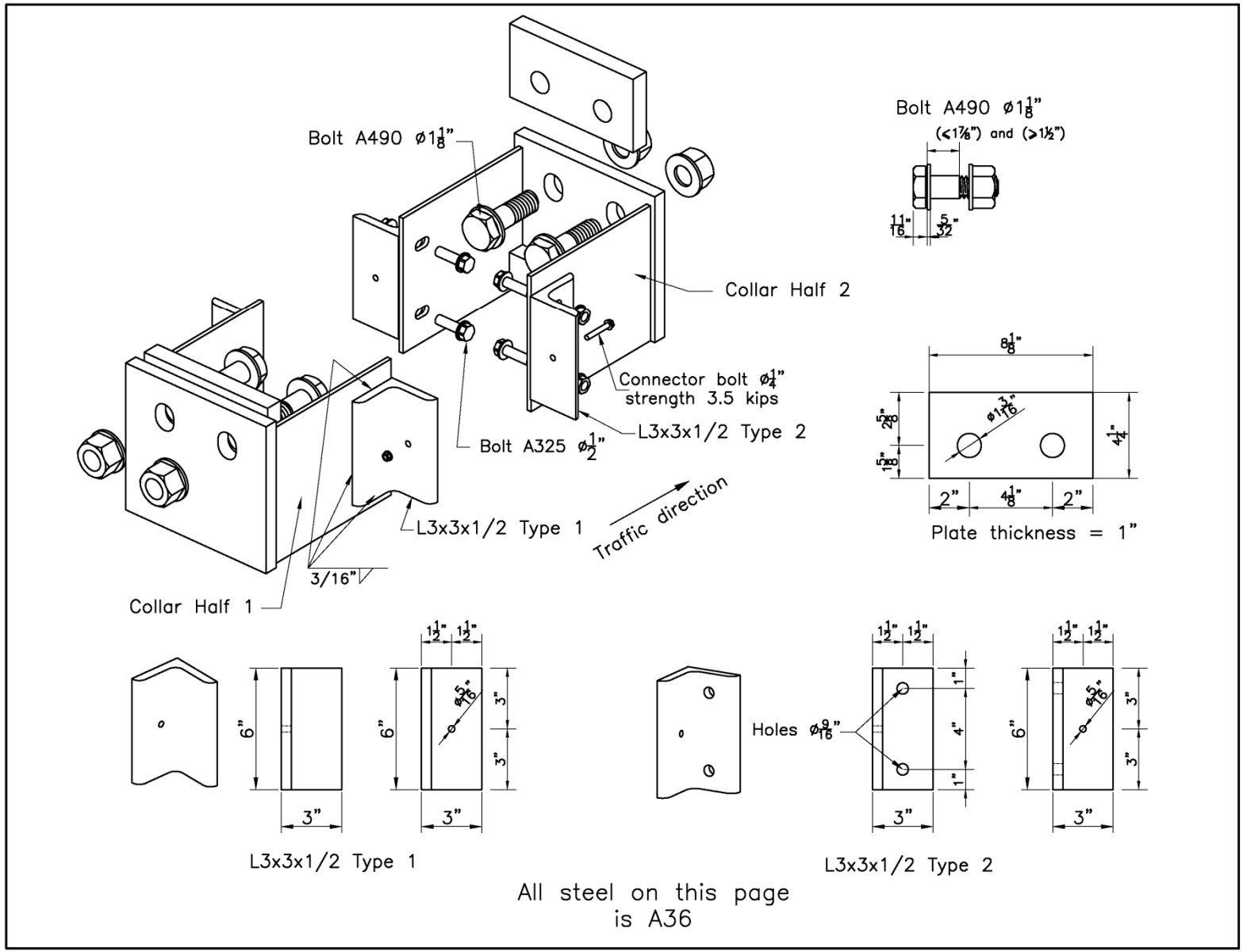
Bolt A490 ø1 1/8"
Collar Half 2
Connector bolt ø1/4" strength 3.5 kips
L3x3x1/2 Type 2
Bolt A325 ø1/2"
L3x3x1/2 Type 1
Traffic direction
3/16"
Collar Half 1
Bolt A490 ø1 1/8"
(≤1 7/8") and (≥1 1/2")
11/16"
5/32"
8 1/8"
2 5/8"
1 5/8"
ø1 3/16"
4 1/4"
2"
4 1/8"
2"
Plate thickness = 1"
1 1/2"
1 1/2"
6"
3"
3"
3"
ø5/16"
Holes ø9/16"
1"
4"
1"
L3x3x1/2 Type 1
L3x3x1/2 Type 2
All steel on this page is A36

APPENDIX E
DRAWINGS OF FINAL DESIGN OF SHEAR-CONTROLLED MOMENT COLLAR BREAKAWAY CONNECTION

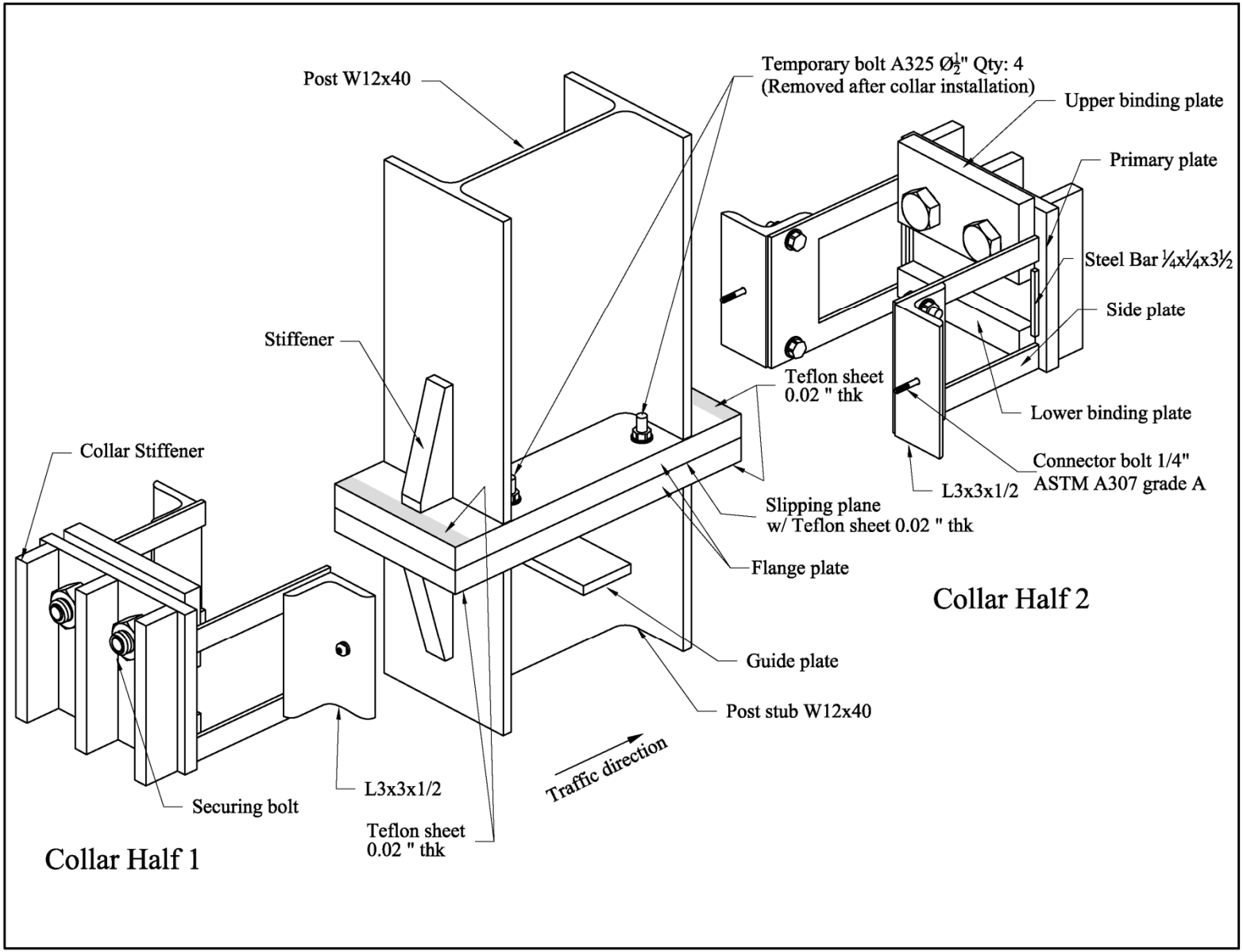
Post W12x40
Temporary bolt A325 Ø½" Qty: 4
(Removed after collar installation)
Upper binding plate
Primary plate
Steel Bar ¼x¼x3½
Side plate
Stiffener
Teflon sheet
0.02 " thk
Lower binding plate
Collar Stiffener
Connector bolt 1/4"
ASTM A307 grade A
L3x3x1/2
Slipping plane
w/ Teflon sheet 0.02 " thk
Flange plate
Collar Half 2
Guide plate
Post stub W12x40
Traffic direction
L3x3x1/2
Securing bolt
Teflon sheet
0.02 " thk
Collar Half 1

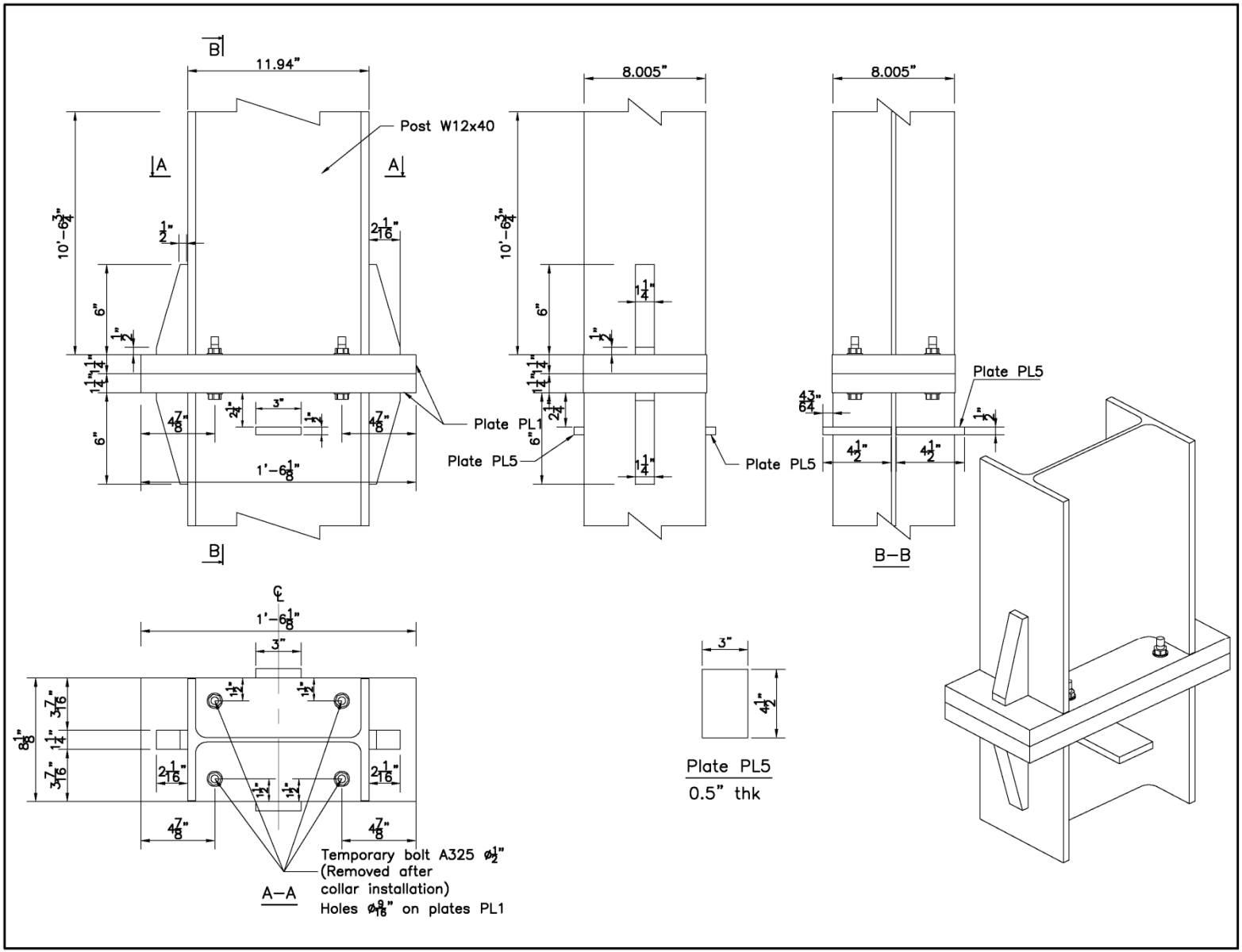
B
11.94"
Post W12x40
A
A
10'-6 3/4"
6"
1"
2 1/16"
1 1/4"
3"
2 1/4"
4 7/8"
1'-6 1/8"
Plate PL1
Plate PL5
8.005"
1 1/4"
Plate PL5
B
B–B
8.005"
Plate PL5
43/64"
4 1/2"
C
1'-6 1/8"
3"
1 1/2"
3 7/16"
1 1/4"
8 1/8"
2 1/16"
4 7/8"
Temporary bolt A325 ø1/2"
(Removed after
collar installation)
Holes ø9/16" on plates PL1
A–A
3"
4 1/2"
Plate PL5
0.5" thk

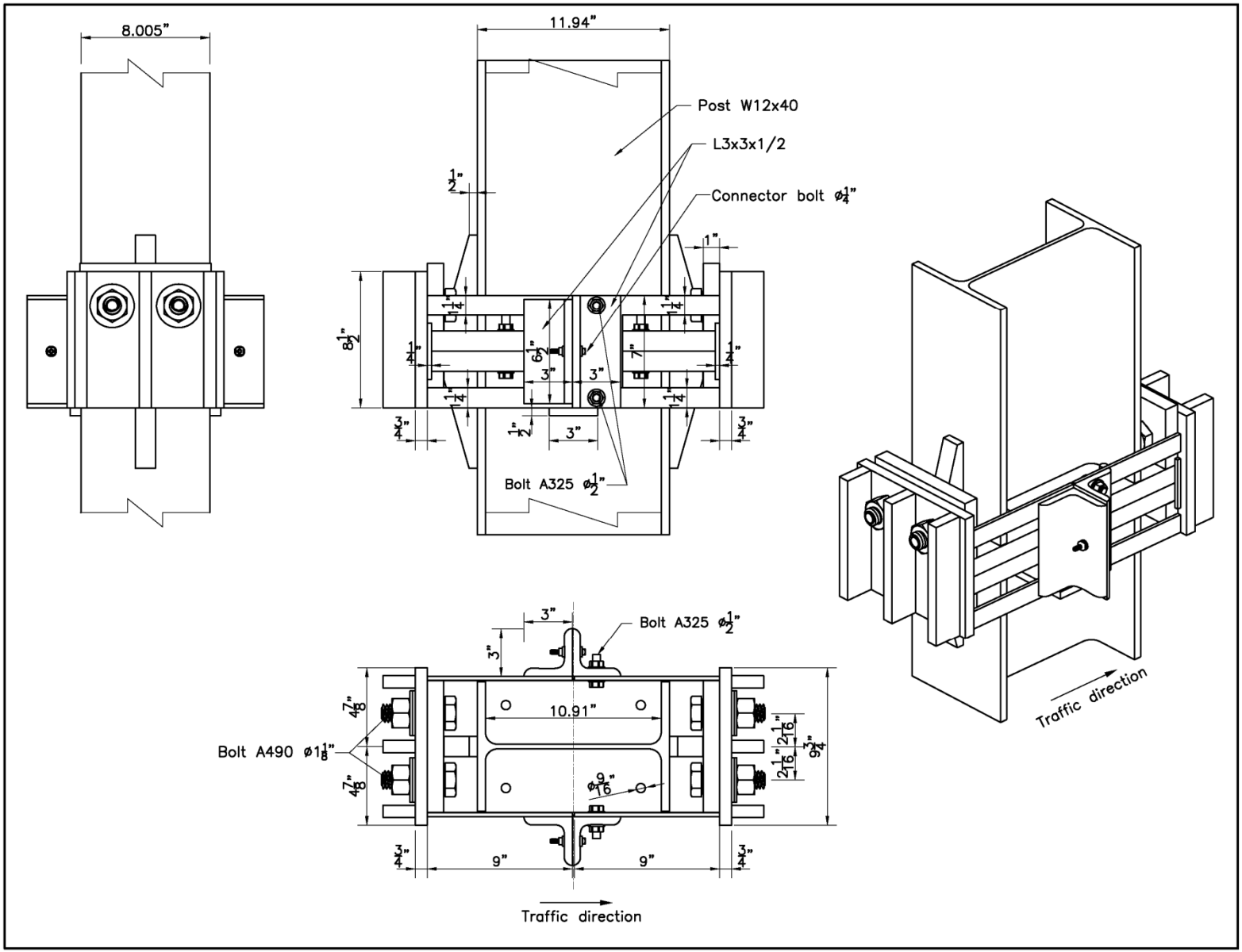
8.005"
11.94"
Post W12x40
L3x3x1/2
Connector bolt ø1/4"
Bolt A325 ø1/2"
Bolt A325 ø1/2"
Bolt A490 ø1 1/8"
10.91"
9"
9"
Traffic direction
Traffic direction

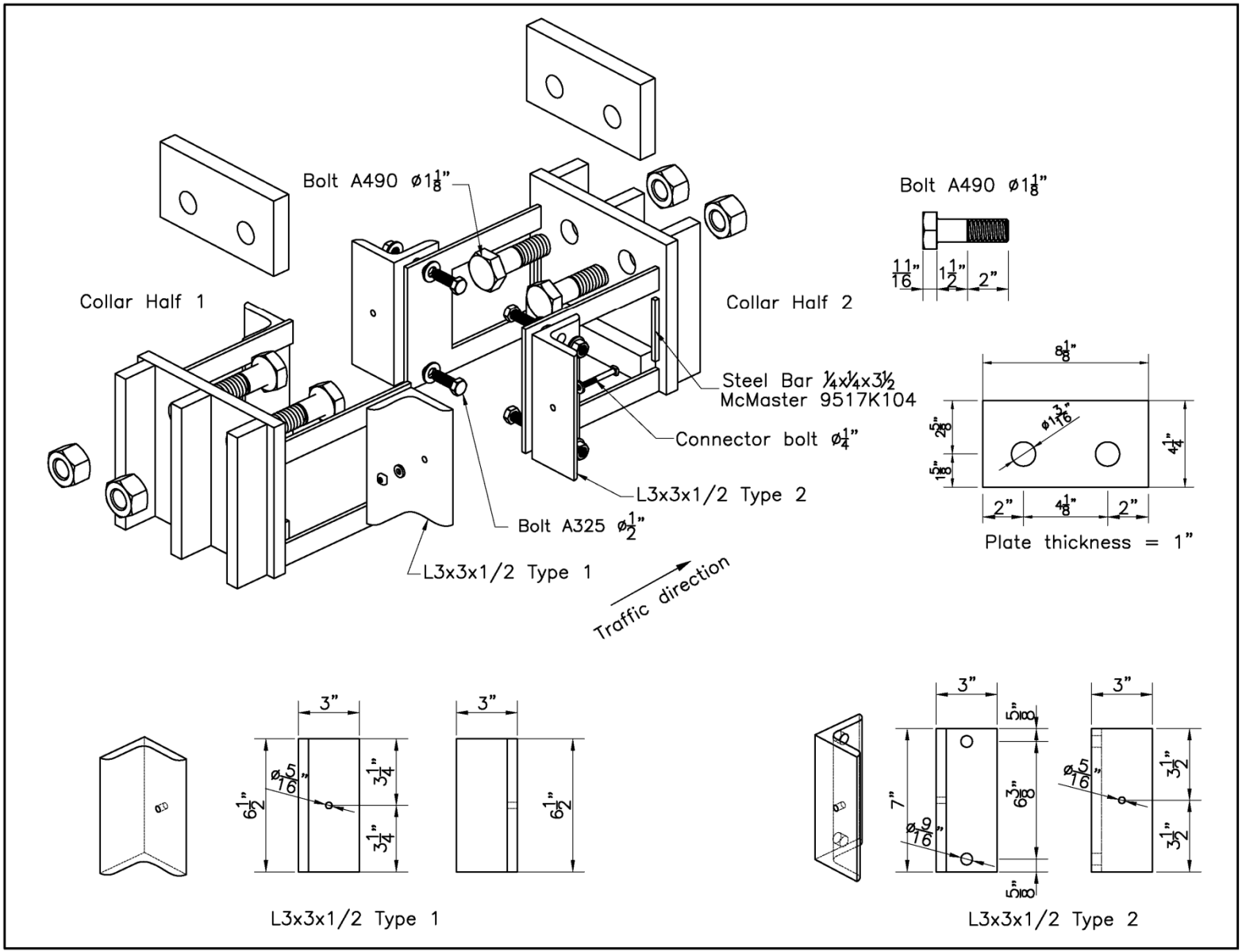
Bolt A490 ø1 1/8"
Collar Half 1
Collar Half 2
Steel Bar ¼x¼x3½
McMaster 9517K104
Connector bolt ø¼"
L3x3x1/2 Type 2
Bolt A325 ø½"
L3x3x1/2 Type 1
Traffic direction
Bolt A490 ø1 1/8"
11/16"
1 1/2"
2"
8 1/8"
ø1 3/16"
5/16"
1 5/16"
4 1/4"
2"
4 1/8"
2"
Plate thickness = 1"
3"
3"
6 1/2"
ø 5/16"
3 1/4"
3 1/4"
6 1/2"
L3x3x1/2 Type 1
3"
3"
5/16"
7"
ø 9/16"
3 6/8"
5/16"
ø 5/16"
3 1/2"
3 1/2"
5/16"
L3x3x1/2 Type 2

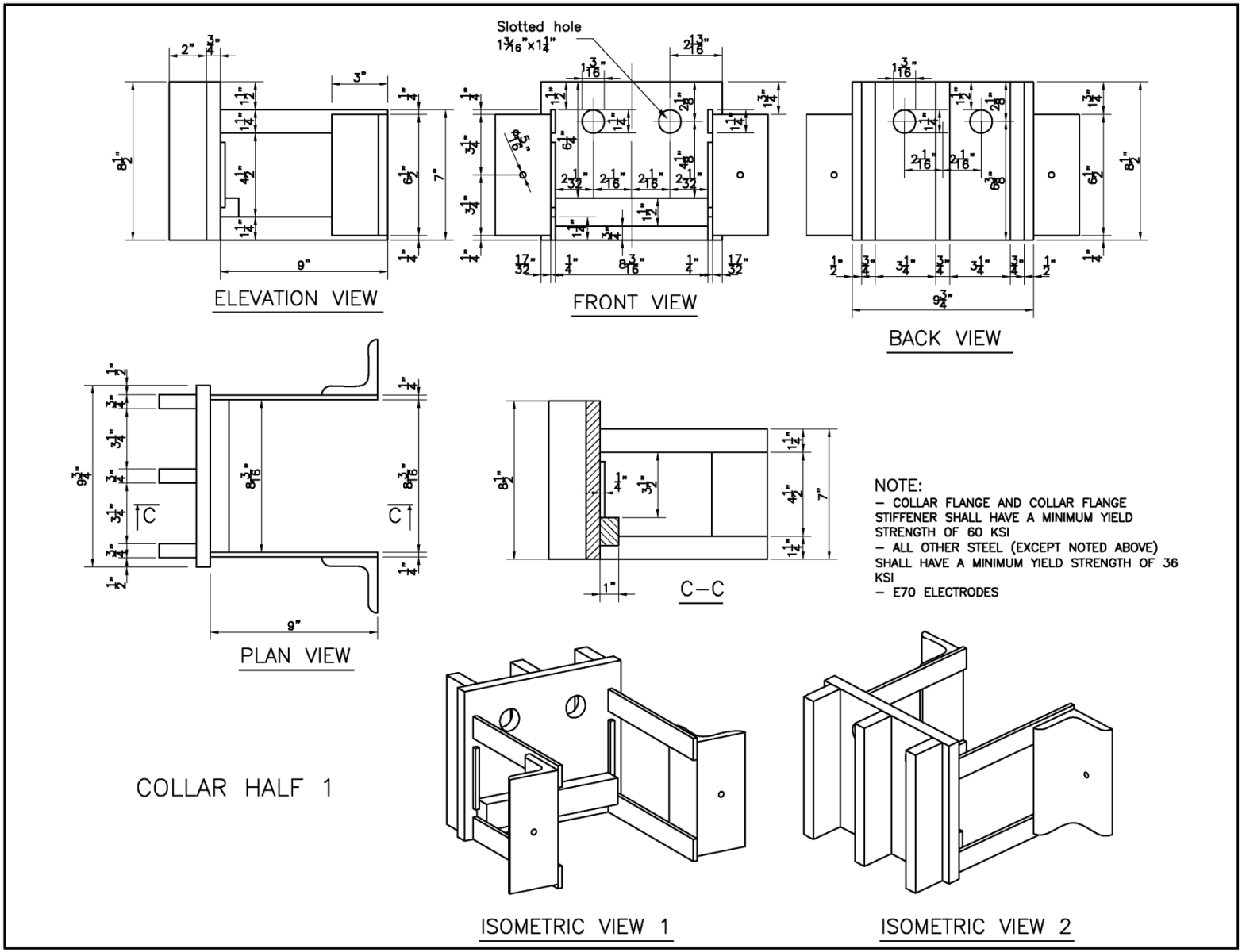
Slotted hole
1 3/16"x1 1/4"
ELEVATION VIEW
FRONT VIEW
BACK VIEW
PLAN VIEW
C–C
NOTE:
– COLLAR FLANGE AND COLLAR FLANGE STIFFENER SHALL HAVE A MINIMUM YIELD STRENGTH OF 60 KSI
– ALL OTHER STEEL (EXCEPT NOTED ABOVE) SHALL HAVE A MINIMUM YIELD STRENGTH OF 36 KSI
– E70 ELECTRODES
COLLAR HALF 1
ISOMETRIC VIEW 1
ISOMETRIC VIEW 2

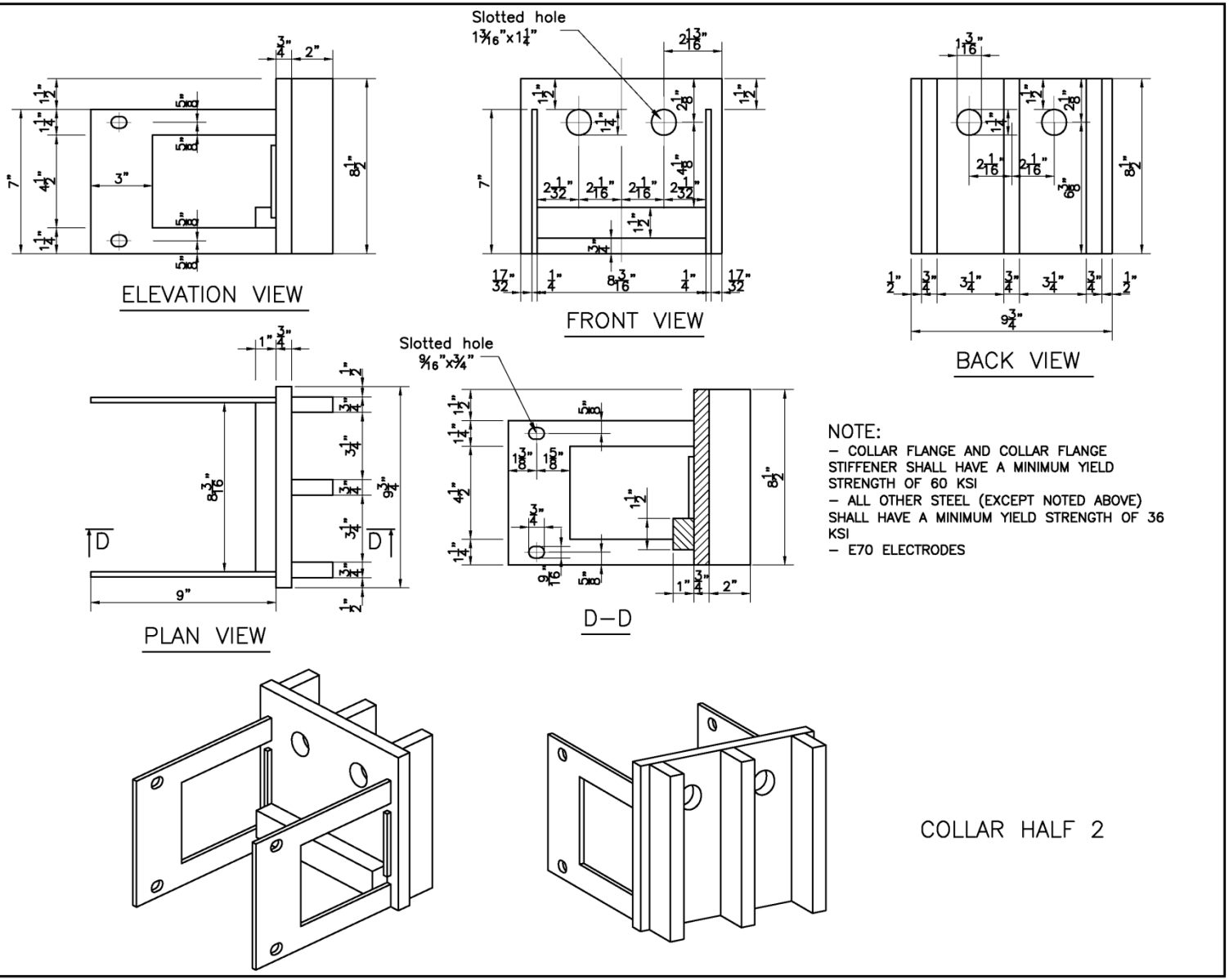
Slotted hole
1 3/16" x 1 1/4"
ELEVATION VIEW
FRONT VIEW
BACK VIEW
Slotted hole
9/16" x 3/4"
PLAN VIEW
D–D
NOTE:
– COLLAR FLANGE AND COLLAR FLANGE STIFFENER SHALL HAVE A MINIMUM YIELD STRENGTH OF 60 KSI
– ALL OTHER STEEL (EXCEPT NOTED ABOVE) SHALL HAVE A MINIMUM YIELD STRENGTH OF 36 KSI
– E70 ELECTRODES
COLLAR HALF 2

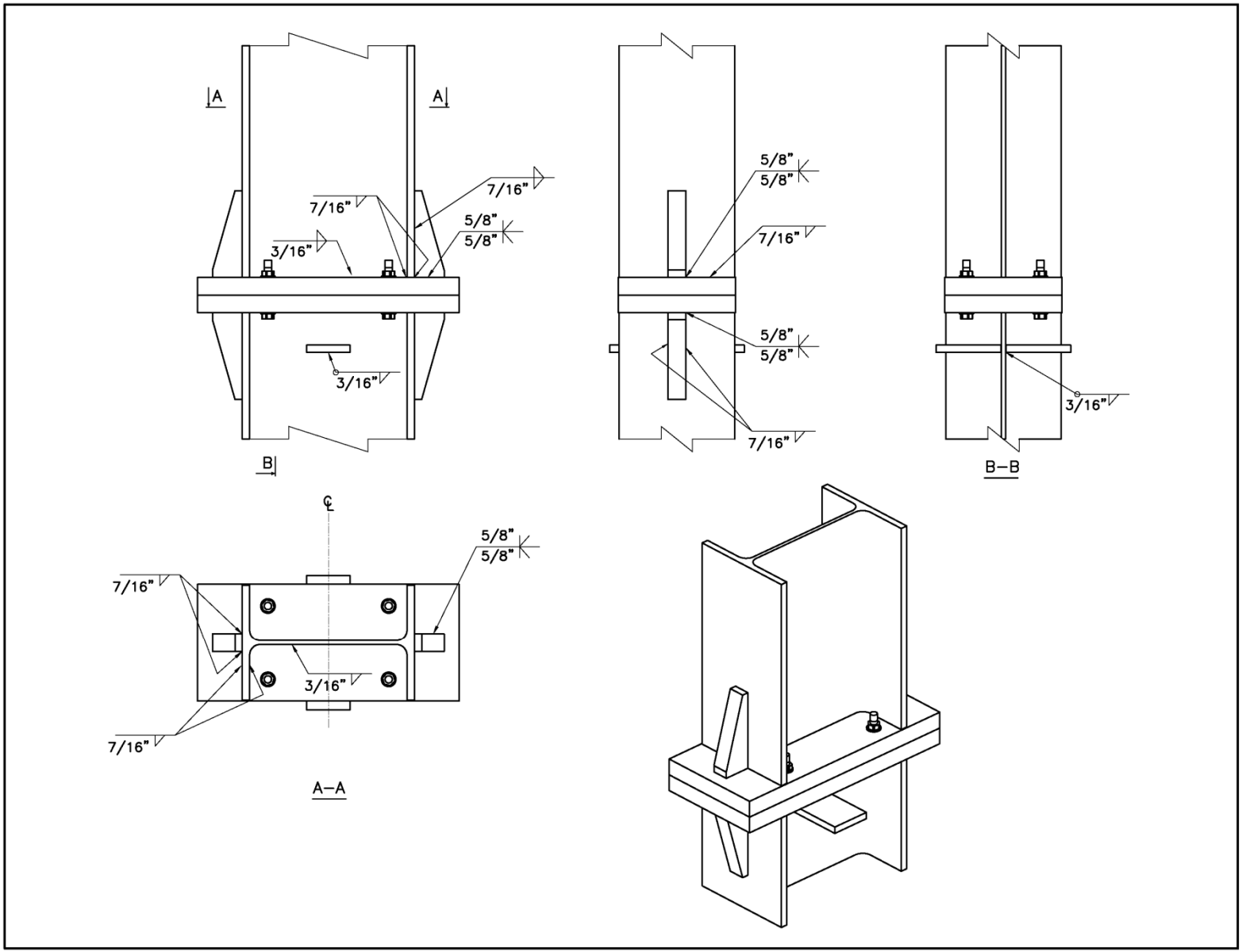
A
A
7/16"
7/16"
5/8"
5/8"
3/16"
3/16"
B
5/8"
5/8"
7/16"
5/8"
5/8"
7/16"
3/16"
B–B
℄
5/8"
5/8"
7/16"
3/16"
7/16"
A–A

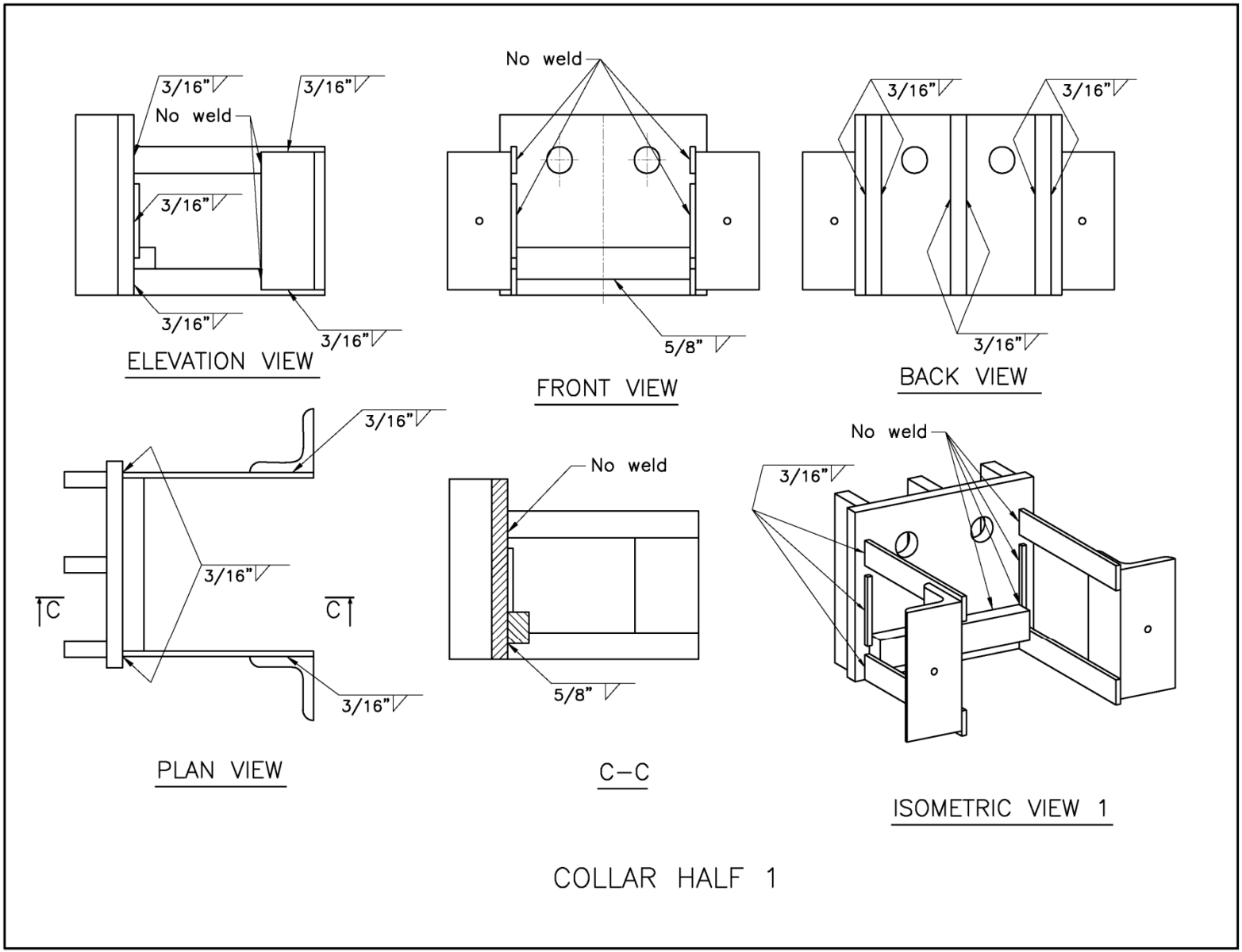
3/16"
No weld
3/16"
3/16"
3/16"
ELEVATION VIEW
No weld
5/8"
FRONT VIEW
3/16"
3/16"
3/16"
BACK VIEW
3/16"
3/16"
3/16"
C
C
PLAN VIEW
No weld
5/8"
C–C
No weld
3/16"
ISOMETRIC VIEW 1
COLLAR HALF 1

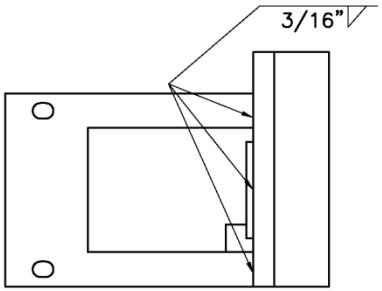

ELEVATION VIEW

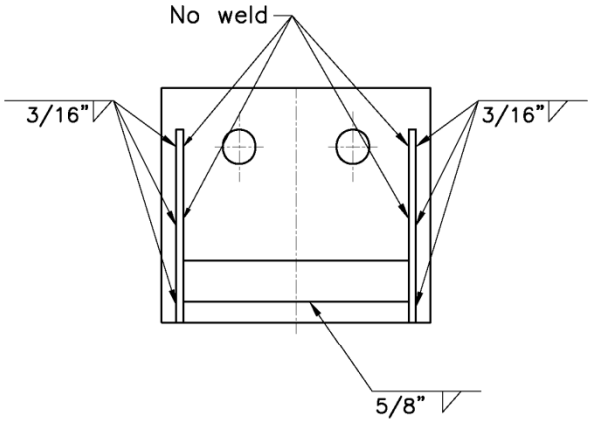

FRONT VIEW

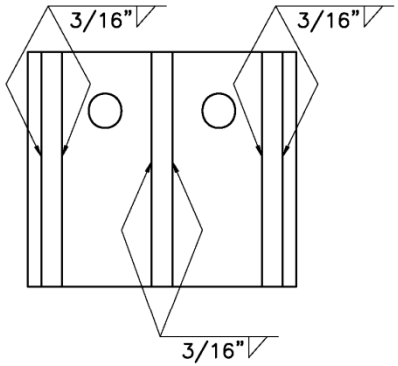

BACK VIEW

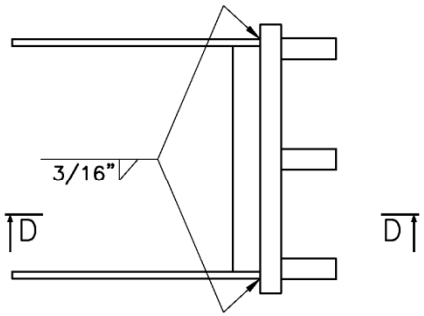

PLAN VIEW

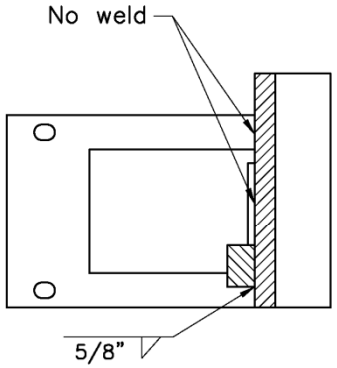

D–D

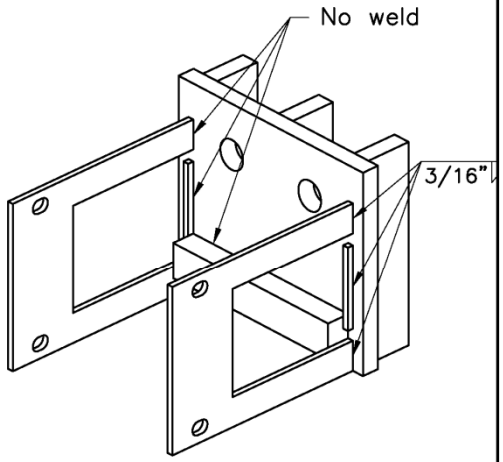

ISOMETRIC VIEW 1

COLLAR HALF 2

APPENDIX F
DRAWINGS OF PENDULUM IMPACTOR AND RIGID NOSE

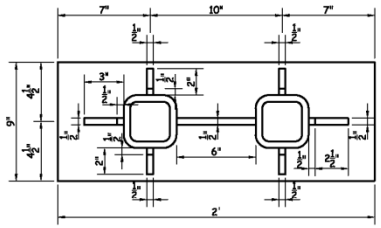

A-A

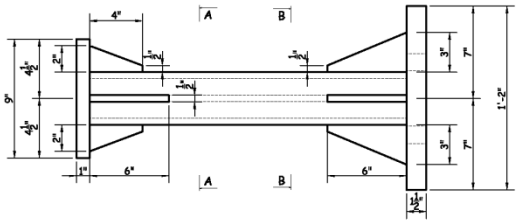

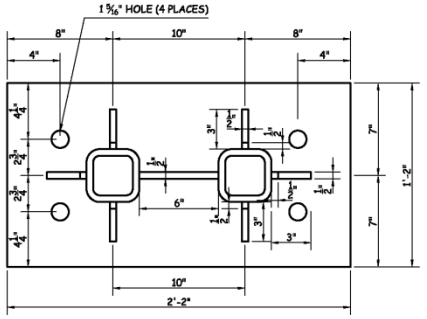

B-B

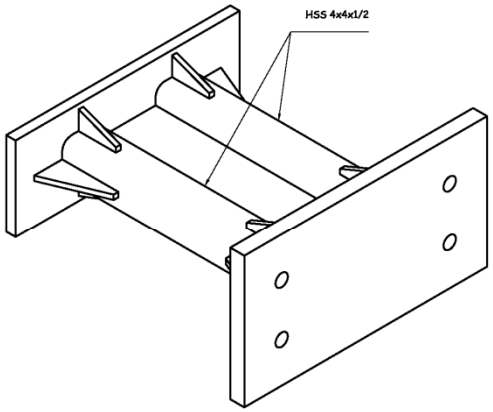

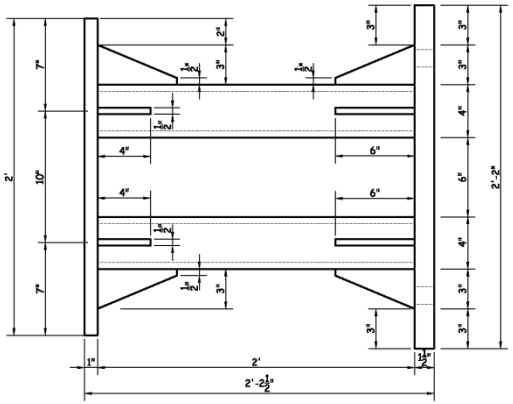

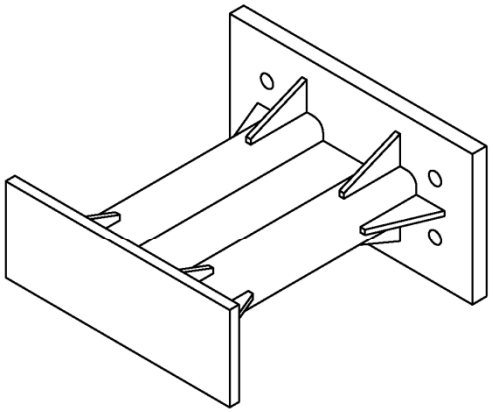

NOTE: Use weld size 3/8" for all weld connections
Steel A36

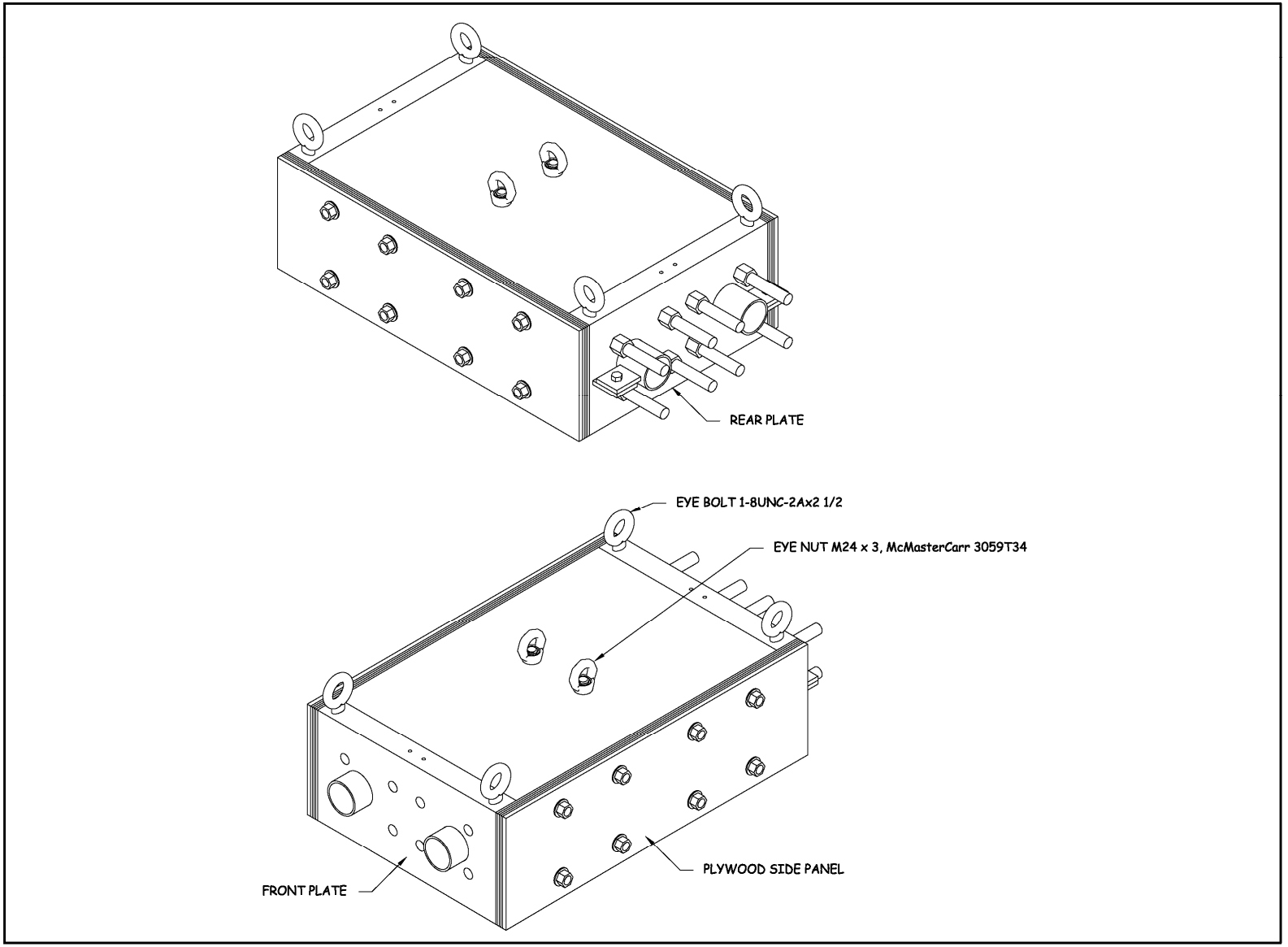
REAR PLATE
EYE BOLT 1-8UNC-2Ax2 1/2
EYE NUT M24 x 3, McMasterCarr 3059T34
FRONT PLATE
PLYWOOD SIDE PANEL

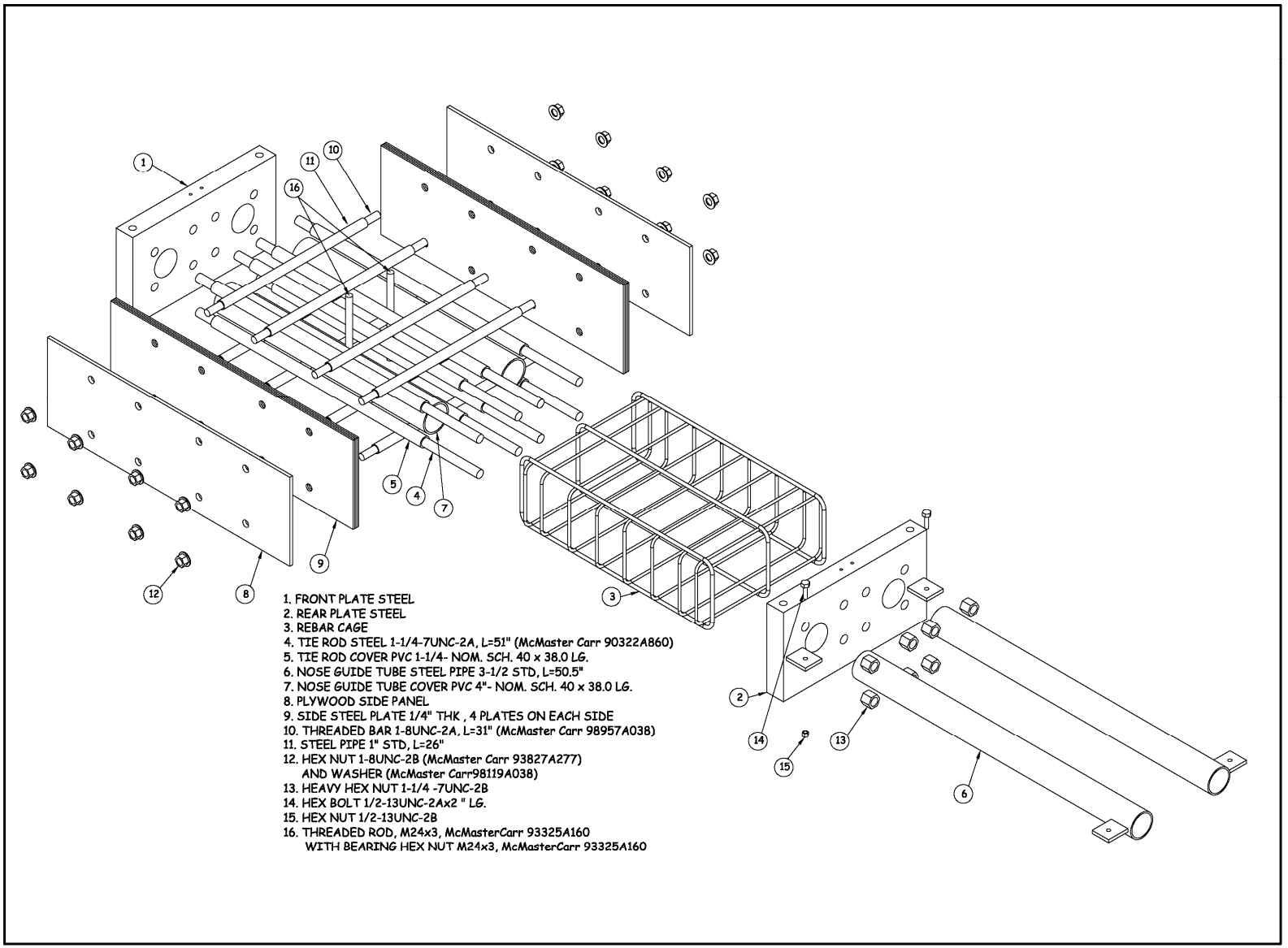

1. FRONT PLATE STEEL
2. REAR PLATE STEEL
3. REBAR CAGE
4. TIE ROD STEEL 1-1/4-7UNC-2A, L=51" (McMaster Carr 90322A860)
5. TIE ROD COVER PVC 1-1/4- NOM. SCH. 40 x 38.0 LG.
6. NOSE GUIDE TUBE STEEL PIPE 3-1/2 STD, L=50.5"
7. NOSE GUIDE TUBE COVER PVC 4"- NOM. SCH. 40 x 38.0 LG.
8. PLYWOOD SIDE PANEL
9. SIDE STEEL PLATE 1/4" THK , 4 PLATES ON EACH SIDE
10. THREADED BAR 1-8UNC-2A, L=31" (McMaster Carr 98957A038)
11. STEEL PIPE 1" STD, L=26"
12. HEX NUT 1-8UNC-2B (McMaster Carr 93827A277)
    AND WASHER (McMaster Carr98119A038)
13. HEAVY HEX NUT 1-1/4 -7UNC-2B
14. HEX BOLT 1/2-13UNC-2Ax2 " LG.
15. HEX NUT 1/2-13UNC-2B
16. THREADED ROD, M24x3, McMasterCarr 93325A160
    WITH BEARING HEX NUT M24x3, McMasterCarr 93325A160

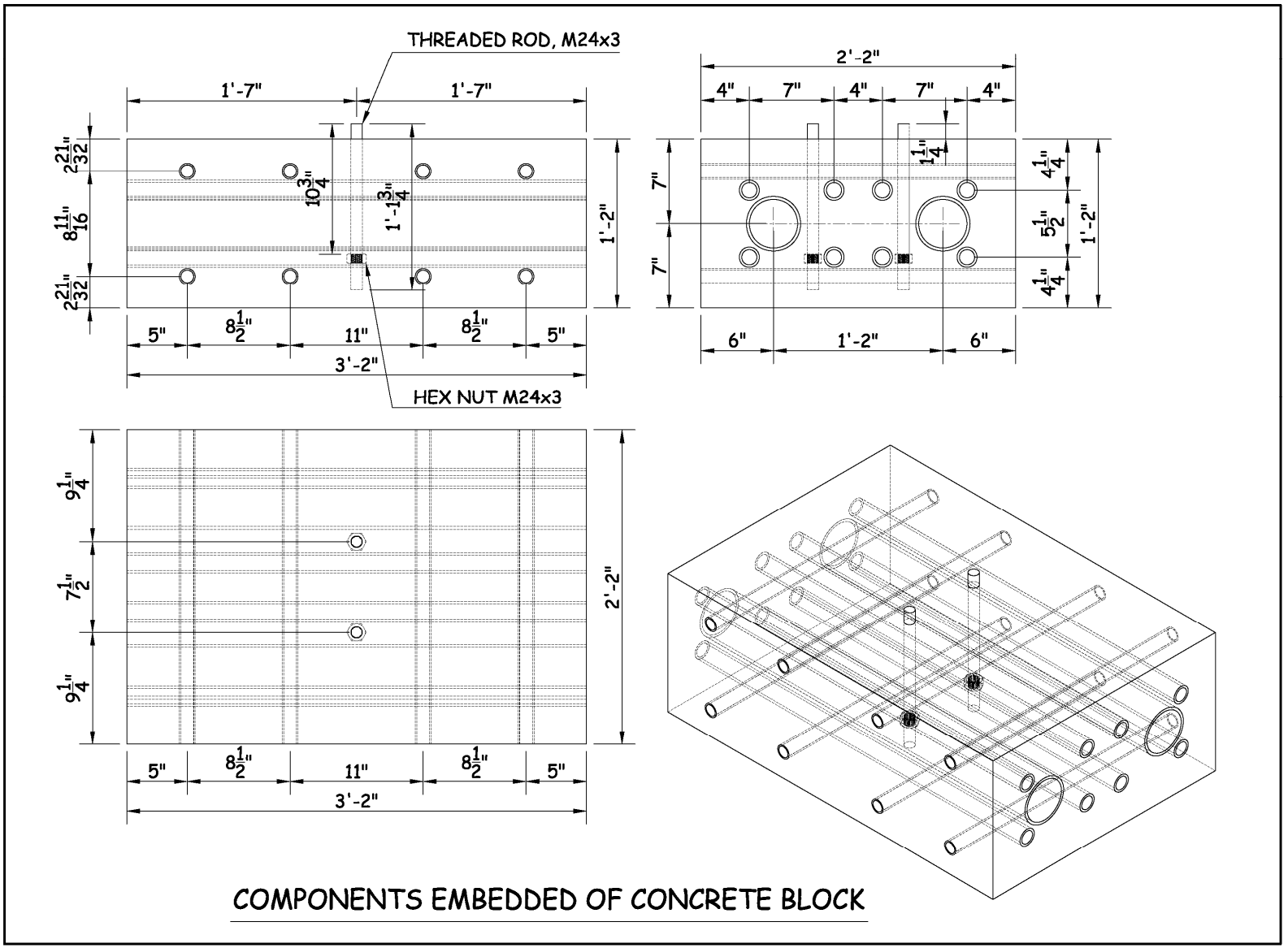

COMPONENTS EMBEDDED OF CONCRETE BLOCK

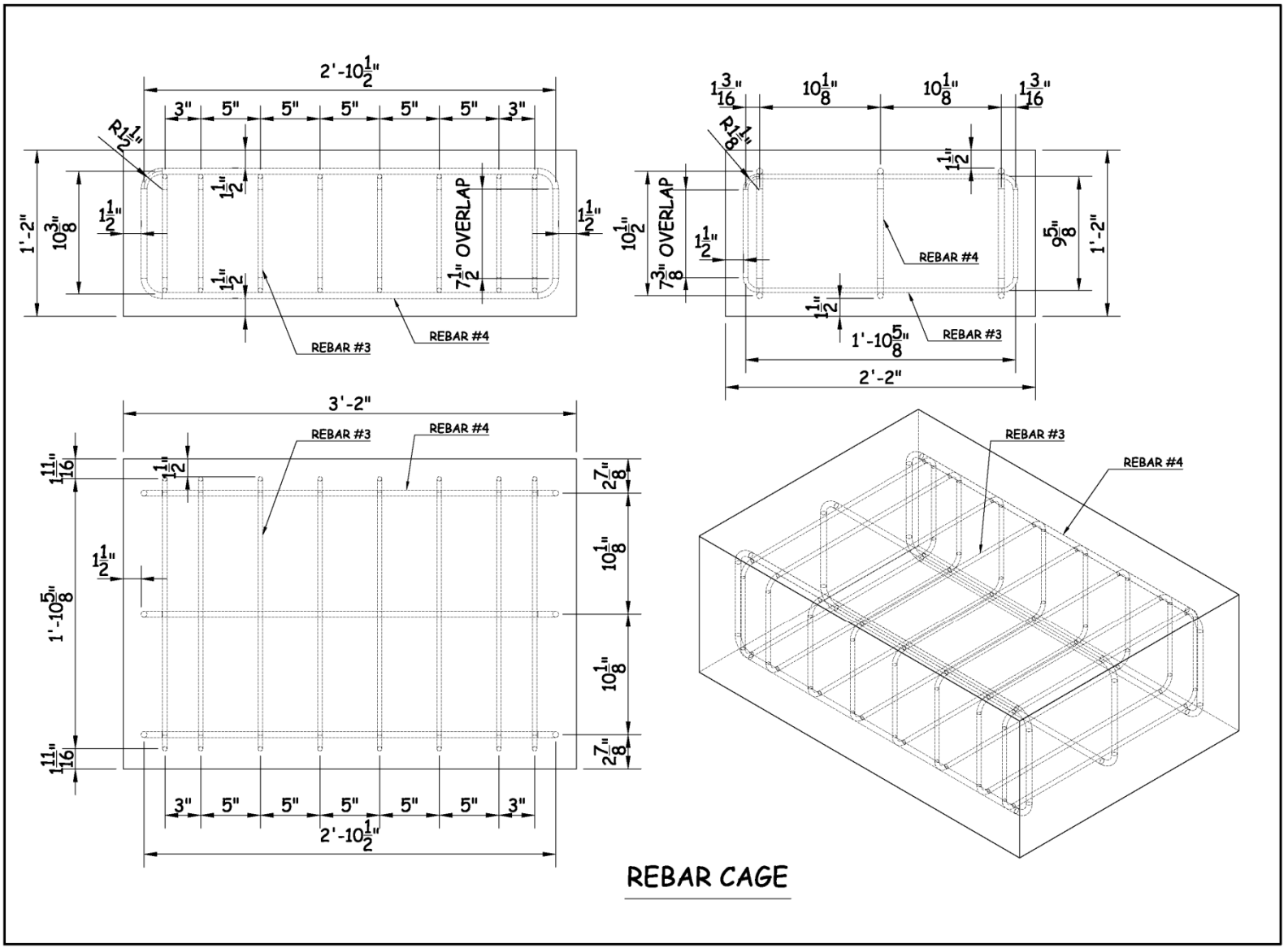
2'-10 1/2"
3" 5" 5" 5" 5" 5" 3"
R1 1/2"
1 1/2"
1'-2"
10 3/8"
1 1/2"
1 1/2"
7 1/2" OVERLAP
1 1/2"
REBAR #3
REBAR #4
1 3/16"
10 1/8"
10 1/8"
1 3/16"
R1 1/4"
1 1/2"
10 1/2"
OVERLAP
7 3/8"
1 1/2"
REBAR #4
9 5/8"
1'-2"
1 1/2"
REBAR #3
1'-10 5/8"
2'-2"
3'-2"
REBAR #3
REBAR #4
1 11/16"
1 1/2"
2 7/8"
1 1/2"
1'-10 5/8"
10 1/8"
10 1/8"
1 11/16"
2 7/8"
3" 5" 5" 5" 5" 5" 3"
2'-10 1/2"
REBAR #3
REBAR #4

REBAR CAGE

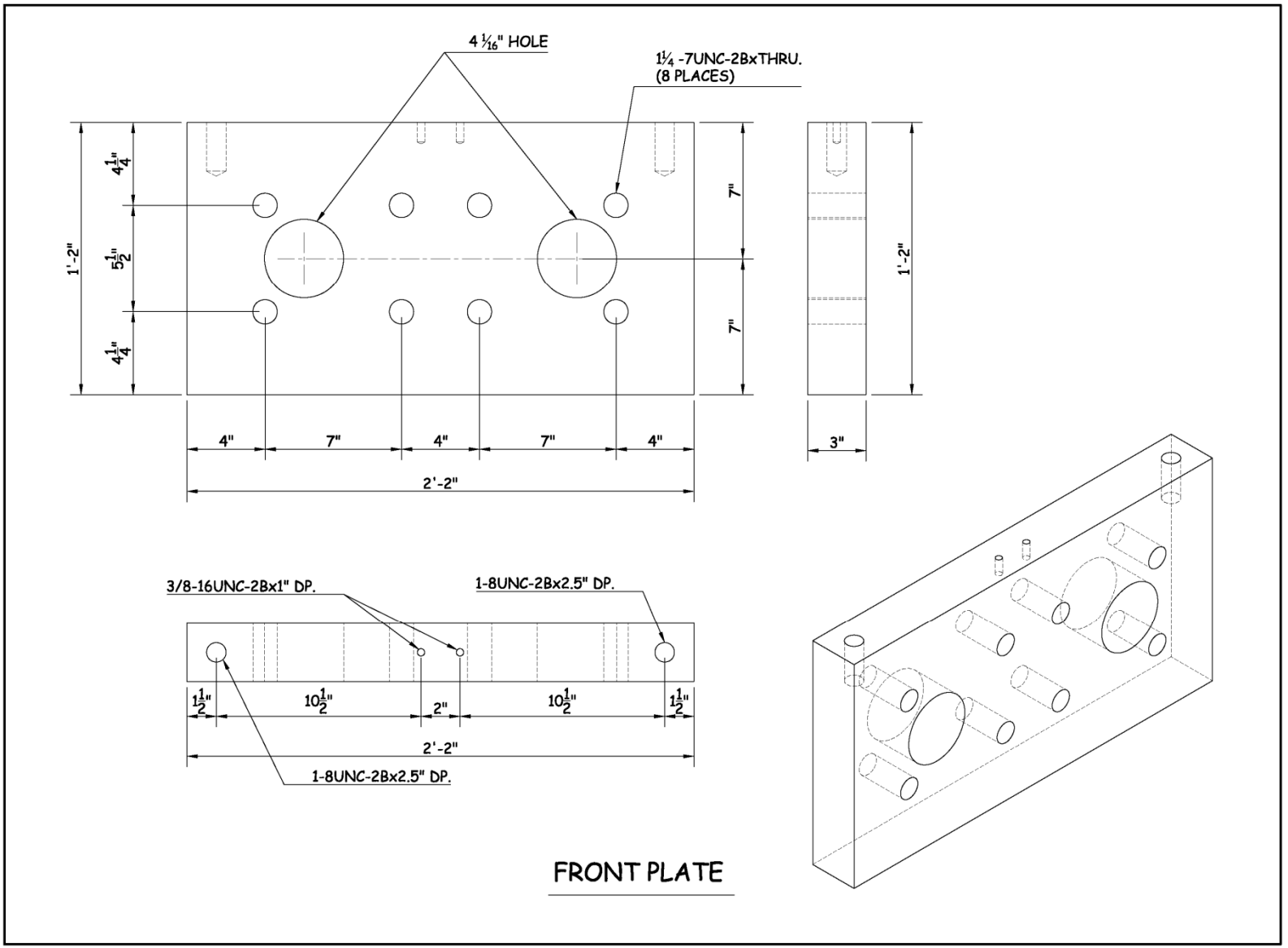
4 1/16" HOLE
1¼ -7UNC-2BxTHRU.
(8 PLACES)
1'-2"
4¼"
5½"
4¼"
7"
7"
1'-2"
4"
7"
4"
7"
4"
3"
2'-2"
3/8-16UNC-2Bx1" DP.
1-8UNC-2Bx2.5" DP.
1½"
10½"
2"
10½"
1½"
2'-2"
1-8UNC-2Bx2.5" DP.
FRONT PLATE

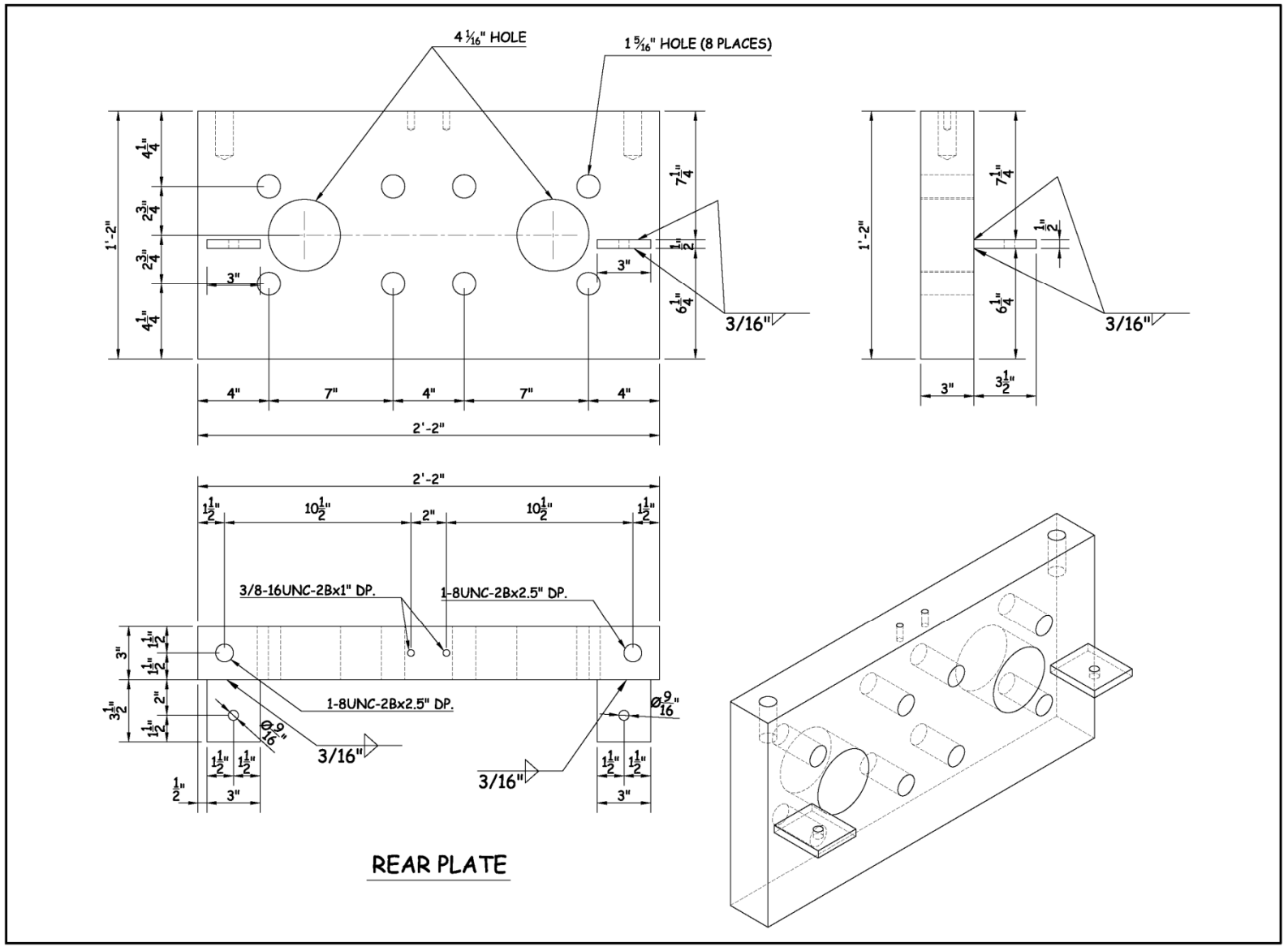
4 1/16" HOLE
1 5/16" HOLE (8 PLACES)
1'-2"
4 1/4"
2 3/4"
2 3/4"
4 1/4"
7 1/4"
1/2"
6 1/4"
3"
3"
3/16"
4"
7"
4"
7"
4"
2'-2"
3"
3 1/2"
2'-2"
1 1/2"
10 1/2"
2"
10 1/2"
1 1/2"
3/8-16UNC-2Bx1" DP.
1-8UNC-2Bx2.5" DP.
1-8UNC-2Bx2.5" DP.
3"
1 1/2"
1 1/2"
2"
3 1/2"
1 1/2"
Ø 9/16"
3/16"
3/16"
1/2"
3"
3"
REAR PLATE

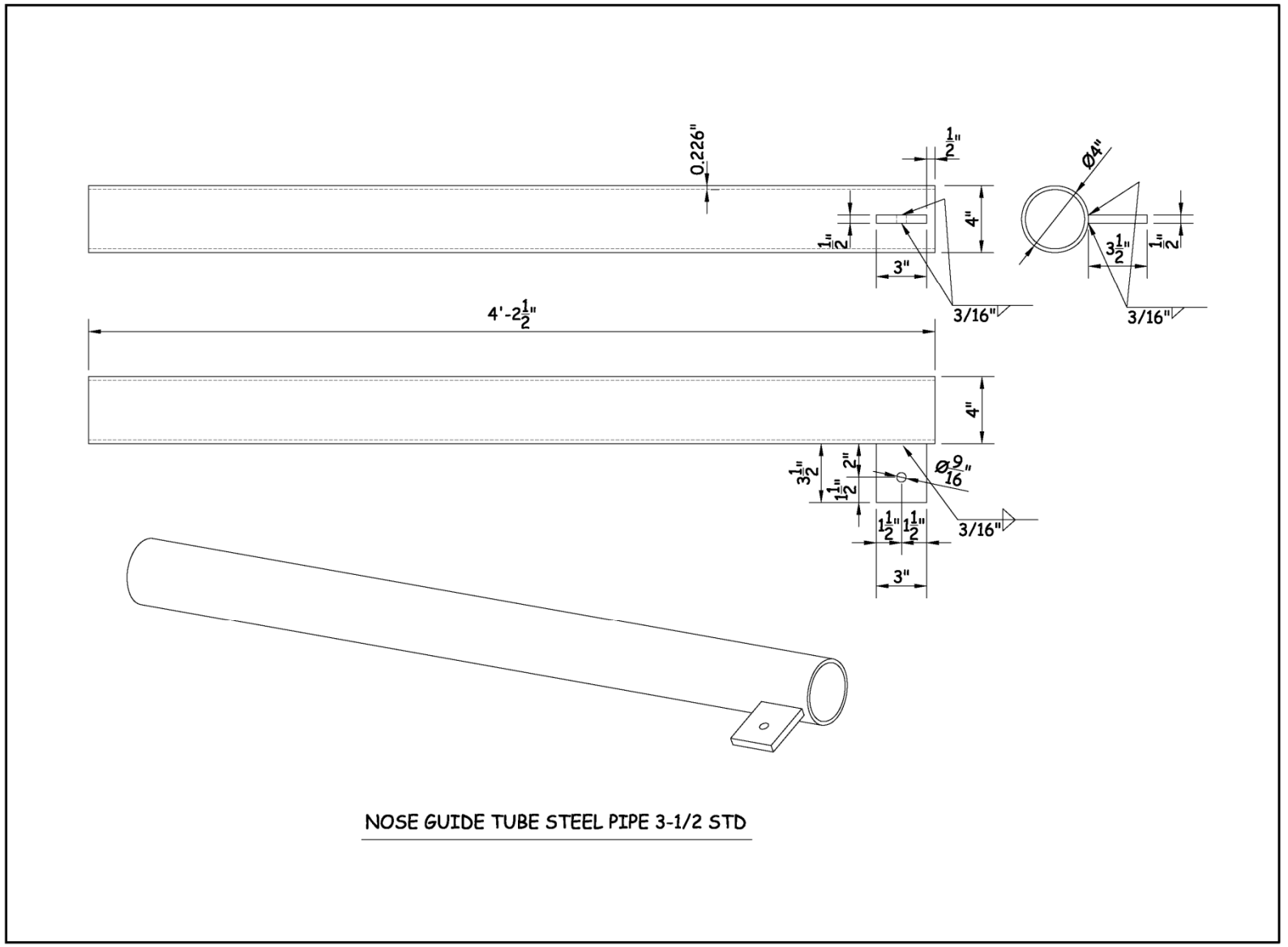

NOSE GUIDE TUBE STEEL PIPE 3-1/2 STD

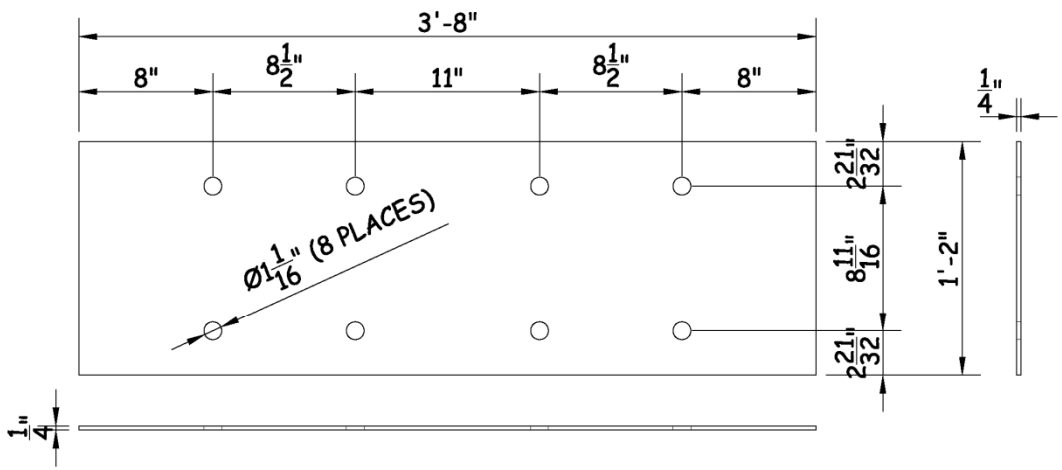

SIDE STEEL PLATE (QTY: 8)

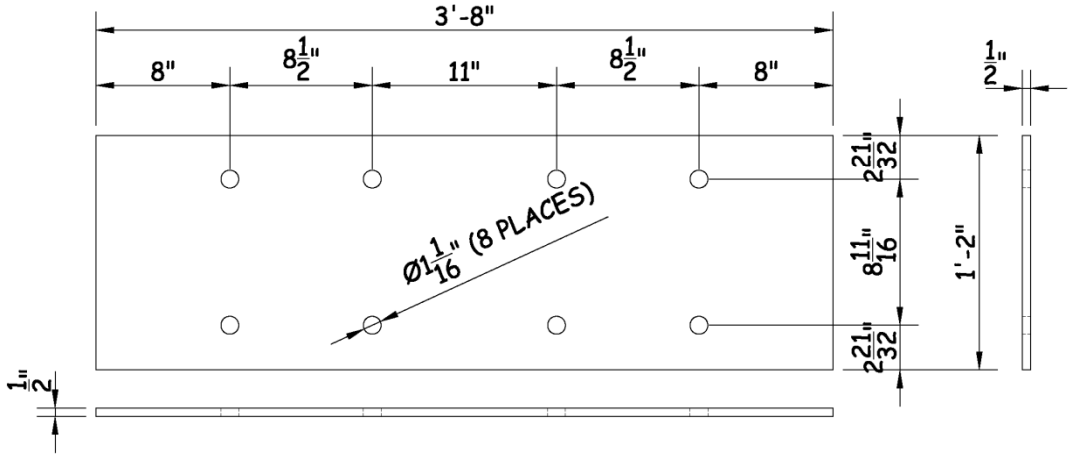

PLYWOOD SIDE PANEL (QTY: 2)

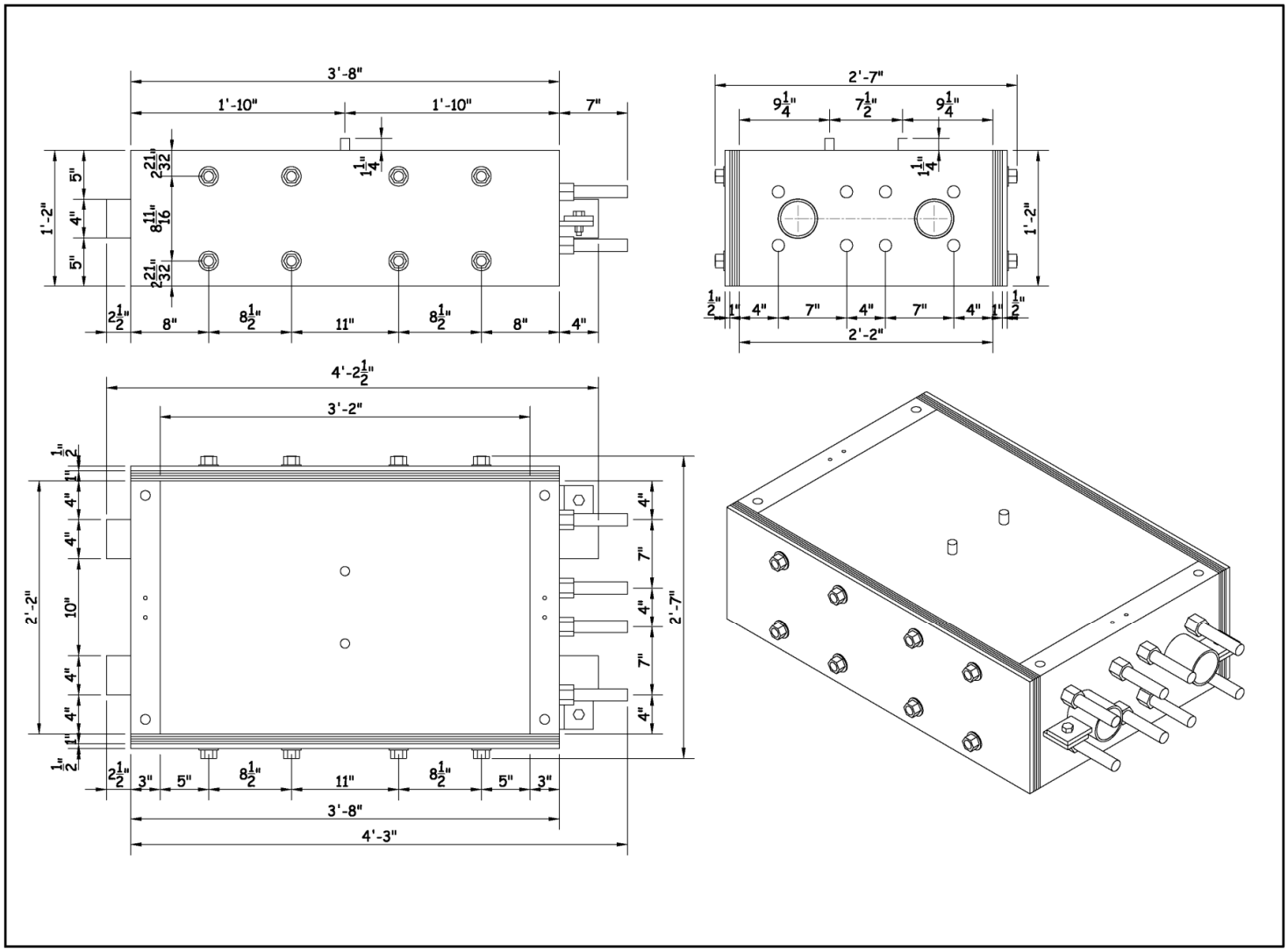
3'-8"
1'-10"
1'-10"
7"
1'-2"
5"
4"
5"
2 21/32"
8 11/16"
2 21/32"
1 1/4"
2 1/2"
8"
8 1/2"
11"
8 1/2"
8"
4"
2'-7"
9 1/4"
7 1/2"
9 1/4"
1 1/4"
1'-2"
1/2"
1"
4"
7"
4"
7"
4"
1"
1/2"
2'-2"
4'-2 1/2"
3'-2"
1/2"
1"
4"
4"
2'-2"
10"
4"
4"
1"
1/2"
4"
7"
4"
7"
4"
2'-7"
2 1/2"
3"
5"
8 1/2"
11"
8 1/2"
5"
3"
3'-8"
4'-3"